Universidad de Valladolid

Escuela de Doctorado Universidad de Valladolid

PROGRAMA DE DOCTORADO EN FISICA

TESIS DOCTORAL:

Modelización de nanodispositivos magnéticos con especial énfasis en los fenómenos de acoplamiento espin-órbita

Presentada por Luis Sánchez-Tejerina San José
para optar al grado de
Doctor por la Universidad de Valladolid

Dirigida por:
Óscar Alejos Ducal y Eduardo Martínez Vecino

Magnetic nanodevices modelization focused on spin-orbit coupling phenomena

Author:
Luis Sánchez-Tejerina San José

Directors:
Óscar Alejos Ducal
&
Eduardo Martínez Vecino

Programa de Doctorado
Doctorado en Física

Departamento de Electricidad y Electrónica
Universidad de Valladolid

Dedicatoria

A mi familia

A Laura

Agradecimientos

Esta tesis se ha escrito en aproximadamente tres años. Podría parecer que tres años es poco tiempo, y realmente lo es. Sin embargo, estos tres años han dado para muchas cosas, muchas experiencias y muchos aprendizajes, la mayoría académicos, un buen número personales. Es de justicia agradecer a aquellas personas que me han acompañado en este viaje y de las que tanto he aprendido.

Quiero empezar expresando mi más profundo agradecimiento a mis tutores, Óscar Alejos y Eduardo Martínez, por lo que me han enseñado, por su apoyo y por su tiempo y esfuerzo. Me gustaría también agradecer el trato recibido por el resto del grupo, tanto en la Universidad de Valladolid (Pablo, Luis, Carlos, José María, etc) como en la Universidad de Salamanca (Víctor, Luis Torres, Luis López, etc). Así mismo, me gustaría agradecer al grupo "Integnano" su acogida y lo mucho que aprendí durante mi estancia en París, especialmente a Liza Herrera, pero también a Carolyna, Sylvain, Tifenn, Maxence, Mamour, Dafiné y Damien. De la misma manera quiero agradecer a Laura Thevenard y Catherine Gourdon por enseñarme su sistema de microscopía magneto-óptica de efecto Kerr y permitirme utilizarlo.

Quiero aprovechar también para agradecer a mis padres, Carmen y Rafael, la educación que me han dado, y a mi padre el apoyo que me sigue dando. Sin él este trabajo no hubiese sido posible. También quiero recordar a mi madre, manifestar que la echo de menos, que sigue señalándome su ausencia. Mención también para mi hermano por su apoyo, cariño y preocupación, aunque no siempre se lo agradezca debidamente. Y por supuesto a mis tíos y a mis primos, que siempre están ahí.

A mis amigos, Carlos, Irene, Santi, Cristina y Álvaro, porque aunque la vida nos haya separado geográficamente seguimos juntos. También a María, Cristina, Andrés y a Marta G. y Marta G^2, porque pocas veces me siento tan cómodo y feliz como en nuestros "cebamientos". Mención aparte merece Fernando con el que he pasado ocho años, desde que empecé la carrera, compartiendo nuestra visión de la Física, y ahora también de la Academia. Fue un placer estudiar con él, y un orgullo contarle entre mis amigos.

Durante estos años he compaginado la tesis con una actividad divulgadora gracias a Physics League. Quiero agradecer a los miembros de esta asociación porque han sido una segunda familia durante estos años. Cuando se madruga un sábado porque nos apetece o pasas un 27 de Diciembre 16 horas fuera de casa puedes plantearte si merece la pena. Pero al final, explicar física a otras personas que no la entienden (o, quiero pensar, que no la entendían) resulta muy satisfactorio. Si además en esa tarea te acompaña esta segunda familia se vuelve un placer. Gracias, de verdad, por esos

momentos. Quiero hacer especial mención a Vero y David, y de nuevo a Fernando, que tanto han contribuido a que este proyecto salga adelante, pero también por las cañas de los Jueves.

Quiero terminar estos agradecimientos con una persona muy especial durante estos años. Gracias, Laura, por prestarme los bolis. Por eso y por alguna cosa más. En particular, “gracias por la parte de esta vida que te corresponde”.

Abstract

Magnetic domain walls are the boundaries between magnetic domains. These structures are efficiently manipulated by means of electric currents due to the spin-orbit coupling phenomena. Thus, new proposals of nanodevices based on magnetic domain wall manipulation are continuously appearing. It is the case of domain wall nano-oscillators or domain wall based magnetic memories. Additionally to its technological appealing, domain walls show a rich complexity which makes them of interest from the fundamental point of view. At the scale considered in the present work, interfacial phenomena play a major role being responsible for the main features considered as the high perpendicular magnetic anisotropy or the presence, along with the strong spin-orbit coupling, of the interfacial Dzyaloshinskii-Moriya interaction. The spin-orbit coupling is the other key feature of the considered system leading to the spin Hall effect. This spin Hall effect along with the interfacial Dzyaloshinskii-Moriya interaction are the main reason for the high efficiency of domain wall motion.

The goal of this thesis is to study and highlight the key role of spin-orbit coupling for the development of spintronic devices. Additionally, the suitability of tailoring the perpendicular magnetic anisotropy to provide a pinning system for domain wall based magnetic memories is shown. Thus, the text is structured in four parts, and an additional conclusions chapter.

The first part deals with the general micromagnetic theory, the numerical solver tools used for micromagnetic simulations, the "general" one dimensional model and a few examples of the experimental techniques that can be used to study multilayered systems, giving the necessary background to understand the work presented.

The second part is devoted to systems with moderate Dzyaloshinskii-Moriya interaction where domain walls are neither Bloch nor Néel but acquire an intermediate configuration. The DW magnetization orientation is a consequence of the equilibrium of all torques. In the absence of external stimuli, all these torques depend on the magnetization configuration. When an external stimulus is applied the previous configuration is, in general, no longer an equilibrium configuration and so the magnetization will evolve in time. It may happen that the magnetization reaches a state characterizes by a constant DW velocity and orientation, which is known as a stationary state. The existence of a stationary state will depend on the amplitude and nature of the applied stimuli. Above a given field, known as Walker's field H_W, there is no longer a stationary state, and a drastic reduction of the DW mean velocity occurs. In systems with moderate DMI three scenarios are possible when applying a stimulus. The first one, when two possible stationary states can be reached. The second one, when there is only one possible stationary state. Finally, the third scenario is characterized by the lack of a stationary state.

Part III analyses the consequences of applying an electric current noncollinear with the longitudinal axis of the ferromagnetic strip. An electric current produces its

maximum torque when it is collinear with the magnetization. However, this torque not only produces a domain wall displacement but also the rotation of the domain wall magnetization, reducing its effect. Then, it is possible to apply a noncollinear current which twists the magnetization to be collinear with it, maximizing the torque, and thereby the DW velocity, at the stationary regime. For a region where the magnetization is pointing along the opposite direction, the current will further misalign the magnetization, reducing the torque and the domain wall velocity. Two consecutive domain walls in a ferromagnetic layer where a rather high interfacial Dzyaloshonskii-Moriya interaction is present have opposite directions due to the quiral character of the Dzyaloshonskii-Moriya interaction. Thus, these two domain walls have different velocities if a noncollinear current is applied, and the magnetic domain between them is reduced or increased depending on which domain wall is faster.

Finally, part IV examines the current-driven domain wall motion in a ratchet ferromagnetic strip. This kind of memory is an enhancement of the racetrack memory which allows for better control of the domain walls position. This control is achieved by tailoring the perpendicular magnetic anisotropy energy profile so as to present a saw-toothed profile. Thereby, in the absence of external stimuli, there is a well-defined set of local energy minima where domain walls are pinned. Such pinning system precisely determines the possible domain wall positions at equilibrium, and so bit size and bit positions.

Contents

Chapter 1

Introduction

1.1 Micromagnetics

Micromagnetics has stimulated the study of magnetism and magnetic materials. It can be said to begin in 1935 with the study of Landau and Lifshitz about magnetic domain walls [1]. However, it is not until 1957, when rigorous nucleation-field theory appeared [2], that micromagnetics obtained the required attention [3]. This interest in micromagnetics is not only based on its theoretical importance, but also on its technological relevance. Micromagnetics has shown its utility in the design of novel spintronic and magnetoelectronic devices [4–6] and has provided insightful answers about its behavior.

This field examines ferromagnetic materials on a scale "*small enough to reveal details of the transition regions between domains, yet large enough to permit the use of a continuous magnetization vector rather than of individual atomic spins*" [3]. At this scale, these transition regions, i.e., domain walls (DW), have a non-negligible thickness and magnetization smoothly changes throughout it. However, this scale must be still rather large so as magnetization can be characterized by a continuous vector field rather than a discrete spin distribution. This theory is the appropriate one to study mesoscopic systems, where Domain Theory cannot be applied but a microscopic study is unapproachable.

The development of fabrication techniques for magnetic nanodevices and the measurement tools to determine its properties has been accompanied by the development of different algorithms to numerically solve the Landau-Lifshitz-Gilbert (LLG) equation. These algorithms have allowed a deeper comprehension of the details of static and dynamic behaviors of magnetization. As a consequence, more efficient and reliable devices have been obtained.

1.2 Multilayered systems and characteristic phenomena.

Multilayered systems, formed by several layers of different materials, have been the focus of intense research in recent years [7–23]. These multilayered systems are

used in several devices nowadays. Magnetic random access memory (MRAM), spin valves, or some kinds of magnetic sensors are based on giant magnetoresistance (GMR) effect [24–26]. Some multilayered systems where two ferromagnetic (FM) layers can be parallel or antiparallel show a different electric resistance for this two configurations. The dramatic dependence of the resistance on the magnetic configuration of the system is known as GMR effect. Nowadays, intense research is focused on the development of a DW-based magnetic memory as the racetrack memory [27, 28] proposed by Parkin. The latest racetrack concepts are based on the use of multilayers [28] since they may exhibit some effects that made them the most promising proposals.

One of these effects is the presence, for rather thin layers of a few nanometers, of high perpendicular magnetic anisotropy (PMA) due to interface phenomena [29–36]. DW based magnetic memory devices can take advantage of this PMA since DW thickness between perpendicular domains are usually narrower than that for in-plane domains [28, 36]. This is the reason why multilayered systems with PMA are said to be a promising structure to obtain denser bit recording than those containing in-plane domains. The systems studied in this thesis always consider FM strips with high PMA and thus perpendicular domains.

Besides, other phenomena that have been demonstrated to have a key role in the fast and efficient DW motion in multilayered systems must be considered. These phenomena are the Dzyaloshinskii-Moriya interaction [14, 17, 21, 37–48] (DMI) and the spin Hall effect [9, 10, 44, 49–56] (SHE). The origin of these effects is the strong spin-orbit coupling (SOC) of a heavy metal (HM) layer. It is well-known [57] that the orbital angular momentum of a charged particle interacts with its spin angular momentum. This interaction causes a splitting of the energy levels as a function of the spin. This effect is called SOC. Throughout this text, a strong SOC is considered to be present in the HM layer of the multilayer, being responsible for an interfacial DMI (iDMI) at the HM/FM layer interface. Moreover, this SOC promotes a perpendicular spin current when an in-plane electric current is applied along the HM due to the SHE.

The DMI arises from a strong SOC along with the lack of inversion symmetry. This lack of inversion symmetry is present in some bulk materials, such as the cubic B20 compound MnSi [58–60], but the interest is focused on iDMI of thin films where the inversion symmetry along the perpendicular axis is broken [61]. In the latter case, the inversion asymmetry is obtained by capping the FM by a layer that differs from the beneath HM which is, as it has been already mention, the layer with strong SOC. The difference may lie either in the thickness [20, 46] of the capping layer or in the material used, commonly an oxide [21] (Ox). Therefore, throughout this thesis, a FM layer sandwiched between a HM and an Ox is considered. One of the most important features of this interaction is that it imposes a given chirality [20, 40, 42, 61], clockwise or counterclockwise, on the magnetization structure. A significant consequence of this chirality is that all DWs are moved coherently when an electric current is applied.

Finally, some comments about the SHE have to be made. The electrons are scattered by the lattice when an electric current is applied. Nevertheless, an anisotropic scattering due to the splitting of the energy levels is produced, caused by the strong

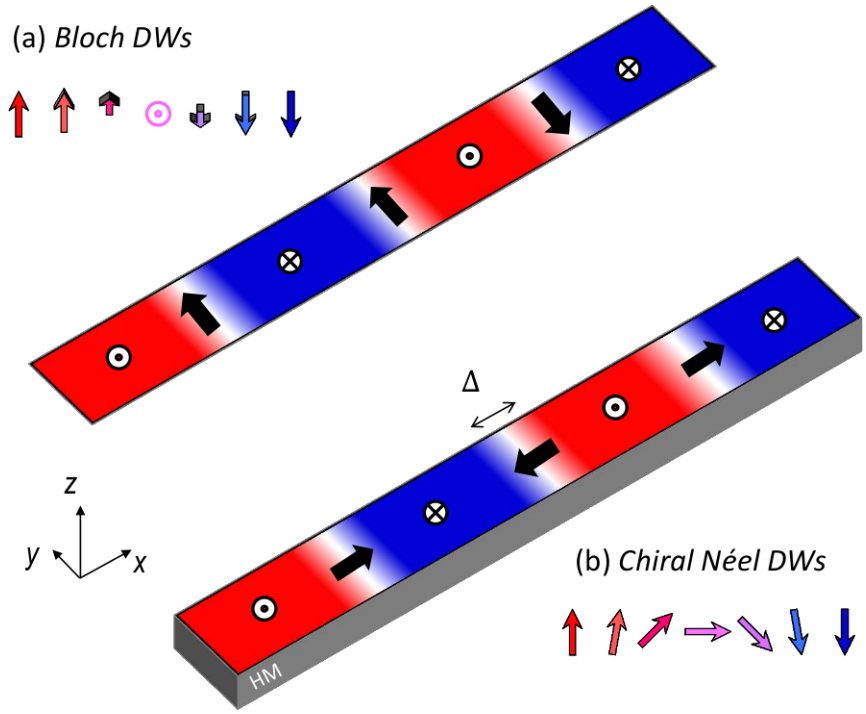

Figure 1.1: Sketch of (a) Bloch domain walls and (b) Néel domain walls. Since Néel domain walls are quiral due to the DMI, magnetization is directed along positive or negative xs depending on the type of transition (up-down or down-up) and the sign of the DMI.

SOC [50, 51]. As a consequence, electrons with different spin are scattered in opposite directions resulting in a net spin current, being the spin current perpendicular to both, the electric current and the spin orientation. Thus, the spin orientation lays along the transverse direction when a longitudinal electric current is applied, and so a perpendicular spin current is obtained.

Hence, the SHE induces a perpendicular spin current in the FM layer. This angular momentum exerts a torque over the magnetization of the FM strip due to the spin transfer torque (STT) [9, 62–64]. This torque is usually referred as spin-orbit torque (SOT) because the spin current induced by a strong SOC generates it. The SOT exerted is maximal when the spin angular momentum[1] and the magnetization are at right angles and is null when both are parallel. Inside the domains, the anisotropy and exchange energies impose a perpendicular direction for the magnetization and only small variations can be promoted by this SOT. However, the effect of the SOT becomes relevant at the transition region causing the DW to be displaced. This movement can be either in the same direction of the electric current or in the opposite one. It depends on the sign of the spin Hall angle, which determines the orientation of the spin angular momentum of the spin current, and the chirality of the DW, and therefore, the sign of the DMI.

Two basic domain wall configurations, sketched in figure 1.1, can be reported [65, 66]: that which has no magnetization component along the normal direction of the plane defined by the DW is called Bloch walls (BDWs), and that which has no

[1]It must be noticed that the spin angular momentum and the spin current are perpendicular to each other.

magnetization component along the direction addressed by the cross product of the perpendicular direction of the slab and the normal to the DW is called Néel walls (NDWs). The above ideas indicate that, if a longitudinal electric current is applied, a spin current is induced in the perpendicular direction, being the spin orientation within the plane defined by the slab and perpendicular to the longitudinal direction. Thus, for a straight strip where a DW without tilting is present, the transversal angular momentum introduced into the FM layer exerts a null torque for a BDW, while this torque is maximum when the DW exhibits a Néel configuration.

The most important features to understand the system studied along this thesis has been briefly discussed. A more detailed explanation of the theory can be found in chapter 2 or in the references.

1.3 Methodology

Two main tools have been used in the present work, micromagnetic simulations and an analytical model. It has been already mentioned that micromagnetics has achieved a fast and deep advancement in recent years thanks to the development and improvement of different numerical techniques [67–69]. These techniques are used to numerically solve the LLG equation, which is the equation followed by a magnetic dipole [1, 70]. A continuous theory of magnetization assumes that this magnetization can be described by a vector field, and therefore, each point of such a field is described by the LLG equation [3, 67]. The LLG equation is solved by means of a finite difference method. A mesh must be defined to apply such a method [67, 69]. Each point is represented by a computational cell of a finite size. Some restrictions apply to the cell size. On the one hand, cell size must be sufficiently large as to contain a number of atomic dipoles which ensures a rather constant modulus of the magnetization. On the other, cell size must be adequately small to avoid sharp changes of the magnetization from one cell to the contiguous one.

LLG equation describes for each cell the evolution in time of the magnetization imposed by the applied torques. Each cell affects each other by a known set of interactions which ought to be added to the external field resulting in an effective field H_{eff}. This field differs from one magnetic configuration to another, and so it must be calculated for each state to solve the LLG differential equation each time step. The differential equation is computed by means of one of the algorithms discussed in chapter 3. The Dormand-Prince method is the one used in chapters 6-7. It is based on a Runge-Kutta scheme and allows adapting the time step. On the contrary, a 4º order Runge-Kutta method is applied in chapters 8-12. The reason is that, in order to include a finite temperature in a simulation, a fixed time step must be adopted.

A full μMag simulation can be a time-consuming task, even though the above-mentioned algorithms are optimized to compute the LLG equation and despite the improvement of the graphics processor units (GPU) that solve it. Then, a simplified model being able to analytically describe the main features of the magnetization dynamics is an interesting tool which can reduce the time required to study those systems. Moreover, such a model gives an insightful knowledge about the keys of such

dynamics and some general rules can be extracted from it. However, it requires some assumptions which makes it less detailed and less reliable than full μMag simulations and so it must be tested against them.

The first analytical model for the DW motion was developed by Walker in 1956 for a FM strip whose longitudinal direction is infinite [71]. It is assumed that magnetization has two semi-infinite domains separated by a DW. As long as it is supposed that magnetization only changes along the infinite longitudinal direction, this model is called one dimensional model (1DM). The model also assumes that the magnetization of the strip can be described by means of two dynamic parameters $q(t)$, the DW position, and $\Phi(t)$, the magnetization angle with respect the longitudinal axis, along with one static parameter, Δ, the DW width.

The two semi-infinite domains studied by Walker are in-plane systems so, two configurations are possible, head-to-head and tail-to-tail. In any case, it is possible to straightforwardly adapt the model from the in-plane case to the out-of-plane case of systems with PMA. However, some modifications must be made to include new phenomena, as the adiabatic and non-adiabatic STT, the SHE, the Rashba effect, the DMI and so on. These new phenomena, or very strong torques, may induce deformations of DWs. As an example, it is known that in systems with high DMI, the current may induce a rotation of the DW plane [17, 19, 72–74]. Thus, an angle between the normal vector of the DW and the longitudinal axis, which is called tilting angle χ, appears. Another common deformation is the variation of DW width after the application of a stimulus. These deformations can be taken into account by introducing this new parameter of tilting χ or by considering a time-dependent DW width, Δ.

Although a general 1DM can be derived, some simplified versions can be proposed depending on the case. For example, an in-plane current noncollinear with the longitudinal axis can be considered, as in chapters 8, 9, and 10, although a collinear current is in general applied. In chapters 11 and 12 a tailored anisotropy profile is considered, while in the other cases a homogenous anisotropy applies. In general, it is possible to consider finite size regions (grains) where the anisotropy slightly differs from one grain to another to mimic realistic conditions. The aim of chapter 4 is to present a general model able to describe each of the systems considered in this thesis. It must be pointed out that such a model has not been developed with the goal of obtaining a general one, but summarizes the modifications that the author had to adopt for each case. Indeed, the presented model is not the most general one. There are multilayered structures with two FM layers that interact with an interlayer exchange coupling (IEC) due to itinerant electrons via the Ruderman-Kittel-Kasuya-Yosida (RKKY) field [74–76]. These systems are known as synthetic ferro- or antiferromagnets, depending on the sign of the IEC. Despite the high DW velocities that they show [77], they are out of the scope of this thesis, and the RKKY field is not included in the model presented in chapter 4.

1.4 This thesis

This thesis is intended to study and highlight the key role of SOC in the development of spintronic devices; especially the DWs based magnetic memories. Additionally, the suitability of tailoring the PMA to provide a pinning system for those kinds of memories is shown. The presence of a pinning system of any nature is mandatory to precisely control the DWs position, even for a current-driven DW motion scheme. Thus, the text is structured in four parts, and an additional conclusions chapter. The first part gives the necessary introduction to the topic while the other three presents the novel results of this thesis.

Part I

The first part is integrated by chapters 2, 3, 4, and 5, which deal with the following topics. First one, the general micromagnetic theory is treated in 2. The numerical solver tools used for μMag simulations are explained in 3. The "general" one dimensional model is developed in 4. Finally, the experimental techniques employed during the research visit in the group "Integnano" in Paris, commonly used to study multilayered systems, are illustrated in 5. These four chapters give the necessary background to understand the present dissertation.

Part II

The second part, formed by chapters 6 and 7, is devoted to systems with moderate DMI. In the studied systems, the geometry of the slabs imposes BDWs. However, the presence of the DMI promotes a NDW type. By moderate DMI we are referring a value of such an interaction sufficiently high to avoid the pure BDW, but too small to set a pure NDW. The intermediate configuration is called Dzyaloshinkii domain wall (DDW). It must be pointed out that, although the definition of NDW allows for the existence of two configurations, the quiral nature of the DMI imposes one of these two possibilities. The two possible configurations for the BDWs are due to the so-called shape anisotropy, and are fully equivalents, giving rise to a degeneracy in the ground state. DDWs inherit the quiral character of the NDWs, but still conserve the degenerate nature of BDWs. These two degenerate states are symmetric with respect to the perpendicular direction of the wall surface, which coincides with the longitudinal axis of the slab.

The DW magnetization orientation is a consequence of the equilibrium of all torques. In the absence of external stimuli, all these torques depend on the magnetization configuration. When an external stimulus is applied the previous configuration is, in general, no longer an equilibrium configuration and so the magnetization will evolve in time. It may happen that the magnetization reaches a state characterized by a constant DW velocity and orientation, which is known as stationary state. The existence of a stationary state will depend on the amplitude and nature of the applied stimuli. The torque due to an external magnetic field H_{ext} does not depend on the DW configuration. If the perpendicular external field H_z is rather low, there is a configuration where this torque can be canceled out by the other terms, which depend on the DW configuration. In this region, the DW velocity increases linearly with H_z. However, if H_z is sufficiently large there is not such a

situation, and no stationary state can be reached. This phenomenon is known as Walker breakdown [71] and leads to a drastic reduction of the DW mean velocity. The field for which the maximum velocity is reached is known as the Walker field H_W.

Nevertheless, if a current J_a is applied, the torque derived from it depends on the magnetization orientation, being null for BDWs. For this reason, when solely an electric current is applied there is always a stationary state, and the DW velocity increases to a saturation value. However, when both, external field H_z and applied current J_a are taking into account, there exists a Walker field $H_W(J_a)$ which depends on the value and sign of the applied current J_a.

In systems with moderate DMI, and thus with two possible ground states, three scenarios are possible when applying a stimulus. The first one occurs when the magnetization is able to vary smoothly from the initial state to the stationary one. It takes place for low values of the perpendicular field H_z and applied current J_a, for which there is always a state close to the initial one, and the smooth evolution is possible no matter which one is the actual initial state. However, the stationary DW velocity will differ from one to the other stationary state. The second scenario happens when there is only one stationary state, and the magnetization is unable to evolve smoothly from the initial state to the final one. Therefore, the DW magnetization suffers a reorientation which affects the dynamic of the DW. Moreover, once the stimuli are switched off, the magnetization does not recover its initial configuration, but it stabilizes at the other possible ground state. Finally, the third scenario is characterized by a lack of a stationary state. In this case, a Walker breakdown takes place. An external magnetic field is always involved in this situation.

Part III

This part, which corresponds to chapters 8, 9, and 10, analyses the consequences of applying an electric current noncollinear with the longitudinal axis of the FM strip. The goal of such a study is to explain the experimental results obtained by Safeer *et. al.* [78] of the switching of FM layers of a given geometry. As it is already stated, an electric current produces its maximum torque when it is collinear with the magnetization. However, this torque not only causes a DW displacement but also the rotation of the DW magnetization, reducing its effect. Then, it is possible to apply a noncollinear current which twists the magnetization to be collinear with it, maximizing the torque, and thereby the DW velocity, at the stationary regime. For a region where the magnetization is pointing along the opposite direction, the current will further misalign the magnetization, reducing the torque and the DW velocity. Two consecutive DWs in a FM layer where a rather high iDMI is present have opposite directions due to the quiral character of the DMI. Thus, these two DWs have different velocities if a noncollinear current is applied, and the magnetic domain between them is reduced or increased depending on which DW is faster.

The above-mentioned phenomenon plays a role in the magnetization reversal of the geometries studied by Safeer *et. al.* [78]. A *U-shaped* FM layer and its mirror image are studied, as well as a *S-shaped* FM layer and its mirror image. Those geometries can be built up from a central straight part, and two spikes tilt from the longitudinal

direction. The *U-shaped* and the *S-shaped* geometries differ from the relative angle between the two spikes; 90º degrees for the *U-shaped* and 180º degrees for the *S-shaped*. The switching process requires two steps to be fulfilled, the nucleation of a reverse domain and the growth of this domain until the switching is completed. Domain wall nucleations which finally collapse are called frustrated switching. The nucleation and growth process fully treated in chapters 9 and 10 are summarized here.

Domain nucleation is produced in those geometries by the boundary conditions imposed by the iDMI. A small in-plane magnetization is promoted by the iDMI at the edges of the FM element. This small in-plane component points inwards or outwards as a function of the sign of the iDMI and the type of domain (Up or Down). Due to this small in-plane component, a torque is generated at the spikes when an electric current is applied. This torque favors in each peak the nucleation of an Up or Down domain, depending on the relative orientation of the magnetization and current direction. Thereby, the domain nucleation is promoted or avoided for the different spikes. However, it must be pointed out that this torque is rather small as to promote such nucleation alone, so this process is indeed assisted by the thermal field. Due to the presence of the thermal field is also possible to nucleate some spurious domains with two DWs which, in general, do not provoke a magnetization reversal, as both DWs will reach the edge of the spike. A DW nucleation which does not produce a magnetization reversal is called frustrated switching. Nevertheless, a nucleated domain with two DWs may induce a complete switching if another domain with a single DW is nucleated and, due to the different DW velocities, this new wall reaches the first domain. Thus, it is possible to obtain a magnetization switching control by geometry as long as the geometry and applied current define which domains are favored and which ones are avoided.

Part IV

Finally, chapters 11 and 12 analyze the current-driven DW motion in a ratchet [79, 80] FM strip. This kind of memory is an enhancement of the racetrack memory [27, 28] which allows for better control of the DWs position. This control is achieved by tailoring the PMA energy profile so as to present a saw-toothed profile. Thereby, in the absence of external stimuli, there is a well-defined set of local energy minima where DWs are pinned. Such pinning system precisely determines the possible DW positions at equilibrium, and so the bit size and its positions.

This proposal has a clear advantage for field-driven devices. As long as an external magnetic field expands the parallel domains at the cost of reducing antiparallel domains, two consecutive DWs are moved towards opposite directions. This eventually causes domain collapse, losing such an information. A system which ensures unidirectional DW motion is then mandatory for a field-driven device. In a ratchet FM strip, when a perpendicular magnetic field is applied, domains can only expand in one direction, while its other DW is blocked. When the wall overcomes the next tooth of the anisotropy profile, the application of a field in the opposite direction fails to reduce the size of the domain from that edge. Then, the domain recovers its initial size by the domain wall displacement on the other side.

Chapters 11 and 12 analyze the current-driven DW motion in a FM layer where the PMA has been modified in such a way. For the current-driven regime every DW is moved in the same direction. Thus, the unidirectional character of the system is no longer a constraint. However, the pinning system provided by this method is still effective in the current-driven regime. Besides, other advantages are reported, as compared with the field-driven regime. In the latter, two teeth per bit are needed to prevent the domain collapse, while only one is needed for the former. The reduction of the bit size and the higher DWs velocities for reasonable values of current, as compared to those for reasonable values of the field, lead to lower bit shifting times. Finally, a symmetric field pulse is needed for the proper working of a field-driven ratchet memory, while a current-driven scheme allows for tuning the pulse and relaxing times as well as to use currents of the opposite polarity to improve system performances and a better control of motion variables.

Part I.
Fundamentals.

Chapter 2

Theoretical basis

The theoretical basis of micromagnetics is introduced in this chapter. The Euler-Lagrange equation for a magnetic system is derived from variational principles, and the conditions for equilibrium are established. The Landau-Lifshitz-Gilbert equation is set as the dynamic equation for these systems. The idea of effective field is presented as well as the different contributions of the free energy. The Landau-Lifshitz-Gilbert equation is augmented by the field-like and Slonczweski-like torques due to spin-polarized currents. A way to include temperature effects for constant and low temperature is also addressed.

2.1 Introduction

The magnetic order is a quantum phenomenon [81] at a macroscopic scale. Thus, a description of a ferromagnetic material based on the spin lattice[1] would be then satisfactory. However, such description is unfeasible for a system larger than a few nanometers due to the vast number of spins involved. Moreover, a macroscopic description as the Domain Theory for system smaller than a few microns is insufficient, as long as these theories do not account for the DWs internal structure, which may play a major role in their dynamics. As it has been previously stated, a suitable theory for such systems must be mesoscopic.

The main assumption of the micromagnetic theory is that magnetization can be expressed as a continuum vector field of constant modulus. The value of the modulus is known as the saturation magnetization M_s of the sample. This assumption lays over two hypotheses. One of them is that the material can be described as a set of infinitesimal volumes dV that contain sufficient spins as to keep a constant magnetization value without significant fluctuations. The size of these volumes must be rather low to ensure that the magnetization changes smoothly with the position. This hypothesis is feasible as long as the exchange, which tends to align all the spins in the same direction, is the prevailing interaction at short ranges. Other free energy terms induce small deviations from one point to the other.

The second hypothesis assumes that the saturation magnetization M_s is constant and equal to its value at zero temperature. This assumption remains valid as long as the sample is well below the Curie temperature [65]. If this hypothesis does not apply, a dependence on the temperature of the material parameters must be taken into account and so, the stochastic Landau-Lifshitz-Bloch equation [82–87] ought to be applied. Although in some cases presented along this thesis a finite temperature has been considered, it has been supposed that the sample is still well below the Curie temperature, and the LLG equation, augmented with a stochastic term, has been used.

The Brown equations for the equilibrium are obtained from Hamilton's variational principle for continuous media in the next section. The LLG equation is also presented as the dynamic equation of these systems. Finally, the different contributions of the free energy are detailed, as well as the torques associated to spin-polarized currents and the thermal field.

2.2 Variational principle. Static condition

The equilibrium equations are obtained but not following the Brown derivation [3], but the one followed in [88] or [67] for the sake of simplicity, since it does not require the use of the variations of an explicit energy functional. The equations of motion of a mechanic system can be derived from Hamilton's variational principles [89], which states that, for conservatives systems, *the motion of the system from time* t_1 *to time*

[1] This lattice would be, in general, different from the crystal lattice, with its own lattice parameter, reciprocal lattice, and excitation spectrum.

t_2 is such that the action,

$$I = \int_{t_1}^{t_2} L\, dt\,, \tag{2.1}$$

has a stationary value for the actual path of the motion, where L is the Lagrangian of the system, which can be defined as the excess of kinetic energy over potential energy. L can be written as the integral over the whole system of a Lagrangian density.

$$L = \int_V l_V\, dV - \int_S u_S\, dS \tag{2.2}$$

The first integral is a volume integral which accounts for kinetic and potential addends, while the second one, linked to the surface of the system, only contains terms of potential origin.

Consider a continuous vector function $\vec{m} = \vec{m}\,(\vec{r}, t)$ in a three-dimensional space for which the Lagrangian density per unit volume l_V is a function of $\vec{m}$ and its temporal $\dot{\vec{m}}$ and spatial derivatives[2] as well as position $\vec{r}$ and time t. Nevertheless, it is assumed that surface Lagrangian density is a function of $\vec{m}$, $\vec{r}$ and t. Summarizing

$$\begin{aligned} l_V &= l_V\left(\vec{m}, \dot{\vec{m}}, \vec{\nabla}\vec{m}, \vec{r}, t\right) \\ u_S &= u_S\left(\vec{m}, \vec{r}, t\right) \end{aligned} \tag{2.3}$$

Hamilton's principle is equivalent to the condition that the variation of the action for fixed t_1 and t_2 is zero. Then, it can be written

$$\begin{aligned} \delta I = \delta \int_{t_1}^{t_2} L\, dt &= \delta \int_{t_1}^{t_2} \left(\int_V l_V\, dV - \int_S u_S\, dS \right) dt \\ &= \int_{t_1}^{t_2} \left(\int_V \delta l_V\, dV - \int_S \delta u_S\, dS \right) dt = 0 \end{aligned} \tag{2.4}$$

$$\delta\vec{m}\,(\vec{r}, t_1) = \delta\vec{m}\,(\vec{r}, t_2) = 0 \tag{2.5}$$

where the restriction that the variation of the vector function is null for t_1 and t_2 has been added. Variations δl_V and δu_S can be written by taking into account (2.3)

$$\begin{aligned} \delta l_V &= \frac{\partial l_V}{\partial \vec{m}} \cdot \delta\vec{m} + \frac{\partial l_V}{\partial\left(\partial\vec{m}/\partial t\right)} \cdot \delta\left(\partial\vec{m}/\partial t\right) + \frac{\partial l_V}{\partial\left(\vec{\nabla}\vec{m}\right)} \cdot \delta\left(\vec{\nabla}\vec{m}\right) \\ \delta u_S &= \frac{\partial u_S}{\partial \vec{m}} \cdot \delta\vec{m} \end{aligned} \tag{2.6}$$

[2]Notation $\vec{\nabla}\vec{m}$ is used for the spatial derivatives being $\vec{\nabla}\vec{m} \equiv \partial m_i/\partial r_j$ a second rank tensor.

As long as δ operator commutes with both $\dfrac{d}{dt}$ and $\vec{\nabla}$, the following identities hold

$$\begin{aligned}
\frac{d}{dt}\left[\frac{\partial l_V}{\partial\left(\partial\vec{m}/\partial t\right)}\cdot\delta\vec{m}\right] &= \frac{d}{dt}\left[\frac{\partial l_V}{\partial\left(\partial\vec{m}/\partial t\right)}\right]\cdot\delta\vec{m} + \frac{\partial l_V}{\partial\left(\partial\vec{m}/\partial t\right)}\cdot\left[\frac{d}{dt}\left(\delta\vec{m}\right)\right] \\
\vec{\nabla}\cdot\left[\frac{\partial l_V}{\partial\left(\vec{\nabla}\vec{m}\right)}\cdot\delta\vec{m}\right] &= \left[\vec{\nabla}\cdot\frac{\partial l_V}{\partial\left(\vec{\nabla}\vec{m}\right)}\right]\cdot\delta\vec{m} + \left(\frac{\partial l_V}{\partial\left(\vec{\nabla}\vec{m}\right)}\right)\cdot\vec{\nabla}\left(\delta\vec{m}\right)
\end{aligned} \tag{2.7}$$

which can be rearranged

$$\begin{aligned}
\frac{\partial l_V}{\partial\left(\partial\vec{m}/\partial t\right)}\cdot\delta\left(\partial\vec{m}/\partial t\right) &= \frac{d}{dt}\left[\frac{\partial l_V}{\partial\left(\partial\vec{m}/\partial t\right)}\cdot\delta\vec{m}\right] - \frac{d}{dt}\left[\frac{\partial l_V}{\partial\left(\partial\vec{m}/\partial t\right)}\right]\cdot\delta\vec{m} \\
\left(\frac{\partial l_V}{\partial\left(\vec{\nabla}\vec{m}\right)}\right)\cdot\delta\left(\vec{\nabla}\vec{m}\right) &= \vec{\nabla}\cdot\left[\frac{\partial l_V}{\partial\left(\vec{\nabla}\vec{m}\right)}\cdot\delta\vec{m}\right] - \left[\vec{\nabla}\cdot\frac{\partial l_V}{\partial\left(\vec{\nabla}\vec{m}\right)}\right]\cdot\delta\vec{m}
\end{aligned} \tag{2.8}$$

Using the divergence theorem and (2.5) another expression can be obtained for Hamilton's principle (2.4)

$$\begin{aligned}
\delta I = \int_{t_1}^{t_2} dt \int_V \left\{\left[\frac{\partial l_V}{\partial\vec{m}} - \frac{d}{dt}\left(\frac{\partial l_V}{\partial\left(\partial\vec{m}/\partial t\right)}\right) - \vec{\nabla}\cdot\left(\frac{\partial l_V}{\partial\left(\vec{\nabla}\vec{m}\right)}\right)\right]\cdot\delta\vec{m}\right\} - \\
- \int_{t_1}^{t_2} dt \int_S \left\{\left[\frac{\partial u_S}{\partial\vec{m}} - \frac{\partial l_V}{\partial\left(\vec{\nabla}\vec{m}\right)}\cdot\vec{n}\right]\cdot\delta\vec{m}\right\}
\end{aligned} \tag{2.9}$$

At this point, it should be pointed out that our system is attained to the constraint that the modulus of the magnetization is constant. The above considered vector field $\vec{m}\left(\vec{r},t\right)$ plays in our theory the role of the normalized magnetization, so it must verify $|\vec{m}|=1$. This constraint can be included by applying the Lagrange multiplier method [3, 88]. However, it can also be included by using the fact that the most general variation compatible with the constraint [65] is

$$\delta\vec{m} = \vec{m}\times\delta\vec{\theta} \tag{2.10}$$

where $\delta\vec{\theta}$ is a vector which describes a small rotation around an arbitrary axis. Substituting (2.10) in (2.9) and applying de vector identity $\vec{a}\cdot\left(\vec{b}\times\vec{c}\right) = \left(\vec{a}\times\vec{b}\right)\cdot\vec{c}$

$$\begin{aligned}
\delta I = \int_{t_1}^{t_2} dt \int_V \left\{\left[\frac{\partial l_V}{\partial\vec{m}} - \frac{d}{dt}\left(\frac{\partial l_V}{\partial\left(\partial\vec{m}/\partial t\right)}\right) - \vec{\nabla}\cdot\left(\frac{\partial l_V}{\partial\left(\vec{\nabla}\vec{m}\right)}\right)\right]\times\vec{m}\right\}\cdot\delta\vec{\theta} - \\
- \int_{t_1}^{t_2} dt \int_S \left\{\left[\frac{\partial u_S}{\partial\vec{m}} - \frac{\partial l_V}{\partial\left(\vec{\nabla}\vec{m}\right)}\cdot\vec{n}\right]\times\vec{m}\right\}\cdot\delta\vec{\theta}
\end{aligned} \tag{2.11}$$

Since the variation of the action must be zero for any arbitrary $\delta\vec{\theta}$ the term inside the braces in each integral must be identically null. This condition leads to the Euler-Lagrange equations of the system

$$\begin{aligned}\left[\frac{\partial l_V}{\partial \vec{m}} - \frac{d}{dt}\left(\frac{\partial l_V}{\partial\left(\partial\vec{m}/\partial t\right)}\right) - \vec{\nabla}\cdot\left(\frac{\partial l_V}{\partial\left(\vec{\nabla}\vec{m}\right)}\right)\right]\times\vec{m} = 0 \qquad \forall\,\vec{r}\in V \\ -\left[\frac{\partial u_S}{\partial\vec{m}} - \frac{\partial l_V}{\partial\left(\vec{\nabla}\vec{m}\right)}\cdot\vec{n}\right]\times\vec{m} = 0 \qquad \forall\,\vec{r}\in S\end{aligned} \tag{2.12}$$

The functional derivative is defined as

$$\frac{\delta}{\delta\vec{m}} \equiv \frac{\partial}{\partial\vec{m}} - \vec{\nabla}\cdot\frac{\partial}{\partial\left(\vec{\nabla}\vec{m}\right)} \tag{2.13}$$

which let us simplify the Euler-Lagrange equation

$$\vec{m}\times\left[\frac{\delta l_V}{\delta\vec{m}} - \frac{d}{dt}\left(\frac{\partial l_V}{\partial\left(\partial\vec{m}/\partial t\right)}\right)\right] = 0 \qquad \forall\,\vec{r}\in V \tag{2.14a}$$

$$\vec{m}\times\left[-\frac{\partial u_S}{\partial\vec{m}} + \frac{\partial l_V}{\partial\left(\vec{\nabla}\vec{m}\right)}\cdot\vec{n}\right] = 0 \qquad \forall\,\vec{r}\in S \tag{2.14b}$$

At static equilibrium, there is no kinetic energy contribution, so the Lagrangian volume density is simplified to the potential term $l_V = -u_V$. Moreover, no temporal evolution occurs for any quantity. Thus, the second term inside square brackets in (2.14a) vanishes. Equations (2.14) are reduced to

$$\begin{aligned}\vec{m}\times\left(-\frac{\delta u_V}{\delta\vec{m}}\right) = 0 \qquad \forall\,\vec{r}\in V \\ \vec{m}\times\left[-\frac{\partial u_S}{\partial\vec{m}} - \frac{\partial u_V}{\partial\left(\vec{\nabla}\vec{m}\right)}\cdot\vec{n}\right] = 0 \qquad \forall\,\vec{r}\in S\end{aligned} \tag{2.15}$$

Using the IS of units, a new vector quantity having dimensions of a magnetic field can be defined from the functional derivative definition

$$\vec{H}_{eff} = -\frac{1}{\mu_0 M_s}\frac{\delta u_V}{\delta\vec{m}} \tag{2.16}$$

where μ_0 and M_s corresponds respectively to the magnetic permeability of vacuum and the magnetization modulus or saturation magnetization. This new quantity is called effective field and allows the simplification of the previous expression

$$\vec{m}\times\vec{H}_{eff} = 0 \qquad \forall\,\vec{r}\in V \tag{2.17a}$$

$$\vec{m} \times \left[-\frac{\partial u_S}{\partial \vec{m}} - \frac{\partial u_V}{\partial \left(\vec{\nabla} \vec{m} \right)} \cdot \vec{n} \right] = 0 \qquad \forall \, \vec{r} \in S \tag{2.17b}$$

These are Brown's equations. When the torque $\vec{\tau} = \mu_0 \vec{M} \times \vec{H}_{eff}$ vanishes for each point of the system static equilibrium is reached, as (2.17a) highlights. Equation (2.17b) holds only for points at the surface of the sample. However, this condition may play an important role as in the cases studied in chapters 9 and 10. It is also possible to define a surface "effective field" which further simplifies those equations

$$\vec{H}_{eff,S} = -\frac{1}{\mu_0 M_s} \left[\frac{\partial u_s}{\partial \vec{m}} + \frac{\partial u_V}{\partial \left(\vec{\nabla} \vec{m} \right)} \cdot \vec{n} \right] \tag{2.18}$$

Although some expressions have been obtained, the solutions of those equations depend on the actual free energy contributions expressions, as shown below.

2.3 LLG equation

Equilibrium states of a system provide insightful information for its understanding and manipulation. Nevertheless, knowing the dynamical processes of that system allows an enhancement of its manipulation. A dynamical equation which describing the temporal evolution of the system is to be called at this point. The torqued induced in a magnetic moment $\vec{\mu}$ by an external field $\vec{H}$ is, at each point, [90]

$$\vec{\tau} = \mu_0 \vec{\mu} \times \vec{H} \tag{2.19}$$

and this torque equals the change of angular momentum $\vec{J}$ associated with the magnetic moment $\vec{\mu}$ at this point

$$\frac{d\vec{J}}{dt} = \vec{\tau} = \mu_0 \vec{\mu} \times \vec{H} \tag{2.20}$$

There is a relation between the electron magnetic moment $\vec{\mu}$ and its total angular momentum $\vec{J} = \vec{L} + \vec{S}$

$$\vec{\mu} = \frac{e}{2m_e} g \vec{J} \tag{2.21}$$

where $e < 0$ is the electron charge, m_e its mass, and $g = 1 + \frac{j(j+1)+s(s+1)-l(l+1)}{2j(j+1)}$ the Landé factor. Nevertheless, most ferromagnetic materials have a small orbital contribution to the total angular momentum, so $\vec{J} = \vec{L} + \vec{S} \approx \vec{S}$ and $g \approx 2$ are rather good approximations. A new constant accounting for the previously mention constants can be defined

$$\gamma = \frac{|e| g}{2m_e} \tag{2.22}$$

so the equation of motion reads

$$\frac{d\vec{\mu}}{dt} = -\gamma \mu_0 \vec{\mu} \times \vec{H} \tag{2.23}$$

γ being the gyromagnetic ratio. Besides, the magnetization is defined as the volume density of magnetic dipoles $\vec{M} = \frac{d\vec{\mu}}{dV}$. Additionally, it is assumed that the external field $\vec{H}$ must be replaced by the effective field $\vec{H}_{eff}$ above to take into account not only the external field but the field due to other possible interactions

$$\frac{d\vec{M}}{dt} = -\gamma_0 \vec{M} \times \vec{H}_{eff} \tag{2.24}$$

here $\gamma_0 = \gamma\mu_0 = 2.21 \times 10^5$ m(As)$^{-1}$. Equation (2.24) implies that temporal evolution of the magnetization is perpendicular to both, magnetization and field. Then, for a constant field, magnetization precesses around the field without reaching an equilibrium state as long as no energy is lost. This is due to the fact that no dissipative mechanisms have been taken into account. It is not the scope of this thesis to describe the different dissipation mechanism in a FM material and so, the dissipation term is included in a strictly phenomenological way. As long as the constraint $|\vec{m}| = 1$ holds any change in $\vec{m}$ must be orthogonal to $\vec{m}$

$$\frac{\partial \vec{m}^2}{\partial t} = 2m_x \frac{\partial m_x}{\partial t} + 2m_y \frac{\partial m_y}{\partial t} + 2m_z \frac{\partial m_z}{\partial t} = 2\left(\vec{m} \cdot \frac{\partial \vec{m}}{\partial t}\right) = 0 \tag{2.25}$$

The easiest way to introduce a dissipative contribution compatible with this requirement is adding to the effective field an expression such as:

$$-\frac{\alpha}{\gamma_0}\frac{\partial \vec{m}}{\partial t} \tag{2.26}$$

where the damping term α is a dimensionless constant. Equation (2.24) reads

$$\frac{\partial \vec{M}}{\partial t} = -\gamma_0 \vec{M} \times \left(\vec{H}_{eff} - \frac{\alpha}{\gamma_0}\frac{\partial \vec{m}}{\partial t}\right) = -\gamma_0 \vec{M} \times \vec{H}_{eff} + \frac{\alpha}{M_s}\left(\vec{M} \times \frac{\partial \vec{M}}{\partial t}\right) \tag{2.27}$$

This is the so-called Gilbert equation. Another way to include a dissipative term is the one due to Landau and Lifshitz [1]. In this case, the contribution to be added is perpendicular to both, $\vec{M}$ and the precessing term $\vec{M} \times \vec{H}_{eff}$.

$$\frac{\partial \vec{M}}{\partial t} = -\gamma_{LL} \vec{M} \times \vec{H}_{eff} - \frac{\alpha_{LL}}{M_s}\vec{M} \times \left(\vec{M} \times \vec{H}_{eff}\right) \tag{2.28}$$

Although equations (2.27) and (2.28) describe the same physical phenomena, they are not completely equivalents. In (2.29) precession and alignment addends are decoupled, while in (2.27) they are not.

The Gilbert equation (2.27) implies that magnetization time derivative is perpendicular to magnetization itself, ensuring the modulus conservation. Moreover, the first addend is also perpendicular to the field, promoting only a precession around $\vec{H}_{eff}$, with angular velocity ω given by the gyromagnetic ratio γ, vacuum magnetic permeability μ_0 and effective magnetic field amplitude $\vec{H}_{eff}$. The second addend is perpendicular to the magnetization and its time derivative. Because of that, this

addend has a component that makes magnetization align to the field but also a component that slows down the precession of the gyroscope.

The first addend in the Landau-Lifshitz (2.28) equation is orthogonal to both, the effective field H_{eff} and the magnetization $\vec{M}$, being responsible for the precessional motion. In this case, the angular velocity ω depends on γ_{LL} instead of γ. The second addend is orthogonal to the magnetization and the first addend. This fact avoids the second addend to affect precessional motion, being solely responsible for the alignment with the field. This alignment depends on the constant α_{LL}. In the Gilbert equation (2.27), the alignment motion depends not only on α but also on γ, due to the contribution of its second addend. Moreover, this leads to a dependence on α for the precession speed ω. As long as both equations describe the same physical phenomenon, ω must be the same in both cases, and so there must be a relation between γ_0, α, γ_{LL} and, α_{LL}.

It is possible to obtain such a relation by uncoupling the precession and alignment terms in Gilbert equation (2.27). It can be done by multiplying both sides by $\vec{M}\times$ and using the vector relation $\vec{M} \times \left(\vec{M} \times \frac{\partial \vec{M}}{\partial t}\right) = -M_s^2 \frac{\partial \vec{M}}{\partial t}$. The expression obtained is known as the Landau-Lifshitz-Gilbert (LLG) equation

$$\frac{\partial \vec{m}}{\partial t} = -\frac{\gamma_0}{1+\alpha^2}\vec{m} \times \vec{H}_{eff} - \frac{\gamma_0 \alpha}{1+\alpha^2}\vec{m} \times \left(\vec{m} \times \vec{H}_{eff}\right) \tag{2.29}$$

where both side have been divided by M_s. From (2.27) and (2.28) it can be established $\gamma_{LL} = \frac{\gamma_0}{1+\alpha^2}$ and $\alpha_{LL} = \frac{\gamma_0}{1+\alpha^2}\alpha$. Angular velocity $\omega = \gamma_{LL} H$ slows down a factor $\frac{1}{1+\alpha^2}$ due to energy dissipation. Additionally, the alignment is not a linear term with α but a more complex expression.

It should be pointed out that $\vec{M}$, $\vec{M} \times \vec{H}_{eff}$, and $\vec{M} \times \left(\vec{M} \times \vec{H}_{eff}\right)$ are three mutually orthogonal vectors which constitute a basis in the three-dimensional space. However, components along $\vec{M}$ are forbidden due to the constraint $|\vec{m}| = 1$. It is shown then that this equation can be obtained from purely mathematical considerations, even though without the information about the constants. It is convenient to write equation (2.29) using dimensionless quantities by dividing by $\gamma_0 M_s$.

$$\left(1+\alpha^2\right)\frac{\partial \vec{m}}{\partial \tau} = -\vec{m} \times \vec{h}_{eff} - \alpha \vec{m} \times \left(\vec{m} \times \vec{h}_{eff}\right) \tag{2.30}$$

where $\tau = \gamma_0 M_s t$ and $\vec{h}_{eff} = \vec{H}_{eff}/M_s$

2.4 Free energy contributions

The effective field $\vec{H}_{eff}$ is computed from its definition (2.13). Then, the expression of the density energy is required. However, due to the additive character of the energy, it is possible to compute the functional derivative of the energy due to each interaction and then, summing up all of them obtaining the effective field $\vec{H}_{eff}$. In the absence of STT, the deterministic motion of the magnetization is determined by this field.

2.4.1 Exchange

The -direct- exchange energy is the shift energy due to electrostatic energy differences between the symmetric and antisymmetric spin parts for the wave function of a spin ensemble. The joint function of a spin ensemble must be antisymmetric [81, 91, 92]. Thus, if the spin part is symmetric (antisymmetric), the orbital part must be antisymmetric (symmetric). Nevertheless, the character of the orbital part leads to electrostatic energy differences in these states, favoring one or the other character, which determines the character of the spin part. This effect favors a parallel or antiparallel alignment of the spins. Although it has a purely electrostatic origin, this effect is commonly referred to as a magnetic interaction as it is the main source of magnetic ordering. The expression added to the Hamiltonian accounting for this effect is usually referred to as Heisenberg Hamiltonian

$$\mathcal{H}_{exch} = -\sum_{i,j} J_{ij} \widehat{S}_i \widehat{S}_j \tag{2.31}$$

J_{ij} is the exchange integral accounting for the electrostatic energy difference between parallel and antiparallel states. The sum is usually limited to first neighbors approximation which is a good approximation for exchange integrals which decay rapidly with distance. A ferromagnetic material is characterized by a positive exchange integral $J_{ij} > 0$, favoring a parallel alignment, while antiferromagnetic materials are characterized by a negative exchange integral $J_{ij} < 0$. $\widehat{S}_k$ represents a spin operator. This description is suitable for a microscopic approach but ought to be adapted for a continuum model. Spin operators $\widehat{S}_k$ are then substituted by classic vectors $\vec{S}_k = S\vec{s}_k$. It is also assumed that the exchange integral is the same for every first neighbor $J_{ij} = J$. The equivalent continuum expression of the Heisenberg Hamiltonian reads

$$\mathcal{U}_{exch} = -JS^2 \sum_{i,j,i\neq j} \cos\phi_{ij} \tag{2.32}$$

where ϕ_{ij} is the angle between $\vec{s}_i$ and $\vec{s}_j$. It is recalled the above mention assumption for the continuum model that this is the most important interaction at short distances. Then, the angle ϕ_{ij} is rather small and a Taylor expansion is justified. Neglecting third and higher orders terms and redefining the energy origin

$$\mathcal{U}_{exch} \approx JS^2 \sum_{i,j,i\neq j} \phi_{ij}^2 \tag{2.33}$$

The unit vectors $\vec{s}_i$ associated with the magnetic dipoles $\vec{\mu}_i$ are here substituted by the unit vector along magnetization direction $\vec{m}_i$. In the assumed approximation, the angle ϕ_{ij} can be expressed as the difference between magnetization vectors of two neighbor points $\phi_{ij} \approx |\vec{m}_i - \vec{m}_j| \approx |\left(\vec{r}_{ij} \cdot \vec{\nabla}\right)\vec{m}|$ where $\vec{r}_{ij}$ is the vector position linked to i and j points. Finally, the summation becomes an integral. For a cubic lattice [3]

$$\mathcal{U}_{exch} = \int_V A\left(\vec{\nabla}\vec{m}\right)^2 dV \tag{2.34}$$

or, for the energy density

$$u_{exch} = A\left(\vec{\nabla}\vec{m}\right)^2 \tag{2.35}$$

where $\left(\vec{\nabla}\vec{m}\right)^2 \equiv \left(\vec{\nabla}m_x\right)^2 + \left(\vec{\nabla}m_y\right)^2 + \left(\vec{\nabla}m_z\right)^2$ for Cartesian coordinates. A (J/m) is a material parameter called exchange constant given for a cubic crystal by the expression

$$A = \frac{JS^2c}{a} \tag{2.36}$$

where a is the length of the edge of the unit cell and where $c = 1, 2$ and 4 for a simple, body-centered, and face-centered cubic lattice, respectively. A similar expression can be obtained for hexagonal lattices. However, (2.36) holds for most of the cases of interest.

The effective field associated with this interaction is computed from its definition (2.16) when applied to the previous expression (2.35)

$$\vec{H}_{exch} = \frac{2A}{\mu_0 M_s}\vec{\nabla}\cdot\left(\vec{\nabla}\vec{m}\right) \tag{2.37}$$

It is possible to quantify the above mentioned assumption that exchange is the predominant interaction at short distances by defining the exchange distance l_{exch}

$$l_{exch} = \sqrt{\frac{A}{\frac{1}{2}\mu_0 M_s^2}} \tag{2.38}$$

This magnitude has units of length and measures the distance for which exchange is stronger than magnetostatic interaction, determining the length over which magnetization changes. The typical length is of a few nanometers.

2.4.2 Magnetic anisotropy

The Heisenberg Hamiltonian is a function of the *relative* orientation of the spins, so it conserves rotational symmetry. Nevertheless, real samples show easy and hard magnetization axis for which such magnetization direction is energetically favorable or unfavorable respectively. There must be an anisotropic energy contribution to produce such an effect. The main origin of the magnetocrystalline anisotropy is the spin-orbit coupling [35, 65]. The electron's orbital angular momentum is affected by the crystallographic structure, favoring some crystallographic directions. Spin-orbit coupling promotes the alignment of the spin angular momentum with the orbital angular momentum along such directions, determining the easy and hard magnetization axis.

It would be possible to evaluate the anisotropy energy contribution from a microscopic model by applying the perturbation quantum theory [93]. However, valid expressions can be obtained from a Taylor expansion accounting for the symmetries of the system. The constants in such expansions are parameters that ought to be determined from experimental data [65]. The anisotropy energy contribution can only be a function of even powers of the magnetization in the case of uniaxial magnetic anisotropy

materials, as those considered along this thesis, since it is required to preserve temporal invariance. One expression fulfilling this condition is

$$u_{ani} = K_0 - K_1 \left(\vec{m} \cdot \vec{u}_k\right)^2 - K_2 \left(\vec{m} \cdot \vec{u}_k\right)^4 - K_3 \left(\vec{m} \cdot \vec{u}_k\right)^6 + \cdots \tag{2.39}$$

Neglecting fourth and higher orders

$$u_{ani} = K_0 - K_1 \left(\vec{m} \cdot \vec{u}_k\right)^2 \tag{2.40}$$

where K_0 and K_1 (J/m^3) are coefficients to be determined from experiments and $\vec{u}_k$ is the unit vector along anisotropy axis. In the case that magnetic anisotropy arises from surface effects, a similar formula can be posed, where $\vec{u}_k$ is, in that case, the normal vector to the surface. Positive values of $K_1 \equiv K_u$ corresponds to an easy magnetization axis while negative ones imply an energetically unfavorable axis, promoting the magnetization to lay in the plane perpendicular to $\vec{u}_k$. No matter the origin of the anisotropy is, applying the functional derivative definition (2.13) to the anisotropy energy density (2.40), the anisotropy field is given by

$$\vec{H}_{eff} = \frac{2K_1}{\mu_0 M_s} \left(\vec{m} \cdot \vec{u}_k\right) \vec{u}_k \tag{2.41}$$

It is possible to define a characteristic length l_K as it has been done before

$$l_K = \sqrt{\frac{A}{K_u}} \tag{2.42}$$

This magnitude has units of length and measures the length for which magnetic anisotropy dominates, determining the maximum size of monodomain particles.

2.4.3 Magnetostatic terms

Macroscopic Maxwell's equations are relations between the electromagnetic field and its sources, for each time and point

$$\begin{gathered} \vec{\nabla} \cdot \vec{D}\left(\vec{r}, t\right) = \rho\left(\vec{r}, t\right) \qquad \vec{\nabla} \times \vec{E}\left(\vec{r}, t\right) = -\frac{\partial \vec{B}\left(\vec{r}, t\right)}{\partial t} \\ \vec{\nabla} \cdot \vec{B}\left(\vec{r}, t\right) = 0 \qquad \vec{\nabla} \times \vec{H}\left(\vec{r}, t\right) = \vec{j}\left(\vec{r}, t\right) + \frac{\partial \vec{D}\left(\vec{r}, t\right)}{\partial t} \end{gathered} \tag{2.43}$$

$\rho\left(\vec{r}, t\right)$ being the electric charge density, $\vec{j}\left(\vec{r}, t\right)$ the electric current density $\vec{D}\left(\vec{r}, t\right)$, $\vec{D}\left(\vec{r}, t\right)$ the electric displacement field, $\vec{B}\left(\vec{r}, t\right)$ the magnetic induction, $\vec{E}\left(\vec{r}, t\right)$ the electric field, and $\vec{H}\left(\vec{r}, t\right)$ the magnetic field. These equations, coupled with the dynamic equation (2.29), are a complex system of equations and its solution is, in general, a tough problem. Some cases would require solving the complete problem. However, for small systems, like those studied in this text, the assumption of a homogenous electric and magnetic field is valid. It is also supposed that the external field is constant, or at least has a frequency rather low so is always at quasi-equilibrium

throughout its temporal evolution [65]. Under these circumstances, it is valid to consider only the static contributions to the field. Moreover, only the external field contribution -Zeeman energy- and the magnetostatic field due to magnetization distribution are to be considered.

Zeeman energy

As stated above, the size of the sample is small enough so as to suppose that the external field is uniform and homogenous in the whole strip. It should be pointed out that this field is an external parameter that it is known and can be controlled. The energy density due to an external field, usually referred as Zeeman energy, is [3, 65]

$$u_{ext} = -\mu_0 \vec{H}_{ext} \cdot \vec{M} \tag{2.44}$$

Demagnetizing field

In the absence of electric field $\vec{E}$, electric current $\vec{j}$, and external field $\vec{H}_{ext}$, Maxwell's equations (2.43) are reduced to

$$\begin{aligned} \vec{\nabla} \cdot \vec{B} &= 0 \\ \vec{\nabla} \times \vec{H} &= 0 \end{aligned} \tag{2.45}$$

Taking into account that $\vec{B} = \mu_0 \left(\vec{M} + \vec{H} \right)$

$$\begin{aligned} \vec{\nabla} \cdot \vec{H} &= -\vec{\nabla} \cdot \vec{M} \\ \vec{\nabla} \times \vec{H} &= 0 \end{aligned} \tag{2.46}$$

A magnetic field $\vec{H}_{dmg}$ arises due to changes in magnetization, i.e., $\vec{\nabla} \cdot \vec{M} \neq 0$ is a source of magnetic field. This change of the magnetization occurs even in uniformly magnetized samples. Since magnetization must follow determined boundary conditions at their edge, a non-zero divergence is promoted. Moreover, the discontinuity at the edge implies also a non-zero divergence. Thus, a magnetostatic field exists inside the sample and around it, known as stray field and demagnetizing field respectively. For a uniform magnetized ellipsoid along one of its axes, the field inside the sample is opposite to magnetization, which justifies the term demagnetizing field in that case. A general magnetization distribution generates a more complex magnetic field which is not, in general, uniform or collinear with the magnetization. Nonetheless, the name "demagnetizing field" is kept because of historical reasons. These considerations along with the latter equations allow for the definition of a magnetic charge density per unit volume ρ_M, and per unit surface σ_M.

$$\rho_M \left(\vec{r} \right) = -\vec{\nabla} \cdot \vec{M} \left(\vec{r} \right) \qquad \sigma_M \left(\vec{r} \right) = \vec{M} \left(\vec{r} \right) \cdot \vec{n} \tag{2.47}$$

where $\vec{n}$ is the normal vector to the surface. These magnetic charge densities let rewrite the expression of the demagnetizing field

$$\vec{H}_{dmg} = \frac{1}{4\pi} \int_V \frac{\rho_M \left(\vec{r'} \right) \left(\vec{r} - \vec{r'} \right)}{|\vec{r} - \vec{r'}|^3} \, dV' + \frac{1}{4\pi} \int_S \frac{\sigma_M \left(\vec{r'} \right) \left(\vec{r} - \vec{r'} \right)}{|\vec{r} - \vec{r'}|^3} \, dS' \tag{2.48}$$

And again, magnetostatic energy density is [65, 70]

$$u_{dmg} = -\frac{1}{2}\mu_0 \vec{H}_{dmg} \cdot \vec{M} \tag{2.49}$$

Two comments are worth to be done. Firstly, the condition $\vec{\nabla} \cdot \vec{B} = 0$ implies that the addition of magnetic charges must be zero. Demagnetizing energy is always positive, so this interaction promotes closed loops for the magnetization, trying to avoid magnetic charges. Secondly, these closed loops are energetically unfavorable from the exchange point of view. Therefore, magnetization configuration is a balance between exchange and magnetostatic energy where anisotropy establishes the privileged directions. In thin film approximation, this term behaves as another source of anisotropy. Thus, the anisotropy and the demagnetizing terms can be combined in a new effective anisotropy, $K_{eff} = K_u - 1/2\mu_0 M_s^2$.

2.4.4 Dzyaloshinskii-Moriya interaction

Dzyaloshinskii-Moriya interaction (DMI) is a chiral energy term due to the lack of inversion symmetry along with the spin-orbit coupling [38–40, 42, 44, 48, 72, 77]. The systems studied along this thesis show a lack of inversion symmetry due to the presence of two non-equivalents interfaces, one between a layer with strong spin-orbit coupling and the ferromagnetic layer, and the other between the ferromagnetic layer and a different layer. The lattice symmetry is connected with the spin symmetry due to the spin-orbit coupling giving rise to the antisymmetric counterpart of the exchange interaction [40, 42]

$$\mathcal{U}_{DMI} = \sum_{i,j} \vec{d}_{ij} \cdot \left(\vec{S}_i \times \vec{S}_j \right) \tag{2.50}$$

$\vec{d}_{ij}$ being the DMI vector for the i^{th} and j^{th} atom, and $\vec{S}_i$ the atomic angular momentum vector. The expression for $\vec{d}_{ij}$ depends on the system considered. For ultrathin isotropic films $\vec{d}_{ij} = d\vec{u}_{ij} \times \vec{u}_n$ where $\vec{u}_{ij}$ is the unit vector linking i and j sites, and $\vec{u}_n$ is a unit vector perpendicular to the interface between the strong spin-orbit coupling layer and the ferromagnetic layer, oriented from the former to the latter. The continuum expression of the DMI assumes that the ferromagnetic layer thickness is small enough to consider a constant Dzyaloshinskii-Moriya parameter d along the surface normal. Then, it is read [42] [3]

$$u_{DMI} = D \left[(\vec{m} \cdot \vec{u}_n) \vec{\nabla} \cdot \vec{m} - \vec{m} \cdot \vec{\nabla} (\vec{m} \cdot \vec{u}_n) \right] \tag{2.51}$$

D (J/m^2) is a material parameter whose relation with d depends on the type of the lattice. The expression of the DMI field is derived from the variation of the DMI energy

$$\begin{aligned} \delta u_{DMI} = D \quad & \Big[(\delta\vec{m} \cdot \vec{u}_n) \vec{\nabla} \cdot \vec{m} - \delta\vec{m} \cdot \vec{\nabla} (\vec{m} \cdot \vec{u}_n) + \\ & + \vec{m} \cdot \vec{u}_n \vec{\nabla} \cdot (\delta\vec{m}) - \vec{m} \cdot \vec{\nabla} (\delta\vec{m} \cdot \vec{u}_n) \Big] \end{aligned} \tag{2.52}$$

[3] It should be pointed out that there is a sign difference. This sign is absorbed by D constant.

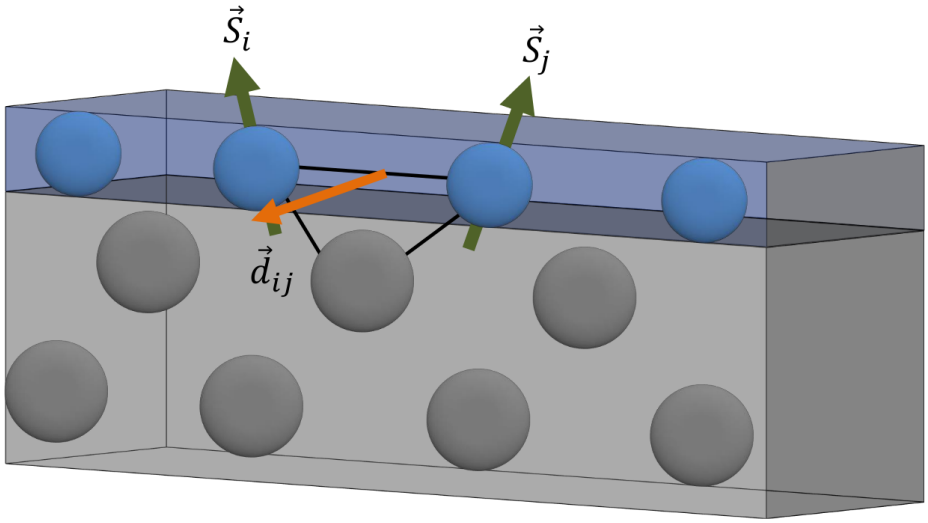

Figure 2.1: Sketch of the Dzyaloshinskii-Moriya interaction at the interface between a ferromagnetic metal (blue) and a heavy metal (grey). The DMI vector $\vec{d}_{ij}$ related to the i^{th} and j^{th} atoms is perpendicular to the plane formed by the i^{th} and j^{th} ferromagnetic atoms and a heavy metal atom with strong spin-orbit coupling.

After doing some algebra it can be rewritten

$$\begin{aligned}\delta u_{DMI} = D\Big[&(\delta\vec{m}\cdot\vec{u}_n)\,\vec{\nabla}\cdot\vec{m} - \delta\vec{m}\cdot\vec{\nabla}\,(\vec{m}\cdot\vec{u}_n) - \delta\vec{m}\cdot\vec{\nabla}\,(\vec{m}\cdot\vec{u}_n) + \\ &+ (\delta\vec{m}\cdot\vec{u}_n)\,\vec{\nabla}\cdot\vec{m} + \vec{\nabla}\cdot\left[\,((\vec{m}\cdot\vec{u}_n)\,\delta\vec{m}) - (\vec{m}\,(\delta\vec{m}\cdot\vec{u}_n))\,\right]\Big]\end{aligned} \tag{2.53}$$

The first four terms are the ones appearing in the volume integral of (2.9), while the last one goes to the surface integral due to the divergence theorem. The field caused by the DMI is the one linked to the volume integral

$$\vec{H}_{DMI} = \frac{2D}{\mu_0 M_s}\left[\vec{\nabla}\,(\vec{m}\cdot\vec{u}_n) - \left(\vec{\nabla}\cdot\vec{m}\right)\vec{u}_n\right] \tag{2.54}$$

while the surface integral gives a surface "effective field"

$$\vec{H}_{DMI,S} = \frac{D}{\mu_0 M_s}\left[\vec{m}\times(\vec{n}\times\vec{u}_n)\right] \tag{2.55}$$

where the vector identity $\vec{a}\times\left(\vec{b}\times\vec{c}\right) = \vec{b}\,(\vec{a}\cdot\vec{c}) - \vec{c}\left(\vec{a}\cdot\vec{b}\right)$ has been used. As it has been already mentioned, this term ought to be added at the surface boundary conditions. As long as no specific surface density energy has been considered, only the volume density energy which depends on $\vec{\nabla}\vec{m}$ appears in the boundary condition equation. These terms are the exchange and the DMI

$$\vec{m}\times\frac{1}{\mu_0 M_s}\left[2A\left(\vec{\nabla}\vec{m}\right)\cdot\vec{n} + D\vec{m}\times(\vec{n}\times\vec{u}_n)\right] = 0 \tag{2.56}$$

Note that $\left(\vec{\nabla}\vec{m}\right)\cdot\vec{n} = \partial\vec{m}/\partial n$ which is the notation commonly used in the bibliography [88, 94]. This equation must be fulfilled at any time, not only at equilibrium.

2.5 Additional terms in the LLG equation

Hitherto, different terms taking into account the different interactions that may be present in our sample have been added to the energy density expression. These terms modify the effective field that ought to be considered but keeping the LLG equation unchanged. However, an electric current is proven to have a role beyond the Joule heating and the Ampère field. Additional torques must be added to the LLG equation to describe these effects, such as the STT [16, 62, 63, 95–104] and the SOT [9, 10, 14, 16, 19, 44, 49–56, 105–110], like the SHE and the Rashba effect.

Moreover, the theory previously introduced considers a deterministic evolution of the samples, i.e., it is assumed that they are at zero temperature. To properly describe the analyzed devices, it is mandatory to evaluate the effect of thermal agitation. One of the most important consequences of a finite temperature is the loss of magnetic stability or superparamagnetic effect [111, 112]. Thermal agitation can be described by means of an additional stochastic field H_{th} which must be added to the deterministic effective field [70, 111, 113–119]. This section is devoted to the description of how the LLG equation (2.29) is modified by these terms.

2.5.1 Spin-transfer torques

There are several mechanisms for which an electric current may produce a torque on the magnetization. The charge carriers, the electrons, also carry angular momentum. In most cases, the up and down states of the electrons are degenerated and the probability for an electron to be in an up state is the same than that of the down state. In such a case, an electric current is said to be spin unpolarized, as long as there are as many up electrons as down electrons. Nevertheless, there are various mechanisms for breaking the degeneracy. When an electric current flows along a ferromagnetic domain, it becomes spin polarized. In that case, there is a spin current in addition to the electric current. When the electric current goes into another domain, electrons become aligned along the new magnetization direction. Because angular momentum ought to be conserved, there must be a spin (angular momentum) transfer between conduction electrons and magnetic lattice. This mechanism is the origin of the STT.

A continuity equation can be cast to describe angular momentum conservation when a spin current flows along the x-direction [103]

$$\vec{\tau}_{ST} = -\frac{\partial\vec{J}_s}{\partial x} \tag{2.57}$$

i.e., in the absence of spin relaxation mechanisms, the change on the spin current is compensated by a torque exerted over the magnetization. It is worth to point out that $\vec{J}_s$ direction is along the spin direction, not the current. For a straight strip, the electric current density is assumed to be homogenous in its cross section. DW

width is supposed to be sufficiently wide to ensure electrons are realigned when they emerged from the DW so the spin polarization is aligned along local magnetization direction (adiabatic limit). This assumption implies that $\vec{J}_s = -J_s\vec{m}$. Besides, it is well known that each electron spin equals $s = \frac{\hbar}{2}$ being $\hbar$ the reduced Planck's constant. Then, spin and electric current are linked by the formula $J_s = \frac{\hbar P}{2e}J$ where J is the electric current, P is the spin polarization, and $e < 0$ is the electron charge. Finally, it is possible to transform the torque into the magnetization time derivative by multiplying both sides by $-\frac{\gamma}{M_s} = -\frac{g\mu_B}{\hbar M_s}$, where g is the Landé factor, and μ_B is the Bohr's magneton. Then, the continuity equation (2.57) for a current flowing along $\vec{u}$ direction is read

$$\frac{\partial\vec{m}}{\partial t} = -\frac{g\mu_B PJ}{2eM_s}\left(\vec{u}\cdot\vec{\nabla}\right)\vec{m} = -b_j\left(\vec{u}\cdot\vec{\nabla}\right)\vec{m} \tag{2.58}$$

b_j has units of velocity, and it is the maximum speed a DW can reach in the adiabatic limit [103]. However, experimental results are not fully reproduced by this expression, and it is needed to consider nonadiabatic contributions. Those contributions can be expressed as [100, 101, 103]

$$\frac{\partial\vec{m}}{\partial t} = b_j\beta\vec{m}\times\left[\left(\vec{u}\cdot\vec{\nabla}\right)\vec{m}\right] \tag{2.59}$$

The new addend $\vec{\tau}_{ST}$, which takes into account these contributions, is included in the Gilbert equation (2.27)

$$\vec{\tau}_{ST} = -b_j\left(\vec{u}\cdot\vec{\nabla}\right)\vec{m} + b_j\beta\vec{m}\times\left[\left(\vec{u}\cdot\vec{\nabla}\right)\vec{m}\right] \tag{2.60}$$

2.5.2 Spin-orbit torque

Additional torques due to the presence of an electric current may appear in systems with SOC and lack of inversion symmetry. These additional torques must be included in the Gilbert equation (2.27). The Rashba effect is an example of such kind of torques. It is present in multilayered systems due to the asymmetric electric -crystalline- potential caused by the lack of inversion symmetry of the heterostructure [108–110]. In the electron frame of reference, the electric field becomes partially a magnetic field which depends on the direction of the electric current. A Hamiltonian accounting for such an effect is written

$$\mathcal{H}_R = \alpha_R\left(\vec{p}\times\vec{n}\right)\vec{\sigma} \tag{2.61}$$

where α_R is the Rashba parameter, $\vec{p}$ the linear momentum operator of the electron, $\vec{n}$ the normal vector of the layer and $\vec{\sigma} = (\widehat{\sigma}_x, \widehat{\sigma}_y, \widehat{\sigma}_z)$ a vector of the Pauli matrices. This Hamiltonian leads to a field-like torque $\vec{\tau} = \mu_0\vec{M}\times\vec{H}_R$ with $\vec{H}_R = \frac{\alpha_R P}{\mu_0\mu_B M_s}\left(\vec{n}\times\vec{J}\right)$

$$\vec{\tau}_R = -\gamma_0\vec{M}\times\left(\frac{\alpha_R P}{\mu_0\mu_B M_s}\left(\vec{n}\times\vec{J}\right)\right) \tag{2.62}$$

This torque behaves like an additional field which is oriented along the transversal strip direction for applied currents along the longitudinal direction.

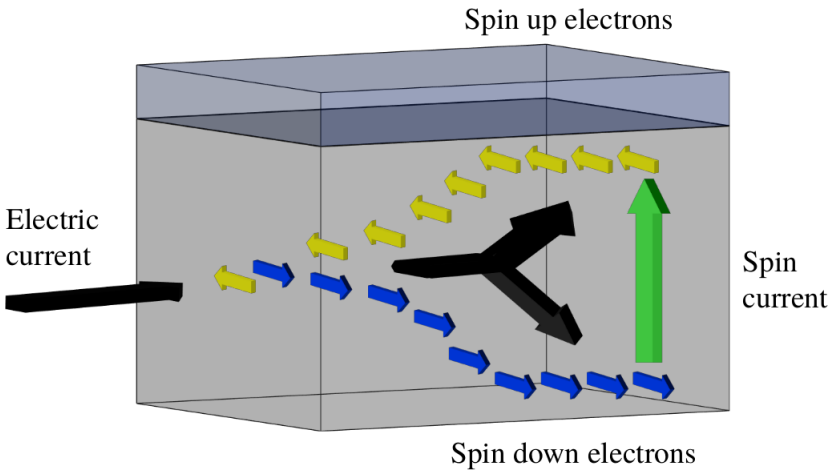

Figure 2.2: Sketch of the spin Hall effect. Spin-orbit interaction promotes an asymmetric scattering as a function of the electron spin. As a consequence, opposite spins are deflected in opposite directions leading to a spin-current $\vec{J}_s$ perpendicular to the charge current $\vec{J}$ and the spin direction $\vec{\theta}_{SH}$.

However, the most appealing source of torque induced by an electric current is the SHE, since this torque is higher for equal electric current density. In that case, the electric current flows along a HM with strong SOC[4] over which the FM layer is grown as it is sketched in figure 2.2. The strong SOC of the HM promotes an asymmetric scattering as a function of the electron spin. This causes a perpendicular spin current to appear along the perpendicular direction of the layer

$$\vec{J}_s = \frac{\hbar}{2e}\left(\vec{J} \times \vec{\theta}_{SH}\right) \tag{2.63}$$

where $\vec{\theta}_{SH}$ is a vector oriented along the spin direction of the induce spin current, its modulus accounting for the strength of the SHE [14, 19, 56]. The magnetic moment going across the surface dS per unit of time normalized to M_s can be obtained by multiplying by $\frac{g\mu_B}{\hbar M_s}dS$. The magnetization, being the volume density of magnetic moment, going across the interface between the HM and the FM layer is written

$$\frac{\partial \vec{m}}{\partial t} = \frac{g\mu_B J}{2etM_s}\vec{\theta}_{SH} \tag{2.64}$$

It can be noticed that this expression does not preserve the magnetization modulus. It is needed to subtract its component along the magnetization direction, i.e., $\left(\vec{\theta}_{SH} \cdot \vec{m}\right)\vec{m}$

$$\frac{\partial \vec{m}}{\partial t} = \frac{g\mu_B J}{2etM_s}\left(\vec{\theta}_{SH} - \left(\vec{\theta}_{SH} \cdot \vec{m}\right)\vec{m}\right) = -\frac{g\mu_B J}{2etM_s}\vec{m} \times \left(\vec{m} \times \vec{\theta}_{SH}\right) \tag{2.65}$$

where the vector identity $\vec{a} \times \left(\vec{b} \times \vec{c}\right) = \left(\vec{a} \cdot \vec{c}\right)\vec{b} - \left(\vec{a} \cdot \vec{b}\right)\vec{c}$ and the constraint $\vec{m} \cdot \vec{m} = 1$ have been applied.

[4]The HM conductivity is usually higher than that of the FM layer allowing higher electric current densities.

2.5.3 Thermal field

A ferromagnetic material has a really intricate free energy landscape, plenty of local minima. At zero temperature, and in the absence of external stimuli such as an applied field or current, the magnetization will keep its configuration indefinitely. Although such behavior would be really interesting for the development of magnetic recording devices, a real sample interacts with a thermal bath from which it can get enough energy to pass over the energy barrier and evolve to another local minimum. The probability per unit time of a jump over the energy barrier is given by the ratio between the height of the barrier and the energy available from the thermal bath $k_B T$. Moreover, since the free energy depends on the size of the sample, smaller samples are less stable than bigger ones for the same temperature. At a given temperature, the samples are no longer stable, and the ensemble behaves as a paramagnetic material. This effect is known as "superparamagnetic effect" [111, 112]. The bit size determines the stability of the saved information for magnetic recording devices.

Smaller bit size allows higher bit densities in magnetic recording devices, but this size must be sufficiently large to ensure the stability of the information for a given time. The knowledge about equilibrium states draw no information about the time required for travelling along these states, but the above presented LLG equation (2.29) is a deterministic theory which is neither able to describe a thermal process as the one described. The use of the theory of stochastic processes [70, 111, 113–119] becomes mandatory to describe samples at a finite temperature. The LLG equation (2.29) transforms into a Langevin equation by adding a fluctuating field $\vec{H}_{th}$

$$\frac{\partial \vec{m}}{\partial t} = -\frac{\gamma_0}{1+\alpha^2}\vec{m} \times \left(\vec{H}_{eff} + \vec{H}_{th}\right) - \frac{\alpha\gamma_0}{1+\alpha^2}\vec{m} \times \left(\vec{m} \times \vec{H}_{eff}\right) \tag{2.66}$$

verifying Gaussian distribution conditions

$$\begin{gathered} \left\langle H_{th,i}\left(\vec{r},t\right)\right\rangle = 0 \\ \left\langle H_{th,i}\left(\vec{r},t\right) H_{th,j}\left(\vec{r'},t'\right)\right\rangle = 2D_{\mu M}\delta_{ij}\delta\left(\vec{r}-\vec{r'}\right)\delta\left(t-t'\right) \end{gathered} \tag{2.67}$$

$\langle \cdots \rangle$ defines the average over different stochastic realizations. $D_{\mu M}$ is a constant accounting for the strength of the thermal field whose value is given by imposing certain conditions to the equilibrium distribution. Gaussian distribution conditions arise because this field has its origin in the interaction of $\vec{m}$ with a large number of microscopic degrees of freedom, such as phonons, magnons, etc. (Central limit theorem). These interactions are also responsible for the relaxation mechanisms of the system given in a phenomenological way by α (Fluctuation-Dissipation theorem). δ_{ij} means that the three components of the field are uncorrelated. In the same way, $\delta\left(\vec{r}-\vec{r'}\right)$ and $\delta\left(t-t'\right)$ mean that the field in two different points and at two different times are also uncorrelated. The condition that the correlation time is zero for any arbitrarily small time is known as white noise condition. The stochastic field appears only in the precession term of equation (2.66). It is possible to develop the theory adding the thermal field also to the alignment term

$$\frac{\partial \vec{m}}{\partial t} = -\frac{\gamma_0}{1+\alpha^2}\vec{m} \times \left(\vec{H}_{eff} + \vec{H}_{th}\right) - \frac{\alpha\gamma_0}{1+\alpha^2}\vec{m} \times \left[\vec{m} \times \left(\vec{H}_{eff} + \vec{H}_{th}\right)\right] \tag{2.68}$$

Although the stochastic trajectories depicted by (2.66) and (2.68) are in general different, the average dynamic properties are the same when the equilibrium condition properties are imposed [113]. The difference between both approaches lays on the relation between $D_{\mu M}$ and the dynamic parameters γ_0 and α in each case.

The general Langevin equation reads

$$\frac{dy_i}{dt} = A_i\left(\vec{y}, t\right) + \sum_k B_{ik}\left(\vec{y}, t\right) L_k \tag{2.69}$$

where $\vec{y} = (y_1 \cdots y_n)$ are the variables of the system, k a given set of indices and L_k a stochastic variable verifying the gaussian conditions (2.67). The noise is said to be multiplicative when $B_{ik}\left(\vec{y}, t\right)$ depends on $\vec{y}$ and additive if not. According to this definition, equation (2.66) has multiplicative noise. Equation (2.69) can be rewritten as an integral equation

$$y_i\left(t + dt\right) = y_i\left(t\right) + \int_t^{t+dt} A_i\left(\vec{y}, t\right)\ dt + \int_t^{t+dt} \sum_k B_{ik}\left(\vec{y}, t\right) L_k\ dt \tag{2.70}$$

Nonetheless, the above equation is not defined. Although the first integral is a common Riemann integral, the second one is the integral of a random number which it is out of the scope of the Riemann integral definition. In order to handle wiht such an expression, the Wiener process is introduced as $dW_k\left(t\right) = L_k\left(t\right) dt$. This process must verify the following conditions

$$\begin{gathered} \left\langle dW_k\left(t\right)\right\rangle = 0 \\ \left\langle dW_k\left(t\right) dW_l\left(t'\right)\right\rangle = 2D_{\mu M}\delta_{kl}dt \end{gathered} \tag{2.71}$$

It is possible to write (2.70) in terms of a Wiener process as

$$y_i\left(t + dt\right) = y_i\left(t\right) + \int_t^{t+dt} A_i\left(\vec{y}, t\right)\ dt + \int_t^{t+dt} \sum_k B_{ik}\left(\vec{y}, t\right)\ dW_k \tag{2.72}$$

The second integral can be defined in different ways. The two most common ones are the Itô (2.73a) and the Stratonovich (2.73b) interpretations.

$$\int_t^{t+dt} X\left(t\right)\ dW_k \underset{\text{Ito}}{\equiv} \lim_{n\to\infty} \sum_{r=0}^{n-1} X\left(t_r\right)\left[W_k\left(t_r + 1\right) - W_k\left(t_r\right)\right] \tag{2.73a}$$

$$\int_t^{t+dt} X\left(t\right)\ dW_k \underset{\text{Strat}}{\equiv} \lim_{n\to\infty} \sum_{r=0}^{n-1} \frac{X\left(t_r + 1\right) - X\left(t_r\right)}{2}\left[W_k\left(t_r + 1\right) - W_k\left(t_r\right)\right] \tag{2.73b}$$

Although the two interpretations are equivalent for systems with additive noise [113], they provide different solutions for multiplicative ones. However, it is possible to link both solutions using the stochastic theory. Physicists usually adopt the Stratonovich interpretation since it is the limit when the autocorrelation time approaches zero from a non-zero correlation time noise.

The Fokker-Planck equation gives the time evolution of the probability distribution of the variables of a stochastic process like (2.69). In the case of multiplicative noise, the Fokker-Planck equation reads [113, 116]

$$\begin{aligned}\frac{\partial P}{\partial t} = &-\sum_i \frac{\partial}{\partial y_i}\left\{\left[A_i\left(\vec{y},t\right) + D\sum_{jk} B_{jk}\left(\vec{y},t\right)\frac{\partial B_{ik}\left(\vec{y},t\right)}{\partial y_j}\right]P\right\} \\ &+ D\sum_{ij}\frac{\partial^2}{\partial y_i \partial y_j}\left\{\left[\sum_k B_{ik}\left(\vec{y},t\right)B_{jk}\left(\vec{y},t\right)\right]P\right\}\end{aligned} \tag{2.74}$$

By inspection of equations (2.66) and (2.69) it is possible to identify

$$\begin{aligned}A_i\left(\vec{m},t\right) &= -\frac{\gamma_0}{1+\alpha^2}\left(\sum_{jk}\epsilon_{ijk}m_j H_{eff,k} + \alpha\sum_k\left(m_i m_k - \delta_{ij}\right)H_{eff,k}\right) \\ B_{ik}\left(\vec{m},t\right) &= -\frac{\gamma_0}{1+\alpha^2}\sum_j \epsilon_{ijk}m_j\end{aligned} \tag{2.75}$$

To solve equation (2.74) the derivative of B_{ik} is needed

$$\frac{\partial B_{ik}}{\partial m_j} = -\frac{\gamma_0}{1+\alpha^2}\sum_j \epsilon_{ijk} \tag{2.76}$$

Multiplying by B_{jk} it can be wirtten

$$\begin{aligned}\sum_{jk} B_{jk}\frac{\partial B_{ik}}{\partial y_j} &= \sum_l\left(\frac{\gamma_0}{1+\alpha^2}\right)^2\left(\sum_{jk}\epsilon_{ijk}\epsilon_{ilk}\right)m_l \\ &= \sum_l -2\delta_{il}m_l = -\left(\frac{\gamma_0}{1+\alpha^2}\right)^2 2m_i\end{aligned} \tag{2.77}$$

The term of the second line of (2.74) can be computed as

$$\begin{aligned}\sum_k B_{ik}B_{jk} &= \left(\frac{\gamma_0}{1+\alpha^2}\right)^2\sum_k\left(\sum_r \epsilon_{irk}m_r\right)\left(\sum_s \epsilon_{isk}m_s\right) \\ &= \left(\frac{\gamma_0}{1+\alpha^2}\right)^2\sum_{r,s} m_r m_s\sum_k \epsilon_{irk}\epsilon_{isk} = \left(\frac{\gamma_0}{1+\alpha^2}\right)^2\left(\delta_{ij} - m_i m_j\right)\end{aligned} \tag{2.78}$$

Using (2.77) and (2.78) equation (2.74) reads

$$\begin{aligned}\frac{\partial P}{\partial t} = &\frac{\gamma_0}{1+\alpha^2}\sum_i\frac{\partial}{\partial m_i}\left\{\left[\sum_{jk}\epsilon_{ijk}m_j H_{eff,k} + \alpha\sum_k\left(m_i m_k - \delta_{ij}\right)H_{eff,k} + \frac{2\gamma_0 D_{\mu M}}{1+\alpha^2}m_i\right]P\right\} \\ &+ D_{\mu M}\left(\frac{\gamma_0}{1+\alpha^2}\right)^2\sum_{ij}\frac{\partial^2}{\partial m_i\partial m_j}\left[\left(\delta_{ij} - m_i m_j\right)P\right]\end{aligned} \tag{2.79}$$

The m_j derivative of the last term equals

$$\sum_j \frac{\partial}{\partial m_j}\left(\delta_{ij} - m_i m_j\right) = \sum_j \left(2m_j\delta_{ij} - \delta_{ij}m_j - m_i\delta_{jj}\right) = -2m_i \tag{2.80}$$

Equation (2.74) becomes

$$\begin{aligned}\frac{\partial P}{\partial t} = {} & \frac{\gamma_0}{1+\alpha^2}\sum_i \frac{\partial}{\partial m_i}\left\{\left[\sum_{jk}\epsilon_{ijk}m_j H_{eff,k} + \alpha\sum_k\left(m_i m_k - \delta_{ij}\right)H_{eff,k} + \frac{2\gamma_0 D_{\mu M}}{1+\alpha^2}m_i\right]P\right\} \\ & + D_{\mu M}\left(\frac{\gamma_0}{1+\alpha^2}\right)^2\sum_i\frac{\partial}{\partial m_i}\left\{-2m_i P + \sum_j\left[\left(\delta_{ij} - m_i m_j\right)\right]\frac{\partial}{\partial m_j}P\right\}\end{aligned} \tag{2.81}$$

Finally, simplifying and recovering vectorial notation

$$\frac{\partial P}{\partial t} = \frac{\gamma_0}{1+\alpha^2}\frac{\partial}{\partial \vec{m}}\left\{\left[\vec{m}\times\vec{H}_{eff} + \vec{m}\times\left(\vec{m}\times\left(\alpha\vec{H}_{eff} - \frac{\gamma_0 D_{\mu M}}{1+\alpha^2}\frac{\partial}{\partial\vec{m}}\right)\right)\right]P\right\} \tag{2.82}$$

Magnetization must have at equilibrium the Maxwell-Boltzman distribution [67, 113], i.e., $P_0 \propto \exp\left(-\mathcal{H}/k_B T\right)$ and must also be stationary $\partial P_0/\partial t = 0$. From the first condition it follows that $\partial P_0/\partial\vec{m} \propto -\mu_0 M_s V\vec{H}_{eff}/\left(k_B T\right)P_0$, and so the rotational vanishes $\vec{m}\times\partial P_0/\partial\vec{m} = 0$. The second condition implies

$$\frac{\partial P_0}{\partial t} = \frac{\gamma_0}{1+\alpha^2}\left(\alpha + \frac{\gamma_0 D_{\mu M}\mu_0 M_s V}{\left(1+\alpha^2\right)k_B T}\right)\frac{\partial}{\partial\vec{m}}\left[\vec{m}\times\left(\vec{m}\times\vec{H}_{eff}\right)P_0\right] = 0 \tag{2.83}$$

from which the value of $D_{\mu M}$ is

$$D_{\mu M} = -\frac{\alpha\left(1+\alpha^2\right)k_B T}{\gamma_0\mu_0 M_s V} \tag{2.84}$$

Given that $d\vec{W} = \vec{H}_{th}dt$, the above relation (2.84) and the Wiener process conditions (2.71) determine that

$$\vec{H}_{th} = \vec{\eta}\sqrt{\frac{2\alpha\left(1+\alpha^2\right)k_B T}{\gamma_0\mu_0 M_s V dt}} \tag{2.85}$$

$\vec{\eta}$ being a vector whose cartesian components are random numbers following a gaussian distribution

$$\begin{aligned}\left\langle\eta_k\left(t\right)\right\rangle &= 0 \\ \left\langle\eta_k\left(t\right)\eta_l\left(t'\right)\right\rangle &= \delta_{ki}\delta\left(\vec{r} - \vec{r}'\right)\delta\left(t - t'\right)\end{aligned} \tag{2.86}$$

The volume V appearing in the above expressions stands for the total volume of the sample in the uniform magnetization model, since this model assumes that magnetization is uniform along the whole sample. For the μMag model, this volume represents the volume of the computational cell, while in the 1DM it accounts for the

total volume of the wall (see Chapters 3 and 4). The additional Kronecker $\delta\left(\vec{r}-\vec{r}'\right)$ guarantees that the thermal field in the μMag model is uncorrelated between two different computational cells.

Chapter 3

Numerical approach

The main necessary ideas to implement a numerical solver for the Landau-Lifshitz-Gilbert and the stochastic Landau-Lifshitz-Gilbert equations are given. The discretized counterparts of the energy and torque contribution presented in chapter 2 are presented along with some comments about the size of the computational cell. The main algorithms for the numerical integration of ordinary differential equation are sketched. The stochastic counterpart for those algorithms is commented. Although the writer does not implement any numerical solver, using already developed ones (GpMagnet and MuMax3), this chapter should serve as a summary of the methods to implement a solver.

3.1 Introduction

The LLG equation (2.29) describes the dynamic of a magnetic dipole. In the case of an extended sample, each point acts as a magnetic dipole under an effective field including the effect of the remaining dipoles. However, the μMag LLG equation (2.29) is not only a non-linear but also a non-local ordinary differential equation (ODE). Hence, analytical solutions are restricted to cases that are too simple. Nonetheless, numerical solvers can provide a solution in most cases. Therefore, numerical micromagnetism has become an extended tool since it is in many cases the only way to test theory against experiments.

3.2 Discretized equation. Discretized energy contributions

Most solvers are based on a finite difference approach [69, 120–122]. Hence, the first issue is to discretize the sample with a finite set of same shape[1] cells, each of them representing a different spatial position. Magnetization is sampled at those positions and, therefore, cell size ought to be small enough to assure a uniform magnetization in each cell. Thus, it must be smaller than any of the characteristic lengths defined in chapter 2.

Summarizing, the system is represented by a set of $N_x \times N_y \times N_z$ identical computational cells where N_i must be an integer number $N_i = L_i/\Delta_i$, i.e., the size of the cell $\Delta x \times \Delta y \times \Delta z$ ought to be a sub-multiple of the sample size $L_x \times L_y \times L_z$, and also must be smaller than any characteristic length. Magnetization is sampled in each computational cell. Therefore, its derivative can be computed as

$$\frac{dm_i}{dx_j}\left(\vec{x}_0\right) \approx \frac{m_i\left(x_{j,0} + \Delta x_j\right) - m_i\left(x_{j,0}\right)}{\Delta x_j} \tag{3.1}$$

Higher order derivatives can be straightforwardly computed from the above expression.

The main problem of the finite difference methods is that is not so accurate when dealing with curved surfaces and some staircase artifacts may appear. Nevertheless, these methods present an easy implementation and, in the case of micromagnetics, allow for an efficient evaluation of the demagnetizing field, which is the most computationally demanding calculus. Section 3.3 is focused on the integration of equation (2.29). However, the effective field has to be previously evaluated. Here it is presented the discrete expressions of the energy densities and the discrete and adimensional[2] expressions of the fields for the different contributions above considered.

[1] Finite element approach is another possible approach. In that case, the system is discretized with elements of different shapes.

[2] In order to obtain the adimensional fields, those are normalized to saturation magnetization $\vec{h}_{eff} = \vec{H}_{eff}/M_s$. Energy densities are normalized to the value $\mu_0 M_s^2$.

3.2.1 Exchange

The discrete expression of the exchange energy density (2.35) requires the discretization of the following expression

$$\left(\vec{\nabla}\vec{m}\right)^2 \equiv \left(\vec{\nabla}m_x\right)^2 + \left(\vec{\nabla}m_y\right)^2 + \left(\vec{\nabla}m_z\right)^2 \tag{3.2}$$

Therefore, the spatial derivatives are substituted by the finite increment of the function at the considered points. For each c Cartesian component it can be written

$$\left(\vec{\nabla}m_c\right)^2 \approx \left(\frac{\Delta_x m_c}{\Delta x}\right)^2 + \left(\frac{\Delta_y m_c}{\Delta y}\right)^2 + \left(\frac{\Delta_z m_c}{\Delta z}\right)^2 \tag{3.3}$$

where Δc is the cell size, and therefore the spatial increment for a given spatial direction. $\Delta_c m_{c'}$ is the increment of the magnetization c' component along c direction. Considering only one first neighbour

$$\left(\frac{\Delta_x m_x}{\Delta x}\right)^2 = \frac{m_x^2\left(i+1,j,k\right) + m_x^2\left(i,j,k\right) - 2m_x\left(i+1,j,k\right)m_x\left(i,j,k\right)}{\left(\Delta x\right)^2} \tag{3.4}$$

Taking into account every direction, component and neighbour, and recalling the constraint $\vec{m}^2 = 1$ and assuming cubic cells $\Delta x = \Delta y = \Delta z$, the discrete exchange energy density at point (i,j,k) is read as

$$\begin{aligned} u_{exch}\left(i,j,k\right) &= \frac{2A}{\left(\Delta x\right)^2}\sum_{i',j',k'}^{NN}\left[1 - \vec{m}\left(i,j,k\right)\cdot\vec{m}\left(i',j',k'\right)\right] = \\ &= NN\frac{2A}{\left(\Delta x\right)^2} - \frac{2A}{\left(\Delta x\right)^2}\vec{m}\left(i,j,k\right)\cdot\sum_{i',j',k'}^{NN}\vec{m}\left(i',j',k'\right) \end{aligned} \tag{3.5}$$

where only nearest neighbours (NN) are considered for the summation.

On the discrete representation of the functional derivative (2.13), the gradient only has second-order terms which can be neglected for smooth magnetization changes as those here considered. Therefore, the functional derivative $\delta/\delta\vec{m}$ becomes a partial derivative $\partial/\partial\vec{m}$ [67]. Taking this fact into account, it is possible to derive from (3.5) the discrete and adimensional counterpart of exchange effective field

$$\begin{aligned} \vec{h}_{exch}\left(i,j,k\right) = \frac{2A}{\mu_0 M_s^2}\Bigg[&\frac{\vec{m}\left(i+1,j,k\right) + \vec{m}\left(i-1,j,k\right)}{\left(\Delta x\right)^2} + \\ &+ \frac{\vec{m}\left(i,j+1,k\right) + \vec{m}\left(i,j-1,k\right)}{\left(\Delta y\right)^2} + \\ &+ \frac{\vec{m}\left(i,j,k+1\right) + \vec{m}\left(i,j,k-1\right)}{\left(\Delta z\right)^2}\Bigg] \end{aligned} \tag{3.6}$$

3.2.2 Magnetic anisotropy

Anisotropy energy arises from a local interaction [67] and does not depend on magnetization derivatives, so the anisotropy energy density (2.40) has a trivial discrete expression

$$u_{anis}\left(i,j,k\right) = K\left[1 - \left(\vec{m}\left(i,j,k\right)\cdot\vec{u}_K\right)^2\right] \tag{3.7}$$

$\vec{u}_K$ being a unit vector along the uniaxial anisotropy direction. Therefore, the adimensional effective field due to magnetic anisotropy reads

$$\vec{h}_{anis}\left(i,j,k\right) = \frac{2K}{\mu_0 M_s^2}\left(\vec{m}\left(i,j,k\right)\cdot\vec{u}_K\left(i,j,k\right)\right)\vec{u}_K\left(i,j,k\right) \tag{3.8}$$

3.2.3 Magnetostatic terms

Zeeman energy has also a local character [67], so its discrete expression is obtained in a trivial way

$$u_{ext}\left(i,j,k\right) = -\mu_0 M_s^2 \vec{m}\left(i,j,k\right)\cdot\vec{h}_{ext}\left(i,j,k\right) \tag{3.9}$$

where the field $\vec{h}_{ext}\left(i,j,k\right)$ is normalized to the saturation magnetization value M_s.

Nonetheless, the magnetostatic interaction responsible for the demagnetizing field is non-local, and it depends on the magnetization of the whole sample. Some assumptions about magnetization of the points not included on the mesh ought to be done. Both GPMagnet [121] and MuMax3 [122] assume that magnetization is constant along the whole computational cell. Then, the c component of the demagnetizing field h^c_{dmg} can be computed as

$$h^c_{dmg}\left(i,j,k\right) = \sum_{c'}^{(x,y,z)} \sum_{(i',j',k')}^{N_t} N_{cc'}\left(i-i',j-j',k-k'\right) m_{c'}\left(i',j',k'\right) \tag{3.10}$$

N_t being the total number of computational cells $N_t = N_x \times N_y \times N_z$ and $N_{cc'}$ the magnetostatic tensor components. These components depend only on the distance between the source and the considered point and the geometry, and thus they can be computed at the beginning of the simulation and used at each time step. The convolution of the magnetostatic tensor with the magnetization can be recognized in the previous equation (3.10) for each component. As long as this field in each point depends on the magnetization in each of the other points, its evaluation requires $O\left(N_t^2\right)$ operations, being the most demanding calculation of a μMag simulation. However, it can be speeded up by using the Fast Fourier Transform [120] method and exploiting the fact that a convolution in real space becomes a product in reciprocal space. The demagnetizing field can then be computed as

$$h^c_{dmg}\left(i,j,k\right) = \mathcal{F}^{-1}\Big[\sum_{c'}^{(x,y,z)} \mathcal{F}\left[N_{cc'}\left(i,j,k\right)\right]\mathcal{F}\left[m_{c'}\left(i,j,k\right)\right]\Big] \tag{3.11}$$

where $\mathcal{F}$ and $\mathcal{F}^{-1}$ are the Fourier transform and the inverse Fourier transform respectively. The number of operations required to compute the demagnetizing field asymptotically tends to $N_t log N_t$ when computed as (3.11), which means a substantial gain when larges N_t are under consideration. Nevertheless, a finite sample inside an infinite space is usually considered, so errors due to the lack of periodicity may arise. Adding external computational cells with null magnetization along every direction in space so as to at least double the number of cells needed to represent the sample (zero-padding [69] method) is a way to avoid such kind of errors.

Demagnetizing energy density (2.49) reads in its discrete version

$$u_{dmg} = -\frac{1}{2}\mu_0 M_s^2 \sum_{c}^{(x,y,z)} h_{dmg}^{c}(i,j,k)\, m_c(i,j,k) \tag{3.12}$$

the $1/2$ comes from the fact that magnetization is the source of the demagnetizing field $\vec{h}_{dmg}$.

3.2.4 Dzyaloshinskii-Moriya interaction

The discrete version of the iDMI requires the discrete form for $\vec{m}\vec{\nabla}(\vec{m}\vec{u}_n)$, where $\vec{u}_n$ is the normal vector to the interface. From now, it is considered that $\vec{u}_n = \vec{u}_z$

$$(\vec{m}\cdot\vec{u}_n)\,\vec{\nabla}\cdot\vec{m} \approx m_z\frac{\Delta_x m_x}{\Delta x} + m_z\frac{\Delta_y m_y}{\Delta y} + m_z\frac{\Delta_z m_z}{\Delta z} \tag{3.13}$$

It is also needed to discretize the following expression

$$\vec{m}\cdot\vec{\nabla}(\vec{m}\cdot\vec{u}_n) \approx m_x\frac{\Delta_x m_z}{\Delta x} + m_y\frac{\Delta_y m_z}{\Delta y} + m_z\frac{\Delta_z m_z}{\Delta z} \tag{3.14}$$

Using (2.51), (3.13) and (3.14) the discrete counterpart of the DMI energy density can be written as

$$u_{DMI} = D\left[m_z\frac{\Delta_x m_x}{\Delta x} + m_z\frac{\Delta_y m_y}{\Delta y} - m_x\frac{\Delta_x m_z}{\Delta x} - m_y\frac{\Delta_y m_z}{\Delta y}\right] \tag{3.15}$$

The field is derived by taking into account that, in this case, the functional derivative $\delta/\delta\vec{m}$ includes first-order terms, which cannot be disregarded. Then, the following expression is obtained

$$\begin{aligned}\vec{h}_{DMI} = \frac{2D}{\mu_0 M_s^2}\Big[&\frac{\Delta_x m_z}{\Delta x}\vec{u}_x + \frac{\Delta_y m_z}{\Delta y}\vec{u}_y + \frac{\Delta_z m_z}{\Delta z}\vec{u}_z - \\ &- \vec{u}_n\left(\frac{\Delta_x m_x}{\Delta x} + \frac{\Delta_y m_y}{\Delta y} + \frac{\Delta_z m_z}{\Delta z}\right)\Big]\end{aligned} \tag{3.16}$$

It may be notice that we do not assumed that $\vec{u}_n = \vec{u}_z$ for the field, so this expression is more general.

3.3 Algorithms for numerical integration

Once a proper way to compute the effective field is known, it is possible to numerically solve the -adimensional- LLG equation (2.30). From an initial magnetic configuration, there are several algorithms to evaluate the magnetization after each time step $\Delta\tau$. However, the initial magnetic configuration is not, in general, an equilibrium one. Thus, it is usually convenient to minimize the energy before starting a simulation. There are various methods which minimize the magnetization, like the conjugate gradient methods [120] or simply let the system evolve in the absence of external stimuli.

3.3.1 Euler Algorithm.

The easiest algorithm to be implemented is the Euler algorithm. It requires only one evaluation of the effective field for each time step and has an error of the order of $\Delta\tau^2$. Once the magnetization $\vec{m}$ and the effective field $\vec{h}_{eff}$ are known in every computational cell $\forall\,(i,j,k)$, magnetization after a time step $\Delta\tau$ is evaluated as

$$\begin{aligned}\vec{m}\,(\tau+\Delta\tau) = \vec{m}\,(\tau) - \frac{\Delta\tau}{(1+\alpha^2)}\Big[&\vec{m}\,(\tau)\times\vec{h}_{eff}\,(\tau) + \\ &+\alpha\vec{m}\,(\tau)\times\Big(\vec{m}\,(\tau)\times\vec{h}_{eff}\,(\tau)\Big)\Big]\end{aligned} \tag{3.17}$$

Nevertheless, it presents some issues. The magnetization modulus is not preserved, so it must be renormalized after each time step. Besides, small time steps are required to be stable, making the simulation longer. More complex algorithms can be used, allowing longer and adaptative time steps, which makes the solver faster at smooth regions without losing accuracy at changeable ones.

3.3.2 Heun Algorithm.

This algorithm requires calculating previously the value

$$\begin{aligned}\tilde{\vec{m}}\,(\tau+\Delta\tau) = \vec{m}\,(\tau) - \frac{\Delta\tau}{(1+\alpha^2)}\Big[&\vec{m}\,(\tau)\times\vec{h}_{eff}\,(\tau) + \\ &+\alpha\vec{m}\,(\tau)\times\Big(\vec{m}\,(\tau)\times\vec{h}_{eff}\,(\tau)\Big)\Big]\end{aligned} \tag{3.18}$$

and evaluating the effective field $\tilde{\vec{h}}_{eff}$ for the magnetization $\tilde{\vec{m}}$. The magnetization after each time step can be computed as

$$\begin{aligned}\vec{m}\,(\tau+\Delta\tau) = \vec{m}\,(\tau) - \frac{\Delta\tau}{2\,(1+\alpha^2)}\Big[&\vec{m}\,(\tau)\times\vec{h}_{eff}\,(\tau) + \\ &+\alpha\vec{m}\,(\tau)\times\Big(\vec{m}\,(\tau)\times\vec{h}_{eff}\,(\tau)\Big) + \\ &+\tilde{\vec{m}}\,(\tau+\Delta\tau)\times\tilde{\vec{h}}_{eff}\,(\tau+\Delta\tau) + \\ &+\alpha\tilde{\vec{m}}\,(\tau+\Delta\tau)\times\Big(\tilde{\vec{m}}\,(\tau+\Delta\tau)\times\tilde{\vec{h}}_{eff}\,(\tau+\Delta\tau)\Big)\Big]\end{aligned} \tag{3.19}$$

This method adopts longer time steps than Runge-Kutta methods, is less accurate (its error is of the order of $\Delta\tau^3$), and does not conserve the magnetization modulus either, so it has to be renormalized after each time step. However, when dealing with stochastic processes, it has the advantage to lead to the Stratonovich solution, which is the interesting one for physics.

3.3.3 Runge-Kutta Methods.

Runge-Kutta methods are widely used in μMag solvers. They evaluate the derivative at different points along the whole step size $(\tau, \tau + \Delta\tau)$ by means of an Euler-type algorithm seeking the minimization of truncation error. The second order Runge-Kutta method [120] has four steps: 1) the derivative is computed from the initial information, 2) the derivative is used to evaluate the function at an intermediate point, renormalizing the magnetization and calculating the effective field, 3) compute the derivative at the new point, and 4) use the new derivative to evaluate the function at the end of the interval. This means

$$\begin{aligned}
\vec{m}\left(\tau + \Delta\tau/2\right) &= \vec{m}\left(\tau\right) - \frac{\Delta\tau}{2\left(1+\alpha^2\right)}\Big[\vec{m}\left(\tau\right) \times \vec{h}_{eff}\left(\tau\right) + \\
&+\alpha\vec{m}\left(\tau\right) \times \Big(\vec{m}\left(\tau\right) \times \vec{h}_{eff}\left(\tau\right)\Big)\Big] \\
\vec{m}\left(\tau + \Delta\tau\right) &= \vec{m}\left(\tau\right) - \frac{\Delta\tau}{\left(1+\alpha^2\right)}\Big[\vec{m}\left(\tau + \Delta\tau/2\right) \times \vec{h}_{eff}\left(\tau + \Delta\tau/2\right) + \\
&+\alpha\vec{m}\left(\tau + \Delta\tau/2\right) \times \Big(\vec{m}\left(\tau + \Delta\tau/2\right) \times \vec{h}_{eff}\left(\tau + \Delta\tau/2\right)\Big)\Big]
\end{aligned} \tag{3.20}$$

This second order method has an error of the order of $\Delta\tau^3$. The truncation error can be minimized by a proper combination of first derivatives. It is possible to write a general formula for Runge-Kutta methods [90, 123]. Once given

$$\frac{d\vec{m}}{dt}\left(t\right) = f\left(t, \vec{m}\left(t\right)\right) \tag{3.21}$$

and the initial magnetization $\vec{m}\left(\tau_0\right) = \vec{m}_0$ it is possible to compute the magnetization at a forward time $\tau + \Delta\tau$ from the magnetization at the previous time τ as

$$\vec{m}\left(\tau + \Delta\tau\right) = \vec{m}\left(\tau\right) + \sum_{i}^{o} b_i \vec{k}_i \tag{3.22}$$

where

$$\begin{aligned}
\vec{k}_1 &= \Delta\tau f\left(\tau, \vec{m}\left(\tau\right)\right) \\
\vec{k}_i &= \Delta\tau f\left(\tau + c_i\Delta\tau, \vec{m}\left(\tau\right) + \sum_{j}^{i-1} a_{ij}\vec{k}_j\right)
\end{aligned} \tag{3.23}$$

and o is an integer which depends on the employed method and a_{ij}, b_i, and c_i are coefficients which also depend on the employed method. The most common Runge-Kutta method is the 4º order Runge-Kutta whose coefficients are shown in 3.1. The error is of the order of $\Delta\tau^5$ in this case, and does not conserve the magnetization modulus either. Nevertheless, Runge-Kutta methods can converge to the Stratonovich

i	a_{ij}				b_i	c_i
1					1/6	0
2	1/2				1/3	1/2
3	0	1/2			1/3	1/2
4	0	0	1		1/6	1
$j=$	1	2	3	4		

a)

i	a_{ij}						b_i	b_i^*	c_i
1							$\frac{11}{108}$	$\frac{35}{432}$	0
2	$\frac{1}{5}$						0	0	$\frac{1}{5}$
3	$\frac{3}{40}$	$\frac{9}{40}$					$\frac{6250}{14553}$	$\frac{8500}{14553}$	$\frac{3}{10}$
4	$\frac{264}{2197}$	$-\frac{90}{2197}$	$\frac{840}{2197}$				$-\frac{2197}{21168}$	$-\frac{28561}{84672}$	$\frac{6}{13}$
5	$-\frac{932}{3645}$	$-\frac{14}{27}$	$\frac{3256}{5103}$	$\frac{7436}{25515}$			$\frac{81}{176}$	$\frac{405}{704}$	$\frac{2}{3}$
6	$-\frac{367}{513}$	$\frac{30}{19}$	$\frac{9940}{5643}$	$-\frac{29575}{8208}$	$\frac{6615}{3344}$		$\frac{19}{196}$	$\frac{1}{4}$	1
7	$\frac{35}{432}$	0	$\frac{8500}{14553}$	$-\frac{28561}{84672}$	$\frac{405}{704}$	$\frac{19}{196}$	$\frac{1}{40}$	0	1
$j=$	1	2	3	4	5	6			

b)

Table 3.1: Butcher tableau for a) Runge-Kutta 4º order algorithm and b) Dormand-Prince method.

solutions when dealing with LLG equation (2.29) [94, 113] for systems with weak noise.

However, most ODE integrators include an adaptative control of the step size [120, 123]. This adaptative control allows for saving time in smooth regions of the function while preserving the accuracy in the sharp ones. The algorithm requires a feedback method to estimate the local error and to act accordingly. Although there are a few other methods, we only deal here with embedded Runge-Kutta formulas [120], as the Dormand-Prince algorithm which is the default solver used in MuMax3 [122]. Those methods are based on the evaluation of two different approximation of the solution at the same points of the interval. The two approximations are characterized by the vectors $\vec{b}$ and $\vec{b}^*$, and their difference is taken as the error estimation.

$$e = \vec{m}\left(\tau + \Delta\tau\right) - \vec{m}^*\left(\tau + \Delta\tau\right) = \sum_{i=0}^{o}\left(b_i - b_i^*\right)\vec{k}_i \tag{3.24}$$

If this difference is small, the step size is enlarged, but if it is large, the solution is computed with a smaller step size equal to

$$\Delta\tau_0 = \Delta\tau_1 \left|\frac{e_0}{e_1}\right|^{1/5} \tag{3.25}$$

where e_0 is the desired error, e_1 the given error, $\Delta\tau_0$ the needed step size to obtain the required error and $\Delta\tau_1$ the employed step size. This algorithm requires computing the effective field seven times. Nevertheless, is usually implemented with the First

Same as Last (FSAL) property meaning that the last point of a time step is the same as the first one of the subsequent step, reducing the effective field evaluation down to six. Moreover, the last coefficient k_7 of a time step is also the same as the first one k_1 of the subsequent step. Thus, two solutions, of 5º and 4º order, are computed, which result in a 4º order method with adaptative step size.

3.4 Numerical integration of Langevin equation

As it has already been mentioned in section 3.3, numerical ODE solvers can converge to either an Itô, Stratonovich or any other solution. As an example, the deterministic Euler algorithm leads to a stochastic algorithm with an Itô solution. The Wiener process dW_k is substituted by its finite increment ΔW_k when discretizing a stochastic equation, so Langevin equation (2.69) becomes

$$y_i\left(t+\Delta t\right) = y_i\left(t\right) + A_i\left(\vec{y},t\right)\Delta t + \sum_k B_{ik}\left(\vec{y},t\right)\Delta W_k \tag{3.26}$$

ΔW_k has analogous properties to those of the Wiener process (2.71)

$$\begin{aligned} \left\langle \Delta W_k\left(t\right)\right\rangle &= 0 \\ \left\langle \Delta W_k\left(t\right)\Delta W_l\left(t'\right)\right\rangle &= 2D\delta_{kl}\Delta t \end{aligned} \tag{3.27}$$

where D is given by (2.84). Although (3.26) provides the Itô solution, it is possible to introduce additional terms to get the Stratonovich one. These terms are given by the relation between both solutions derived from stochastic process theory [67].

However, the most common solver for stochastic ODE is the Heun solver as a Stratonovich solution directly arises from it [113]. Like in the deterministic case, an auxiliary value must be calculated

$$\tilde{m}_i\left(t+\Delta t\right) = m_i\left(t\right) + A_i\left(\vec{m},t\right)\Delta t + \sum_k B_{ik}\left(\vec{m},t\right)\Delta W_k \tag{3.28}$$

which is used to compute the magnetization after each time step

$$\begin{aligned} m_i\left(t+\Delta t\right) = m_i\left(t\right) + \frac{1}{2}\Big[A_i\left(\tilde{\vec{m}},t+\Delta t\right) + A_i\left(\vec{m},t\right)\Big]\Delta t + \\ + \frac{1}{2}\left[\sum_k B_{ik}\left(\tilde{\vec{m}},t+\Delta t\right) + \sum_k B_{ik}\left(\vec{m},t\right)\right]\Delta W_k \end{aligned} \tag{3.29}$$

Nevertheless, magnetization must be renormalized at this time.

Chapter 4

One dimensional model

A general one dimensional model is derived from the Landau-Lifshitz-Gilbert equation and a set of simplifications. The main ideas of Walker's original one dimensional model are discussed and Walker's ansatz is presented. This ansatz is adapted to cover more general systems. The energy density terms presented in chapter 2 are integrated and related to the dynamic variables. Finally, four general equations describing the magnetic domain wall dynamic along with some comments about them are addressed.

4.1 Introduction

Chapter 3 is devoted to the numerical tools generally used to solve the LLG equation (2.29). These tools are of great importance since, as we have already seen, the analytic solution is not achievable. In spite of this fact, it is possible to seek an analytic solution by making some assumptions. This simplified solution would allow us to make predictions without running -sometimes really time demanding- μMag simulations and favoring a deeper comprehension of the physical system under consideration. Results of such a one dimensional model (1DM) were first obtained by Walker in 1956 [71, 124], who derived an analytic solution for the DW dynamic under the application of an applied magnetic field. This solution also predicts the existence of an upper limit for the applied field, above which the DW is no longer stable and its configuration evolves in time. This upper limit is known as the Walker field H_W. Due to the unstable DW configuration, DW shows a periodic velocity, with a mean velocity which drops from the values of the velocity close to, but below, the Walker field H_W.

Spherical coordinates are much more convenient than Cartesian ones for these types of problems.

$$\vec{M} = M_s \left(\sin\theta\cos\varphi\vec{u}_x + \sin\theta\sin\varphi\vec{u}_y + \cos\theta\vec{u}_z\right) = M_s\vec{u}_r \tag{4.1}$$

being θ and φ the polar and azimuthal angle respectively commonly used for spherical coordinates, as it can be seen from figure 4.1. It is worthy to note that since magnetization modulus is fixed $|\vec{M}| = M_s$, only two degrees of freedom remain, θ and φ. Its differential reads

$$d\vec{M} = M_s \left(d\theta\vec{u}_\theta + \sin\theta d\varphi\vec{u}_\varphi\right) \tag{4.2}$$

Moreover, Gilbert's equation (2.27) augmented by the current induced torques and the thermal field, and normalized to saturation magnetization value is

$$\begin{aligned}\frac{\partial\vec{m}}{\partial t} &= -\gamma_0\vec{m}\times\left(\vec{H}_{eff}+\vec{H}_{th}\right)+\alpha\vec{m}\times\frac{\partial\vec{m}}{\partial t}-b_j\left(\vec{u}\cdot\vec{\nabla}\right)\vec{m}+b_j\beta\vec{m}\times\left[\left(\vec{u}\cdot\vec{\nabla}\right)\vec{m}\right]-\\ &-\frac{g\mu_B J}{2etM_s}\vec{m}\times\left(\vec{m}\times\vec{\theta}_{SH}\right)-\gamma_0\vec{m}\times\left(\frac{\alpha_R P}{\mu_0\mu_B M_s}\left(\vec{n}\times\vec{J}\right)\right)\end{aligned} \tag{4.3}$$

which in spherical coordinates transforms to

$$\begin{aligned}\dot{\theta} &= -\frac{\gamma_0}{\mu_0 M_s\sin\theta}\frac{\delta u_V}{\delta\varphi}+\gamma_0\left(-H_{x,th}\sin\varphi+H_{y,th}\cos\varphi\right)-\alpha\sin\theta\dot{\varphi}-\\ &-b_j\left(\frac{j_x}{J}\frac{\partial\theta}{\partial x}+\frac{j_y}{J}\frac{\partial\theta}{\partial y}\right)-b_j\xi\sin\theta\left(\frac{j_x}{J}\frac{\partial\varphi}{\partial x}+\frac{j_y}{J}\frac{\partial\varphi}{\partial y}\right)+\\ &+\gamma_0 H_{SH}\cos\theta\left(j_x\sin\varphi-j_y\cos\varphi\right)+\gamma_0 H_{Ra}\left(j_x\cos\varphi+j_y\sin\varphi\right)\end{aligned} \tag{4.4a}$$

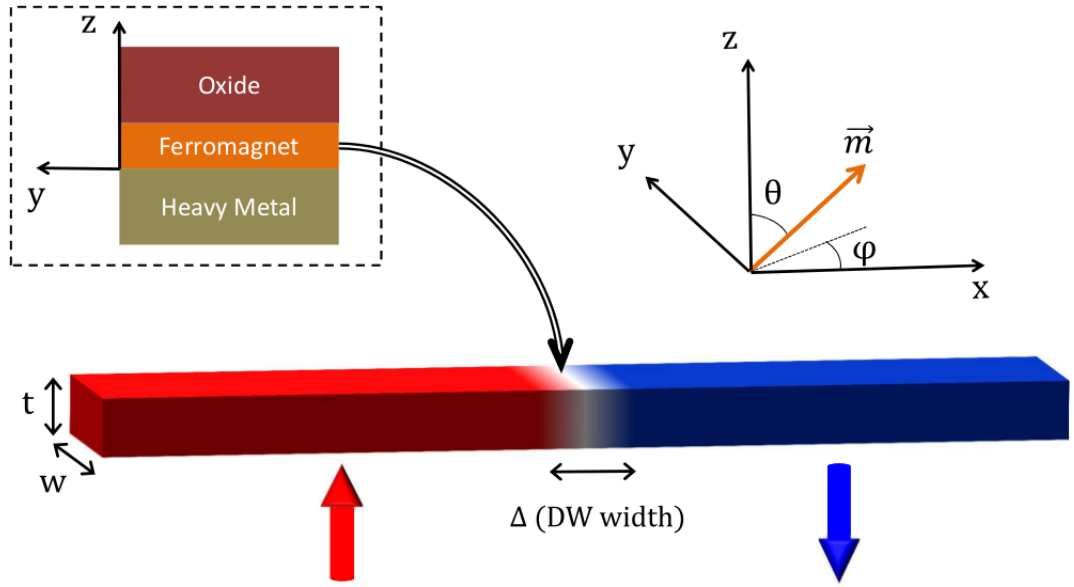

Figure 4.1: Generic considered system. Infinite strip of width w and thickness t for which $w >> t$, grown over a HM and beneath another layer, commonly an oxide. It is assumed that there are two domains, UP (red) and DOWN (blue), separated by a DW of thickness Δ. It is also shown the coordinate system employed: x is the axis for which the strip is infinite, while y and z are the transversal ones. The strip width along y-axis is w, and its thickness along z equals t. It can be checked that the azimuthal φ and polar θ angles keep the convention (see equation (4.1)).

$$\begin{aligned}\sin\theta\dot{\varphi} &= \frac{\gamma_0}{\mu_0 M_s}\frac{\delta u_V}{\delta\theta} + \alpha\dot{\theta} - \gamma_0\left[\left(H_{x,th}\cos\varphi + H_{y,th}\sin\varphi\right)\cos\theta - H_{z,th}\sin\theta\right] - \\ &-b_j\sin\theta\left(\frac{j_x}{J}\frac{\partial\varphi}{\partial x} + \frac{j_y}{J}\frac{\partial\varphi}{\partial y}\right) + b_j\xi\left(\frac{j_x}{J}\frac{\partial\theta}{\partial x} + \frac{j_y}{J}\frac{\partial\theta}{\partial y}\right) + \\ &+\gamma_0 H_{SH}\left(j_x\cos\varphi + j_y\sin\varphi\right) - \gamma_0 H_{Ra}\cos\theta\left(j_x\sin\varphi - j_y\cos\varphi\right)\end{aligned} \tag{4.4b}$$

where $H_{SH} = \dfrac{\hbar\theta_{SH}}{2et\mu_0 M_s}$ and $H_{Ra} = \dfrac{\alpha_R P}{\mu_0\mu_B M_s}$ and j_x and j_y are the x and y component of a general in-plane applied current $\vec{J}$. There are two equations which relate the temporal derivatives of the angles defining the magnetization in each point with the variational derivatives of the energy, i.e., the effective field. We are going to work on these equations to obtain a simplified expression accounting for the time evolution of a DW in a ferromagnetic strip, considering the system as a whole.

4.2 Walker's ansatz and Landau-Lifshitz-Gilbert

Walker assumed for his work an infinite strip for which the symmetry axis is an easy axis, having two domains in this direction [71]. He also assumed that magnetization only depends on the axis given by the DW normal. Finally, it is assumed that φ is constant all along the strip and equals $\varphi = \pm\pi/2$ in the absence of external stimuli. In our case, we considered a quasi-infinite strip along the x-direction, and much larger along y-direction than in the z-direction, i.e., $L >> w >> t$ being w and t as defined on figure 4.1 and being L the length of the strip. It is assumed that our FM layer is grown over a HM with a SOC and beneath another different layer, commonly an oxide. Strip geometry promotes a shape anisotropy along the x-axis as it would

minimize the demagnetizing energy. Nevertheless, the small thickness t of the strip along with surface effects causes that this kind of strips exhibits a high PMA which makes the z-axis the easy one in spite of the demagnetizing energy. It is considered that two perpendicular domains are present. As long as φ is considered constant along the whole strip, each domain is characterized by a constant value of θ, $\theta = 0$ for UP domains and $\theta = \pi$ for DOWN ones. In our case, magnetization is allowed to change not only along x but also along the y-direction.

So the system under consideration has already been defined, and the first assumption has been made. Our description characterizes magnetization with two angles θ and φ, both constants inside each domain. However, even though φ is constant along the whole strip, θ is not, and since we are using a continuous description, this angle should evolve smoothly from the value in one domain to the value in the other domain. The region where this smooth change takes part is known as the magnetic domain wall, or simply DW. It is possible to get the values of θ across this region from μMag simulations but, in order to obtain purely analytical results, a given transition of θ is assumed for this region. The original profile assumed by Walker [71]

$$\begin{aligned} \theta &= 2\arctan\left[\exp\left(\frac{x-q}{\Delta}\right)\right] \\ \varphi &= cte \end{aligned} \tag{4.5}$$

is modified to include some other dependencies, resulting in the following expression [19, 41]

$$\begin{aligned} \theta &= 2\arctan\left[\exp\left(Q\frac{(x-q)\cos\chi + y\sin\chi}{\Delta}\right)\right] \\ \varphi &= cte = \Phi \end{aligned} \tag{4.6}$$

(4.6) defines the magnetization along the entire strip as a function of the DW position q, its orientation Φ, its width Δ and its tilting angle χ defined as the angle between the DW normal and the longitudinal strip axis. Constant Q defines the DW type. $Q = 1$ is an UP-DOWN transition while $Q = -1$ defines a DOWN-UP one. It is assumed that transition occurs from lower xs to higher xs. It is supposed that this structure remains while a stimulus is applied and so these four parameters are time-dependent. Equations (4.4a) and (4.4b) can be then simplified by computing an energy density. In that way, four equations accounting for the **global** behavior of the strip and depending only on q and Φ and, if needed, on Δ and/or χ are obtained. Note the difference with the previous equation which is **local** even though only depends on θ and φ.

4.3 Surface and linear energy density

As it has already been stated, the assumption that properties are constant along at least one of the axis allows the simplification of the volume energy density u_V by integrating along the other axes. The result is a surface energy density σ if there are two axes along which variables are constant, or a linear energy density λ if there is

only one. In our case changes along y-axis may be possible so now we focus on the linear energy density λ. Nevertheless, chapters 6-12 use the surface energy density σ since it is supposed that changes along y are not significant. Then, it can be written

$$\lambda = \int_{-w/2}^{w/2} \sigma dy = \int_{-w/2}^{w/2} \int_{-\infty}^{\infty} u_V dy dx \tag{4.7}$$

from which it is possible to derive an expression for the variation of λ [125]

$$\delta\lambda = \int_{-w/2}^{w/2} \int_{-\infty}^{\infty} \left(\frac{\delta u_V}{\delta\theta}\delta\theta + \frac{\delta u_V}{\delta\varphi}\delta\varphi \right) dydx \tag{4.8}$$

Taking into account that $\delta\theta$ can be expressed as

$$\delta\theta = \frac{\partial\theta}{\partial q}\delta q + \frac{\partial\theta}{\partial\Delta}\delta\Delta + \frac{\partial\theta}{\partial\chi}\delta\chi \tag{4.9}$$

$\delta\lambda$ is read

$$\delta\lambda = \int_{-w/2}^{w/2} \int_{-\infty}^{\infty} \left[\frac{\delta u}{\delta\theta} \left(\frac{\partial\theta}{\partial q}\delta q + \frac{\partial\theta}{\partial\Delta}\delta\Delta + \frac{\partial\theta}{\partial\chi}\delta\chi \right) + \frac{\delta u}{\delta\varphi}\delta\varphi \right] dydx \tag{4.10}$$

It may be notice that only partial with respect q, Δ and χ are considered, but no with respect its gradients ∇q, $\nabla\Delta$ and $\nabla\chi$. The reason is that we are not considering a pure bidimensional system, i.e., DW can tilt with an angle χ, but it cannot bend. This means that those gradients, and also $\nabla\varphi$, are zero [66]. Each term can be now identified with a derivative of λ with respect to each variable [125]

$$\frac{\partial\lambda}{\partial q} = \int_{-w/2}^{w/2} \int_{-\infty}^{\infty} \frac{\delta u_V}{\delta\theta}\frac{\partial\theta}{\partial q} dxdy \tag{4.11}$$

$$\frac{\partial\lambda}{\partial\varphi} = \int_{-w/2}^{w/2} \int_{-\infty}^{\infty} \frac{\delta u_V}{\delta\varphi} dxdy \tag{4.12}$$

$$\frac{\partial\lambda}{\partial\Delta} = \int_{-w/2}^{w/2} \int_{-\infty}^{\infty} \frac{\delta u_V}{\delta\theta}\frac{\partial\theta}{\partial\Delta} dxdy \tag{4.13}$$

$$\frac{\partial\lambda}{\partial\chi} = \int_{-w/2}^{w/2} \int_{-\infty}^{\infty} \frac{\delta u_V}{\delta\theta}\frac{\partial\theta}{\partial\chi} dxdy \tag{4.14}$$

Each equation must be integrated by using equation (4.4) giving four partial derivatives (details are given in the Appendix 12.6)

$$\begin{aligned} \frac{\partial\lambda}{\partial q} = -\frac{\mu_0 M_s w}{\gamma_0} \Big[\alpha\frac{2\dot{q}}{\Delta}\cos\chi + Q2\dot{\Phi} - \frac{2b_j\xi}{\Delta}\left(\frac{j_x}{J}\cos\chi + \frac{j_y}{J}\sin\chi \right) - \\ -\gamma_0 Q 2H_{z,th} - \gamma_0 Q\pi H_{SH}\left(j_x\cos\Phi + j_y\sin\Phi \right) \Big] \end{aligned} \tag{4.15}$$

$$\frac{\partial\lambda}{\partial\varphi} = \frac{2\mu_0 M_s w}{\gamma_0}\Big[Q\dot{q} - \frac{\alpha\Delta\dot{\Phi}}{\cos\chi} - Qb_j\left(\frac{j_x}{J} + \frac{j_y}{J}\tan\chi\right) + \\ +\gamma_0\frac{\Delta}{\cos\chi}\frac{\pi}{2}\left(-H_{x,th}\sin\Phi + H_{y,th}\cos\Phi\right) + \\ +\gamma_0 H_{Ra}\frac{\Delta}{\cos\chi}\frac{\pi}{2}\left(j_x\cos\Phi + j_y\sin\Phi\right)\Big] \tag{4.16}$$

$$\frac{\partial\lambda}{\partial\Delta} = -\frac{\mu_0 M_s}{\gamma_0}\alpha\frac{w}{\cos\chi}\frac{\pi^2}{6}\Big(\tan\chi\dot{\chi} + \frac{\dot{\Delta}}{\Delta}\Big) \tag{4.17}$$

$$\frac{\partial\lambda}{\partial\chi} = -\frac{\mu_0 M_s}{\gamma_0}\alpha\left[\frac{\pi^2}{6}\frac{w\Delta}{\cos\chi}\tan^2\chi\dot{\chi} + \frac{2}{\Delta\cos^3\chi}\frac{w^3}{12}\dot{\chi} + \frac{\pi^2}{6}\frac{\tan\chi}{\cos\chi}w\dot{\Delta}\right] \tag{4.18}$$

Four equations relating the partial derivatives of the linear energy density and the dynamic variables have been derived. However, a useful expression of such linear energy density is still needed. Density energies given in chapter 2 are integrated in order to calculate such an expression. The additive character of the energy allows us to calculate each contribution separately and then, summing all contribution up to get the total linear energy density. In that way, the exchange energy contribution has a linear energy density equal to

$$\lambda_{exch} = \frac{2Aw}{\Delta\cos\chi} \tag{4.19}$$

The term accounting for the applied field is

$$\lambda_{ext} = -\mu_0 M_s\frac{\Delta w}{\cos\chi}\left(\pi H_x\cos\Phi + \pi H_y\sin\Phi + 2QH_z q\frac{\cos\chi}{\Delta}\right) \tag{4.20}$$

while the accountant for the demagnetizing energy reads

$$\lambda_{dmg} = \frac{\Delta\mu_0 M_s^2 w}{\cos\chi}\left(N_x\cos^2(\Phi-\chi) + N_y\sin^2(\Phi-\chi) - N_z\right) \tag{4.21}$$

N_x, N_y and N_z are the diagonal components of the demagnetizing field (see appendix 12.6). Finally, the term accounting for the DMI can be written as

$$\lambda_{DMI} = \frac{Q\pi Dw}{\cos\chi}\cos(\Phi-\chi) \tag{4.22}$$

Especial attention requires the term accounting for the linear magnetic anisotropy energy density. In the case of a uniform and homogeneous strip, it is simply

$$\lambda_{anis} = \frac{2K_1\Delta w}{\cos\chi} \tag{4.23}$$

Nevertheless, systems with a variable magnetic anisotropy are also considered along this manuscript. Although there are studies where a linear variation of the anisotropy in a region has been considered [79], the study of periodic variations of the anisotropy is a novel contribution of this thesis. It is assumed that anisotropy might increase or decrease but always in a linear manner and only along the x-direction. In fact, it is assumed a periodic change of the anisotropy. So it is considered that anisotropy

grows linearly from a minimum value K_u^- to a maximum value K_u^+ in a distance d_1. Then, anisotropy decreases linearly from this maximum value K_u^+ to the minimum one K_u^- in a distance d_2. It is also assumed that the minimum value K_u^- is still high enough to preserve the perpendicular anisotropy[1]. This profile is repeated periodically. The addition of d_1 and d_2 is called $d_t = d_1 + d_2$

$$K_u = \begin{cases} K_u^- + \dfrac{K_u^+ - K_u^-}{d_1}\left(x - d_t\left(\left\lfloor \dfrac{q}{d_t}\right\rfloor - n\right)\right) \\ if\ d_t\left(\left\lfloor \dfrac{q}{d_t}\right\rfloor - n\right) < x < d_t\left(\left\lfloor \dfrac{q}{d_t}\right\rfloor - \left(n - \dfrac{d_1}{d_t}\right)\right) \\ K_u^+ - \dfrac{K_u^+ - K_u^-}{d_2}\left(x - d_t\left(\left\lfloor \dfrac{q}{d_t}\right\rfloor - \left(n - \dfrac{d_1}{d_t}\right)\right)\right) \\ if\ d_t\left(\left\lfloor \dfrac{q}{d_t}\right\rfloor - \left(n - \dfrac{d_1}{d_t}\right)\right) < x < d_t\left(\left\lfloor \dfrac{q}{d_t}\right\rfloor - (n-1)\right) \end{cases} \tag{4.24}$$

where $\lfloor\rfloor$ stands for the floor function. So the linear magnetic anisotropy energy density reads

$$\lambda_{anis} = \iint K \sin^2\theta dx dy = \int \left(\sum_{n=-m}^{m'} I_n + I'_n\right) dy \tag{4.25}$$

As long as K only change along x, it is possible to focus on this integral. Nevertheless, comments about integral along y will be made along this subsection. So I_n and I'_n are the integrals along x of the rise and fall intervals of the anisotropy function respectively. Since there are $m' + m$ of such integrals, the summation is needed, which tends to infinity for and infinite strip. In that case, this limit is well defined and addends due to slopes far from the DW vanish. It is worthy to highlight that even though q appears in (4.24), the anisotropy **does not** depend on the DW -or even on the existence of such a wall-. Any integer replacing the floor function leads to the same profile. However, the above expression makes the following calculations easier by choosing a proper coordinate origin, depending on the DW position.

First, I_n is considered, accounting for the linear anisotropy rising

$$\begin{aligned} I_n &= \int_{d_t\left(\left\lfloor \frac{q}{d_t}\right\rfloor - n\right)}^{d_t\left(\left\lfloor \frac{q}{d_t}\right\rfloor - \left(n - \frac{d_1}{d_t}\right)\right)} K_u^- + \frac{K_u^+ - K_u^-}{d_1}\left(x - d_t\left(\left\lfloor \frac{q}{d_t}\right\rfloor - n\right)\right)\sin^2\theta dx = \\ &= \int_{\zeta_{min}}^{\zeta_{max}} K_u^- + \frac{K_u^+ - K_u^-}{d_1}\left(\frac{Q\Delta\zeta + y\sin\chi}{\cos\chi} + d_t\left(\left\{\frac{q}{d_t}\right\} + n\right)\right)\sin^2\theta\frac{Q\Delta}{\cos\chi}d\zeta \end{aligned} \tag{4.26}$$

[1]It should be pointed out that, from the magnetostatic point of view, this axis is the least favorable.

with

$$\zeta_{max} = \frac{Q}{\Delta}\left[d_t\left(-\left\{\frac{q}{d_t}\right\} - \left(n - \frac{d_1}{d_t}\right)\right)\cos\chi - y\sin\chi\right]$$
$$\zeta_{min} = \frac{Q}{\Delta}\left[d_t\left(-\left\{\frac{q}{d_t}\right\} - n\right)\cos\chi - y\sin\chi\right]$$

where x has been replaced by the auxiliary variable ζ as defined in the appendix 12.6, and the fact that $\frac{q}{d_t} - \left\lfloor\frac{q}{d_t}\right\rfloor = \left\{\frac{q}{d_t}\right\}$ is used, being $\{\}$ the fractional part function. I_n is computed term by term

$$I_n^1 = \int_{\zeta_{min}}^{\zeta_{max}} K_u^- \sin^2\theta \frac{Q\Delta}{\cos\chi} d\zeta =$$
$$= \frac{\Delta K_u^-}{\cos\chi}\left[\tanh\left[\frac{d_t}{\Delta}\left(-\left\{\frac{q}{d_t}\right\} - \left(n - \frac{d_1}{d_t}\right)\right)\cos\chi - \frac{y}{\Delta}\sin\chi\right] - \right. \tag{4.27}$$
$$\left. - \tanh\left[\frac{d_t}{\Delta}\left(-\left\{\frac{q}{d_t}\right\} - n\right)\cos\chi - \frac{y}{\Delta}\sin\chi\right]\right]$$

$$I_n^2 = \int_{\zeta_{min}}^{\zeta_{max}} \frac{K_u^+ - K_u^-}{d_1} d_t\left(\left\{\frac{q}{d_t}\right\} + n\right)\sin^2\theta\frac{Q\Delta}{\cos\chi}d\zeta =$$
$$= \frac{K_u^+ - K_u^-}{d_1}\frac{d_t\Delta}{\cos\chi}\left(\left\{\frac{q}{d_t}\right\} + n\right)\left[\tanh\left[\frac{d_t}{\Delta}\left(\left\{\frac{q}{d_t}\right\} + n\right)\cos\chi + \frac{y}{\Delta}\sin\chi\right] - \right.$$
$$\left. - \tanh\left[\frac{d_t}{\Delta}\left(\left\{\frac{q}{d_t}\right\} + \left(n - \frac{d_1}{d_t}\right)\right)\cos\chi + \frac{y}{\Delta}\sin\chi\right]\right] \tag{4.28}$$

$$I_n^3 = \int_{\zeta_{min}}^{\zeta_{max}} \frac{K_u^+ - K_u^-}{d_1}\frac{Q\Delta\zeta + y\sin\chi}{\cos\chi}\sin^2\theta\frac{Q\Delta}{\cos\chi}d\zeta =$$
$$= \frac{K_u^+ - K_u^-}{d_1}\left(\frac{\Delta}{\cos\chi}\right)^2\left[\zeta_{max}\tanh\zeta_{max} - \zeta_{min}\tanh\zeta_{min} + \right. \tag{4.29}$$
$$\left. + \log\left(\frac{\cosh\zeta_{min}}{\cosh\zeta_{max}}\right)\right]$$

where the term with y of I_n^3 has been discarded because it vanishes when integration along y is made. In the case of the fall of the anisotropy, a similar expression can be cast

$$I_n' = \int_{d_t\left(\left\lfloor\frac{q}{d_t}\right\rfloor - (n-1)\right)}^{d_t\left(\left\lfloor\frac{q}{d_t}\right\rfloor - \left(n - \frac{d_1}{d_t}\right)\right)} K_u^+ - \frac{K_u^+ - K_u^-}{d_2}\left(x - d_t\left(\left\lfloor\frac{q}{d_t}\right\rfloor - \left(n - \frac{d_1}{d_t}\right)\right)\right)\sin^2\theta dx =$$
$$= \int_{\zeta_{min}'}^{\zeta_{max}'} K_u^+ - \frac{K_u^+ - K_u^-}{d_2}\left(\frac{Q\Delta\zeta + y\sin\chi}{\cos\chi} + d_t\left(\left\{\frac{q}{d_t}\right\} + n - \frac{d_1}{d_t}\right)\right)\sin^2\theta\frac{Q\Delta}{\cos\chi}d\zeta \tag{4.30}$$

with

$$\zeta'_{max} = \frac{Q}{\Delta}\left[d_t\left(-\left\{\frac{q}{d_t}\right\} - (n-1)\right)\cos\chi - y\sin\chi\right]$$
$$\zeta'_{min} = \frac{Q}{\Delta}\left[d_t\left(-\left\{\frac{q}{d_t}\right\} - \left(n - \frac{d_1}{d_t}\right)\right)\cos\chi - y\sin\chi\right]$$

So in this case

$$I'^1_n = \int_{\zeta'_{min}}^{\zeta'_{max}} K_u^+ \sin^2\theta \frac{Q\Delta}{\cos\chi} d\zeta =$$
$$= \frac{\Delta K_u^+}{\cos\chi}\left[\tanh\left[\frac{d_t}{\Delta}\left(-\left\{\frac{q}{d_t}\right\} - (n-1)\right)\cos\chi - \frac{y}{\Delta}\sin\chi\right] - \right. \tag{4.31}$$
$$\left. - \tanh\left[\frac{d_t}{\Delta}\left(-\left\{\frac{q}{d_t}\right\} - \left(n - \frac{d_1}{d_t}\right)\right)\cos\chi - \frac{y}{\Delta}\sin\chi\right]\right]$$
$$I'^2_n = \int_{\zeta'_{min}}^{\zeta'_{max}} -\frac{K_u^+ - K_u^-}{d_2} d_t\left(\left\{\frac{q}{d_t}\right\} + n - \frac{d_1}{d_t}\right)\sin^2\theta\frac{Q\Delta}{\cos\chi}d\zeta =$$
$$= \frac{K_u^+ - K_u^-}{d_2}\frac{d_t\Delta}{\cos\chi}\left(\left\{\frac{q}{d_t}\right\} + n - \frac{d_1}{d_t}\right)\left[\tanh\left[\frac{d_t}{\Delta}\left(\left\{\frac{q}{d_t}\right\} + (n-1)\right)\cos\chi + \frac{y}{\Delta}\sin\chi\right] - \right.$$
$$\left. - \tanh\left[\frac{d_t}{\Delta}\left(\left\{\frac{q}{d_t}\right\} + \left(n - \frac{d_1}{d_t}\right)\right)\cos\chi + \frac{y}{\Delta}\sin\chi\right]\right] \tag{4.32}$$
$$I'^3_n = \int_{\zeta'_{min}}^{\zeta'_{max}} -\frac{K_u^+ - K_u^-}{d_2}\left(\frac{Q\Delta\zeta + y\sin\chi}{\cos\chi}\right)\sin^2\theta\frac{Q\Delta}{\cos\chi}d\zeta =$$
$$= -\frac{K_u^+ - K_u^-}{d_2}\left(\frac{\Delta}{\cos\chi}\right)^2\left[\zeta'_{max}\tanh\zeta'_{max} - \zeta'_{min}\tanh\zeta'_{min} + \right. \tag{4.33}$$
$$\left. + \log\left(\frac{\cosh\zeta'_{min}}{\cosh\zeta'_{max}}\right)\right]$$

At this point it can be assumed that DW width is much smaller than the anisotropy period d_t. This means that I^1_n and I'^1_n vanish for $n > 1$ and $n < -1$. Then it can be written

$$\sum_{-m}^{m'} I^1_n = \frac{\Delta K_u^-}{\cos\chi}\left[1 - \sum_{-1}^{1}\tanh\left[\frac{d_t}{\Delta}\left(\left\{\frac{q}{d_t}\right\} + \left(n - \frac{d_1}{d_t}\right)\right)\cos\chi + \frac{y}{\Delta}\sin\chi\right] + \right.$$
$$\left. + \sum_{-1}^{0}\tanh\left[\frac{d_t}{\Delta}\left(\left\{\frac{q}{d_t}\right\} + n\right)\cos\chi + \frac{y}{\Delta}\sin\chi\right]\right] \tag{4.34}$$
$$\sum_{-m}^{m'} I'^1_n = \frac{\Delta K_u^+}{\cos\chi}\left[1 + \sum_{-1}^{1}\tanh\left[\frac{d_t}{\Delta}\left(\left\{\frac{q}{d_t}\right\} + \left(n - \frac{d_1}{d_t}\right)\right)\cos\chi + \frac{y}{\Delta}\sin\chi\right] - \right.$$
$$\left. - \sum_{-1}^{0}\tanh\left[\frac{d_t}{\Delta}\left(\left\{\frac{q}{d_t}\right\} + n\right)\cos\chi + \frac{y}{\Delta}\sin\chi\right]\right] \tag{4.35}$$

Summing up both contributions one gets

$$A = \sum_{-m}^{m'} I_n^1 + I_n'^1 = \frac{\Delta}{\cos\chi}\left(K_u^+ + K_u^-\right) + \\ + \frac{\Delta}{\cos\chi}\left(K_u^+ - K_u^-\right)\left[-\sum_{-1}^{0}\tanh\left[\frac{d_t}{\Delta}\left(\left\{\frac{q}{d_t}\right\} + n\right)\cos\chi + \frac{y}{\Delta}\sin\chi\right] + \right. \\ \left. + \sum_{-1}^{1}\tanh\left[\frac{d_t}{\Delta}\left(\left\{\frac{q}{d_t}\right\} + \left(n - \frac{d_1}{d_t}\right)\right)\cos\chi + \frac{y}{\Delta}\sin\chi\right]\right] \tag{4.36}$$

Again I_n^2 and $I_n'^2$ vanish for $n > 1$ and $n < -1$. It can be defined $a_n = \left\{\frac{q}{d_t}\right\} + n$ so in this case

$$\sum_{-m}^{m'} I_n^2 = \frac{K_u^+ - K_u^-}{d_1}\frac{d_t\Delta}{\cos\chi}\left[\sum_{-1}^{1} a_n\left[\tanh\left(\frac{d_t}{\Delta}a_n\cos\chi + \frac{y}{\Delta}\sin\chi\right) - \right.\right. \\ \left.\left. - \tanh\left(\frac{d_t}{\Delta}\left(a_n - \frac{d_1}{d_t}\right)\cos\chi + \frac{y}{\Delta}\sin\chi\right)\right]\right] \tag{4.37}$$

$$\sum_{-m}^{m'} I_n'^2 = \frac{K_u^+ - K_u^-}{d_2}\frac{d_t\Delta}{\cos\chi}\left[\sum_{-1}^{1}\left(a_n - \frac{d_1}{d_t}\right)\left[\tanh\left(\frac{d_t}{\Delta}\left(a_n - 1\right)\cos\chi + \frac{y}{\Delta}\sin\chi\right) - \right.\right. \\ \left.\left. - \tanh\left(\frac{d_t}{\Delta}\left(a_n - \frac{d_1}{d_t}\right)\cos\chi + \frac{y}{\Delta}\sin\chi\right)\right]\right] \tag{4.38}$$

and its addition is

$$B = \sum_{-m}^{m'} I_n^2 + I_n'^2 = \left(K_u^+ - K_u^-\right)\frac{d_t\Delta}{\cos\chi}\sum_{-1}^{1}\left[\frac{a_n}{d_1}\tanh\left(\frac{d_t}{\Delta}a_n\cos\chi + \frac{y}{\Delta}\sin\chi\right) + \right. \\ + \frac{1}{d_2}\left(a_n - \frac{d_1}{d_t}\right)\tanh\left(\frac{d_t}{\Delta}\left(a_n - 1\right)\cos\chi + \frac{y}{\Delta}\sin\chi\right) - \\ \left. - \left(a_n\left(\frac{1}{d_1} + \frac{1}{d_2}\right) - \frac{d_1}{d_2 d_t}\right)\tanh\left(\frac{d_t}{\Delta}\left(a_n - \frac{d_1}{d_t}\right)\cos\chi + \frac{y}{\Delta}\sin\chi\right)\right] \tag{4.39}$$

It is convenient to work on tanh addends and log addends separately when taking into account I_n^3 and $I_n'^3$. In the case of tanh terms it can be written

$$c_n = \left(K_u^+ - K_u^-\right)\frac{Q\Delta}{\cos\chi}\left[\frac{d_t}{d_1}\Big[a_n\tanh\zeta_{min} - \left(a_n - \frac{d_1}{d_t}\right)\tanh\zeta_{max}\Big] + \right. \\ \left. + \frac{d_t}{d_2}\Big[\left(a_n - 1\right)\tanh\zeta'_{max} - \left(a_n - \frac{d_1}{d_t}\right)\tanh\zeta'_{min}\Big]\right] \tag{4.40}$$

where terms with y has been discarded as they vanish when making the integral along y. It can be checked that for $n > 1$ and $n < -1$ the integral vanishes again.

Then, taking into account that $\zeta_{max} = \zeta'_{min}$ it is possible to write the addition

$$\begin{aligned} C = &- \left(K_u^+ - K_u^-\right) \frac{d_t \Delta}{\cos\chi} \sum_{-1}^{1} \left[\frac{a_n}{d_1} \tanh\left[\left(\frac{d_t}{\Delta} a_n \cos\chi + \frac{y}{\Delta} \sin\chi \right) \right] - \right. \\ &- \left(\frac{1}{d_1} + \frac{1}{d_2} \right) \left(a_n - \frac{d_1}{d_t} \right) \tanh\left[\left(\frac{d_t}{\Delta} \left(a_n - \frac{d_1}{d_t} \right) \cos\chi + \frac{y}{\Delta} \sin\chi \right) \right] + \\ &\left. + \frac{1}{d_2} \left(a_n - 1 \right) \tanh\left[\left(\frac{d_t}{\Delta} \left(a_n - 1 \right) \cos\chi + \frac{y}{\Delta} \sin\chi \right) \right] \right] \end{aligned} \tag{4.41}$$

It can be checked that the addition of B (4.39) and C (4.41) cancels out most of their addends

$$\begin{aligned} B + C = &\left(K_u^+ - K_u^-\right) \frac{d_t \Delta}{\cos\chi} \sum_{-1}^{1} \left[\frac{1}{d_2} \left(1 - \frac{d_1}{d_t} \right) \tanh\left[\left(\frac{d_t}{\Delta} \left(a_n - 1 \right) \cos\chi + \frac{y}{\Delta} \sin\chi \right) \right] + \right. \\ &\left. + \left(\frac{d_1}{d_2 d_t} - \frac{d_t}{d_1 d_2} \frac{d_1}{d_t} \right) \tanh\left[\left(\frac{d_t}{\Delta} \left(a_n - \frac{d_1}{d_t} \right) \cos\chi + \frac{y}{\Delta} \sin\chi \right) \right] \right] = \\ = &\left(K_u^+ - K_u^-\right) \frac{\Delta}{\cos\chi} \sum_{-1}^{1} \left[\tanh\left[\left(\frac{d_t}{\Delta} \left(a_n - 1 \right) \cos\chi + \frac{y}{\Delta} \sin\chi \right) \right] - \right. \\ &\left. - \tanh\left[\left(\frac{d_t}{\Delta} \left(a_n - \frac{d_1}{d_t} \right) \cos\chi + \frac{y}{\Delta} \sin\chi \right) \right] \right] \end{aligned} \tag{4.42}$$

and finally summing A (4.36) up it is obtained

$$A + B + C = \frac{2\Delta}{\cos\chi} K_u^- \tag{4.43}$$

where the assumption that $\Delta << d_t$ has been used. Finally, the log terms from I_n^3 and $I_n'^3$ must be considered. It can be checked that for $|n| > 1$

$$\frac{\Delta}{d_1} \log\left(\frac{\cosh\zeta_{min}}{\cosh\zeta_{max}} \right) \approx \frac{n}{|n|} \qquad \frac{\Delta}{d_2} \log\left(\frac{\cosh\zeta'_{max}}{\cosh\zeta'_{min}} \right) \approx -\frac{n}{|n|}$$

So the addition of log terms is

$$\begin{aligned} C' = &\frac{\left(K_u^+ - K_u^-\right)\Delta}{\cos^2\chi} \sum_{-m}^{m'} \frac{\Delta}{d_1} \log\left(\frac{\cosh\zeta_{min}}{\cosh\zeta_{max}} \right) + \frac{\Delta}{d_2} \log\left(\frac{\cosh\zeta'_{max}}{\cosh\zeta'_{min}} \right) = \\ = &\frac{\left(K_u^+ - K_u^-\right)\Delta}{\cos^2\chi} \Big[\left(m' - 2\right) - \left(m - 2\right) - \left(m' - 2\right) + \left(m - 2\right) \Big] + \\ + &\frac{\left(K_u^+ - K_u^-\right)}{\cos^2\chi} \sum_{-1}^{1} \left[\frac{\Delta^2}{d_1} \log\left(\frac{\cosh\left(\frac{d_t}{\Delta} a_n\right)}{\cosh\left(\frac{d_t}{\Delta}\left(a_n - \frac{d_1}{d_t}\right)\right)} \right) + \frac{\Delta^2}{d_2} \log\left(\frac{\cosh\left(\frac{d_t}{\Delta}\left(a_n - 1\right)\right)}{\cosh\left(\frac{d_t}{\Delta}\left(a_n - \frac{d_1}{d_t}\right)\right)} \right) \right] \end{aligned} \tag{4.44}$$

Taking into account both, (4.43) and (4.44), the final expression for the linear

magnetic anisotropy energy density can be written as

$$\lambda_{anis} = \frac{w\Delta}{\cos\chi}\left[2K_u^- + \frac{(K_u^+ - K_u^-)}{\cos\chi}\sum_{-1}^{1}\frac{\Delta}{d_1}\log\left(\frac{\cosh\left(\frac{d_t}{\Delta}a_n\right)}{\cosh\left(\frac{d_t}{\Delta}\left(a_n - \frac{d_1}{d_t}\right)\right)}\right) + \right.$$
$$\left. + \frac{\Delta}{d_2}\log\left(\frac{\cosh\left(\frac{d_t}{\Delta}\left(a_n - 1\right)\right)}{\cosh\left(\frac{d_t}{\Delta}\left(a_n - \frac{d_1}{d_t}\right)\right)}\right)\right] \tag{4.45}$$

Expression (4.45) is still valid even though $\Delta << d_t$ is not true if just the summation is extended to take into account more slopes. In order to derive the expression used in chapters 11 and 12 it must be noticed that the limit when $d_2 \to 0$ is

$$\lim_{d_2\to 0}\frac{1}{d_2}\log\frac{\cosh\frac{d_t a_n}{\Delta}}{\cosh\frac{d_t\left(a_n - \frac{d_1}{d_t}\right)}{\Delta}} = \frac{1}{\Delta}\tanh\left(\frac{d_1}{\Delta}\left(1 - a_n\right)\right)$$

4.4 Final expressions and comments

Adding all energy contributions up leads to an expression for the linear energy density

$$\lambda = \frac{w}{\cos\chi}\left[\frac{2A}{\Delta} - \mu_0 M_s\Delta\left(\pi H_x\cos\Phi + \pi H_y\sin\Phi + 2QH_z q\frac{\cos\chi}{\Delta}\right) + \right.$$
$$+ \Delta\mu_0 M_s^2\left(N_x\cos^2\left(\Phi - \chi\right) + N_y\sin^2\left(\Phi - \chi\right) - N_z\right) + \tag{4.46}$$
$$\left. + Q\pi D\cos\left(\Phi - \chi\right) + 2\Delta K_u^- + \frac{(K_u^+ - K_u^-)\,\Delta^2}{\cos\chi}S\left(q,\Delta\right)\right]$$

where S is

$$S\left(q,\Delta\right) = \sum_{-1}^{1}\frac{1}{d_1}\log\left(\frac{\cosh\left(\frac{d_t}{\Delta}a_n\right)}{\cosh\left(\frac{d_t}{\Delta}\left(a_n - \frac{d_1}{d_t}\right)\right)}\right) + \frac{1}{d_2}\log\left(\frac{\cosh\left(\frac{d_t}{\Delta}\left(a_n - 1\right)\right)}{\cosh\left(\frac{d_t}{\Delta}\left(a_n - \frac{d_1}{d_t}\right)\right)}\right)$$

Taking into account (4.46), (4.11), (4.12), (4.13) and (4.14) and the following definitions

$$H_D = -\frac{\pi D}{2\mu_0 M_s\Delta} \qquad H_k = M_s\left(N_x - N_y\right)$$
$$H_r = \frac{(K_u^+ - K_u^-)}{2\mu_0 M_s} \qquad H_{exch} = \frac{A}{\mu_0 M_s\Delta^2}$$

$$r\left(q,\Delta\right) = \sum_{-1}^{1}\frac{\Delta}{d_1}\left(\tanh\frac{d_t}{\Delta}a_n - \tanh\frac{d_t}{\Delta}\left(a_n - \frac{d_1}{d_t}\right)\right) +$$
$$+\frac{\Delta}{d_2}\left(\tanh\frac{d_t}{\Delta}\left(a_n - 1\right) - \tanh\frac{d_t}{\Delta}\left(a_n - \frac{d_1}{d_t}\right)\right)$$

it is possible to derive four equations describing the system dynamics

$$\begin{aligned}\dot{q} = Q\frac{v_0}{\cos\chi}\Big[&\alpha\left(H_z + H_{z,th} - \frac{QH_r}{\cos^2\chi}r\left(q,\Delta\right)\right) + \\ &+ \frac{\pi}{2}\left(j_x\cos\Phi + j_y\sin\Phi\right)\left(\alpha H_{SH} - H_{Ra}\right) + \\ &+ \frac{\pi}{2}\left(H_x + H_{x,th}\right)\sin\Phi - \frac{\pi}{2}\left(H_y + H_{y,th}\right)\cos\Phi + \\ &+ \left(QH_D - H_k\cos\left(\Phi-\chi\right)\right)\sin\left(\Phi-\chi\right) + \\ &+ Q\frac{b_j}{\gamma_0\Delta}\left(\frac{j_x}{J}\cos\chi + \frac{j_y}{J}\sin\chi\right)\left(1+\alpha\xi\right)\Big]\end{aligned} \tag{4.47}$$

where $v_0 = \dfrac{\Delta\gamma_0}{1+\alpha^2}$,

$$\begin{aligned}\dot{\Phi} = \frac{v_0}{\Delta}\Big[&H_z + H_{z,th} + Q\frac{b_j}{\gamma_0\Delta}\left(\frac{j_x}{J}\cos\chi + \frac{j_y}{J}\sin\chi\right)\left(\xi-\alpha\right) + \\ &+\frac{\pi}{2}\left(j_x\cos\Phi + j_y\sin\Phi\right)\left(H_{SH} + \alpha H_{Ra}\right) - \frac{QH_r}{\cos^2\chi}r\left(q,\Delta\right) - \\ &-\alpha\frac{\pi}{2}\left(H_x + H_{x,th}\right)\sin\Phi + \alpha\frac{\pi}{2}\left(H_y + H_{y,th}\right)\cos\Phi + \\ &+\alpha\left(H_k\cos\left(\Phi-\chi\right) - QH_D\right)\sin\left(\Phi-\chi\right)\Big]\end{aligned} \tag{4.48}$$

$$\begin{aligned}\dot{\chi} = \frac{12\gamma_0}{\alpha}\left(\frac{\Delta}{w}\right)^2\Big[&QH_D\sin\Phi\cos\chi - H_{exch}\sin 2\chi - \\ &-\frac{d_t}{\Delta}H_r r\left(q,\Delta\right)\sin\chi - H_k\frac{\sin 2\left(\Phi-\chi\right)}{4}\cos^2\chi\Big]\end{aligned} \tag{4.49}$$

$$\begin{aligned}\frac{\dot{\Delta}}{\Delta} = \frac{12\gamma_0}{\pi^2\alpha}\Big[&H_{exch}\left(1 + 2\left(\frac{\pi\Delta}{w}\right)^2\sin^2\chi\right) + \frac{\pi}{2}\left(H_x\cos\Phi + H_y\sin\Phi\right) - \\ &-\frac{M_s}{2}\left(N_x\cos^2\left(\Phi-\chi\right) + N_y\sin^2\left(\Phi-\chi\right) - N_z\right) - \frac{K_u^-}{\mu_0 M_s} - \\ &-\frac{2\Delta}{\cos\chi}H_r S\left(q,\Delta\right) + \frac{d_t}{\Delta\cos\chi}H_r r\left(q,\Delta\right)\left(1 + \left(\frac{\pi\Delta}{w}\right)^2\sin^2\chi\right) - \\ &-\left(\frac{\pi\Delta}{w}\right)^2\left(QH_D - \frac{H_k}{2}\sin\left(\Phi-\chi\right)\cos\chi\right)\sin\Phi\sin\chi\Big]\end{aligned} \tag{4.50}$$

Equations (4.47), (4.48), (4.49) and (4.50) describe in a simplified manner the dynamic behaviour of the sample. They have been computed in a rather general way, so some of their terms do not appear in the next chapters. It is the case of the terms accounting for the STT, which has been considered only for the sake of completeness and because they must play a role in real devices [126]. However, these terms have not been considered in the following chapters since their effect is low in the cases considered. In the same way, the addend accounting for the Rashba effect has been only considered in chapter 7, for the same reason. The term describing an inhomogeneous anisotropy profile only appears in part IV. It should be highlighted

that results from μMag simulations and 1DM have always been in good agreement, so there was no necessity to consider neither tilting angle χ neither a time dependence of the DW width Δ.

Finally, it must be pointed out that it has been assumed that the thermal field only plays a role due to its z-component as it has already been assumed in other works [114]. The main reason for such assumption is because it allows for avoiding the presence of multiplicative noise in the equations, so no considerations about the use of Itô or Stratonovich calculus are made. Other works introduce those components, but without their multiplicative noise character [115]. The validity of this assumption is certified by the good agreement between 1DM and μMag simulations, which take into account all the three components.

Chapter 5

Experimental tools

The experimental techniques employed during my research visit at the research group "Integnano" from Université Paris Sud in Paris are commented in this chapter. The synthesis of multilayer systems is addressed by the sputtering technique. Hall voltage measurements are used to obtain hysteresis loops. Those loops are used to determine the in-plane or out-of-plane effective anisotropy. Some procedures to modify the magnetic anisotropy are considered. These procedures are alternatives to induce anisotropy gradients.

5.1 Introduction

Hitherto, a detailed explanation of the theoretical background for the study of magnetic properties of multilayered systems has been stated. However, this theoretical background would be meaningless if it could not be verified by experiments. This chapter is devoted to some of those techniques which permit such verification, particularly, those learned during my research visit at the group "Integnano" in Paris. First of all, a multilayered synthesis technique is explained. Even though it is not the only possibility, this technique is able to produce multilayers where the thickness of each layer is controlled. On the other hand, one of the most important parameters of these systems is the effective anisotropy and the PMA. This characteristic can be determined from the hysteresis loops of the system. These hysteresis loops can be depicted from both, Hall voltage measurements and Magneto-optic Kerr effect data. Finally, part IV deals with systems with variable PMA. In order to check these studies with an experimental setup, it is needed to produce an anisotropy gradient. Although it is possible to use a wedge during the synthesis process to get a space dependent thickness, and so a space dependent anisotropy, a finer tuning is provided by other techniques as it is shown here.

5.2 Multilayers synthesis. Sputtering

Sputtering was discovered in 1852 by Grove [127] and has become one of the most important techniques to synthesize thin films and multilayered systems [128–130]. The process consists of bombing with ions a target of the material that it is desired to be deposited. Ions impacts are able to pulverize some atoms from the target. The atoms detached from the target are finally deposited at a substrate. Some samples of Pt/Co/Pt, Pt/CoFeB/MgO, and Pt/CoFeB/Pt have been synthesized using the sputtering setup shared by the groups of the University of Paris-Sud.

The source of positive ions is a plasma of a specified gas. The system shared by the groups of the University of Paris-Sud uses Ar because no chemical reaction is desired and so a non-reactive gas is required, Ar being the cheapest non-reactive gas and so the most commonly used [131]. The vacuum chamber where the process takes place is prepared to a pressure of $\sim 10^{-8}$mbar before pumping the Ar in. This vacuum allows for the synthesis of samples with high purity and low imperfection densities. The plasma is generated by a discharge between two electrodes. Once ignited, the plasma requires a minimum flow of gas to be maintained. During the process, the sputtering chamber reaches a pressure of $\sim 10^{-3}$mbar. The positive Ar^+ ions are then accelerated to the cathode, where the target is placed. A DC voltage is applied for metallic targets, while an AC voltage of radio frequency (RF) is employed in the case of insulating targets. Thus, the target atoms are detached with a given kinetic energy due to this bombing process and finally are deposited at the substrate placed in the anode. Nevertheless, it is required that the atoms have a long free path to achieve the substrate, so a high Ar pressure is undesirable. But a low Ar pressure means a low density of ions to be accelerated to the target and then low deposition rates. Deposition rate cannot be improved by using higher voltage since this procedure heats the substrate up, limiting material choices [131]. In order to increase this rate the following strategy, known as magnetron sputtering, is employed. It consists on

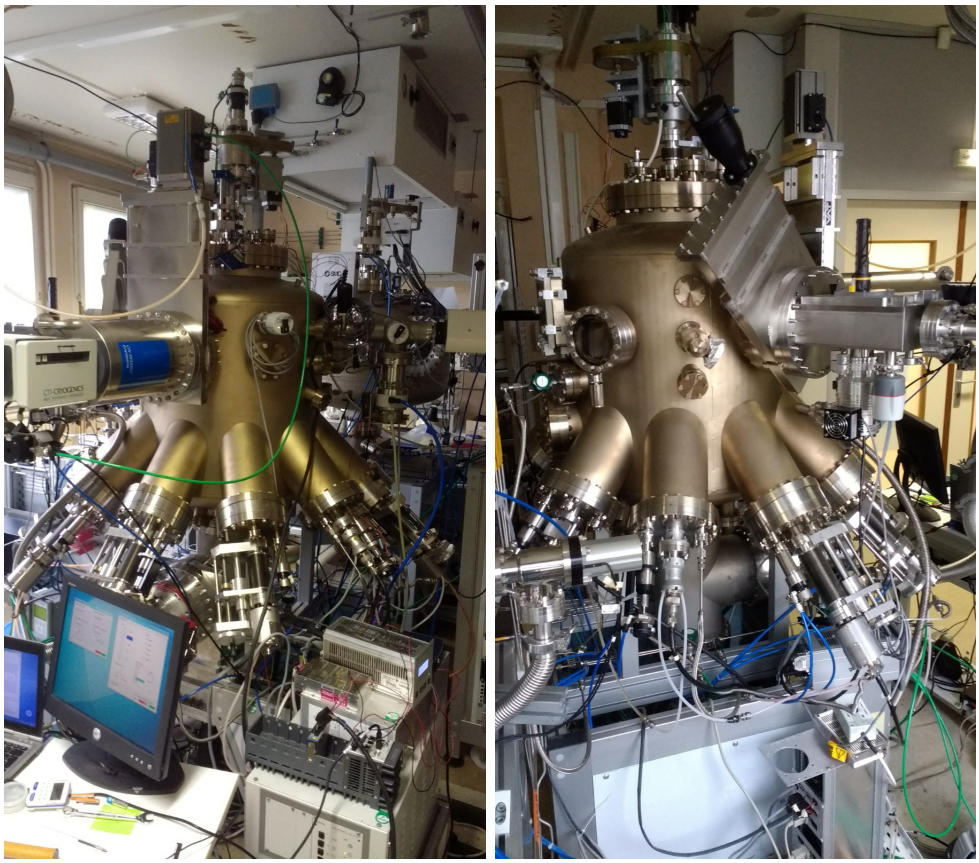

Figure 5.1: Sputtering setup. Some of the guns can be seen in the bottom of the chamber along with the refrigerating system and also the prechamber in the right figure. The motor of the rotating system can be found at the top of both images.

the application of a magnetic field to take advantages of the secondary electrons produced by the process. These electrons follow helicoidal trajectories which increase the probability of collision against gas atoms. These collisions induce the ionization of Ar leading to a denser plasma. Summarizing, due to this bombing system a certain flux of the material to be deposited is promoted depending on the gas used to produce the plasma and the target material. Once these parameters are fixed, the layer thickness is determined by the sputtering time. In multilayers, this process is repeated sequentially for each layer, changing in each case the material to deposit. Since the bombing of the target heats the system, a refrigerating mechanism is also required.

It must be pointed out that the setup is prepared with nine guns, so nine different targets can be prepared. This makes it possible to change the material for each layer. Nevertheless, this configuration has its drawbacks. As long as none of the guns is perpendicular to the plane formed by the substrate, some inhomogeneities in the samples must be expected. This is caused by the different material flux at the edge facing the gun and the opposite edge. In order to produce homogeneous samples, the following technique is applied: the substrate holder rotates along the process with a certain angular velocity. The used angular velocity has been proved to be the most suitable to produce homogeneous samples. On the other hand, the fact that the flux of material is not uniform can be exploited to produce gradients of thickness, and so gradients of magnetic anisotropy since the HM/FM and FM/Ox interfaces change.

Moreover, a wedge can be used to enlarge this effect by obstructing the flux in some regions more than in others. Even though most of the samples have been synthesized rotating the sample holder, some of them have been made without rotation in one or more layers to obtain a thickness gradient and so an anisotropy gradient. Finally, it must be highlighted that the setup also has a prechamber. This prechamber allows the sample to be extracted and introduced without losing the ultrahigh vacuum of the main chamber. However, it is required to wait until this prechamber acquires similar pressure to that of the main chamber ($\sim 10^{-6}$mbar) during sample insertion or an atmospheric pressure during sample extraction.

5.3 Hysteresis loops measurements

The effective anisotropy $K_{eff} = K_u - \frac{1}{2}\mu_0 M_s$ of a sample with PMA can be determined from its hysteresis loops when the field is applied along its hard axis [131]. The assumption that the thin film behaves as a magnetic monodomain is made. In that case, the terms accounting for the DMI and the exchange vanish, and the energy of the sample under an applied in-plane magnetic field reads

$$u = -K_u \cos^2\theta + \frac{1}{2}\mu_0 M_s^2 \cos^2\theta - \mu_0 H M_s \cos\left(\pi/2 - \theta\right) \tag{5.1}$$

where θ is the angle between the z- (easy) axis and the magnetization (see figure 4.1) and $\pi/2$ is the angle between the hard in-plane axis and the z-axis. Equations (2.40), (2.44) and (2.49) have been used. From the K_{eff} definition and neglecting some constants it is possible to rearrange the above expression

$$u = K_{eff} \sin^2\theta - \mu_0 H M_s \sin\theta \tag{5.2}$$

Equilibrium conditions

$$\left(\frac{\partial u}{\partial \theta}\right) = 0 \quad \text{and} \quad \left(\frac{\partial^2 u}{\partial \theta^2}\right) > 0 \tag{5.3}$$

are in this case

$$\left(K_{eff}\sin\theta - \mu_0 H M_s\right)\cos\theta = 0 \tag{5.4}$$

so there are two possible solutions, $\theta = \pi/2$ and $2K_{eff}\sin\theta = \mu_0 H M_s$. The stability condition stablishes that $\theta = \pi/2$ stands for $H > \frac{2K_{eff}}{\mu_0 M_s}$ while the other solution applies otherwise. In that way,

$$H = \frac{2K_{eff}}{\mu_0 M_s} \tag{5.5}$$

is the lowest value needed to set $\theta = \pi/2$ and thus cancel M_z out. This field is usually known as anisotropy field and, along with the saturation magnetization and remanent magnetization, defines a hysteresis loop. There are several methods to obtain these loops as those based on the anomalous Hall effect (AHE) or by using magneto-optic Kerr effect (MOKE) microscopy. Since MOKE microscopy is explained in other section, here the AHE method is treated.

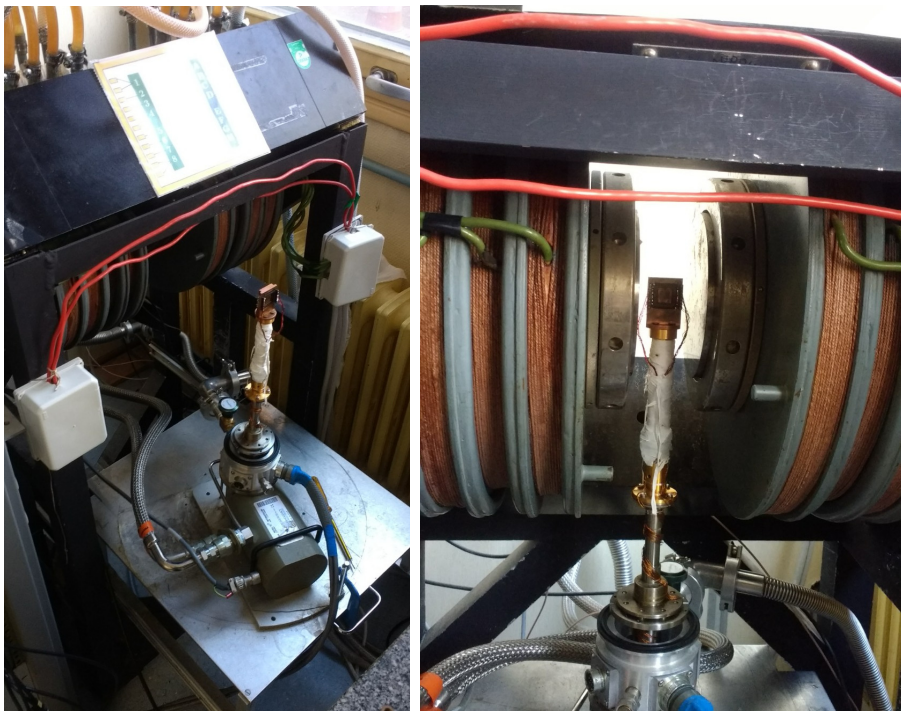

Figure 5.2: Anomalous Hall voltage measurements device. The sample holder is placed over a platform which can be moved. Position (a) allow manipulating the sample holder which can be turned to perform in-plane or out-of-plane measurements. Position (b) allow for placing the sample holder between the two magnets.

The ordinary Hall effect gives rise to a voltage in the transverse direction when a longitudinal current flows through a conductor immersed in a perpendicular magnetic field [81, 132]. A similar effect called anomalous Hall effect [133] (AHE) appears when no magnetic field is applied, but the conductor is magnetized. In that way, when an in-plane current is applied, a transverse voltage is induced in the direction perpendicular to the current and the magnetization. The Hall voltage is then sensitive to the magnetization perpendicular to the plane formed by the applied current contacts and the Hall voltage pick up contacts. If this plane coincides with the film plane, as it is the case, the Hall voltage stands for the perpendicular magnetization.

Figure 5.3 depicts the Hall voltage signal of a sample in such a configuration when an out-of-plane (figure 5.3.(a)) or in-plane (figure 5.3.(b)) field is applied. Since the initial discussion assumed a field applied along a hard axis, it is only valid for the case depicted in figure 5.3.(b). Nevertheless, the maximum field that can be applied is 1T which can be checked to be not sufficiently high to reorient the magnetization along the in-plane direction. The continuous rotation of the magnetization is avoided here by a small misalignment inducing a small out-of-plane component. This small component is responsible for the jumps around $\pm$200mT, but they are not related to the effective anisotropy K_{eff}. From those results, it can be concluded that the anisotropy field is in that case greater than 1T, but higher fields are required to determine the precise value.

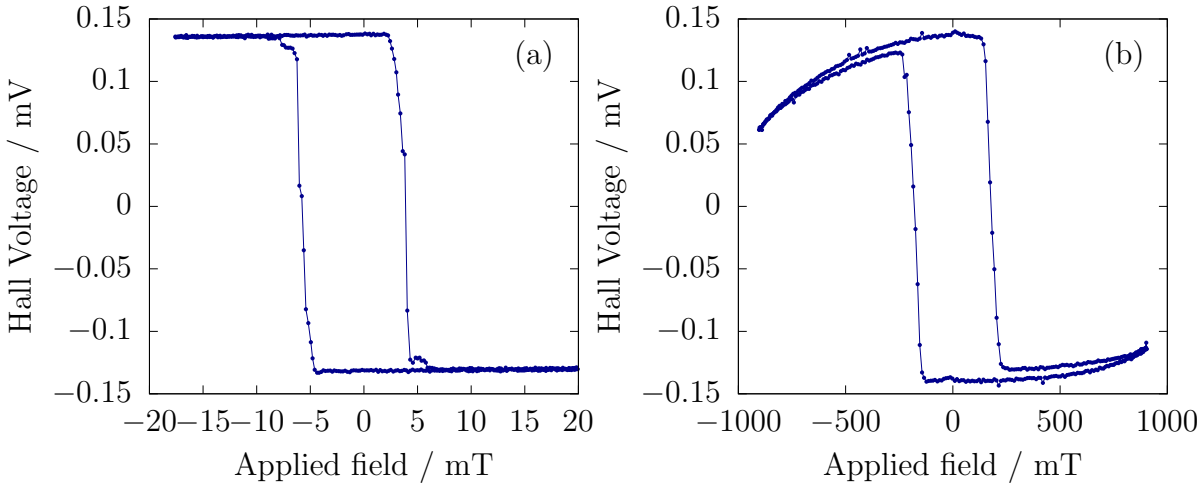

Figure 5.3: Hysteresis loops from a sample with high PMA for (a) perpendicular applied field and (b) in-plane applied field obtained from AHE measurements. The effective anisotropy K_{eff} can only be deduced from (b) since it is the case when the applied field is perpendicular to the anisotropy axis. However, the maximum applied field H is lower than the effective field $\frac{2K_{eff}}{\mu_0 M_s}$.

5.4 Methods to modify the magnetic anisotropy

It has been already mentioned that the magnetic anisotropy can be tuned by adjusting the layer thickness during the sputtering process. However, there are other procedures to modify, permanently or temporarily, the PMA. Here, two of them, both available for the group "Integnano", are briefly commented.

5.4.1 Application of a voltage

Samples of Co/Pt/HfO_2, in general, do not exhibit PMA. However, it is possible to modify this property by applying a voltage changing its effective anisotropy K_{eff} permanently. In order to do that an ionic liquid is deposited over the top oxide layer. When a voltage is applied between the surface formed by the ionic liquid and the bottom, the sample loses its in-plane behavior and becomes out-of-plane. This is probably caused by the ion displacement at the interfaces and the consequent changes on the surface properties. It is possible to measure the in-plane/out-of-plane evolution as a function of the applied voltage and the time. Since the ionic liquid does not cover, in general, the whole sample, only the part of it beneath the ionic liquid becomes out-of-plane, while the rest of the sample remains in-plane. Nevertheless, there is a transition between both behaviors, and so an anisotropy gradient. It is worthy to mention that the part of the sample that becomes out-of-plane changes its color. Thus, it is possible to determine approximately where the transition takes place. This can be used to place there a mask with which is possible to make a nanodevice. This nanodevice allows for more precise experiments, particularly, to determine precisely where the transition occurs and its size.

Nevertheless, the electric field also modifies the anisotropy in a non-permanent way, as it does in other samples. Those characteristics are very promising in order to tailor high efficiency devices, since a very low current and thus very low dissipation,

is expected in those cases.

5.4.2 Ion irradiation

Another procedure to modulate the PMA is the irradiation with an ion beam [36, 79, 80, 134, 135]. It should be noticed that this procedure also affects the DMI [48]. A vacuum chamber is needed to irradiate a sample with an ion beam. The ions source is a gas excited due to the collision between the atoms and the electrons accelerated by a RF signal. These ions are accelerated with a definite voltage which allows for controlling the energy of the irradiation beam. After that, it is necessary to deviate the ion beam towards the target using a set of magnets. Finally, the beam is focalized by means of an einzel lens. In this case, the induced modification of the PMA is permanent. It can be used to irradiate a large area, but it is also possible to focus on a small area of few nanometers. This feature is one of their advantages since it allows a fine tuning of the PMA. The change on the anisotropy depends mainly on the irradiation dose while the modification on the DMI depends mainly on the energy of the ions [48]. The "Integnano" group has an irradiation device of He^+ allowing for the investigation of anisotropy variation on thin films.

5.5 Magneto-optic Kerr effect

The magneto-optic Kerr effect (MOKE) is the rotation of the polarization plane of a light beam when it is reflected by a magnetic surface [66, 81, 136, 137]. This rotation is of a different sign for Up and Down domains. The effect can be used to measure the magnetization along one axis, so three different configurations are used: Polar MOKE is sensitive to out-of-plane magnetization, and so it is the one in which we are interested. Longitudinal and transverse MOKE are sensitive to the in-plane directions: the longitudinal case to the in-plane direction along the reflection plane

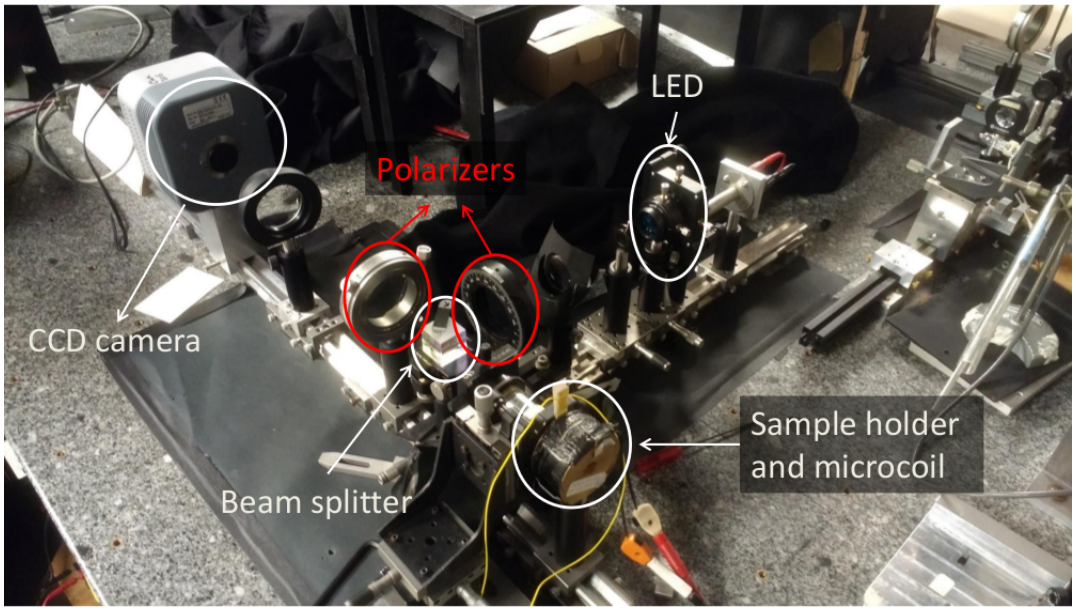

Figure 5.4: Experimental setup for polar MOKE measurements. The main components are indicated: the light source, the sample, the detector and the two polarizers.

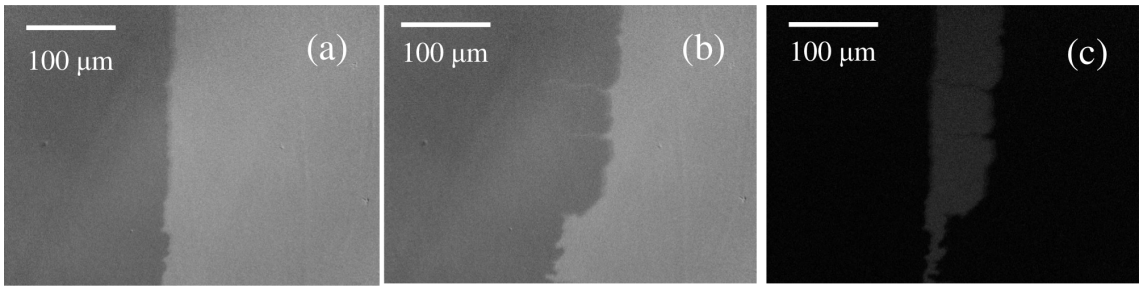

Figure 5.5: (a) and (b) MOKE images obtained after normalizing the images to a reference one. (c) difference between (a) and (b).

and the transverse one the in-plane direction perpendicular to it. Since this effect is proportional to the polarization perpendicular to the magnetization direction, the two in-plane configurations require high incident angles and have usually lower intensities.

Figure 5.4 shows the polar MOKE set up of the group "Photons - Magnons et Technologies Quantiques" of the "Institut des Nanosciences de Paris". A red LED lighting a diaphragm up is used as a light source. The first lens focuses the light beam on the focal plane of the objective. Then, the light is polarized and lights the beam splitter up. One of the secondary beams reaches the objective and the sample. At this time, the polarization plane varies depending on the magnetization state of the sample. Afterward, the light beam goes through the beam splitter and reaches the second polarizer. This polarizer is not set in the perpendicular direction with respect to the first one, but with a small angle from it in order to circumvent some issues derived from the total extinction geometry [138]. Finally, the last lens forms the image on the CCD camera which picks up the signal. The CCD camera counts photons reaching each pixel to form an image. Figures 5.5.(a) and 5.5.(b) are examples of the images produced by a polar MOKE experiment when a reference image is used to more clearly show the magnetic behavior. Figure 5.5.(a) corresponds to a sample where a DW can be seen between the darker and brighter area, while 5.5.(b) corresponds to the same sample after the application of a magnetic field pulse. As it can be checked, DW has been displaced. This displacement can be measured in pixels by subtracting both images. In that case, figure 5.5.(c) is got. In that way, this technique can be employed to obtain DWs velocities since the conversion from pixels to μm is known provided the focal length of the employed lenses and the velocity is derived from the length of the magnetic field pulse. As it has been already indicated, these measurements are also used to obtained hysteresis loops.

Part II.
Dzyaloshinkii domain walls dynamics.

Chapter 6

Asymmetric driven dynamics of Dzyaloshinskii domain walls in ultrathin ferromagnetic strips with perpendicular magnetic anisotropy*

The dynamics of domain walls in ultrathin ferromagnetic strips with perpendicular magnetic anisotropy is studied from both numerical and analytical micromagnetics. The influence of a moderate interfacial Dzyaloshinskii-Moriya interaction associated to a bi-layer strip arrangement has been considered, giving rise to the formation of Dzyaloshinskii domain walls. Such walls possess under equilibrium conditions an inner magnetization structure defined by a certain orientation angle that make them to be considered as intermediate configurations between Bloch and Néel walls. Two different dynamics are considered, a field-driven and a current-driven dynamics, in particular, the one promoted by the spin torque due to the Spin-Hall effect. Results show an inherent asymmetry associated with the rotation of the domain wall magnetization orientation before reaching the stationary regime, characterized by a constant terminal speed. For a certain initial DW magnetization orientation at rest, the rotation determines whether the reorientation of the DW magnetization prior to reach stationary motion is smooth or abrupt. This asymmetry affects the DW motion, which can even reverse for a short period of time. Additionally, it is found that the terminal speed in the case of the current-driven dynamics may depend on either the initial DW magnetization orientation at rest or the sign of the longitudinally injected current.

*Adapted from L. Sánchez-Tejerina, Ó. Alejos, E. Martínez, and J.M. Muñoz. Asymmetric driven dynamics of Dzyaloshinskii domain walls in ultrathin ferromagnetic strips with perpendicular magnetic anisotropy. *Journal of Magnetism and Magnetic Materials*, 409(Supplement C):155 – 162, 2016. doi:10.1016/j.jmmm.2016.02.067.

6.1 Introduction

Domain walls (DWs) in ferromagnetic materials are boundaries separating regions (domains) that are magnetized differently. The efficient displacement of DWs along thin ferromagnetic strips is a prerequisite condition for the application of the DW-based spintronic devices. [27, 140] DWs in soft ferromagnetic strips, with Permalloy being the most commonly used material, have been extensively analyzed during the last decades, both from theoretical and experimental points of view (see [103] for an extended review). Nowadays most of the interest is focused on ultrathin strips sandwiched between a nonmagnetic heavy metal and an insulator, which depict high perpendicular magnetocristalline anisotropy (PMA) and where the current-induced DW motion is anomalously efficient. [141] Due to the narrow DW widths and lower threshold current densities for motion of DWs, these asymmetric PMA systems are promising platforms for solid-state magnetic devices based on electrically manipulated DWs.

Apart from their potential for technological applications, and due to the rich physics involved, the analysis of the static properties of DWs in asymmetric stacks with strong PMA, and their field- and current-driven DW dynamics, are both also interesting from a pure fundamental point of view. The high efficiency of the current-induced DW dynamics was initially attributed to a Rashba effective field that stabilizes Bloch DWs against deformation, permitting high-speed motion through conventional non-adiabatic spin-transfer torque (STT). [141] However, a number of recent findings suggest that STT contributes negligibly to DW dynamics in these ultrathin structures and interfacial phenomena are instead responsible. [10–12, 21] Spin-orbit coupling (SOC) is at the basis of several effects in these systems. Firstly, SOC between the ferromagnetic strip and the insulating oxide overlayer induces the strong PMA in the ferromagnetic strip. Besides, SOC at the interface between the ferromagnetic layer and the heavy metal underlayer may result in different key phenomena explaining the experimental observations.[10–12, 21] Indeed, the spin Hall effect (SHE) in the adjacent heavy metal has emerged as a possible alternative mechanism to the STT. The SHE produces a spin current from charge scattering in the heavy metal, and the resulting spin accumulation at the heavy-metal/ferromagnet interface generates a Slonczeswski-like torque [9, 142, 143] sufficiently strong to drive the DW motion.[10–12, 21] However, the SHE-induced torque alone cannot directly drive the magnetostatically preferred Bloch DWs in these materials.[105] The Dzyaloshinskii-Moriya interaction (DMI), arising from the SOC and asymmetric interfaces, determines the magnetization texture of the DWs [38, 40, 41, 144]. The DMI is a form of magnetic exchange interaction in which adjacent magnetic moments prefer to align orthogonal to each other with a certain handedness, in contrast with the ferromagnetic exchange interaction in which the magnetic moments prefer to align parallel. The DMI provides the missing ingredient to explain the current-induced DW motion stabilizing Néel DWs with a built-in longitudinal chirality, such that the SHE alone drives them uniformly and with high efficiency. [12, 17, 19, 41, 72, 145]

Although significant advances have been achieved during the last three years in the analysis of these systems, there exist still some interesting effects which have not studied so far. In particular, in asymmetric PMA heterostructures with moderate DMI

interaction, the internal magnetization of the DWs do not depict neither pure Bloch (perfectly aligned along the transverse in-plane axis) nor pure Néel configurations (perfectly aligned along the longitudinal in-plane axis), but it adopts an intermediate state between them. [41] Here we report an analytical and micromagnetic study which indicates that the internal magnetization moment is indeed degenerate, i.e., under moderate DMI, two DW configurations are energetically possible. While the longitudinal magnetization component is governed by the chirality of DMI, the transverse component is independent of this chirality, so that it can take either a positive or a negative value. This degeneracy of equilibrium states results in asymmetric field-driven and current-driven DW dynamics, which are both analytically and numerically analyzed here in detail.

This work is structured as follows. Section 6.2 describes the one-dimensional model, which is used in section 6.3 to explore the equilibrium DW configurations at rest, with emphasis on describing in details the introduced DW degeneracy. The field-driven and the current-driven DW dynamics is evaluated in section 6.4, where one-dimensional predictions are compared to full micromagnetic simulations. The main conclusions of our study are discussed in section 6.5.

6.2 One-dimensional model

The one dimensional model (1DM), as it was originally meant,[71, 146] considers the existence of magnetic domains within the medium, separated by domain walls (DWs), transitional areas which establish an interface between two neighbor domains. These DWs can be schematically represented by a certain surface defined implicitly by an analytical function $\psi(x, y, z, t) = 0$.[147] In fact, the expression $\psi(x, y, z, t) = \psi_0$ defines a collection of surfaces that propagates at every point in a direction given by the unit vector $\left.\frac{\nabla\psi}{|\nabla\psi|}\right|_{\psi=\psi_0}$ at a speed that can be calculated as $\left.\frac{\partial_t\psi}{|\nabla\psi|}\right|_{\psi=\psi_0}$.

Since the orientation of the magnetization at every point is expressed by means of a couple of angles which are, in general, dependent on the space coordinates and time, there must exist a couple of extremal values for both angles defining each magnetic domain. In the simplest case, the orientation of the magnetization propagates coherently, and the interface is determined by a constant value of a certain component of the magnetization, which is given by any intermediate value of either one or both orientation angles. The instantaneous position of the interface can be then connected with a certain variable defined all over the interface trajectory.

In the case of large strips, a 1DM can be derived from the Landau-Lifchitz-Gilbert equation of the magnetization along with the commonly named Walker trial's functions, after the application of variational principles.[124] Walker trial's functions introduce the concepts of DW position, DW magnetization orientation and DW width Δ, the latter obtained in terms of exchange and anisotropy free energies. In

the absence of any external torque, one pair of coupled equations can be derived:

$$\frac{\dot{q}}{\Delta} - \alpha\dot{\Phi} = \frac{\gamma_0}{2\mu_0 M_s \Delta}\frac{\partial\sigma}{\partial\Phi}, \tag{6.1}$$

$$\alpha\frac{\dot{q}}{\Delta} + \dot{\Phi} = -\frac{\gamma_0}{2\mu_0 M_s}\frac{\partial\sigma}{\partial q}, \tag{6.2}$$

where γ_0 and α correspond respectively to the gyromagnetic ratio and the Gilbert damping constant, μ_0 is the vacuum permeability, and M_s is the saturation magnetization of the medium. The variable q represents the instantaneous position of the DW along the strip, and Φ determines in the case of strips with PMA the homogeneous orientation of the in-plane component of the magnetization with respect to the longitudinal direction, as it will be further revised. Finally, σ represents the free energy density per unit surface associated to the presence of the DW, which is obtained by integrating the volume free energy density along the longitudinal direction. This free energy density per unit surface originally included exchange, anisotropy and magnetostatic interactions. However, previous equations can be straightforwardly used in order to add Zeeman interactions by considering them as part of such energy density. Some upgrades can also be made to include other external torques,[16, 125] pinning,[148] or thermal effects.[117] Besides, the suitability of the use of the abovementioned trial's functions for strips with moderate interfacial DMI has been adequately stated by other authors,[41] that introduced the concept of Dzyaloshinskii domain walls (DDWs). In this way, DDWs are intermediate cases when the orientation of the in-plane component of the magnetization with respect to the longitudinal direction differs from the extreme situations known as Néel DWs or Bloch DWs, as it will be further detailed.

In this work, previous equations have been tailored to study the deterministic dynamic of DDWs in perfect strips with PMA driven by both external perpendicular field and SHE, being then written as follows for an up to down transition of the magnetization:[12]

$$\begin{aligned}\dot{\Phi}\left(1+\alpha^2\right) &= \gamma_0\left(H_z + \frac{\pi}{2}H_{SH}\cos\Phi\right) + \\ &+ \alpha\gamma_0\sin\Phi\left(H_K\cos\Phi - H_D\right),\end{aligned} \tag{6.3}$$

$$\begin{aligned}\frac{\dot{q}}{\Delta}\left(1+\alpha^2\right) &= \alpha\gamma_0\left(H_z + \frac{\pi}{2}H_{SH}\cos\Phi\right) - \\ &- \gamma_0\sin\Phi\left(H_K\cos\Phi - H_D\right).\end{aligned} \tag{6.4}$$

The different H-values stand for both the effective fields equivalent to the inner interactions within the ferromagnet, and the external stimuli. In this way, $H_K = M_s\left(N_x - N_y\right)$, where M_s is the saturation magnetization and N_x and N_y are respectively the so-called demagnetizing terms along the longitudinal and transverse axes, whose difference is approximately proportional to the film thickness t.[149] Additionally, H_D is proportional to the Dzyaloshinskii-Moriya parameter D as $H_D = -\frac{\pi D}{2\mu_0 M_s \Delta}$.[†] Finally, H_z is the applied out-of-plane field and H_{SH} defines the

[†]The definition of H_D has been made according to the expression of the volume density free energy associated to DMI given by $\varepsilon_{DMI} = \frac{D}{M_s^2}\left[\left(\mathbf{M}\cdot\mathbf{u}\right)\nabla\cdot\mathbf{M} - \mathbf{M}\cdot\nabla\left(\mathbf{M}\cdot\mathbf{u}\right)\right]$, $\mathbf{u}$ being a unit

spin-orbit torque (SOT) associated to SHE, depending on the Spin-Hall angle in the heavy metal θ_{SH}[105] and being proportional to the longitudinally injected current j_x as $H_{SH} = \frac{\hbar\theta_{SH}}{2\mu_0 e M_s t} j_x$, with e representing the electron charge, and $\hbar$ the reduced Planck constant.

6.3 Equilibrium condition

Previously to the dynamic characterization, a brief review of the equilibrium condition for DDWs is needed. In the absence of external stimuli the DW magnetization is oriented along a certain angle $\Phi|_{eq} = \varphi_0$. The equilibrium condition is then derived from the minimization of the free energy density per unit surface as calculated in [41] with regard to the orientation angle. This leads to the equations:

$$\sin\varphi_0 \left(H_K \cos\varphi_0 - H_D\right) = 0, \tag{6.5}$$

$$H_K \left(\cos^2\varphi_0 - \sin^2\varphi_0\right) - H_D \cos\varphi_0 \leqslant 0, \tag{6.6}$$

that admit a solution in the form:

$$\cos\varphi_0 = \text{sign}\left(\frac{H_D}{H_K}\right) \min\left(1, \left|\frac{H_D}{H_K}\right|\right), \tag{6.7}$$

which includes the extreme cases of absence of DMI, that is, $H_D = 0$ and $\varphi_0 = \pm\frac{\pi}{2}$, as for Bloch DWs, or strong DMI, so that $\left|\frac{H_D}{H_K}\right| \geqslant 1$, and $\varphi_0 = 0$ or $\varphi_0 = \pi$, as for Néel DWs. Any other values of the DMI lead to DDWs, so that two orientations of the magnetization within the wall are possible for every single value of the DMI parameter, being these two orientations symmetric with respect to the longitudinal axis. This is schematically depicted in figure 6.1, where some axes have been proposed in order to clarify the geometry and the magnitudes here defined. A strip with three micromagnetically calculated domains (up-down-up) is presented, with m_z corresponding to the out-of-plane component of the magnetization, and m_x and m_y being respectively the longitudinal and transverse in-plane components. Details on how micromagnetic calculations have been carried out are further given along the paper. The stacked color maps in each subfigure show the strength of any of these components at the domains and at the DWs. Since the out-of-plane component of the magnetization goes through zero within the DW, the in-plane component take at such point a maximum of magnitude m_{DW} oriented along the Φ angle. As it has been stated, under equilibrium conditions this angle is fixed to one of the two possible values of φ_0 which are a solution of eq. 6.7. In this way, while the longitudinal component of the magnetization within the DW is governed by the chirality due to DMI, the transverse component can take two symmetric values. In the case of figure 6.1.a) both DWs have a positive transverse component, while in figure 6.1.c) both DWs have a negative transverse component. Different signs of the transverse component for neighbor DWs are also possible, as it is shown in figure 6.1.b)

vector perpendicular to the interface between the ferromagnet and the heavy metal. This definition is coherent with the numerical expressions used by software packages such as MuMax^3[122] or GPMagnet[150]

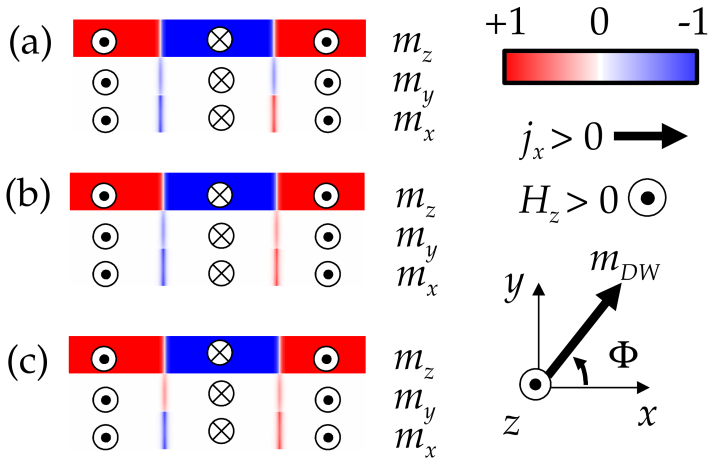

Figure 6.1: Definition of the geometry and some of the magnitudes involved in this study, in particular, the applied stimuli in the form of out-of-plane magnetic fields H_z and longitudinal currents j_x. Some DDW static configurations are also depicted. In particular, subfigures (a), (b) and (c) show how the chiral character of the DMI forces the longitudinal component of the magnetization m_x within a DW to rotate either clock- or counterclockwise, but not both. However, the transversal component of the magnetization m_y is achiral, so that, this component is free to rotate within the DW. In this way, this rotation can take either the same direction within two consecutive DWs, as in subfigure (b), or different directions, as in subfigures (a) and (c).

Next section shows that these two degenerate equilibrium states of DDWs for a given value of the DMI parameter present dynamic behaviors under the same external stimulus, such as out-of plane applied fields or SHE associated to longitudinally injected currents, which are intrinsically different. These differences can be also revealed by applying the external stimulus in opposite directions to a certain DDW, as it is further demonstrated.

6.4 Dynamics of Dzyaloshinskii DWs

As the above referenced experimental results evidence, the dynamic of a DW admits a stationary motion under the application of certain stimuli, which is characterized by a constant DW speed. The range of the applied stimuli that allows such a stationary behavior depends on the type of torque or interaction. For example, field-driven dynamics is characterized by two different regimes, the abovementioned stationary one for low applied fields, and a lower-velocity regime with a region of negative mobility just above the critical field called Walker field. Nevertheless, current-driven dynamics as this induced by the SHE is characterized by a single and stationary regime. This can be straightforwardly deduced from eq. (6.3), which states that $\dot{\Phi}$ is a continuous and bounded function of Φ. If the DW starts from an equilibrium condition, the immediate application of either external stimulus gives to $\dot{\Phi}$ a certain finite value, whose sign defines if the DW magnetization orientation initially rotates clock- or counterclockwise. Two behaviors may occur from this point on. On the one hand, $\dot{\Phi}$ may vary without a change of sign as Φ varies in time. This situation occurs when both the upper and lower bounds of $\dot{\Phi}$ have the same sign, then limiting the rotation speed of the DW magnetization orientation, but preventing the stationary

regime from being reached. That is the case of large applied out-of-plane fields, that may mask the other terms in the RHS of eq. (6.3), and Walker breakdown occurs. On the other hand, the rotation of the DW magnetization orientation may reach a certain angle so that $\dot{\Phi}$ goes through zero. From this instant on, rotation stops and the stationary motion is reached.

According to the previous discussion, it can be stated that the stationary motion is characterized through the conditions $\dot{\Phi} = 0$, and then $\dot{q} = const$, the former leading to the relationship:

$$H_z + \frac{\pi}{2} H_{SH} \cos\varphi_s = \alpha \sin\varphi_s \left(H_D - H_K \cos\varphi_s\right), \tag{6.8}$$

φ_s representing the DW magnetization orientation when the stationary regime is reached. From the comparison between eqs. (6.7) and (6.8), and the characteristics and dependences of $\dot{\Phi}$ given by eq.(6.3), it can be immediately inferred that the transition from the DW equilibrium state to its stationary motion involves a monotonous rotation of the DW magnetization orientation from φ_0 to φ_s.

6.4.1 Field-driven dynamics

As abovementioned, the DDW dynamics driven by the application of an out-of-plane external field admits two different regimes. For the sake of a lighter notation, let us rewrite eq.(6.8) in the absence of SHE as:

$$h = \sin\varphi_s \left(\delta - \cos\varphi_s\right), \tag{6.9}$$

where $h = \frac{H_z}{\alpha H_K}$ is a normalized value of the applied field, and $\delta = \frac{H_D}{H_K}$ defines the normalized strength of DMI. Since the RHS of previous equation is bounded, there are h-values so that the equation has no solution. These h-values are then above Walker breakdown, and the frontier can be delimited by considering the global maxima of eq.(6.9). At the frontier, the DW magnetization orientation φ_W is such so that $\left.\frac{\partial h}{\partial \varphi_s}\right|_{\varphi_s=\varphi_W} = 0$. This is a necessary, but not sufficient condition. In any case, this condition leads to the relationship:

$$\cos\varphi_W = \frac{\delta \pm \sqrt{\delta^2 + 8}}{4}. \tag{6.10}$$

For strong DMI, characterized by absolute values of δ greater than one, only one sign in the equation above leads to a valid result, i.e., the minus sign for positive δ, then defining the positive and negative Walker fields. It must be noted that the equilibrium condition for such δ-values establishes pure Néel walls, that present a perfectly symmetric behavior under the proposed stimuli, as it is further discussed. However, in the case of moderate DMI, when DDWs are present, both signs in eq.(6.10) are possible, one of them corresponds to global extrema while the other correspond to local extrema. As in the case of large δ, global extrema define the limit of the stationary motion under an external applied field, i.e., Walker breakdown.

In order to analyze the importance of local extrema, let us consider a DDW ini-

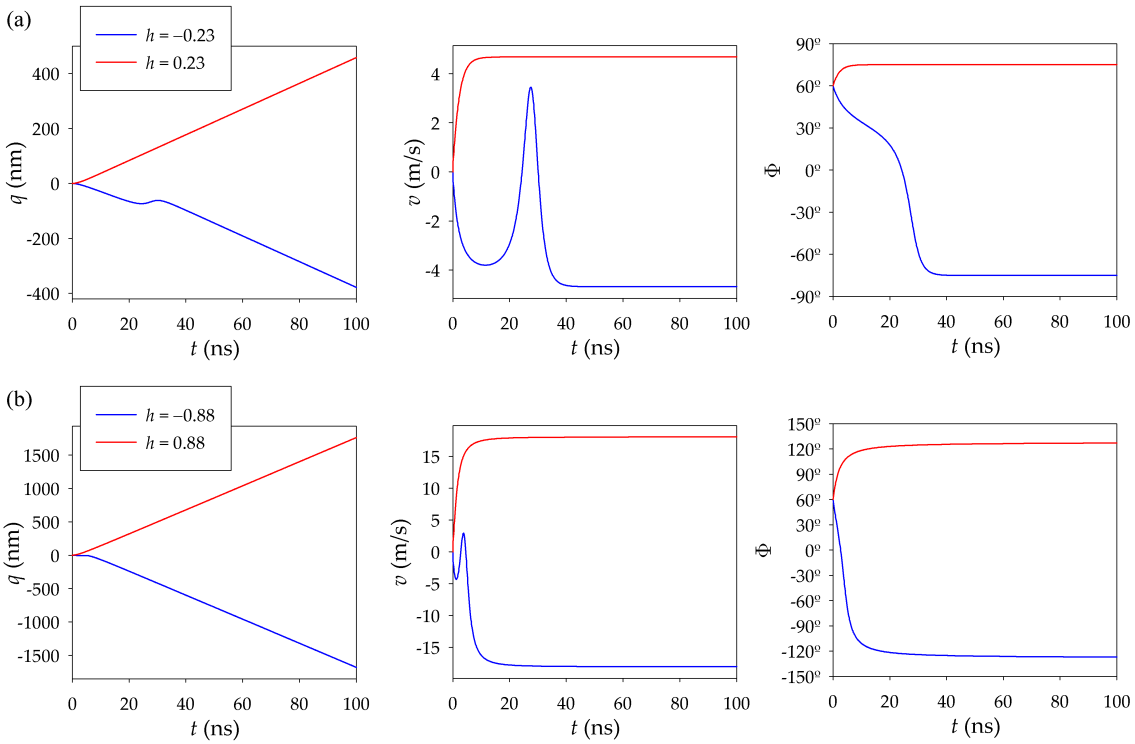

Figure 6.2: DDW dynamics under the influence of an out-of-plane external field. In these graphs, h represents a normalized value as it has been defined along the text. Positive h-values stand for fields applied along the direction of the magnetization in the up-domain, while negative values stand for fields applied in the opposite direction, i.e., the magnetization in the down-domain. q represents the instantaneous DDW position, and v is the instantaneous speed. Φ corresponds to the DW magnetization orientation. Plots correspond to the numerical calculation of eqs.(6.3) and (6.4). Figure a) is obtained for applied fields of $h = \pm 0.23$, and figure b) is obtained for applied fields of $h = \pm 0.88$. The sign of the applied field may promote completely different DDW dynamics.

tially in equilibrium with a DW magnetization orientation fulfilling the condition $\cos\varphi_0 = \delta$, according to eq.(6.7) and the definition of δ. The application of the external field h gives rise to a counterclockwise rotation for positive h, that is, applied field along the direction of the magnetization in the up-domain, and a clockwise rotation for negative h, as it can be inferred from eq.(6.3). For a certain sign of h, and provided h is sufficiently strong, the DW magnetization orientation can reach this local extremum. However, if this h-value is fixed, but its sign is changed, no local extrema are reached. This is clearly shown in Figure 6.2. Plots represent the DDW dynamics under the influence of an out-of-plane external field, calculated by numerically solving eqs.(6.3) and (6.4) by means of the classical Runge-Kutta method. In order to depict realistic values of time, DW position q and DW speed v, a value of Δ of about 6nm has been considered in the graphs. An initial DW magnetization orientation $\varphi_0 = 60^o$, corresponding to a δ-value of 0.5, has been taken. Figure 6.2.a) is obtained for applied fields of $h = \pm 0.23$, slightly higher in absolute terms than the value need to reach a local minimum. A clear asymmetry with the sign of h is shown. While the positive h-value promotes a soft transition from the equilibrium condition to the stationary motion, the negative h-value gives rise to an abrupt transition of the DW magnetization orientation prior to reach the stationary

motion. During this transition, the DDW motion even reverses for a short period of time, as shown in the evolution of the DW position q. Similar results can be obtained if the applied field is increased close to the Walker breakdown (Figure 6.2.b). However, the shown asymmetry do not affect the terminal speed which is given by $\gamma_0 H_z \Delta$.

Micromagnetic simulations have been carried out with the help of the GPMagnet software package[150] in order to support these analytical results. Along these simulations, a ferromagnetic strip of 1nm thickness and 160nm width with PMA grown on a heavy metal layer has been considered. Since this software performs $2\frac{1}{2}$D simulations in finite differences, computational cells of 4nm×4nm×1nm have been considered. The geometry has then been mimicked by means of an array of 40×1024 cells with appropriate boundary conditions. Values of the material parameters that are usually found in the literature have been taken: saturation magnetization of $M_s = 7 \cdot 10^5 \frac{\mathrm{A}}{\mathrm{m}}$, exchange constant of $A = 10^{-11} \frac{\mathrm{J}}{\mathrm{m}}$, uniaxial anisotropy constant $k_u = 4.8 \cdot 10^5 \frac{\mathrm{J}}{\mathrm{m}^3}$. A DMI parameter D of the order of $10^{-5} \frac{\mathrm{J}}{\mathrm{m}^2}$ has been used.

As an example, Figure 6.3 presents the micromagnetic results obtained in the case of a sample with $\delta = -0.5$. In this case, equilibrium conditions determine that one of the two possible orientations at rest of the DW magnetization is $\varphi_0 = 120^\mathrm{o}$, as it can be checked in the graph for $h = 0$. The figure shows the dependence of the DW magnetization orientation at stationary motion as a function of the external field h. Dots are calculated by means of micromagnetic simulations, while the continuous plot corresponds to the results provided by eq.(6.9) obtained after the 1DM analytical treatment. Some small discrepancies are found, mainly where discontinuities are present. These discrepancies can be considered as inherent to the approximations made by the 1DM model, in particular to the calculation of the wall width by means of Δ and the computation of the energy densities depending on this parameter. However, the degree of self-consistency of the results shown allows to draw some conclusions. In this particular example, the stationary motion is smoothly reached

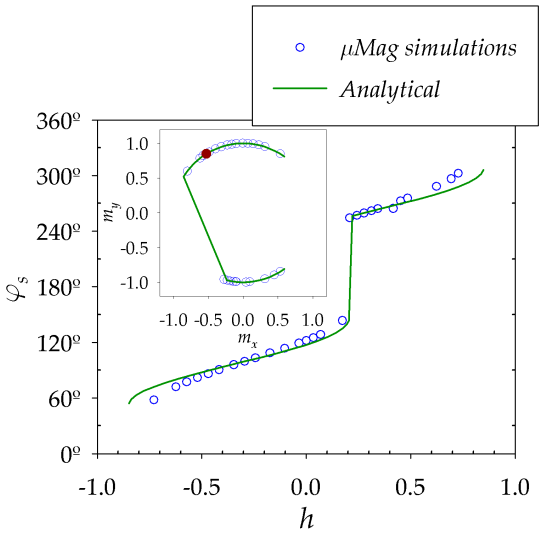

Figure 6.3: Comparison between micromagnetic simulations and the predictions of the 1DM analytical model. Different signs of the applied fields lead to different behaviors of the DDW.

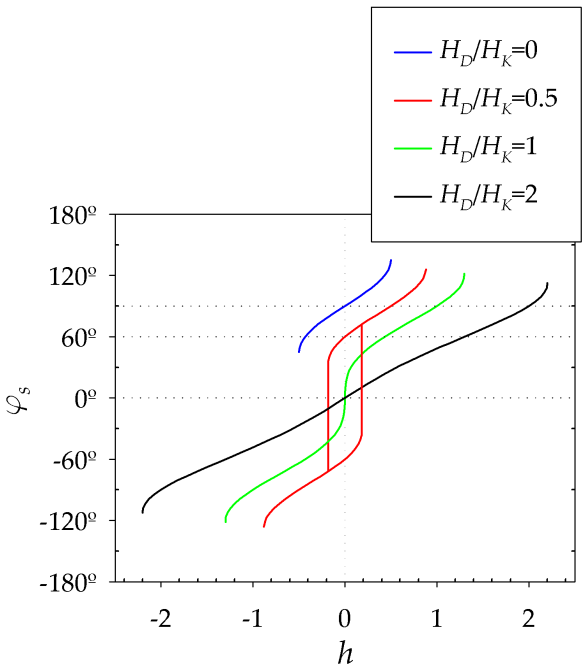

Figure 6.4: Dependence of the DW magnetization orientation at stationary motion on the applied out-of-plane field with $\frac{H_D}{H_K}$ as a parameter. While both Bloch and Néel walls present symmetric behavior, DDWs present a clear asymmetry with the applied field governed by the strength of the DMI.

from the equilibrium orientation for negative fields, up to the corresponding negative Walker field. However, an abrupt transition occurs for positive h-values, before the Walker field is reached. The inset shows the normalized in-plane components of the magnetization at the center of the DDW. m_x is the component along the longitudinal axis, while m_y is the transverse component. Starting from equilibrium conditions (filled dot), negative fields give rise to a smooth clockwise rotation of the DW magnetization orientation for all applied fields up to the Walker field. On the contrary, positive fields leads to a counterclockwise rotation that pass through an abrupt reorientation of the DW magnetization prior to reach Walker breakdown.

In order to complete the 1DM analytical study, Figure 6.4 shows the dependence of the DW magnetization orientation at stationary motion on the normalized out-of-plane field h with δ, i.e., $\frac{H_D}{H_K}$, as a parameter. On the one hand, large $\frac{H_D}{H_K}$ ratios promote Néel walls, their chirality depending on the sign of the DMI parameter D, whose behavior is completely symmetric with regard to the sign of h. As it is well-known, the larger the ratio is, the farther the two endpoints of the corresponding curve are from each other, meaning that Walker breakdown requires larger applied fields. On the other hand, no DMI allows the existence of Bloch walls. In this case, the dependence of the DW magnetization orientation at stationary motion is depicted for a Bloch DW with $\varphi_0 = 90^o$. The behavior is also symmetric with regard to the sign of h. However, DDWs present a clear asymmetry under the application of an external out-of plane field. This behavior can be considered as hysteretic in the following sense. Under equilibrium conditions, a DDW may take two possible orientations, symmetric with respect to the longitudinal axis. The application of an

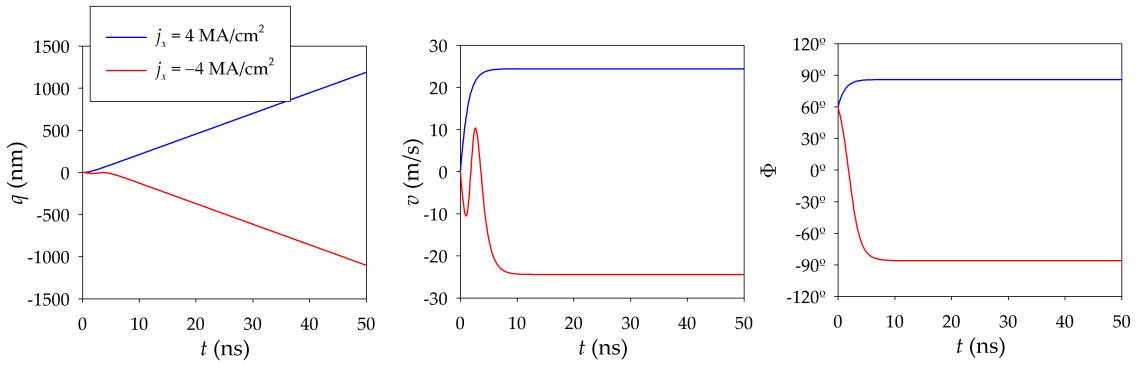

Figure 6.5: Current-driven DDW dynamics under the influence of SHE for positive and negative longitudinal currents as calculated analytically with the help of the 1DM. As in the case of the field-driven dynamics, asymmetry with the sign of the stimulus is also noticeable.

out-of-plane field promotes the rotation of the initial DW magnetization orientation before a state of stationary motion is reached. Depending on the sign and the strength of the applied field, the DW magnetization orientation may undergo an abrupt reorientation prior to the stationary state. If this reorientation occurs, the DDW do not recover its original orientation at rest, but the symmetric one with respect to the longitudinal axis, after field removal. The existence or absence of these DW magnetization reorientation noticeably defines DDW dynamics, as the dynamic plots in Figure 6.2 showed.

6.4.2 Current-driven dynamics

As it has been already stated, field-driven dynamics and current-driven dynamics governed by SHE present a noticeable difference, that is, the absence for the latter of Walker breakdown. This can be straightforwardly proved from eq.(6.8). Analogous to the precedent study, a lighter version of this equation can be proposed in the following way:

$$h = \tan\varphi_s \left(\delta - \cos\varphi_s\right), \tag{6.11}$$

where now $h = \frac{\frac{\pi}{2} H_{SH}}{\alpha H_K}$. Since the RHS of previous equation is not bounded, a stationary motion is always possible under the SHE torque. However, the function defined in eq. (6.11) may possess local extrema for absolute δ-values ranging from 0 to 1, that is, for DDWs. This local extrema are reached when the DW magnetization orientation fulfills the condition $\cos\varphi_L = \sqrt[3]{\delta}$. As in the precedent case, when the DW magnetization orientation reaches either of the two local extrema, an abrupt reorientation occurs prior to the establishment of the stationary motion.

As a first example, Figure 6.5 shows the DDW dynamics under SHE for a certain current flowing longitudinally in both one and the opposite direction calculated by means of the 1DM analytical description. In order to give a much clearer idea about orders of magnitude, one set of concrete values has been chosen, which are current density $j_x = \pm 4 \cdot 10^{10} \frac{\mathrm{A}}{\mathrm{m}^2}$, Spin-Hall angle $\theta_{SH} = 0.11$, with a damping constant $\alpha = 0.013$ and a DW width Δ of about 6nm, values that can be also found in the

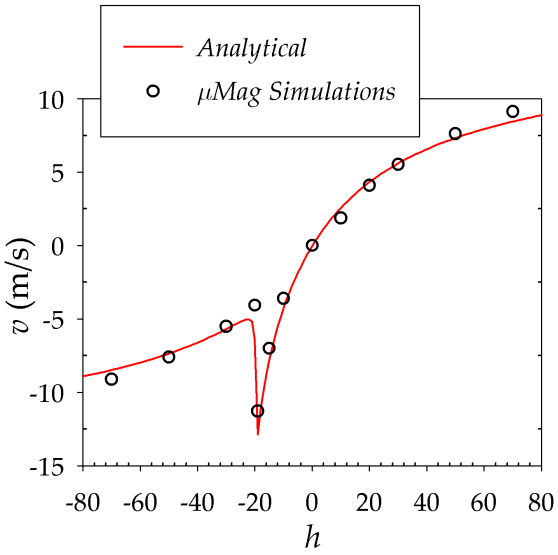

Figure 6.6: Dependence of the DDW terminal speed at stationary motion on the applied longitudinal current due to SHE. The h-value in the graph is defined as proportional to the current density (see text). The graph compares micromagnetic simulations and the results obtained from the 1DM model. A noticeable asymmetry is found if the stimulus is reversed, leading to a sharp transition of the terminal speed in a certain range of applied currents.

referenced literature. In a similar fashion to the field-driven dynamics, a smooth rotation of the DW magnetization is promoted if the current flows in one direction, while an abrupt transition occurs when the current flows in the opposite direction.

Differently from the field-driven dynamics, the 1DM also predicts the asymmetry of the terminal speed at stationary motion, which undergoes a sharp transition for currents that lead the DW magnetization orientation to values close to the local extrema. Figure 6.6 shows the dependence of this terminal speed on the h-value defined after eq.(6.11). Dots correspond to numerical simulations carried out with GPMagnet using the abovementioned parameters, while the continuous plot has been analytically calculated from the 1DM. A rather good agreement between numerical and analytical calculations is obtained. Both show the sharp transition predicted by the 1DM, in this case, for an h-value around -20. It can be noticed that the terminal speed at the peak of this sharp variation, calculated from the 1DM as $\frac{\gamma_0 \Delta \sqrt[3]{\delta}}{\alpha} \frac{\pi}{2} H_{SH}$, may surpass the terminal speed for infinite current given by $\gamma_0 H_D \Delta$.

As a summary, the analytically calculated dependence of the DW magnetization orientation at stationary motion on the applied current with $\frac{H_D}{H_K}$ as a parameter is depicted in Figure 6.7. The case of Bloch DWs is not considered, since SHE do not promote their motion in the system under study. For $\frac{H_D}{H_K}$ ratios greater or equal to one, the plots show that Néel walls behave symmetrically under the influence of the torque due to SHE. However, DDWs have a hysteretic-like behavior, rather analogous to the one found for the field-driven dynamics. It must be noticed that, according to this hysteretic-like behavior, the terminal speed depends on the initial DW magnetization orientation under equilibrium conditions, i.e., for the same applied longitudinal current, the dynamics depends on whether the initial DW magnetization

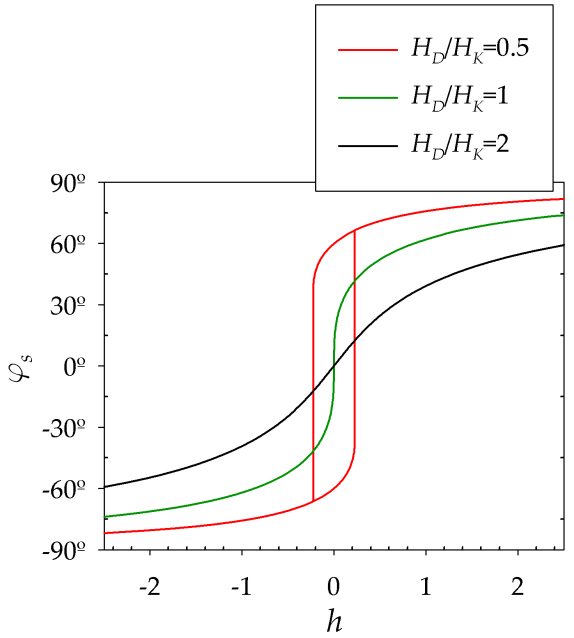

Figure 6.7: Dependence of the DW magnetization orientation at stationary motion on current through the normalized h-value (see text) with $\frac{H_D}{H_K}$ as a parameter. It is shown that Néel walls present symmetric behavior, while DDWs present a hysteretic-like behavior. As a consequence, a DDW may reach different terminal speeds depending on either the sign of the current or its initial orientation at rest.

orientation at rest is pointing in one of the two possible directions, symmetric with respect to the longitudinal axis, that this orientation can take.

6.5 Conclusions

The dynamics of Dzyaloshinskii DWs in ferromagnetic strips with PMA has been analytically studied with the help of the 1DM, and the results compared with micromagnetic simulations. Two different stimuli have been considered: out-of-plane applied magnetic fields and torques induced by longitudinal currents due to SHE. The application of such stimuli may lead to a stationary regime characterized by a constant terminal DW speed. However, the behavior of the DDW dynamics has been found to be asymmetric with respect to either the sign of the applied stimulus, or the initial DW magnetization orientation. This asymmetry arises from the fact that the DW magnetization orientation may rotate clock- or counterclockwise, depending on this sign. The stationary regime is then reached when this rotation stops. However, the transition from the DW magnetization orientation at rest to the orientation at stationary motion can be either smooth or abrupt depending on the rotation. The initial DW magnetization orientation under equilibrium conditions then determines which sign of the stimulus promotes its abrupt reorientation prior to reach the stationary regime. This process can be characterized in the presented results by a reverse of the DDW motion for a short period of time.

Additionally, some differences between field-driven and current-driven dynamics have been reported. Some of them have been already highlighted by other authors, such as the absence of Walker breakdown in the case of current-driven dynamics governed by SHE. Besides, the asymmetry here reported do not affect the DW terminal speed in the case of field-driven dynamics. However, the terminal speed for current-driven dynamics is found to be asymmetric in the range of lower injected currents, then depending on either the initial DW magnetization orientation or the sign of the applied stimulus.

Finally, since the abrupt reorientation of the DW magnetization occurs for higher injected currents, the degenerate condition of the initial DW magnetization orientation also determines different traveled distances for a train of current-driven DWs in a strip, which may be also of experimental relevance.

6.6 Acknowledgment

This work was supported by project WALL, FP7-PEOPLE-2013-ITN n. 608031 from European Commission, project MAT2014-52477-C5-4-P from Spanish Government and project SA282U14 from Junta de Castilla y León.

Chapter 7

Steady-state configurations of Dzyaloshinskii domain walls driven by field and current*

The dynamics of Dzyaloshinskii domain walls (DDW) in ultrathin ferromagnetic strips with perpendicular magnetic anisotropy, for different values of both perpendicular field and longitudinal current excitation associated to the Spin-Hall effect, has been studied, taking into account different values of the interfacial Dzyaloshinskii-Moriya interaction (DMI). This study has been carried out with the help of the q-Φ one-dimensional model and micromagnetic simulations. We have found that Walker breakdown may be avoided by applying a certain threshold current, even though the inverse effect is also possible. We have also found that, for particular values of field and current, the magnetization within the DDW experiences an abrupt change of orientation, which provokes a change on the contribution of current to the terminal DDW velocity. This effect disappears for sufficiently strong DMI, as it is expected from the model.

*Adapted from L. Sánchez-Tejerina, O. Alejos, and E. Martínez. Steady-state configurations of dzyaloshinskii domain walls driven by field and current. *Journal of Magnetism and Magnetic Materials*, 423(Supplement C):405 – 410, 2017. doi:10.1016/j.jmmm.2016.09.116.

7.1 Introduction

The dynamics of a domain wall (DW) in a ferromagnetic strip driven by the solely application of external magnetic fields Hz, parallel to the magnetizations within the two adjacent domains, is a well-known issue, characterized by a monotonic increasing of the DW velocity until the phenomenon known as Walker breakdown occurs at $H_z \geqslant H_W$ where H_W is the so-called Walker field [71]. The main difference between both behaviors, below $H_z < H_W$ and above $H_z > H_W$ this breakdown, is that the former promotes a DW dynamics characterized by a stationary regime, where the inner DW magnetic structure holds, while the latter is characterized by a DW magnetization precessing around the applied magnetic field. The maximum speed for the DW is then reached in the limit between both behaviors, for $H_z = H_W$. Besides, asymmetric structures consisting in a ferromagnetic (FM) layer sandwiched between a heavy-metal (HM) and an oxide, which exhibit high perpendicular magnetic anisotropy (PMA), present a particularly efficient current-driven DW dynamics [7–9, 11–13, 17, 18, 20–23, 71, 152]. The spin-orbit coupling (SOC) and the interfacial Dzyaloshinskii-Moriya interaction (DMI) have been revealed to be the main ingredients that explain this effectiveness, in particular, the establishment of a spin current connected with the Spin-Hall effect (SHE), that promotes spin accumulation at the FM-HM interface [9, 11, 12]. The DW driven by the solely application of longitudinal currents, then transverse to the DW, has also been adequately characterized in these systems [41, 139], showing that, contrary to the field-driven case, there is not such a Walker breakdown. An initial linear increase of the DW velocity with current occurs, which tends asymptotically to a finite value for higher currents as the orientation of the magnetization within the DW approaches the direction perpendicular to the current.

As a further step, studies of the DW dynamics driven by stimuli resulting from the combination of fields and currents, which have not been reported so far, may contribute to a deeper knowledge of the underlying physical mechanisms that govern magnetization textures. Accordingly, this work has been conceived as a contribution in this direction, and both the micromagnetics and the one-dimensional approach have been taken as its basis. The dependence of the DW inner structure on the strength of the DMI has been considered in this study, since this interaction governs the formation of achiral, homochiral or intermediate DWs, the latter referred to as weak Dzyaloshinskii domain walls (wDDW) in this paper. Results are depicted as phase diagrams which show at a glance the most outstanding features of such a driven DW dynamics. In particular, it can be confirmed its inherent asymmetric nature, and the boundaries that determine whether a precessional regime occurs or not, then defining the conditions of highest dynamic efficiency.

7.2 One dimensional model and field-current driven dynamics

The one dimensional model (1DM) was developed to study the behavior of the transitional area between two magnetic domains, i.e, DWs, where the magnetization changes smoothly from the magnetization in one domain to the magnetization

within the other one [41, 124, 139]. The 1DM for an infinite strip with high PMA and moderate interfacial DMI excited by a perpendicular magnetic field Hz and a longitudinal current j_a predicts that the DW position and its orientation with respect to the longitudinal in-plane (x-axis), as represented in the inset of 7.1.(b), are described by a set of two equations:

$$\dot{q} = \frac{\gamma_0 \Delta}{1+\alpha^2} \left[\Omega_A + \alpha \Omega_B\right] \tag{7.1a}$$

$$\dot{\Phi} = \frac{\gamma_0}{1+\alpha^2} \left[-\alpha \Omega_A + \Omega_B - \alpha \Omega_A\right] \tag{7.1b}$$

γ_0, α and M_s being respectively the gyromagnetic ratio multiplied by the vacuum permeability μ_0, the Gilbert damping parameter, and the saturation magnetization of the medium. Besides, $\Delta \equiv \sqrt{A/K_{eff}}$ determines the DW width, A being the exchange parameter, and K_{eff} including the perpendicular anisotropy constant and the shape effect as $K_{eff} \approx K_u - \frac{1}{2}\mu_0 M_s^2$ for the strip geometry. The other terms are defined as:

$$\Omega_A \equiv H_D \sin\Phi - H_k \sin\Phi\cos\Phi - \frac{\pi}{2} H_{FL} \cos\Phi \tag{7.2a}$$

$$\Omega_B \equiv H_z + H_{SL} \cos\Phi \tag{7.2b}$$

where H_k is a constant field related to magnetostatic interactions, which takes into account geometric and material characteristic parameters [149], and $H_D \equiv \frac{\pi}{2}\frac{D}{\mu_0 M_s \Delta}$ is a constant field accounting for the DMI through the parameter D. The torque exerted by the applied current j_a is in general composed of two main contributions [10], a Slonzceswskii-like torque (SL-SOT) and a Field-like torque (FL-SOT) expressed respectively by means of the constants H_{SL} and H_{FL}. The first one has been already introduced as due to the spin accumulation at the FM-HM interface associated with the spin current caused by the SHE in the way $H_{SL} \equiv \frac{\hbar \theta_{SH}}{2e\mu_0 M_s t} j_a$, where the parameter θ_{SH} stands for the spin-Hall angle, $\hbar$ is the reduced Planck constant, and t accounts for the strip thickness. The second constant can be written as proportional to the former through a certain factor k so that $H_{FL} \equiv k H_{SL}$. Finally, it must be pointed out that the suitability of the use of the above mentioned trial's functions for these strips was initially stated by other authors [41], who introduced the concept of Dzyaloshinskii domain walls (DDWs). Depending on the strength of the DMI, three types of DWs can be then reported: achiral DWs, usually named as Bloch DWs (BDW), that appear in the total absence of such an interaction, homochiral DWs, i.e., Néel DWs (NDW), for large values of the DMI, and intermediate cases between both of them. As it has been stated in the introduction section, the latter are referred to as wDDWs in this text. These three types of DWs are represented in the case of an up to down (UD) transition of the magnetization, sketching 7.1.(a) the magnetization for a BDW, 7.1.(b) a wDDW in the case of a material with negative DMI parameter, and 7.1.(c) a NDW. It must be reminded at this point that, similarly to BDWs, such wDDWs admit a doubly-degenerate equilibrium state, symmetric with respect to the x-axis, that can be straightforwardly determined from the condition in the absence of any external stimulus. 7.1.(b) depicts indeed only one of the two equilibrium states for the wDDW.

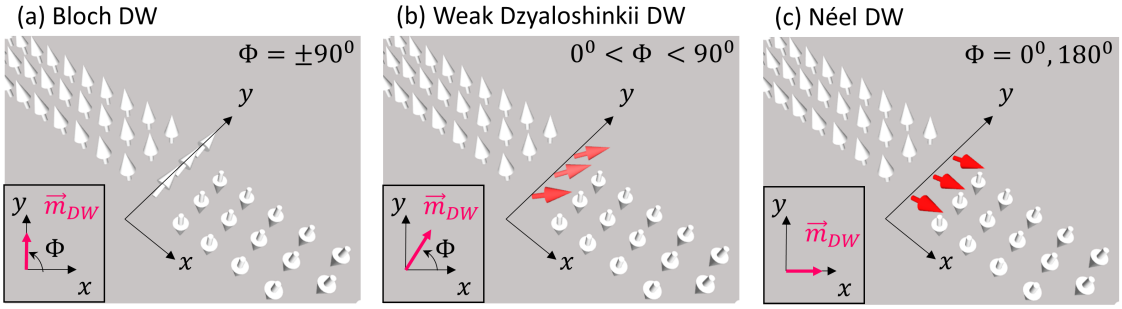

Figure 7.1: Schematic representation of a) Bloch domain wall, b) weak Dzyaloshinskii domain wall for a material with negative DMI constant, c) Néel domain wall and inset b) domain wall orientation (Φ) with respect to the longitudinal in-plane axis (x) as the one dimensional model defines it.

In the present work, the DW dynamics is studied under the combined application of both an external field (H_z) and a longitudinal current (j_a). According to the 1DM, the rotation speed of the DW orientation, i.e., equation (7.1b), possesses one term independent of Φ, which is associated with the external field torque H_z, and whose sign then remains along the DW dynamics. This term is to be named as H_z-term in the following discussion. Oppositely, the other terms may change its sign depending on Φ, and are due to the magnetostatic (H_k-term) and Dzyaloshinskii-Moriya interactions (H_D-term), and the effect of the applied current (j_a-term), the latter including both SL-SOT and FL-SOT. According to the signs of these four terms and the amplitude of the applied stimuli H_z and j_a, a wide variety of dynamic behaviors can be described. However, the further discussion can be reduced to a set of six states as follows:

1. H_D-, j_a- and H_z-terms, jointly acting, contribute to the rotation of the DW magnetization in a certain direction. The DW magnetization may undergo an abrupt reorientation if the H_k-term is not sufficiently intense.

2. The H_D-term opposes the effect of the other three.

3. The combined effect of H_D-, j_a- and H_k-terms counteracts the torque due to H_z.

4. Both H_D- and j_a-terms, oppose the joint effect of H_z- and H_k-terms. For sufficiently high j_a the DW magnetization rotates so that the H_k-term overcomes a maximum and then becomes weaker. The DW orientation is then unstable, and a reorientation process finishing in state 3 occurs.

5. The H_D-term, together with the $H-k$-term, opposes the change in Φ imposed by H_z and j_a. If the H_D-term is rather weak, the longitudinal in-plane component of the DW magnetization (m_x) may even reverse, leading to state 3.

6. Both H_D- and H_z-terms, impose an orientation of the DW magnetization towards the x-axis. If the j_a-term, together with H_k-term, cannot balance out the effect of the former, the DW undergoes an abrupt reorientation.

ϕ	(-180º:-90º)				(-90º:0º)				(0º:90º)				(90º:180º)			
H_z	⊙	⊙	⊗	⊗	⊙	⊙	⊗	⊗	⊙	⊙	⊗	⊗	⊙	⊙	⊗	⊗
j_a	⊗	⊙	⊗	⊙	⊙	⊗	⊙	⊗	⊙	⊗	⊙	⊗	⊗	⊙	⊗	⊙
H_D	⊗				⊗				⊙				⊙			
H_k	⊙				⊗				⊙				⊗			
state	4	2	1	6	5	3	n_a	n_s	n_s	n_a	3	5	6	1	2	4

⊙ counter-clockwise torque
⊗ clockwise torque

Table 7.1: Schematic description of the six DW stationary states defined in Section 7.2. Each state results from the balance of the torques associated with the applied stimuli, as either out-of-plane field (H_z) or longitudinal current (j_a), and the intrinsic interactions within the magnetic material in form of magnetostatic (H_k) and Dzyaloshinskii-Moriya (H_D) contributions. A positive DMI parameter has been considered in this table. Since the direction of the torques depends on the actual DW magnetization orientation Φ , four columns have been established so as to consider Φ-values ranging within any of the four quadrants. Red/blue boxes indicate positive/negative values for the applied stimuli, as further defined in the text. Even though sixteen combinations are possible, four of them can be discarded. Those are the cases when either all torques act likewise, so that $\dot{\Phi}$ never vanishes, and a non stationary state (n_s) is reached, or states when the torque associated with the current j_a oposses the other three torques. The latter case require that the DW magnetization orientation lays on either the first or the fourth quadrant, which cannot be achieved from equilibrium unless the torque due to the applied field oposses the effect of the DMI, i.e., the applied field and the DMI must act oppositely. These are then non achievable states (n_a). The other twelve can be grouped into only six twin states, in agreement with the state degeneracy that is to be explained in Section 7.3. According to the discussion in that section, each twin state can be separated into a green and a blue-purple state, as the colored boxes within the row of possible states reflect.

Next section will refer then to these six behaviors as states $1-6$, so that all the DW stationary regimes lie on one of them. In order to show briefly the previous description of states, a schematic diagram has been included in 7.1.

7.3 Micromagnetic Simulations

7.3.1 Field and current induced dynamics of wDDWs.

In our study, a 4800nm long, 160nm wide and 0.6nm thick slab has been considered. Material parameters usually found on the literature have been taken [17] saturation magnetization M_s of $7 \cdot 10^5 \frac{\mathrm{A}}{\mathrm{m}}$, exchange constant A of $10^{-11} \frac{\mathrm{J}}{\mathrm{m}}$, uniaxial anisotropy constant K_u of $4.8 \cdot 10^5 \frac{\mathrm{J}}{\mathrm{m}^3}$, and Gilbert damping parameter $\alpha = 0.2$. The study has been performed for five different values of the DMI parameter D: $10^{-5} \frac{\mathrm{J}}{\mathrm{m}^2}$, $2 \cdot 10^{-5} \frac{\mathrm{J}}{\mathrm{m}^2}$, $3 \cdot 10^{-5} \frac{\mathrm{J}}{\mathrm{m}^2}$, which promote a wDDW, $4.77 \cdot 10^{-5} \frac{\mathrm{J}}{\mathrm{m}^2}$, which is close to the minimum value required to promote a pure Néel wall, and $10^{-4} \frac{\mathrm{J}}{\mathrm{m}^2}$, even though only the most relevant results are to be shown here. Finally, values of $\theta_{SH} = 0.1$ for the spin-Hall angle and $k = 31.4$, according to the above reference. The application of these values leads to a magnetostatic field $H_k \approx 11.5 \frac{\mathrm{kA}}{\mathrm{m}}$, that is to be used within the framework of the 1DM.

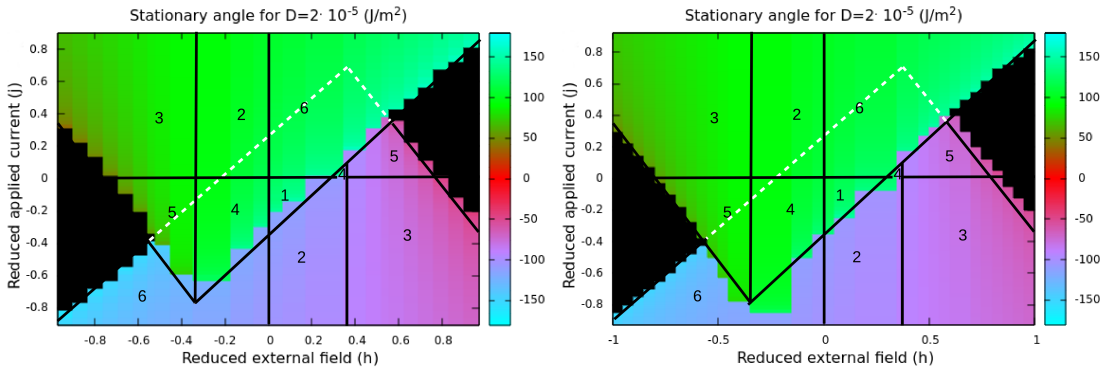

Figure 7.2: DW angle as a function of the applied field h (perpendicular) and the applied current j (through heavy metal) for a DMI parameter of $D = 2 \cdot 10^{-5} J/m^2$ obtained from: a) full μM simulations and b) the application of the 1DM. The black area corresponds to pairs of field and current values leading to a non-stationary, i.e., precessional regime. An abrupt change of the orientation of the wall for specific pairs of values of the applied field and current may also occur, as discontinuities in the color map indicate (see text).

Therefore, micromagnetic (μM) simulations have been performed with the package MuMax3 [122] so as to validate the self-consistency of the 1DM. Within both approaches, 1DM and μM, H_z and j_a have been taken as input variables. Since the dependence of $\dot{\Phi}$ is linear with these variables, results are presented by means of the normalized variables $h = \frac{H_z}{\alpha H_k}$ and $j = \frac{\pi}{2}\frac{H_{SL}}{\alpha H_k}(1 + \alpha k)$, so as to reduce the dependence on other parameters to only one, i.e., the DMI constant. In order to clarify the signs of both magnitudes within this context, a positive field means a field directed along the positive out-of-plane axis (z-axis), and a positive current means a longitudinal current along the positive x-axis.

A first set of results are shown in Fig. 7.2, where a value of the DMI parameter $D = 2 \cdot 10^{-5} \frac{J}{m^2}$, leading to the formation of wDDWs, has been considered. Hence, calculations have been made starting from one of the two possible equilibrium states for such a DW. In this way, Fig. 7.2.(a) represents the DW orientation angle Φ as a function of the reduced external field h and longitudinal current j, obtained from μM simulations. A similar color map can be depicted for the results provided by the 1DM, as it is shown in Fig. 7.2.(b). Prior to further discussions, it must be noticed that the color map obtained from the application of the 1DM possesses a higher resolution than its counterpart obtained from μM simulations, since the latter requires a rather high computational effort to conveniently define every pixel within the map. In any case, black areas within both figures represent field-current pairs (h, j) leading to DW displacements out of the stationary regime, i.e, in the precessional regime. Despite the different image resolutions, it can be said that results are rather similar, showing discrepancies mainly for values of j and h near to the ones where discontinuities of Φ are present. These slight discrepancies may arise from the fact that a constant wall width Δ has been considered in the calculations made by using the 1DM. Hence, the considered 1DM seems to perfectly reproduce the DW behavior.

From a first sight, an evident asymmetric DW behavior can be remarked. This

asymmetry does not only lie on the (h, j)-pairs leading to a precessional regime, but also on the stationary DW orientation angles reached. In fact, the green area, corresponding to stationary angles Φ ranging from 0^o to 180^o, prevail over the blue-purple area, characterized by the condition $-180^o \leqslant \Phi \leqslant 0^o$. The first asymmetry will be left for further discussion, so the explanation of the second one is to be addressed now. It must be mentioned that such behavior has already been reported by the authors for the individual application of fields and currents [139], and it is related to the DW degenerate state already mentioned in this text. The maps confirm that this behavior can be extended to the combined application of both stimuli. So as to clarify this, different regions have been delimited within the figures by means of black solid lines over the areas where a stationary regime is reached. Each region has been numbered according to the list of states given in the previous section. Some additional white dotted lines have been added over the colored areas that define, along with the corresponding parallel solid black lines, a rotated rectangle: its tilt depending on the value of the DMI parameter, i.e., the dimensionless quantity $\delta \equiv \frac{H_D}{H_k}$, within the framework of the 1DM. This rectangle sets the conditions in which the DW degeneracy holds, and it can be understood as the intersection of two overlapping corners, the one that limits the green area, which conceals the second one limiting the blue-purple area.

As an example, let start by applying a positive field and a positive current. Under the adequate choice of this pair of stimuli, the DW remains in state 6. Similarly, if a negative field is applied along with a positive current, the DW may go through states 2 and 3. The combination of negative currents and fields may lead the DW to states 4 and 5, while a positive field together with a negative current drive the DW within state 1. Starting from the DW equilibrium state, all the latter states are smoothly reached, since all of them are green colored, that is, the DW rotates to its stationary orientation in a gradual manner. Oppositely, steep transitions may occur if the DW is driven across the black continuous boundary of the rotated rectangle mentioned above. The origin of this abrupt DW reorientation is related to the existence of local extrema of $\dot{\Phi}$. For example, state 5 in the purple area can be reached from green state 6, by simply lowering the applied current, provided the applied field is sufficiently strong. Nevertheless, state 6 cannot be reached again by increasing the applied current unless the applied current is sufficiently high as to cross the white dotted border. In fact, this color map shows green state 6 overlapping blue-purple states 4 and 5, as green states 4 and 5 overlap blue state 6 for negative fields and currents. States 1 and 2 would act likewise.

Hence, the stationary orientation angle for a current and field-driven wDDW behaves in a hysteretic-like manner, since the final value for this angle depends not only on the applied values of both stimuli, but also on the procedure of application. It is then expected to obtain a similar plot if the initial orientation of the magnetization takes the other possible equilibrium state [139]. In such a case, the color map would show blue and purple areas overlapping green ones. Moreover, for positive DMI values, DW stationary orientations close to 0^o are not achievable, which can be confirmed by the absence of red areas on the color map. Finally, it is interesting to note that states 4 and 5 form the corner of the green area shown in both Fig. 7.2.(a) and (b), and so the boundary where abrupt reorientations of the DW magnetization may occur. The corners of the green area (shown in the figure) and blue-purple area (not

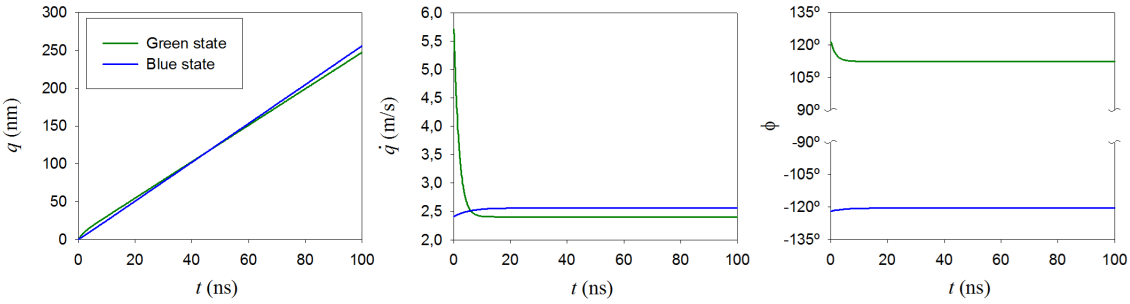

Figure 7.3: Transient behavior of a DDW after the combined application of a reduced field h=0. 10 , and a reduced current of j=0. 35 . Plots represent the DW instantaneous position q, speed $\dot{q}$, and orientation angle Φ, but taking into account the two possible equilibrium states for the wDDW have been considered as the respective initial states for the curves, which have been named as "green" and "blue", according to the color maps in Fig. 7.2. This point can be also checked in the initial DW orientation angle, being close to 120° for the "green" state, and close to -120° for the "blue" state.

shown, but delimited by the dotted white line) are located exactly where the effect of the applied current on the direction of rotation of the DW orientation reverses. The strength of h, that is, the applied field, is in this case sufficiently high to make the DW angle pass through the value $\Phi = \pm 90^{\circ}$ then inverting the contribution of the applied current to the rotation of the DW magnetization. This is the reason why the intensity of the applied current must be reduced to avoid the reorientation process.

Another important conclusion related to the existence of overlapping states is that the terminal speed of a wDDW is consequently not a state function, within the traditional meaning of this concept, since this speed depends on the DW stationary orientation, as (7.1b) establishes [139]. As an example of this point, Fig. 7.3 shows the evolution from equilibrium of the DW position q, speed $\dot{q}$, and orientation angle Φ for the two degenerate states of a wDDW. Each evolution has been named "green" and "blue" respectively, according to the states presented in the color maps in Fig. 7.2. The evolution has been calculated by using the 1DM, for a reduced field of $h = 0.10$, together with a reduced current of $j = 0.35$. Despite showing apparently similar instantaneous positions, the respective DW speeds for each DW have completely different behaviors, their terminal values being appreciably different, which can be significant for long time evolutions. Contrary to the latter example, the combined application of a reduced field $h = 0.085$ and a reduced current of $j = 0.44$ leads both wDDW to identical final states, as shown in the time evolution of Φ plotted in Fig. 7.4. However, one of them must go through an abrupt reorientation prior to reach such a stationary regime. Since the contribution of the j_a-term to the DW stationary speed depends on Φ, this contribution may change appreciably during the transient. This results in a large peak of the DW speed during the reorientation process, that makes the run distances for either wDDW rather different in this example. This difference may be in general shorter or larger because the effect of h can veil the contribution of j to the stationary DW speed, since the former effect is independent of Φ.

As mentioned above, the second important asymmetry lies on the (h, j)-pairs leading

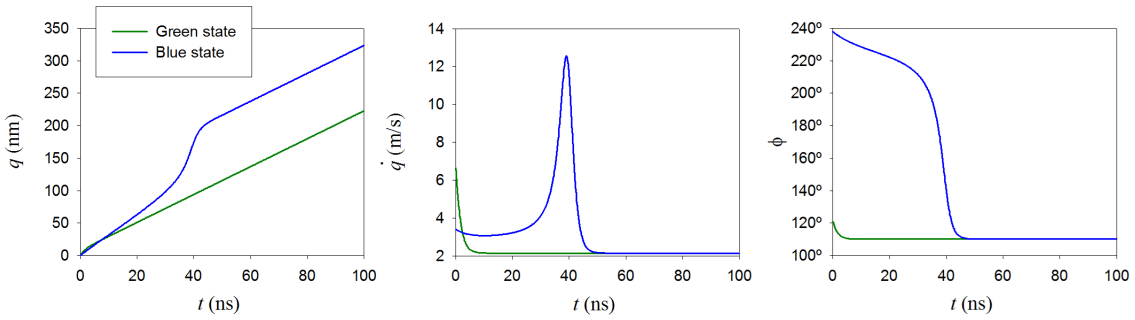

Figure 7.4: Transient behavior of two DDWs after the combined application of a reduced field h=0. 085 , and a reduced current of j=0. 44 . Plots represent the DW instantaneous positions q, speeds $\dot{q}$, and orientation angles Φ, the latter defined now within the range $[0^o : 360^o]$, so as to better show the DW inner magnetization sharp reorientation during the dynamics. The two possible equilibrium states for the DWs have been considered as the respective initial states for the curves, which have been named as "green" and "blue", according to the color maps in Fig. 7.2. This point can be also checked in the respective initial DW orientation angles, being close to 120^o for the "green" state, and close to $240^o (= -120^o)$ for the "blue" state. Both wDDWs reach identical stationary regimes, but the reorientation process gives rise to rather different run distances.

to a precessional regime. This results in the fact that applied fields higher than H_W may lead to stationary regimes if they are combined with sufficiently high currents, the threshold of the current depending on its sign. States 3 (higher) and 3 (lower) define in absolute terms such thresholds, so that the black areas within this color map are symmetric with respect to the origin of (h, j)-pairs. As an example, the solely application of a reduced field h of $+0.9$ leads the wDDW to the precessional regime. However, the stationary regime is recovered if an additional reduced current j of either above $+0.7$ or below -0.2 is applied. It must be noticed the large difference between the absolute values of such thresholds. Additionally, since the applied field may overcome the limit given by H_W without giving rise to precessional regimes, higher values of the DW terminal speed are achievable, which should be relevant for applications. Oppositely, such precessional regimes may appear for applied fields lower than H_W, depending on the sign of the applied current, as it occurs when a reduced field h of $+0.7$ is applied along with a positive current, within a certain range of positive currents. The same effect never occurs for a similar applied reduced field along with a negative current.

7.3.2 Effect of the DMI parameter

As it has been mentioned previously, the 1DM predicts the existence of local extrema of $\dot{\Phi}$, which explain the existence of abrupt DW reorientations. For values of $\delta \geqslant 1$, δ as defined above, such local extrema disappear, and the variations of the DW magnetization orientation become smoother. This is shown in Fig. 7.5, which displays in (a) the results obtained from μM simulations for $\delta = 1$, j and h defined as they were before, and in (b) the results obtained from the 1DM. The rather good agreement between μM results and those provided by the 1DM can be also checked in this case. As it can be seen, the rotated rectangle delimiting the area of degenerate states has

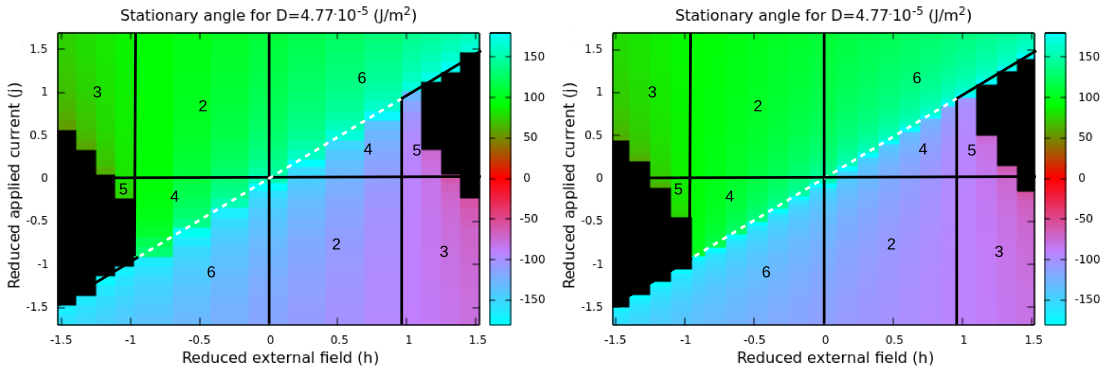

Figure 7.5: DW angle as a function of applied field (perpendicular) and applied current (through heavy metal) for a DMI parameter of $D = 4.77 \cdot 10^{-5}$J/m2 ($\delta = 1$) obtained from a) full μM simulations and b) the application of the 1DM. The black area corresponds to pairs of field and current values leading to a precessional regime.

collapsed into the white dotted line, so that only one state is available for the NDW within the stationary regime, and such a state is gradually achieved from any other previous stationary state.

Besides, since the condition $\delta \geqslant 1$ lead to the existence of NDWs, both DMI and magnetostatic interaction energies are extrema, i.e., the H_D- and H_k-terms vanish, so that, as long as the effect of the applied stimuli on the DW magnetization orientation cancels out, that is, $h = j$, the DW orientation angle at equilibrium holds during the dynamics. Under such a condition the NDW is maintained and the dynamics acquires its maximum efficiency [153].

Finally, it should be highlighted that the pairs of values (h, j) required to promote the non-stationary DW displacement increase in absolute terms with increasing the DMI parameter, as it can be inferred by comparing the scales in the different color maps in Figs. 7.2 and7.5. From such a comparison, it can be derived also that the boundary between the green and blue areas, which defines the abrupt DW reorientation processes, possesses a gentler slope as the value of the DMI parameter increases. This is because of the fact that for stronger DMI the DW takes, in general, an orientation closer to the x-axis. Actually, stronger applied fields are required to lead the DW stationary angle to an orientation closer to the transverse in-plane axis (y-axis).

In any case, for higher DMI parameters, the non-stationary area holds asymmetric since the $H - k$-term together with the H_D-term may act likewise or oppositely to the effect of j_a, depending on the sign of the latter.

7.4 Conclusions

A systematic numerical study of the DW dynamics in asymmetric structures consisting in a ferromagnetic (FM) layer sandwiched between a heavy-metal (HM) layer and an oxide layer has been carried out. The combined effect on such dynamics of stimuli in the form of out-of-plane applied fields and longitudinal currents has been considered. Despite slight discrepancies, the 1DM reproduces the main trends obtained by means of full μM modeling, then proving the selfconsistency of our results. In fact, the 1DM is able to adequately explain the complexity of such DW dynamics, which may be of interest for improving the control of spintronic devices by increasing the efficiency of the applied stimuli. Furthermore, discrepancies are basically limited to the DW state boundaries where abrupt reorientations of the magnetization within the DW may occur.

As the most remarkable conclusions, it can be mentioned, first, that our results confirm the inherent asymmetric character of the wDDW dynamics, derived from the existence of DW degenerate states. This asymmetry may result in different DW terminal speeds reached after the application of the same couple of stimuli. Secondly, it is demonstrated that DW precessional regimes can be avoided by combining applied fields with sufficiently high currents, then resulting in a faster DW dynamics. Moreover, within certain ranges of applied fields leading to DW stationary regimes, provided no longitudinal currents are applied, the application of the former in a certain direction may lead the DW dynamics to the precessional regime, while the same current oppositely applied maintains the stationary DW dynamics.

7.5 Acknowledgment

This work was supported by project WALL, FP7-PEOPLE-2013-ITN 608031 from the European Commission, project MAT2014-52477-C5-4-P from the Spanish Government and project SA282U14 from the Junta de Castilla y Leon.

Part III.
The effect of current's angle

Chapter 8

Angular dependence of current-driven chiral walls*

The current-driven dynamics of chiral domain walls is theoretically studied by means of realistic micromagnetic simulations. Trains of current pulses flowing through the heavy metal underneath the ferromagnetic layer are injected with different directions with respect to the ferromagnetic strip axis. The wall displacement is highly sensitive to the wall configuration and to the angle between the current and the longitudinal axis of the strip. These simulations can account for the experimental behavior at large currents, but preliminary results at lower current density point towards incompatibilities between the model and the experiment that need further experimental and theoretical efforts.

*Adapted from E. Martínez, O. Alejos, M. A. Hernandez, V. Raposo, L. Sanchez-Tejerina, and S. Moretti. Angular dependence of current-driven chiral walls. *Appl. Phys. Express*, 9:063008, 2016. doi:10.7567/APEX.9.063008.

Owing to its technological relevance and the underlying physics involved, understanding and controlling the current-driven magnetization dynamics in multilayers with structural asymmetry and consisting of an ultrathin ferromagnetic (FM) layer sandwiched between a heavy metal (HM) and an oxide are nowadays the focus of intense research. [7–9, 11–13, 17, 18, 20–23, 152] These systems exhibit high perpendicular anisotropy (PMA), and owing to the presence of antisymmetric exchange interaction, i.e., Dzyaloshinskii-Moriya interaction (DMI) present at the FM/HM interface, [41] the magnetization adopts chiral patterns, such as homochiral Neel domain walls (DWs). [11, 12, 17, 21, 152] Recent experiments have demonstrated that these DWs are efficiently driven along patterned FM strips under injection of the electrical current along the HM underneath. [11, 12, 17, 21, 152] These observations are linked to the generation of a spin current due to the spin Hall effect (SHE), which induces spin accumulation at the FM/HM interface and interacts with the local magnetic moment in FM. [9, 11, 12] When the charge current flows parallel to the FM strip axis, the effective field due to the SHE is maximized if the local magnetization is collinear with the charge current. As a consequence, the interfacial DMI stabilizes Neel walls with a given chirality, which are efficiently driven by the SHE. [11, 12]

The switching of the magnetization of a patterned FM nanodot has also been observed experimentally in multilayers with strong DMI under the additional presence of an in-plane magnetic field parallel to the charge current. [7, 9, 13, 18, 22] In this case, magnetization reversal takes place universally by DW nucleation followed by its current-driven propagation. [23] Most of the studies up to now have analyzed the DW dynamics when the current in the HM is collinear with the FM strip axis. However, more recently, a further development has been experimentally reported: [18, 78] when both the FM and HM are patterned independently, the current-driven magnetization switching can be achieved in the absence of in-plane fields by exploding the geometry of the FM and the noncollinear direction of the charge current in the HM. In these experiments, [78] the magnetization reversal still takes place by the DW motion, but its displacement is found to be highly dependent on the angle at which the current flows in the HM, and it is asymmetric and nonlinear with respect to the current polarity. This opens the doors to novel architectures for logic and memory devices, which could be controlled solely by electrical currents. However, a complete understanding of the physics governing these processes is still missing, and consequently, theoretical investigations and realistic numerical descriptions are very timely and in demand.

Here, we theoretically investigate the current-driven DW dynamics in different systems with strong DMI where the longitudinal axis of the FM layer is noncollinear with the direction of the electric charge flowing along the independently patterned HM. On the basis of our micromagnetic simulations under ideal conditions, we provide a simple analytical description of the angular dependence of the DW displacement with respect to the current orientation. After that, a more realistic analysis including disorder and thermal effects is performed, which indicates that these ingredients play a significant role in the dynamics.

The current-induced DW dynamics is governed by the Gilbert equation augmented

by the Slonczewskii-like SOT, [19, 145]

$$\frac{d\mathbf{m}}{dt} = -\gamma_0 \mathbf{m} \times (\mathbf{H}_{eff} + \mathbf{H}_{th}) + \alpha \mathbf{m} \times \frac{d\mathbf{m}}{dt} + \boldsymbol{\tau}_{SL} \tag{8.1}$$

where γ_0, α, and $\mathbf{m}(\mathbf{r}, t) = \mathbf{M}(\mathbf{r}, t)/M_s$ denote the gyromagnetic ratio, the Gilbert damping constant, and the normalized local magnetization to the saturation value (M_s), respectively. H_eff is the deterministic effective field, which includes the exchange, the magnetostatic, the uniaxial anisotropy, and the DMI. H_th is the stochastic thermal field. [117] The last term $\boldsymbol{\tau}_{SL}$ is the Slonczewskii-like spin orbit torque (SL-SOT) due to the SHE, [9]

$$\boldsymbol{\tau}_{SL} = -\gamma_0 H_{SH}^0 \mathbf{m} \times (\mathbf{m} \times \boldsymbol{\sigma}) \tag{8.2}$$

where $H_{SH}^0 = \dfrac{\hbar \theta_{SH} J}{2\mu_0 \mid e \mid M_s t}$, $\hbar$ is the Planck constant, $\mid e \mid$ is the electric charge, μ_0 is the permeability of free space, t is the thickness of the ferromagnetic layer, and θ_{SH} is the spin Hall angle. J is the magnitude of the density current [$J\mathbf{J} = J(t)\mathbf{u}_J$] and $\sigma = \mathbf{u}_z \times \mathbf{u}_J$ is the unit vector of the spin current generated by the SHE in the heavy metal, which is orthogonal to both the direction of the electric current ($\mathbf{u}_J$) and the perpendicular direction ($\mathbf{u}_z$). Typical parameters for a HM/FM/oxide multilayer with strong DMI are considered: [15] $M_s = 1.1 \times 10^6 A/m$, $A = 1.5 \times 10^{-11}$J/m, $K_u = 1.25 \times 10^6 \mathrm{J}/m^3$, $D = -1.8\mathrm{mJ/m}^2$, $\alpha = 0.5$, and $\theta_{SH} = 0.07$. The thickness of the Co layer is fixed to $t = 0.6$nm. The samples were discretized using a 2D grid of 4-nm-wide cells. Except that the contrary is indicated, disorder and thermal effects are taken into account in order to mimic realistic conditions. The local disorder and imperfections are taken into account in the simulations by considering both randomly generated roughness at the strip edges [117] and grains in the strip body. A typical edge roughness with a characteristic length of 12nm is assumed in the present study. [117] In addition, we assume that the easy axis anisotropy direction is distributed among a length scale defined by a characteristic grain size of 5nm. The direction of the uniaxial anisotropy of each grain is mainly directed along the perpendicular direction (z-axis) but with a small in-plane component, which is randomly generated over the grains. The maximum percentage of the in-plane component of the uniaxial anisotropy unit vector is 5%. In this work, five different grain patterns have been evaluated to obtain statistic results. All numerical details can be found in Ref. [122].

We firstly focus our attention on the sample depicted in Fig. 8.1(a), where the FM layer is patterned with the shape of *a quarter-of-a-star* on top of an extended HM. The FM consists of seven strips, each one forming a different angle ϕ_S with the x-axis ($\phi_S = 0^\mathrm{o}, \ldots, 90^\mathrm{o}$, in steps of $\Delta\phi_S = 15^\mathrm{o}$). This geometry was produced by firstly generating a strip along the x-axis with edge roughness and random dispersion of the easy axis of each grain as defined above. Then, the strip was replicated seven times, and each replica is rotated in steps of $\Delta\phi_S = 15^\mathrm{o}$ to form the final geometry shown in Fig. 8.1(a). Initially, each strip contains an up–down DW as shown in Fig. 8.1(a). A train of five current pulses is injected in the extended HM along the transverse y-axis ($u_J = u_y$, i.e., $\phi_J = 90^\mathrm{o}$). The length of each pulse (t_p) and the time between them (t_w) are fixed to $t_p = t_w = 2$ns, and the amplitude is $\mid J \mid = 2\mathrm{TA/m}^2$. Figure 8.1(b) depicts the difference between the final state [$m_{z,f}(\mathbf{r})$] after the injection of five

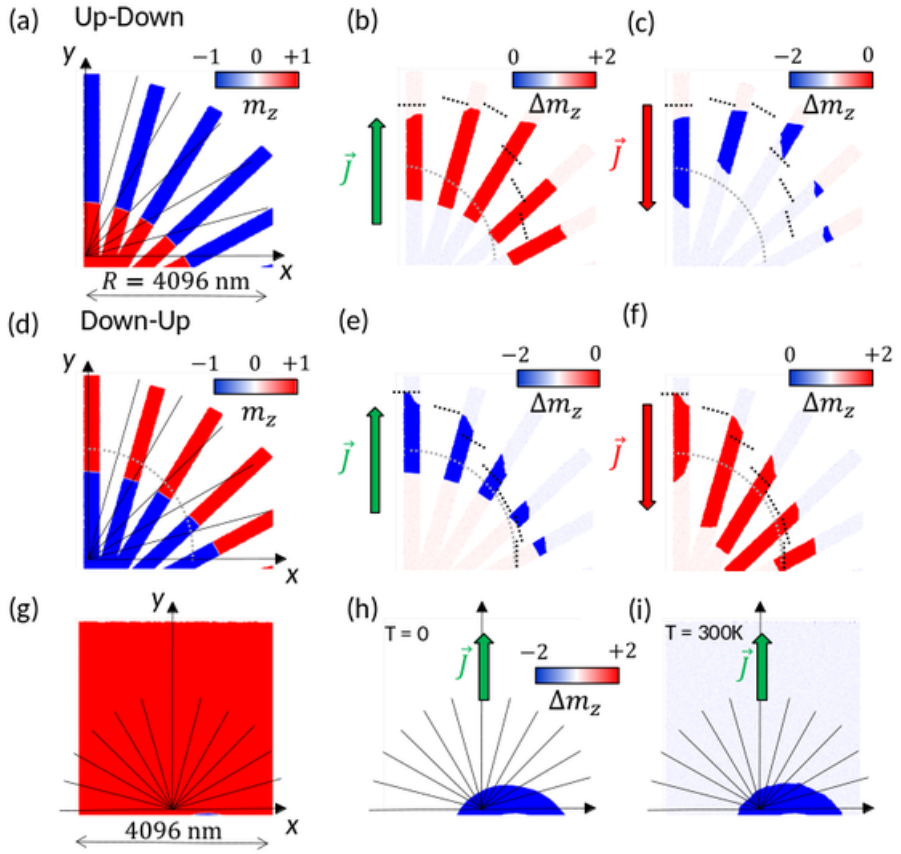

Figure 8.1: DW dynamics along different strips with different orientations with respect to the current. (a) Initial state of up–down DWs. (b) Forward displacement of the DWs (d_F) under five positive current pulses (2ns at $J = +2\text{TA/m}^2$). Grey dotted lines represent the initial positions of the DW in each strip. The DW displacement is shown by plotting the differential images $\Delta m_z(\mathbf{r}) = m_{z,f}(\mathbf{r}) - m_{z,i}(r)$, where the sub-indexes i and f indicate the initial and final states, respectively. (c) Backward displacement of the DWs (d_B) under five negative current pulses (2ns at $J = -2\text{TA/m}^2$). Black dotted lines represent the initial positions of the DW in each strip. (d)–(f) correspond to a similar study but starting from a down–up DW. (g)-(i) Semibubble DW dynamics under five positive current pulses ($1ns$ at $J = +1\text{TA/m}^2$) at zero and at room temperature.

positive pulses ($J > 0$) minus the initial state $[m_{z,i}(\mathbf{r})]$ [Fig. 8.1(a)]. Therefore, the red color along each strip in Fig. 8.1(b) represents the terminal DW displacement (d_DW) of the corresponding DW $[\Delta m_z(\mathbf{r}) = [m_{z,f}(\mathbf{r})] - [m_{z,i}(\mathbf{r})]$. From Fig. 8.1(b), it is evident that the d_DW depends significantly on the relative orientation of the strip axis with respect to the direction of the current ($\phi = \phi_J - \phi_S = 90^o - \phi_S$): d_DW increases from $\phi = 0$ to 30^o, where the DW displacement reaches a maximum. From $\phi = 30$ to 90^o, the displacement decreases monotonically. Starting from the state of Fig. 8.1(b), a new train of five negative pulses ($J < 0$) is applied, and the new differential micromagnetic image is shown in Fig. 8.1(c). During this back motion, only the DW in the strip with $\phi_S = 90^o$ returns to its initial position, and the DW displacement monotonically decreases as $\phi = \phi_J - \phi_S = 90^o - \phi_S$ increases. Similar trends are observed when the initial state is prepared to have a down–up DW on each strip [see Figs. 8.1(d)– 8.1(f)]. The asymmetry of the displacement reverses with the current polarity ($J > 0$ or $J < 0$) or with the DW configuration (up–down

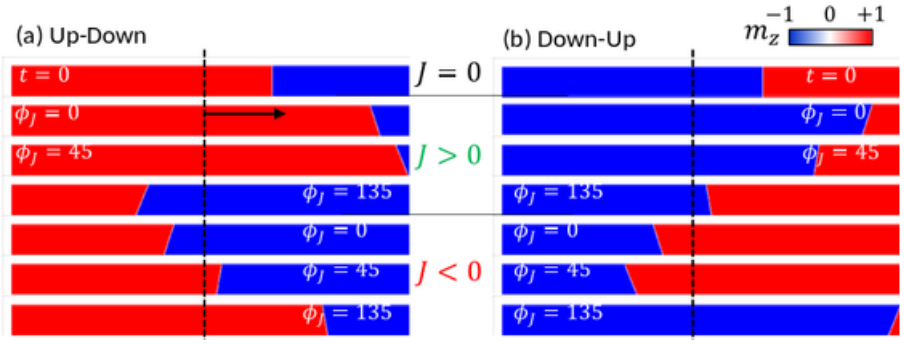

Figure 8.2: Snapshots of the DW displacement after $t = 10$ns under DCs of $\mid J \mid = 2\text{TA/m}^2$ injected in the HM with different orientations (ϕ_J) with respect to the FM strip axis ($\phi_S = 0$): (a) up–down DW, (b) down–up DW. The FM strip is ideal, without imperfections.

or down–up).

A similar study was also performed for an unpatterned square pad initially containing two semibubble DWs [see Fig. 8.1(g)]. The final state after injection of five pulses with $J = +1\text{TA/m}^2$ and $t_p = t_w = 1$ns is shown in Figs. 8.1(g)(h) and 8.1(g)(i) at zero and room temperature, respectively. In both cases and similarly to the case of the patterned strips, the DW displacement is largest for $\mid \phi \mid = \mid \phi_J - \Phi \mid \approx 30^o$. This proves that the angular dependence of the DW displacement is not due to the DW tilting [19] present in the patterned strips [see Figs. 8.1(b), 8.1(c), 8.1(e), and 8.1(f)]. The asymmetric angular dependence of the DW displacement observed when the current polarity reverses ($J > 0$ to $J < 0$) also occurs, inverting the angle $\phi = 90^o - \phi_S$ ($+\phi$ to $-\phi$) or the configuration of the DW (up–down to down–up). Although a roughly estimated set of material parameters for the evaluated samples have been considered, our simulations exhibit rather similar features to recent observations. [78] See the online supplementary data at http://stacks.iop.org/APEX/9/063008/mmedia for an additional description of the angular dependence of semibubbles when the current is reduced.

To understand these observations, a systematic study of the DW dynamics is carried out for a single strip along the x-axis ($\phi_S = 0^o$) by varying the direction of the current from $\phi_J = 0$ to 180^o. The strip length is 8192nm and its width is 512nm. We firstly discuss the case of DW motion under direct current (DC), which is applied for a total time of 10ns. Some representative snapshots of the initial and final DW positions are shown in Fig. 8.2 for both up–down (a) and down–up (b) DWs. The DW displacements along a perfect strip (PS) under DC are shown in Figs. 8.3(c)- 8.3(f) for both up–down and down–up DWs. The terminal DW angle (Φ) and the tilting angle of the DW plane (ξ) as defined in Figs. 8.3(a) and 8.3(b) are also represented as a function of ϕ_J. As expected, no DW motion is achieved when the current $J = J_x\mathbf{u}_x + J_y\mathbf{u}_y$ is perpendicular to the strip axis ($\phi_J = 90$ or 270^o). The DW displacement (d_{DW}) is symmetric with respect to the current polarity ($J > 0$ or $J < 0$) only when the current is collinear with the strip axis ($\phi_J = \phi_S = 0^o$). The DWs move along the direction of the longitudinal component of the current ($J_x = J\cos\phi_J$), but d_{DW} strongly depends on the direction of the current ($\phi_J, \mathbf{u}_J = \mathbf{J}/J$). Under positive current [$J > 0$, Fig. 8.3(c)], the displacement of the

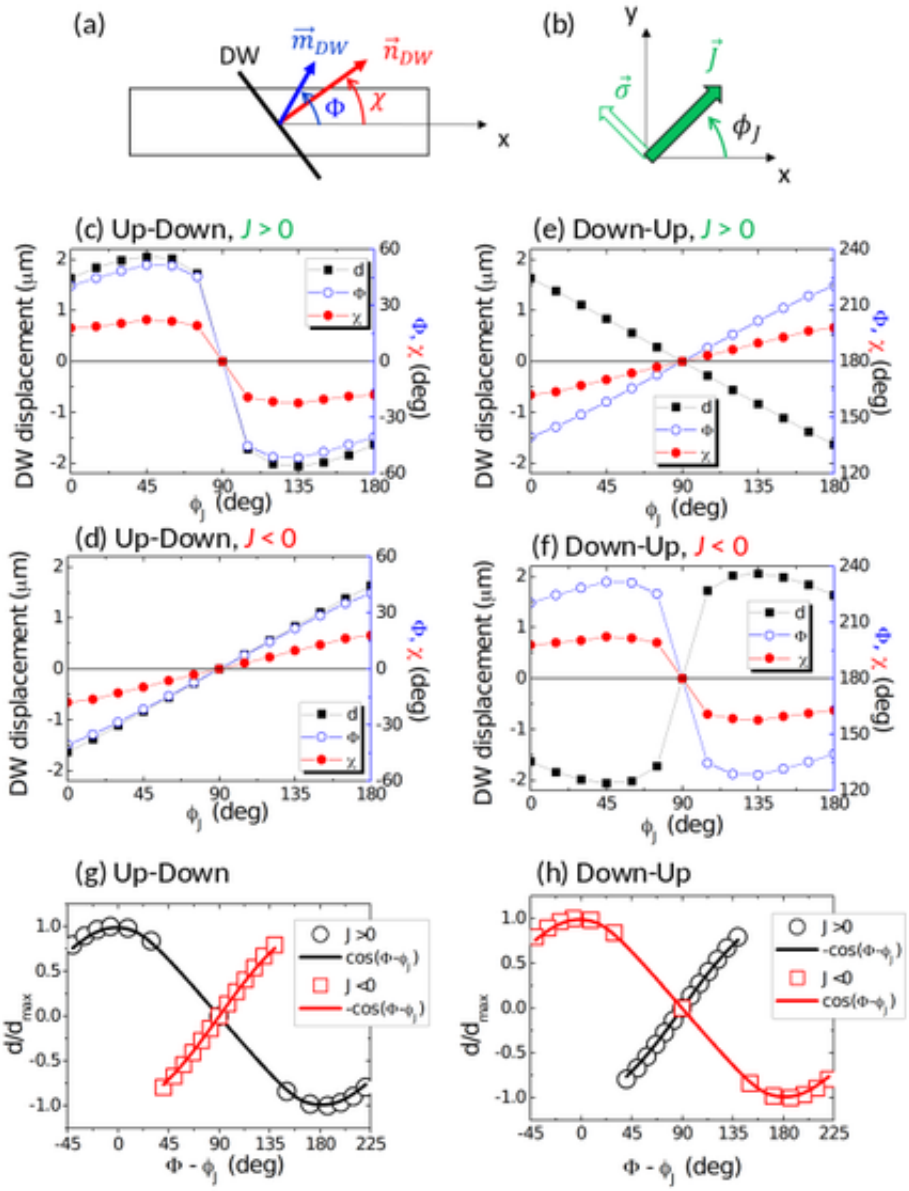

Figure 8.3: (a) Schematic representation of a tilted DW with the definitions of the DW angle (Φ) and the tilting angle of the DW plane (ξ). (b) Definition of the direction of the injected current (ϕ_J). DW displacement after t = 10ns under DCs of $\mid J \mid = 2\text{TA} = \text{m}^2$ injected in the HM with different orientations (ϕ_J) with respect to the FM strip axis ($\phi_S = 0$). Left graphs (c, d, g) correspond to the up–down DW. Right graphs (e, f, g) correspond to the down–up DW. The FM strip is ideal, without imperfections, and the results were obtained at zero temperature. The DWs are initially placed at the center of the strip.

up–down DW [$d_{UD}\left(J>0,\phi_J J\right)$] firstly increases from $\phi_J = 0$ to 45°, where it reaches its maximum value $d_{max} = d_{UD}\left(J>0,\phi_J = 45^{\text{o}}\right)$. From $\phi_J = 45$ to 90°, $d_{UD}(\phi_J)$ decreases to zero. For $90^{\text{o}} \leqslant \phi_J \leqslant 180^{\text{o}}$, the direction of the DW motion reverses with respect to the range $0 \leqslant \phi_J \leqslant 90^{\text{o}}$, and again, the maximum displacement along the negative x-axis is achieved at $\phi_J = 135^{\text{o}}$. The angular dependence of the DW displacement is completely different when the current polarity reverses [$J<0$, Fig. 8.3(d)]. In this case, the displacement $\mid d_U D\left(J<0,\phi_J\right) \mid$ decreases linearly and monotonically from $\phi_J = 0$ to 90°. Similar results are obtained for the down–up DW [Figs. 8.3(e) and 8.3(f)], which can be summarized as follows: $d_{DU}\left(J>0,\phi_J\right) = -d_{UD}\left(J<0,\phi_J\right)$ and $d_{DU}\left(J<0,\phi_J\right) = -d_{UD}\left(J>0,\phi_J\right)$. It is clearly observed that the maximum DW displacement is reached when the internal DW angle (Φ) becomes closer to the angle at which the current is injected ($\Phi \approx \phi_J$). Therefore, we replot using dots the normalized displacement to the maximum value $d\left(J,\phi_J\right)/d_{max}$ as a function of $(\phi_J - \Phi)$ in Figs. 8.3(g) and 8.3(h) for both up–down and down–up DWs, respectively. As shown, these data can be successfully reproduced by a simple analytical formula:

$$\frac{d\left(J,\phi_J\right)}{d_{max}} = Q\frac{J}{\mid J \mid}\cos\left(\phi_J - \Phi\right) \tag{8.3}$$

where $Q = \pm 1$ corresponds to up–down ($Q = +1$) and down–up ($Q = -1$) DW configurations, and $J/\mid J \mid$ determines the polarity of the applied current: positive ($J>0$) and negative ($J>0$), respectively. Note that in general, Φ is a function of the amplitude of the injected current J and the time during which it is applied. It also depends on the geometry and on the material parameters. As can be easily understood, the current direction ϕ_J, which maximizes the displacement, is also a function of the current J, the geometry, and the material parameters, particularly the DMI parameter and the spin Hall angle.

These results can be understood in terms of the torque $\boldsymbol{\tau}_{SL}$ due to the SHE, (8.2), and the corresponding effective field $\mathbf{H}_{SHE} = \frac{\hbar\theta_{SH}J}{2\mu_0|e|M_s t}\left(\mathbf{m}_{DW}\times\boldsymbol{\sigma}\right)$. This spin Hall effective field depends on the internal DW magnetization ($\mathbf{m}_{DW}$) and the direction of the spin current applied current $\boldsymbol{\sigma} = \mathbf{u}_z \times \mathbf{u}_J$, which directly depends on the current direction [$\mathbf{J} = J\left(t\right)\mathbf{u}_J$]. In systems with strong DMI, the internal DW magnetization at rest, $\mathbf{m}_{DW}$, points along the strip axis (x-axis). Its direction, either $\mathbf{u}_x$ or $-\mathbf{u}_x$, depends on the chirality, imposed by the sign of the DMI parameter D, and on the DW configuration (up–down or down–up). [11, 12] Let us consider here for clarity an up–down DW with right-handed chirality, where $\mathbf{m}_{DW} = +\mathbf{u}_x$ at rest. When a current is applied along the x-axis ($\mathbf{J} = J\mathbf{u}_x$; $\sigma = +\mathbf{u}_y$), the effective field $\mathbf{H}_{SHE} = \frac{\hbar\theta_{SH}J}{2\mu_0|e|M_s t}m_{DW,x}\mathbf{u}_z$, points along $+\mathbf{u}_z$ for $\theta_{SH}>0$, and consequently, drives the DW motion along the $+\mathbf{u}_x$. However, owing to the SHE torque, the internal magnetization of the DW rotates clockwise from the x-axis ($\Phi>0$), and thus it is no longer collinear with the current. In other words, the longitudinal component of the DW moment is reduced with respect to the initial state before the current injection [$\Phi\left(t=0\right)=0$], and thus $m_{DW,x} = \cos\Phi < 1$ for $\Phi > 0$. If the current is applied at a different orientation from the x-axis, $\mathbf{J} = J\mathbf{u}_J = J\cos\Phi_J\mathbf{u}_x + J\sin\phi_J\mathbf{u}_y$ with $\phi_J > 0$, the unit vector along the spin polarized current is $\sigma = -\sin\phi_J\mathbf{u}_x + \cos\phi_J\mathbf{u}_y$, and the internal DW moment has

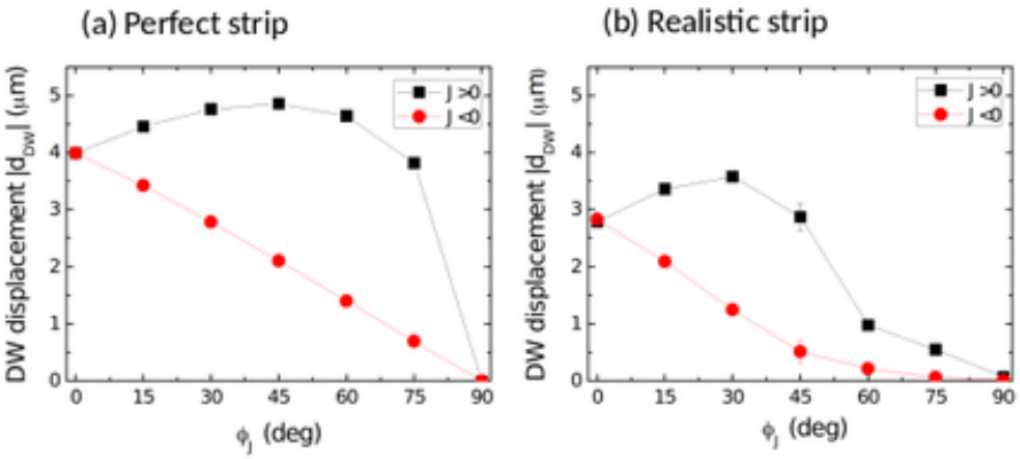

Figure 8.4: Displacement of the up–down DW as a function of the DC (J) for different orientations of the injected current (ϕ_J): (a) Perfect strip (PS), without imperfections at zero temperature. (b) Results obtained for a realistic strip (RS), which has edge roughness and a dispersion of the out-of-plane easy axis. (c) and (d) show the comparison of the DW displacement between PS and RS for two different amplitudes of the DC: $\mid J \mid = 0.8\text{TA/m}^2$ and $\mid J \mid = 2\text{TA/m}^2$.

both x and y components: $\mathbf{m}_{DW} = \cos\Phi\mathbf{u}_x + \sin\Phi\mathbf{u}_y$. The SHE effective field is $\mathbf{H}_{SHE} = \frac{\hbar\theta_{SH}J}{2\mu_0|e|M_s t}\cos(\phi_J - \Phi)\,\mathbf{u}_z$, which reaches a maximum when $\phi_J = \Phi$. The DW velocity under DC is therefore $v_{DW} = \frac{\gamma_0\Delta}{\alpha}\frac{\hbar\theta_{SH}J}{2\mu_0|e|M_s t}\cos(\phi_J - \Phi)$ where Δ is the DW width. Consequently, the DW displacement $[d_{DW}(J,\phi_J) = v_D W\Delta t$, with Δt being the time during the DC is applied] is enhanced when the internal DW moment m DW becomes collinear with the current $\mathbf{J} = J\mathbf{u}_J$, as shown in Figs. 8.3(g) and 8.3(h).

A similar study was performed by applying a train of ten pulses. The amplitude of each pulse is $\mid J \mid = 2\text{TA/m}^2$ and its length is $t_p = 2$ns. The interval between two consecutive pulses is also $t_w = 2$ns. The absolute value of the DW displacement, $\mid d_{DW} \mid$, as a function of ϕ_J of the up–down DW is shown in Fig. 8.4 for both the perfect strip at zero temperature (a) and the realistic strip at room temperature (b). The results for the realistic strip case were averaged over five different grain and roughness patterns, with error bars indicating the standard deviation. The main features of the DW displacement as a function of ϕ_J remain similar to the previous analysis of DCs. Under positive currents, we found a maximum in the DW displacement for $\phi_J \approx 30^o$. For negative currents, no DW motion is found for $\phi_J > 60^o$. Actually, our results [8.4] are qualitatively analogous to the experimental measurements by Safeer et al. The obtained DW displacements are indeed in good quantitative agreement, despite the fact that the present work does not search for a quantitative replication of such experiments. The quantitative discrepancies are expected owing to the different strip widths, different evaluated current pulses, and also possible differences in the material parameters. The disorder (grain and edge roughness), which has been shown to play a significant role, may also differ from the one of the samples studied experimentally. Nevertheless, further theoretical and experimental efforts are needed to completely elucidate the physics governing these systems. Particularly demanding are the theoretical/numerical study of the angular dependence of the DW displacement under non-collinear currents in the creep regime,

where the experiments [78] indicate a similar asymmetry with velocities two orders of magnitude smaller. The realistic analysis of the creep regime requires a huge computational effort, which is beyond the scope of the present study.

In summary, we theoretically investigated the current-induced DW dynamics in heterostructures with high PMA and strong DMI for different orientations of the current with respect to the strip axis. Under ideal conditions (without disorder and at zero temperature), the DW displacement is largest when the internal magnetization of the DW is parallel to the direction of the applied current for both direct current and train of current pulses. Analytical expressions were obtained to explain these results in the framework of the spin Hall effect. Realistic conditions (with disorder and at room temperature) were also evaluated. This analysis indicates that the direction of maximum displacement is significantly modified with respect to the ideal case, and it takes place at current angles relative to the strip axis of around 15–30°. Although our simulations can account for the experimental behavior at large currents in the flow regime, preliminary results at lower current density in the creep regime point towards incompatibilities (see the online supplementary data at http://stacks.iop.org/APEX/9/063008/mmedia) between the model and the experiment, which need further experimental and theoretical efforts. Our work, which at present does not exclude other more complex driving mechanisms, constitutes a first theoretical attempt to describe the DW dynamics in multilayers where the current is not collinear with the axis of the patterned ferromagnetic strip and/or the bubble expansion in extended thin films. It also provides insightful contributions to a further understanding of the physics involved and it is expected to be useful for the future development of DW-based logic and memory devices in the absence of applied fields, by just designing the geometry of the ferromagnetic samples.

8.1 Acknowledgment

This work was supported by project WALL, FP7-PEOPLE-2013-ITN 608031 from the European Commission, project MAT2014-52477-C5-4-P from the Spanish government, and project SA282U14 from the Junta de Castilla y Leon.

Chapter 9

Micromagnetic analysis of geometrically controlled current-driven magnetization switching*

The magnetization dynamics induced by current pulses in a pair of two isolated "S-shaped" ferromagnetic elements, each one consisting on two oppositely tilted tapered spikes at the ends of a straight section, is theoretically studied by means of micromagnetic simulations. Our results indicate that the magnetization reversal is triggered by thermal activation, which assists the current-induced domain nucleation and the propagation of domain walls. The detailed analysis of the magnetization dynamics reveals that the magnetization switching is only achieved when a single domain wall is nucleated in the correct corner of the element. In agreement with recent experimental studies, the switching is purely dictated by the shape, being independent of the current polarity. The statistical study points out that successful switching is only achieved within a narrow range of the current pulse amplitudes.

*Adapted from O. Alejos, V. Raposo, M. A. Hernandez, L. Sanchez-Tejerina, S. Moretti, and E. Martinez. Micromagnetic analysis of geometrically controlled current-driven magnetization switching. *AIP Advances*, 7(5):055909, 2017. doi:10.1063/1.4973749.

9.1 Introduction

Understanding and controlling the current-driven magnetization dynamics in multilayers with structural inversion asymmetry, where an ultra-thin ferromagnetic layer (FM) is sandwiched between a heavy metal (HM) and an oxide, is the focus of intense research. [7, 9, 11, 12, 17, 18, 21, 22] These systems present high perpendicular magnetocrystalline anisotropy (PMA) and a sizable Dzyaloshinskii–Moriya interaction (DMI) which promotes the emergence of chiral magnetization patterns. [11, 12, 17, 21, 155, 156] The switching of the magnetization of a patterned FM element has been observed experimentally in these multilayers under the additional presence of an in-plane magnetic field parallel to the charge current which flows along the HM. [7, 9, 18, 22] However, recent experiments have shown that the current-driven magnetization switching (CDMS) of an independently patterned FM element on top of an extended HM can be achieved in the absence of in-plane fields by solely exploding its geometry and the non-collinear direction of the current in the HM underneath. [78] The lithographically defined shape of the FM determines its reversal, and therefore, objects with identical composition and subjected to the same electric current undergo different magnetization reversal.

Safeer et al. [78] studied two geometries, "U-shaped" and "S-shaped" (see figure 4a and 4b of Ref. [78]), and show how with an adequate election of the amplitude, duration and number of pulses, it is possible to control the magnetization without any external field, with the only application of electrical current. Both "U-shaped" and "S-shaped" FM elements consist on two tilted tapered spikes at the ends of a straight section. They suggested that current density should be larger in the spikes. Consequently, the nucleation of reversed domains, flanked by two domain walls (DWs), would take place predominantly at the tapered spikes of the patterned FM element as caused by the non-uniform Joule heating. As the spike has a tilt angle of $\approx 45^{\circ}$ with respect to the central straight section, the different speeds of the up-down and down-up walls cause the propagation of the two DWs or their collapse depending on the current polarity. [78, 153] In these cases, the magnetization reversal is not achieved. However, when the reversed domain occurs exactly at the corner of the spike, a single DW is nucleated, and the current polarity and the location of the spike determine whether the switching is or not achieved by its current-driven propagation. Therefore, the final magnetic state of the FM element can be controlled with its geometry and the current polarity. These observations open the door to the development of high-performance memory or logic devices, but the underlying mechanisms responsible for the DW nucleation have not been clarified yet, and a complete understanding of the physics governing these processes is still missing. Here, we analyze these reversal processes by means of micromagnetic simulations.

As the underlying mechanism is essentially the same for both "U shaped" and "S shaped" geometries studied in, [78] here we focus our attention on a pair of two isolated "S-shaped" FM elements, each one consisting on two oppositely tilted tapered spikes at the ends of a straight section. These FM elements are independently patterned on top of an extended HM. A scheme of the system is shown in Fig. 9.1(a). In order to elucidate whether the nucleation takes place predominantly at the spikes, the current distribution and the Joule heating are characterized in Sec. 9.2. After

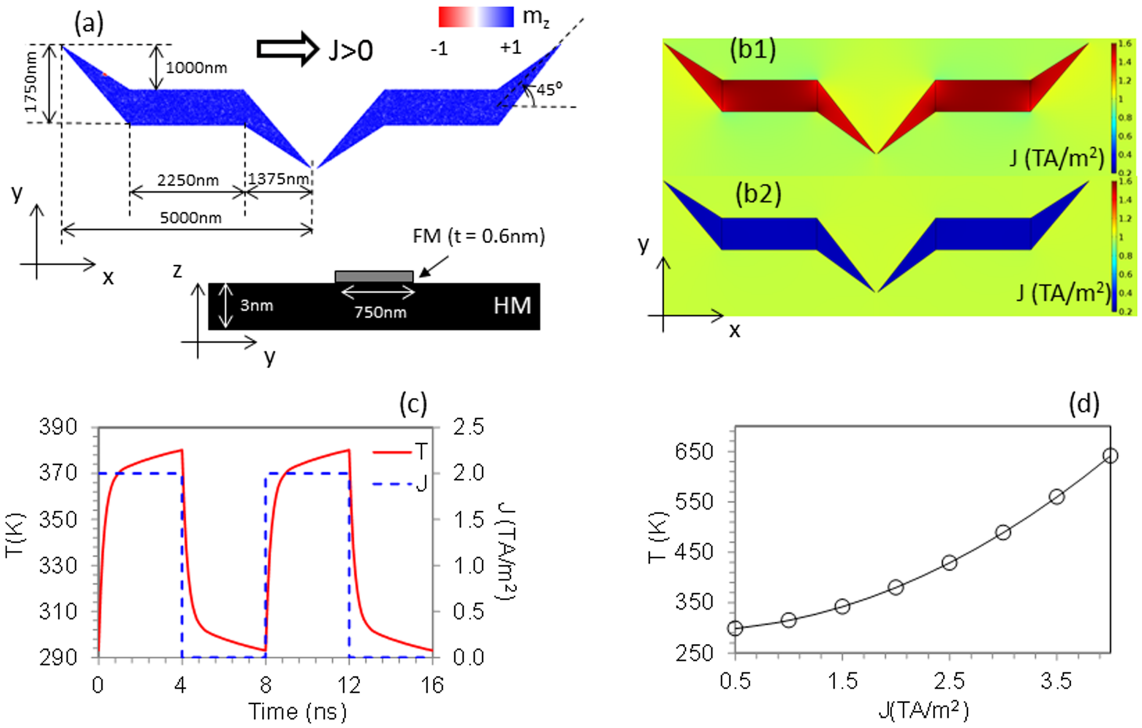

Figure 9.1: (a) Schematic view and dimensions of the S-shaped FM device along with the vertical HM/FM structure. Spatial distribution of the current density ($\mathbf{J}(\mathbf{r})$) for the bulk (b1) and thin-films (b2) resistivities. Green color correspond to the current density in the conductive HM underlayer. (c) Temporal evolution of the device temperature for a series of pulses of 2TA/m^2. (d) Temperature in the FM dots as function of the current density in the HM.

that, the magnetization dynamics under a train of current pulses is evaluated by means of micromagnetic simulations in Sec. 9.3, which allow us to characterize the reversal mechanism under realistic conditions. The manuscript ends with the main conclusions of the study.

9.2 Current Distribution and Joule Heating

As the non-uniform current distribution at the spikes, and the resulting Joule heating effects were proposed in Ref. [78] to be the main cause of the DW nucleation, a preliminary study of the current distribution and the Joule heating of the system was performed with the techniques described in. [86, 157] Two different cases were evaluated for the 3D structure Pt(3)/Co(0.6)/AlO, where numbers indicate the thickness the HM and FM layers. We firstly considered the bulk resistivities of the FM and HM layers: $\rho\,(\text{C}) = 62.4 \times 10^{-9}\Omega\text{m}$ and $\rho\,(\text{Pt}) = 105 \times 10^{-9}\Omega\text{m}$. Due to the higher resistivity of the Pt, the current flows mainly through the Co layer where it is present (Fig. 9.1 (b1)), but its distribution is quite uniform, with no higher densities at the spikes (Fig. 9.1 b1). Alternatively, we also take into account the thickness dependence of the resistivity that becomes very relevant for ultrathin layers. [158] If resistivity values for the Co and Pt ultrathin layers are assumed ($\rho\,(\text{Co}) = 9.6 \times 10^{-7}\Omega\text{m}$ and $\rho\,(\text{Pt}) = 2.7 \times 10^{-7}\Omega\text{m}$), the roles invert, and now the current flows mainly through the Pt uniformly (Fig. 9.1 (b2)) in such a manner that

the Joule heating is again uniform along the FM elements of the device. In both cases, as the current distribution is essentially uniform over FM elements, the same probability of domain nucleation along the FM is expected due to thermal agitation. The temporal evolution of the temperature resulting from two current pulses is shown in Fig. 9.1(c), and the variation of the maximum temperature in the FM with the amplitude of the current pulse is shown in Fig. 9.1(d). The current distribution and the Joule heating effects considering the realistic thinfilm resistivities of the FM and HM layers was taken into account to study the magnetization dynamics in the following section.

9.3 Magnetization Dynamics

Once it has been verified that the current is almost uniform over the FM layer, we theoretically investigate the current-driven magnetization dynamics (CDMD). As the underlying physics responsible for the reversal mechanism is similar for the two geometries proposed in, [78] here we focus on S-shaped devices as depicted in Fig. 9.1(a). This geometry was intentionally designed to achieve switching purely dictated by the shape, then being independent of the current polarity. [78] The CDMD is governed by the Gilbert equation augmented by the Slonczewskii-like spin-orbit torque (SL-SOT) [19, 145]

$$\frac{d\mathbf{m}}{dt} = -\gamma_0 \mathbf{m} \times (\mathbf{H}_{eff} + \mathbf{H}_{th}) + \alpha \mathbf{m} \times \frac{d\mathbf{m}}{dt} - \gamma_0 \mathbf{H}_{SH}^0 \mathbf{m} \times (\mathbf{m} \times \boldsymbol{\sigma}) \tag{9.1}$$

where γ_0, α, and $\mathbf{m}(\mathbf{r}, t) = \mathbf{M}(\mathbf{r}, t)/M_s$ denote respectively the gyromagnetic ratio, the Gilbert damping constant, and the normalized local magnetization to the saturation value (M_s). H_eff is the deterministic effective field, which includes the exchange, the magnetostatic, the uniaxial anisotropy, and the DMI. H_th is the stochastic thermal field. [117] The last term in eq. (9.1) is the SL-SOT due to the spin Hall effect [12] $H_{SH}^0 = \frac{\hbar \theta_{SH} J(t)}{2\mu_0 |e| M_s t}$, $\hbar$ is the Planck constant, $|e|$ is the electric charge, μ_0 is the permeability of free space, t is the thickness of the FM layer, and θ_{SH} is the spin Hall angle. $J(t)$ is the magnitude of the density current $\mathbf{J} = J(t)\mathbf{u}_x$, and $\boldsymbol{\sigma} = \mathbf{u}_z \times \mathbf{u}_x$ is the unit vector of the spin current generated by the SHE in the HM, which is orthogonal to both the direction of the electric current ($\mathbf{u}_x$) and the perpendicular direction ($\mathbf{u}_z$). Typical parameters for a HM/FM/oxide multilayer with strong DMI are considered: [153] $M_s = 1100$kA/m, exchange constant $A = 15$pJ/m, uniaxial magnetocrystalline anisotropy constant $K_u = 1250$kJ/m^3, DMI parameter $D = -1.8$mJ/m^2, $\alpha = 0.5$, and $\theta_{SH} = 0.07$. The thickness of the Co layer is fixed to $t = 0.6$nm. The samples were discretized using a 2D grid of $4-$nm-wide cells. Micromagnetic simulations were performed with $Mumax^3$[122] using a time step of 1ps. Realistic analysis including disorder and thermal effects is performed, which indicates that these ingredients play a significant role in the dynamics. To simulate realistic samples a characteristic grain size of 5nm was considered. [153] The direction of the uniaxial anisotropy of each grain ($\mathbf{u}_K$) is mainly directed along the perpendicular direction (z-axis, $\mathbf{u}_z$) but with a small in-plane component, which is randomly generated over the grains. [153] The maximum percentage of the in-plane component of the uniaxial anisotropy unit vector is 5%. In what follows, the results were computed by taking into account the temperature dependence

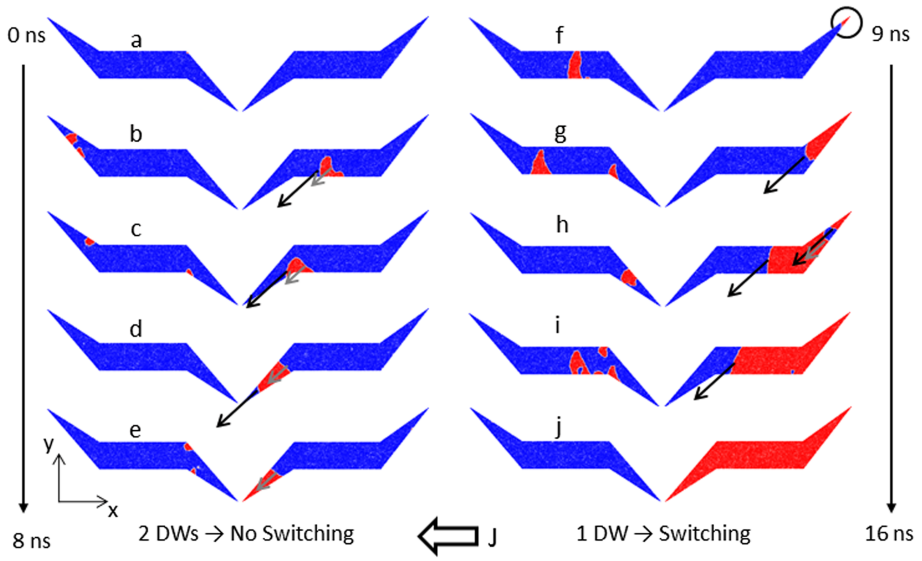

Figure 9.2: Micromagnetically computed inversion of S-shaped device for the up-up initial state. Blue and red represent up and down magnetization respectively. White arrow indicates the electric current direction in the HM. Black arrow indicates the faster up-down DW speed while the grey arrow indicates the slower down-up DW speed. Circle indicates the point where a single DW triggers the switching of the element. Images correspond to representative snapshots of the temporal evolution of the magnetization under a series of 8 current pulses with $\mathbf{J} = -3TA/m2$ and length of $t_p = 4$ns.

on the current density as described in the previous section using thin-film resistivities.

Fig. 9.2 illustrates the inversion mechanism of the "S-shaped" device starting from an initial state with both the left and the right elements magnetized along positive out-of-plane direction: up-up configuration. Here a train of 8 negative current pulses with $J = -3\text{TA/m}^2$ and length of $t_p = 4$ns is injected. The time between consecutive pulses is also 4ns. Blue and red represents up and down magnetization respectively. After some time, due to thermal fluctuations, reversed domains (magnetized down, red color) are randomly generated within the device, both in the left (Fig. 9.2f) and/or in the right (Fig. 9.2b) elements. For example, the semi-bubble nucleated in the central part of the left element (Figs. 9.2b and 9.2c) turns into two DWs when it reaches the spike as driven by the current (Fig. 9.2d). The left and the right DWs are up-down and down-up respectively. Due to the non collinear direction of the current and the spike axis (which forms an angle of 45° with **J**) these DWs are displaced with different velocities along the current direction. [78, 153] Black and grey arrows represent the fastest and slowest DW velocities. The up-down DW is firstly expelled from the bottom-left spike of the right element (Fig. 9.2e), and the down-up DW afterwards, the spike then recovering its initial state with uniform up magnetization. The domain generated in the left element undergoes a similar annihilation process (Fig. 9.2f). This type of reversed domain, being either a semi-bubble or flanked by two DWs, leads always to unsuccessful switching.

On the contrary, when a reversed domain appears exactly at the upper-right corner of the right element (marked with the circle in Fig. 9.2f), only a single DW is nucleated. This DW propagates along the current direction from right to left (Figs. 9.2f–j)

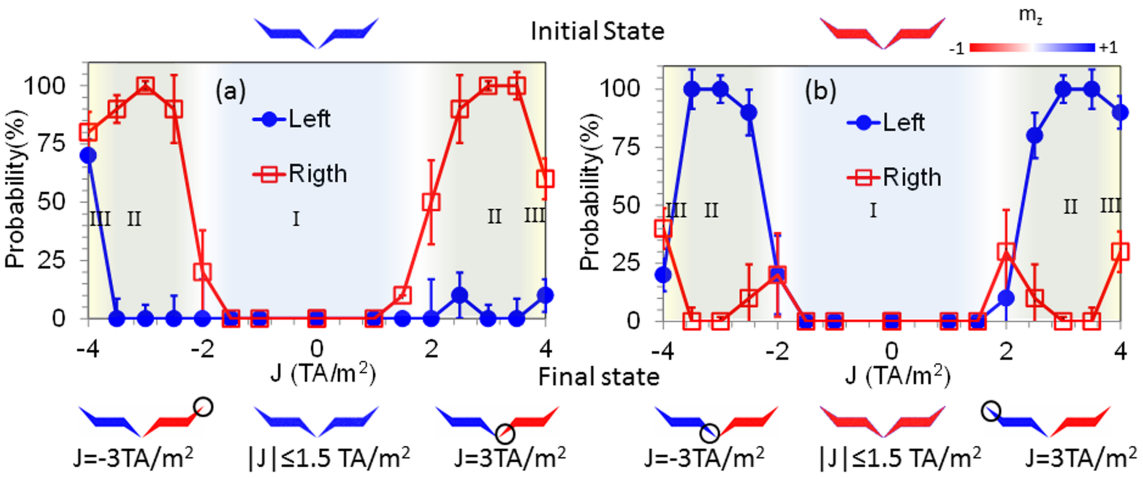

Figure 9.3: Switching probability for the left and right S-shaped elements as a function of the applied current starting from the up-up (a) and down-down (b) initial states. Full and open symbols correspond to the left and right elements respectively. I, II and III correspond to the no switching, switching and stochastic regions respectively. The open circle in the snapshots at the bottom indicate the corner where the nucleation of the DW which leads to the switching. Error bars indicate the standard deviation from the mean value computed from each realization and initial state.

successfully completing the switching of the right element (Fig. 9.2j). Note also that eventually the magnetization may reverse again within the already switched region (see the spurious blue domain in the right spike in Fig. 9.2h). However, due to the different speeds of the left and right DWs, such a spurious domain finally collapses (Fig. 9.2i). If the current polarity reverses, the final state will be the same, but now the nucleation corner which leads to the switching is the opposite one. [78] Our study, which indicates that the Joule heating is uniform in the FM elements of the device, predicts that the reversed domain is due to thermal fluctuations. This local inversion of the magnetization can occur with the same probability in any point of the two FM elements, but not necessarily at the spikes. Moreover, the switching mechanism, which is triggered by the thermally-assisted DW nucleation at the correct corner of the element and its subsequent current-driven propagation, is consistent with recent experimental observations. [78]

As the origin of the switching processes is the random inversion of a domain with opposite orientation than the original state due to the thermal fluctuations, it is necessary to carry out a statistical study of the process. Fig. 9.3 presents the switching probability (P_s) for the right and left S-shaped elements, considering the up-up (a) and down-down (b) initial configurations, and both current polarities of the pulse train. The probability was obtained by evaluating ten different realizations for each current density. Starting from the up-up state (Fig. 9.3(a)), the Joule heating is negligible for low currents ($|J| < 2\mathbf{TA/m^2}$), and therefore no P_s is achieved (see region I of Fig. 9.3(a)). For intermediate currents ($2.75\mathrm{TA/m^2} \lesssim |J| \lesssim 3.25\mathrm{TA/m^2}$), the switching of the right element is achieved with $P_s \approx 100\%$, while the left element maintains its initial state (region II in Fig. 9.3(a)). If the current is further increased ($|J| > 3.5\mathrm{TA/m^2}$), the device presents a stochastic behavior dominated by thermal agitation caused by the Joule heating (indicated as region III in Fig. 9.3(a)). This

restricts the current range of $P_s \approx 100\%$. A similar explanation describes the magnetization dynamics starting from the down-down configuration, but in this case the switching is triggered in the left element of the device (Fig. 9.3(b)). The open circles in the final snapshots of Fig. 9.3 indicate the corner where the switching is triggered.

9.4 Conclusions

The current-driven magnetization dynamics of patterned ferromagnetic devices proposed by Safeer et al.[78] has been studied by realistic micromagnetic simulations taking into account both the current distribution and Joule heating. Our results provide an explanation of this geometry-controlled switching mechanism, which consists on the proper DW nucleation and subsequent propagation. Reversed domains are assisted by thermal fluctuations anywhere in the FM elements of the device, but the switching is only achieved with $\approx 100\%$ of probability for a restricted range of current amplitudes, when a single DW is nucleated at the correct corner in agreement with recent experimental observations.

9.5 Acknowledgment

This work was supported by project WALL, FP7-PEOPLE-2013-ITN 608031 from the European Commission, project MAT2014-52477-C5-4-P from the Spanish government, and project SA282U14 from the Junta de Castilla y Leon.

Chapter 10

Chiral-triggered magnetization switching in patterned media*

The current triggered switching of patterned ferromagnetic elements over a heavy metal layer is analyzed in this work. A couple of symmetrically placed, but isolated, *U-shaped* elements, each one consisting of two oppositely tilted tapered spikes at the ends of a straight section, is theoretically studied by means of micromagnetic simulations. Our results indicate that the magnetization reversal processes deterministically start at a corner of the spikes selected by the direction of the current, as other experimental evidences claimed. Our study also reveals that the thermal agitation plays a supporting rather than a main role to promote complete switching. Temperature assists the local magnetization reversal at the corners, resulting in the nucleation of domain walls. This inversion is mainly due to the Slonczewskii-like torque exerted by the spin current associated with the spin Hall effect. When domain walls are nucleated, the angular dependence of the current-driven dynamics of those walls, already reported in the literature, determines whether the process results in either a complete or a frustrated switching attempt. Besides, our statistical study reflects that complete switching is only achieved within a narrow range of current pulse amplitudes.

*Adapted from Óscar Alejos, Eduardo Martínez, Víctor Raposo, Luis Sánchez-Tejerina, and María Auxiliadora Hernández-López. Chiral-triggered magnetization switching in patterned media. *Applied Physics Letters*, 110(7):072407, 2017. doi:10.1063/1.4976693.

The current-driven magnetization dynamics in multilayers where an ultra-thin ferromagnetic layer (FM) is sandwiched between a heavy metal (HM) and an oxide is being the matter of thorough research in the recent years. [7, 9, 11, 12, 17, 18, 21, 22] Some important phenomena arise from such a structural inversion asymmetry. The high perpendicular magnetocristalline anisotropy (PMA) along with a strong Dzyaloshinskii-Moriya interaction (DMI) present in these systems lead to the formation of chiral magnetization textures. [11, 12, 17, 21, 106, 155, 156] In particular, patterned FM elements have been experimentally observed to switch when a current flows through the HM layer, either in the presence [7, 9, 18, 22] or absence [78] of applied in-plane magnetic fields. Actually, the election of the amplitude, duration and number of current pulses made it possible in the latter case to control the magnetization with the only application of electrical currents. This current-driven magnetization switching (CDMS) would require combining the adequate design of the shape of the FM element with the correct application of the current in a certain direction. Thus, magnetization reversal would depend not only on the current magnitude but also on the relative orientation between the element and the current flow direction. This switching was studied for two different geometries consisting of two tilted tapered spikes at the ends of a straight section, either *S-shaped* or *U-shaped*, [78] as Figures 4a and 4b of the referenced work depict. A selective switching took place, and the domain walls (DWs) resulting from magnetization inversions in the spikes of the FM element were declared as a cornerstone of this process. Indeed, due to the tilt angle of about 45º of the spikes with respect to the central straight section, the two possible types of DWs in the FM layer, either *up-down* or *down-up* according to the magnetization transitions within them, acquire different speeds, causing the propagation of the DWs or their collapse depending on the current polarity. [78, 153] Thus, this unequal propagation of DWs might favor some switching attempts against others. However, the exact origin of the DWs nucleation processes and its selective characteristics still remain unclear. The only argument pointed out in this direction is that a higher density current through the tapered spikes, leading to a non-uniform Joule heating at their corners, might be responsible for triggering such magnetic reversal mechanisms. [78]

Since these results open the door to the development of high-performance memory or logic devices, a special effort must be made to completely understand the underlying physical mechanisms that originate them. As an additional contribution, this letter analyzes the CDMS of FM patterned elements over HM layers, focusing on the above-mentioned *U-shaped* geometries. [78] In this way, numerical simulations have been performed trying to mimic as much as possible realistic conditions. Our results reveal that the thermal agitation plays an aiding rather than a leading role to promote complete CDMS.

The Gilbert equation augmented by the spin-orbit torque (SOT) governs the current-driven magnetization dynamics (CDMD) of the proposed systems: [19, 145]

$$\frac{d\vec{\mathbf{m}}}{dt} = -\gamma_0 \vec{\mathbf{m}} \times \left(\vec{\mathbf{H}}_{eff} + \vec{\mathbf{H}}_{th} \right) + \alpha \vec{\mathbf{m}} \times \frac{d\vec{\mathbf{m}}}{dt} + \vec{\tau}_{SOT}, \tag{10.1}$$

γ_0, α, and $\vec{\mathbf{m}}\left(\vec{\mathbf{r}}, t\right) = \frac{\vec{\mathbf{M}}(\vec{\mathbf{r}},t)}{M_s}$ being respectively the gyromagnetic ratio, the Gilbert

damping constant, and the normalized local magnetization to its saturation value (M_s). $\vec{\mathbf{H}}_{eff}$ is the deterministic effective field, which includes the exchange, the magnetostatic, the uniaxial anisotropy, and the DMI, while $\vec{\mathbf{H}}_{th}$ accounts for the stochastic thermal field. [70, 117] $\vec{\tau}_{SOT}$ consists of the sum of two terms, a Slonczewskii-like torque $\vec{\tau}_{SL} = -\gamma_0 \vec{\mathbf{m}} \times \vec{\mathbf{H}}_{SL}$ and a field-like torque $\vec{\tau}_{FL} = -\gamma_0 \vec{\mathbf{m}} \times \vec{\mathbf{H}}_{FL}$, with $\vec{\mathbf{H}}_{SL} = H^0_{SL} \vec{\mathbf{m}} \times \vec{\sigma}$ and $\vec{\mathbf{H}}_{FL} = H^0_{FL} \vec{\sigma}$ being the respective effective fields. Here, $\vec{\sigma} = \vec{\mathbf{u}}_z \times \vec{\mathbf{u}}_x$ is the unit vector along the direction of the polarization of the spin current generated by the spin Hall effect (SHE) in the HM, being orthogonal to both the direction of the electric current $\vec{\mathbf{u}}_x$ and the vector $\vec{\mathbf{u}}_z$ standing for the normal to the HM-FM interface. Finally, $H^0_{SL} = \frac{\hbar \theta_{SH} J(t)}{2\mu_0 |e| M_s t_{FM}}$ determines the strength of the SHE, [12] where $\hbar$ is the Planck constant, $|e|$ is the electron charge, μ_0 is the vacuum permeability, t_{FM} is the thickness of the FM layer, and θ_{SH} is the spin Hall angle. $J(t)$ is the magnitude of the current density $\vec{\mathbf{J}}(t) = J(t)\, \vec{\mathbf{u}}_x$, while H^0_{FL} can be taken without lack of generality as proportional to H^0_{SL} by a certain factor k: $H^0_{FL} = k H^0_{SL}$.

So as to draw some light to the consequences derived from the application of the Gilbert equation, some results are to be presented here. The corresponding problem has been fully described elsewhere from both the experimental [78] and the theoretical [153] points of view, by means of micromagnetic (μMag) simulations in the latter case. Figures 10.1(a) to (d) present the CDMD in the case of a *quarter-of-a-star* shaped FM element independently patterned over a HM layer. The FM element possesses seven arms directed along regularly spaced directions from 0° to 90°. Every arm has its magnetization in the out-of-plane direction, so as to present two magnetic domains, either *up* ($m_z > 0$, white areas) or *down* ($m_z < 0$, black areas). DWs separate adjacent domains and all of them are initially located equidistant from the center of the star. A train of ten current pulses, 2-ns long, and 2-$\frac{\mathrm{TA}}{\mathrm{m}^2}$ amplitude, are injected through the HM layer along the direction defined by the vertical green arrow. Pulses are also 2ns spaced in time. The displacement of each DW depends on the magnetization transition, either *up-down* or *down-up*, and the relative angle between the current and the considered arm of the star. In order to adequately estimate the run distances as a function of this relative angle, Fig. 10.1(e) shows the DW displacement in a FM strip of comparable dimensions to any of the arms of the star, when a pulsed current of equal characteristics is injected at different angles ϕ_J. While the displacement of the *down-up* DW decreases monotonously with ϕ_J, the distance run by the *up-down* DW has a maximum at an angle $\phi_J \approx 30°$. This different behavior has been described in terms of the interaction between the DW inner magnetization orientation and the Slonczewskii-like torque associated with the SHE. [153]

These results are to be considered in the explanation of the current-triggered mechanisms of switching of patterned FM elements. The device under study consists of two elements symmetrically placed, that is, one *U-shaped* and one *inverse U-shaped* element, which will be referred to respectively as *upper* and *lower* elements, as those blue colored in the image of Fig. 10.2(a). It must be mentioned that the geometry of such elements was intentionally meant to promote switching depending on the current polarity and the initial magnetization state. [78] The multilayered system can be described as Pt(3)/Co(0.6)/AlO, over a Si(200) substrate, the numbers indicating the respective thicknesses in nm of the layers. The structure is depicted in the subfigure in Fig. 10.2 (the AlO layer is not shown). Dimensions of the layout are

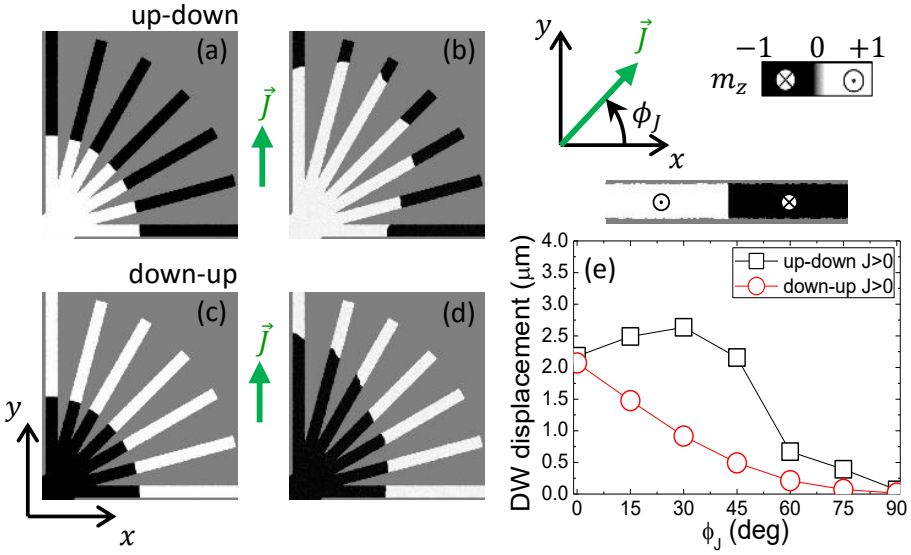

Fig. 10.1: Run distances for DWs in FM strips due to SOT. Pictures (a) to (d) mimic by means of μMag simulations the experimental evidences [78] (see text). The initial magnetization state is presented in (a)/(c) for the *up-down*/*down-up* configuration, while (b) and (d) represent the DWs displacements after the application of the current pulses in the direction given by the adjacent arrows. Besides, the subfigures in the upper-right corner present the direction of the injected current and an *up-down* DW in a FM strip. (e) An unequal dynamics for *up-down* and *down-up* DWs, also depending on the relative angle ϕ_J between the orientation of the FM strip and the direction of $\vec{\mathbf{J}}$ is revealed. [78, 153]

also given. μMag simulations of the device under study were carried out by means of Mumax. [122] Typical parameters for such a typical HM/FM/oxide multilayer with strong DMI are considered: [153] $M_s = 1100\frac{\text{kA}}{\text{m}}$, exchange constant $A = 15\frac{\text{pJ}}{\text{m}}$, uniaxial magnetocristalline anisotropy constant $K_u = 1250\frac{\text{KJ}}{\text{m}^3}$, DMI parameter $D = -1.8\frac{\text{mJ}}{\text{m}^2}$, $\alpha = 0.5$, $\theta_{SH} = 0.07$, and $k = 0.5$. The samples were discretized using a 2D grid of 4-nm wide cells, and simulations were performed using a time step of 1ps. Analysis including thermal effects and non-homogeneities characterized by a random granularity have been considered so as to mimic realistic samples and conditions. Five-nm size grains, whose direction of the uniaxial anisotropy ($\vec{\mathbf{u}}_K$) is mainly directed along the out-of-plane direction (z-axis, $\vec{\mathbf{u}}_z$), but with an in-plane component being randomly generated over the grains, with a maximum percentage of 5%, define such a granularity. [153]

Since Joule heating effects due to a non-uniform current distribution at the spikes were proposed [78] as the origin of the DW nucleation in these systems, a preliminary study of such a current and the Joule heating is a need. The study has been carried out by means of computational techniques as those detailed elsewhere. [86, 157] A 3D-structure of the multilayered system was numerically analyzed, where values of resistivity for the Co and Pt ultra-thin layers, $\rho_{\text{Co}} = 9.6 \cdot 10^{-7}\Omega \cdot \text{m}$ and $\rho_{\text{Pt}} = 2.7 \cdot 10^{-7}\Omega \cdot \text{m}$, were taken. A rather uniform current density is obtained in both the FM and the HM layer, although the current mainly flows through the latter, resulting in a uniform heating of the whole FM-HM ensemble (see the stationary temperature distribution in Fig. 10.2(b)). The quadratic dependence of the temperature on density current is plotted in Fig. 10.2(c), as obtained from simulations. The

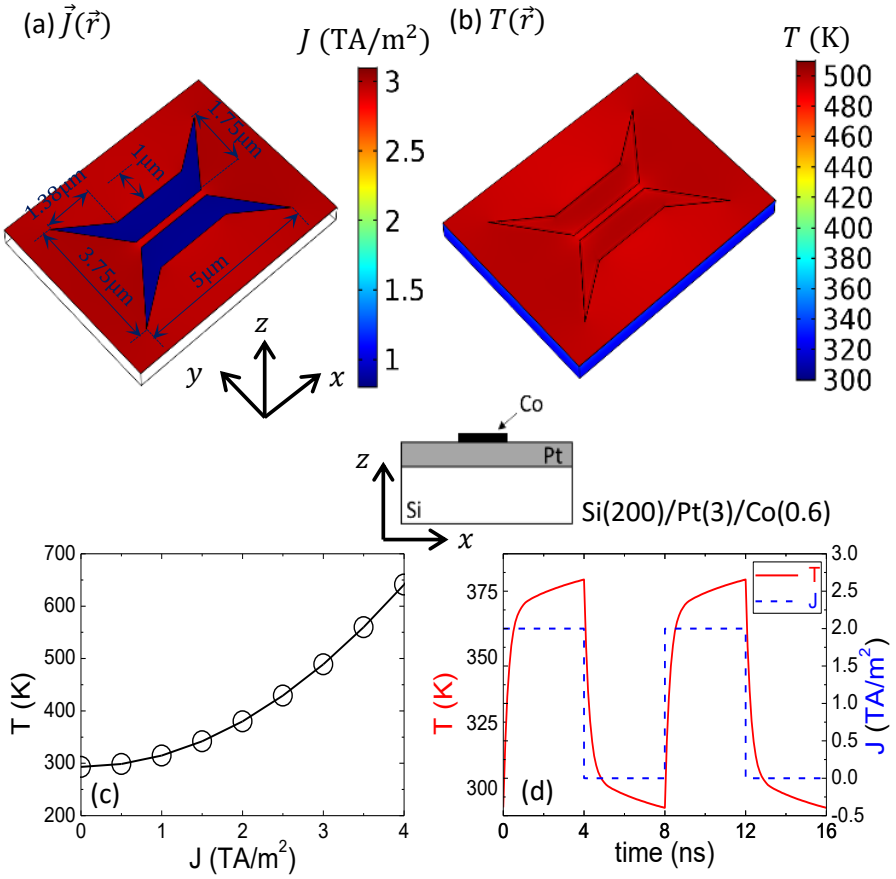

Fig. 10.2: Current distribution and Joule heating for the device under study. The geometry parameters of both *U-shaped* elements, together with the layer thicknesses are drawn. The thin-film resistivity model is considered (see text). (a) shows that current flows uniformly through both the FM and HM layers, although the current density is higher for the latter. This leads to an almost uniform heating of the HM-FM ensemble (b). The stationary temperature as a function of the current density is plotted in (c). This temperature is rapidly reached as soon as the current is injected and decreases to room temperature once the current ceases (d).

graph of Fig. 10.2(d) shows that a certain time constant defines the heating rate of the ensemble. Briefly, this thin-film resistivity approach results in uniform currents within the FM and HM layers, and consequently, a uniform Joule heating of the FM layer. Accordingly, a rather uniform probability of domain nucleation throughout the FM layer would be expected as due to the thermal agitation. However, the experimental evidences [78] reveal the existence of nucleation points for the DWs at the corners of the patterned elements.

To elucidate the origin of the current-triggered DW nucleation, the CDMD is now to be analyzed. This CDMD results in the reversal mechanisms for either the *U-shaped* elements depicted in Fig. 10.2.a or other patterned elements that share similar underlying physics. [78] In order to adequately incorporate the influence of the thermal agitation in the CDMD, the results were computed by considering the thin-film resistivity model described above.

The switching mechanisms are revealed in Fig. 10.3 by means of μMag simulations.

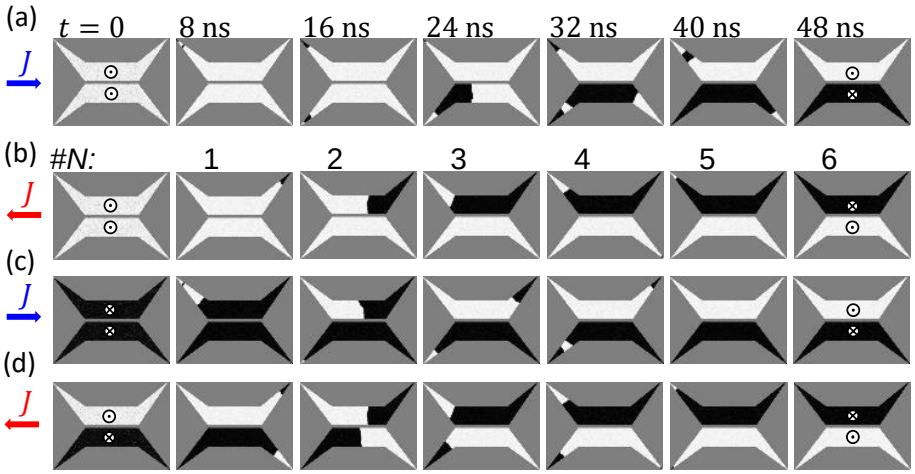

Fig. 10.3: Micromagnetically computed magnetization switching of couples of *U-shaped* and *inverse U-shaped* elements due to the injection of a train of current pulses along the direction that the arrows at the left indicate. Each row depicts several initial states ($t = 0$ column) of the upper and the lower element, either *up* for the white elements or *down* for the black elements, depending on the sign of the out-of-plane magnetization component. The ordinal $\#N$ accounts for the number of applied pulses, i.e, the simulation time. A total number of pulses $N = 8$, with amplitude $J = 3\frac{\mathrm{TA}}{\mathrm{m}^2}$ and duration $t_p = 4$ns were applied (only the first six pulses are shown). Magnetization reversal occurs at the corners determined by the current polarity. DWs appearing at these corners have unequal current-driven propagation, resulting in complete or frustrated magnetization switching processes.

Four rows of images are shown, each corresponding to the evolution of the out-of-plane component of the magnetization from a certain initial state, either *up* or *down*, after the injection of eight current pulses. The pulses are 4-ns long, and with different polarity, in the direction of the x-axis, the time between consecutive pulses being also of 4ns. The current amplitude has been fixed to $3\frac{\mathrm{TA}}{\mathrm{m}^2}$, and its polarity is depicted using a blue arrow for positive currents (directed along the positive x-axis), and red otherwise. The first row starts from an *up-up* configuration, and a positive current is applied. Reversed domains appear randomly at the left corners of both elements, the randomness bound to the thermal fluctuations, as it is the most evident after the second pulse. The corresponding DWs are then current-driven from left to right. However, the angular dependence of the current-driven DW dynamics [78, 153] leads to complete switching from *up* to *down* after the sixth pulse for the lower element and frustrated switching attempts for the upper element. What is meant by frustrated switching is any process of DW generation leading to spurious domains which collapse due to the different speeds of the limiting DWs. Contrarily, currents with the opposite polarity promote magnetization inversions at the right corners, resulting in complete switching of the upper element and no switching of the lower element (see Fig. 10.3(b)). The third row shows the case when the elements starts from a *down-down* configuration. The current polarity determines again the corners where magnetization inversion occurs, leading to a complete switching of the upper element and no final switching of the lower element, which is coherent with the results above. Finally, in order to confirm this coherence, the case when the upper element is initially in the *up* state, and the lower one in the *down* state, with a negative current is included as Fig. 10.3(d). In such a case, switching is complete for both elements, and is triggered from the right corners.

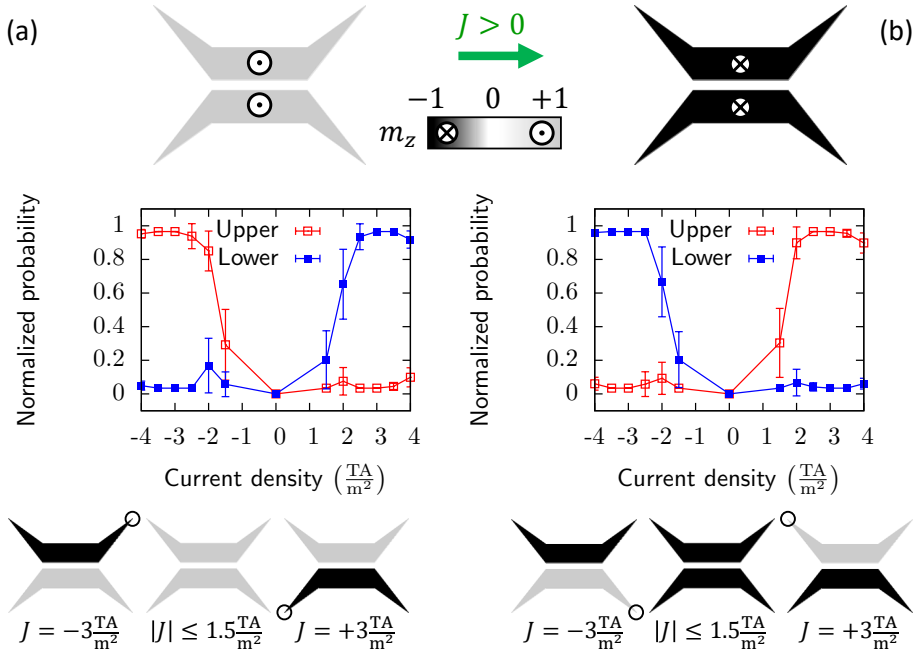

Fig. 10.4: Switching probabilities of couples of *U-shaped* and *inverse U-shaped* elements starting from either an (a) *up-up* or (b) *down-down* initial state. Open/full symbols correspond to the upper/lower element. Vertical error bars reflects the statistical standard deviation. Complete *up-to-down* switching for the upper/lower element is achieved for negative/positive currents. Conversely, complete *down-to-up* switching for the upper/lower element is achieved for positive/negative currents. No switching occurs otherwise. The open circle in the snapshots at the bottom indicate the corner where the nucleation of DWs leading to complete switching occurs, due to the current driven DW dynamics afterwards.

Since these switching mechanisms require the random DW nucleation at the corners of the spikes of the elements, and its subsequent current-driven propagation, a statistical study of the dependence of the completeness of the switching on the current amplitude must be performed. Fig. 10.4 shows the results drawn by the μMag simulations in the form of probability of switching as a function of the current amplitude for currents ranging from $-4\frac{TA}{m^2}$ to $4\frac{TA}{m^2}$, starting either from an (a) *up-up* configuration or a (b) *down-down* configuration. Results from other initial configurations have been also obtained, and no significant differences have been found. Those have been omitted in Fig. 10.4 for the sake of a clearer view of the plots in the graphs. Such probabilities have been calculated from the mean value of the out-of-plane component of the magnetization of each element at the end of the simulation ($< m_z >|_{t=64ns}$). The probability of switching is given approximately by $\frac{1 \pm < m_z > |_{t=64ns}}{2}$, where the sign $+/-$ determines *up-to-down*/*down-to-up* switching. Statistics have been carried out by considering 8 different realizations for each current density over a total of 5 granularity patterns of the elements. Completely complete/frustrated switching is achieved for absolute currents of the order of $3\frac{TA}{m^2}$, being the switching probability close to 1/0 with a rather low standard deviation. Note that switching probabilities as they have been defined cannot reach exactly the values 0 or 1, since thermal agitation prevents the magnetization of the FM elements from reaching the exact values $< m_z >= \pm 1$.

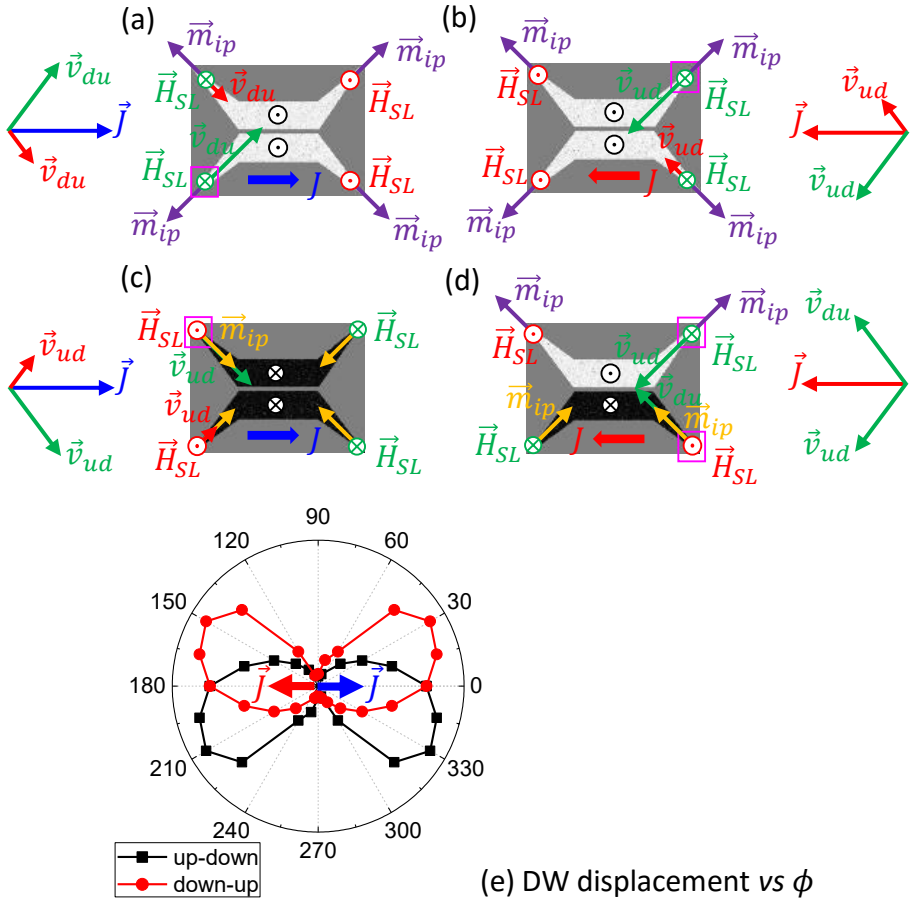

Fig. 10.5: Effect of the out-of-plane component of the Slonczewskii effective field due to the SHE on the magnetization at the corners of the spikes. The in-plane component of the magnetization determines the orientation of this field and so whether this effective field favors the destabilization of the magnetization and the nucleation of DWs. Each nucleated DW travels at a speed, either $\vec{\mathbf{v}}_{ud}$ or $\vec{\mathbf{v}}_{du}$, which can be estimated from the plots in (e). These plots present the DW displacement vs. its relative orientation ϕ with respect to $\vec{\mathbf{J}}$, as derived from the results in the graph in Fig. 10.1(e). Pink squares indicate for each initial state (*up/down*) and current polarity ($J > 0/J < 0$) the corners where the DWs responsible for complete switching attempts are nucleated.

The presented μMag results are fully consistent with recent experimental observations, [78] where the magnetization reversal processes were proved to deterministically start at certain corners of the FM elements, selected by the current polarity. This fact cannot be simply explained in terms of the Joule heating due to the current injection, since it has been shown in Fig. 10.2(b) that a uniform temperature of the FM layer is achieved. Temperature only assists the magnetization destabilization and the propagation of DWs. An additional ingredient must be given so as to explain the chiral-triggered character of this CDMS. At this point, the following argument can be proposed. The DMI present is indeed the responsible for the formation of chiral magnetization textures in these systems. In particular, boundary conditions (BCs) at the edges of the element require the existence of a certain in-plane component of the magnetization ($\vec{\mathbf{m}}_{ip}$) throughout them, [23] which points inwards/outwards for the *down/up* domains. The average $\vec{\mathbf{m}}_{ip}$ at the tapered spikes points along the direction defined by the tilting angle of the spikes, as shown in Figures 10.5(a) to (d),

while the corresponding average $\vec{\mathbf{m}}_{ip}$ at the straight sections points along the in-plane direction $\vec{\mathbf{u}}_y$ (not shown), perpendicular to $\vec{\mathbf{J}}$. The effective field associated with the Slonczewskii-like torque due to the SHE then possesses a foremost out-of-plane component $\vec{\mathbf{H}}_{SL}$ at the tapered spikes, i.e., where magnetization reversals take place, due to the component of $\vec{\mathbf{m}}_{ip}$ directed along the current flow. The magnitude of $\vec{\mathbf{H}}_{SL}$ depends then on the relative direction between the current flow and $\vec{\mathbf{m}}_{ip}$. For *up* domains, $\vec{\mathbf{H}}_{SL}$ favors the stabilization/destabilization of the element magnetization if the projection of $\vec{\mathbf{m}}_{ip}$ along $\vec{\mathbf{J}}$ is parallel/antiparallel, as the depicted vectors on the corners of Figures 10.5(a) and (b) determine. Conversely, $\vec{\mathbf{H}}_{SL}$ favors the stabilization/destabilization of the element magnetization if the projection of $\vec{\mathbf{m}}_{ip}$ along $\vec{\mathbf{J}}$ is antiparallel/parallel for *down* domains, as in Fig. 10.5(c). In summary, magnetization reversal processes take place at the left/right corners if the current flows from left to right/right to left, triggered by the resulting $\vec{\mathbf{H}}_{SL}$. After each magnetization reversal, the nucleated DW is driven by the current at a speed $\vec{\mathbf{v}}_{ud}/\vec{\mathbf{v}}_{du}$ for *up-down*/*down-up* DW transitions, as the plots in Fig. 10.5(e) reveal. In agreement with the experiments, [78] in particular with the discussion in Fig. 10.3(c) of the referenced work, such different DW speeds determine if the process lead to either a complete or a frustrated switching attempt.

In summary, the CDMS in independlently patterned FM elements on top of an extended HM has been evaluated by means of realistic μMag simulations, coupled to the heat dynamics over the full multilayer heterostructure. Our results indicate that Joule heating per se is not the responsible for DW nucleations at the spikes. Actually, DW nucleations are promoted by the Slonczewskii-like torque due to the SHE, being determined by the magnetization in-plane component, as imposed by the DMI BCs, and the current polarity. In agreement with recent experimental observations, the nucleated DWs depicts an angular dependence which determines the completeness of the switching.

We acknowledge the support by project WALL, FP7-PEOPLE-2013-ITN 608031 from the European Commission, project MAT2014-52477-C5-4-P from the Spanish government and project SA282U14 from the Junta de Castilla y León.

Part IV.
Current-driven domain wall motion in a ratchet ferromagnetic strip.

Chapter 11

Analysis of the current-driven domain wall motion in a ratchet ferromagnetic strip*

The dynamics of magnetic domain walls along ferromagnetic strips with spatially modulated perpendicular magnetic anisotropy is theoretically studied by means of micromagnetic simulations. Ferromagnetic layers with a periodic sawtooth profile of the anisotropy depict a well-defined set of energy minima where the walls are pinned in the absence of external stimuli, and favor the unidirectional propagation of domain walls. The performance of the current-driven domain wall motion along these ratchet-like systems is compared to the field-driven case. Our study indicates that the current-driven domain wall motion exhibits significant improvements with respect to the field-driven case in terms of bit shifting speed and storage density, and therefore, it is suggested for the development of novel devices. The feasibility of these current-driven ratchet devices is studied by means of realistic micromagnetic simulations and supported by a one-dimensional model updated to take into account the periodic sawthooth anisotropy profile. Finally, the current-driven domain wall motion is also evaluated in systems with a triangular modulation of the anisotropy designed to promote the bidirectional shifting of series of walls, a functionality that cannot be achieved by magnetic fields.

*Adapted from Luis Sánchez-Tejerina, Óscar Alejos, Víctor Raposo, and Eduardo Martínez. Current-driven domain wall motion along ferromagnetic strips with periodically-modulated perpendicular anisotropy. *Journal of Applied Physics*, 2018. doi:10.1063/1.5036601 (just accepted).

11.1 Introduction

The ability to propagate series of magnetic domain walls (DWs) along ferromagnetic strips is the basis of several proposed logic and memory devices [27, 28]. There are some requirements for successful DW-based memory devices, where the information is coded within the magnetic domains between DWs. Firstly, it is needed to nucleate (write operation) a magnetic domain and its DWs [161]. The nucleated or written domain (which acts as the data bit) should be efficiently shifted along the ferromagnetic strip to the location of the reading head. Therefore, other issue is to control the exact pinning positions where the DWs stop after propagation. Recent studies focused on multilayers with inversion structural asymmetry, where a ultrathin ferromagnetic layer (FM) is sandwiched between a heavy metal (HM) and an oxide (Ox) [8, 10–12, 21] have opened new promising ways of efficient DW motion. These systems exhibit a high perpendicular magnetic anisotropy (PMA), and the interfacial Dzyaloshinskii-Moriya interaction (DMI) [41] at the HM/FM interface makes DWs adopt a Néel configuration. These homochiral DWs are efficiently driven by the torque exerted by an injected electrical current through the HM, due to the spin Hall effect (SHE) [11, 12]. In contrast, an applied out-of-plane magnetic field drives adjacent DWs in exactly opposite directions; this is the main reason why the manipulation of DWs with electrical currents is so useful.

As mentioned, apart from the high efficient current-driven DW motion, the design of DW-based devices requires to develop an adequate pinning strategy to precisely control the DW positions along the device. In HM/FM/Ox multilayers, adjacent homochiral DWs experience magnetostatic interaction [145, 162, 163], which imposes a limit in the stored bit density. Moreover, under current pulses, these homochiral DWs can also depict inertia [164] which results in some after-effect DW motion once the current pulse is switched off. The introduction of notches along the strip was initially suggested to fix the DW positions [165]. However, these shape-induced effects were initially designed for systems with in-plane magnetization, while in systems with high PMA this effect is rather weak, and typically induces deformations of the DW [166]. For these reasons, some alternatives have been proposed, such as the control of the DW pinning (and DW nucleation) by means of a tailored PMA. These alternatives include the application of a voltage in an epitaxial magnetic tunnel junction [167] , or a strain-mediated coupling in piezoelectric/magnetostrictive bilayer structures [168]. The irradiation of the sample with heavy ions is another procedure [48, 79] which can produce an anisotropy landscape along the ferromagnetic strip.

The PMA is known to be reduced by irradiation with highly energetic ions, and therefore, the anisotropy can be controlled very locally at a scale of a few nanometers. Using different doses of local irradiation with heavy ions, Franken et al. [80] generated a sawtooth profile, where the local PMA anisotropy ($K_u = K_u(x)$) varies linearly from a minimum (K_u^-) to a maximum (K_u^+) over a distance d, and this tooth is repeated periodically along the ferromagnetic strip. This idea led to a new proposal for a magnetic memory, known as ratchet memory, which was studied under the field-driven regime. The periodic sawtooth PMA profile was intended to fix the DW positions and to establish one direction of bit shifting by avoiding backwards DW movement due to the applied field. As adjacent up-down ($\uparrow\downarrow$) and down-up ($\downarrow\uparrow$) DWs

move in opposite directions under a fixed out-of-plane field orientation, an alternate applied magnetic field (bipolar field pulse) is needed to promote the shifting of the DWs. Moreover, as one DW is driven by the field whereas the other one remains pinned for a fixed field polarity (either along the $+z$ or the $-z$ direction), two teeth are needed to store a single bit of information, a fact which imposes the minimum bit size $b_s = 2d$. In the present work we go deeper into this conception and study theoretically for the first time the DW dynamics in a ratchet memory device by means of unipolar current pulses. Using micromagnetic simulations (μM), we evaluate the dynamics of DWs under perfect and realistic conditions to explore the feasibility of the proposed current-driven ratchet device. Additionally, the one-dimensional model (1DM) is also updated here to include the effective field accounting for the periodic anisotropy landscape. This 1DM is used to clarify some aspects of the DW dynamics and will be of help in the further development of the proposed devices. We will show that the current-driven mechanism ensures the proper bit shifting along the FM strip. Indeed, it constitutes a much more interesting alternative from the technological point of view to the field-driven basis, since the current promotes the dynamics of all DWs in the same direction. Moreover, the current-driven ratchet also contributes to reduce bit sizes (increasing bit densities) and to speed up the bit shifting. Besides, we also suggest other systems where the PMA is periodically modulated to achieve the bidirectional DW motion, and theoretically analyze the current-driven DW back and forth shifting along them.

The present manuscript is structured as follows: Sec. 11.2 presents the system under study along the details of the Micromagnetic model (μM) and the one-dimensional model (1DM) developed to describe the DW dynamics in systems with periodically modulated PMA. Sec. 11.3.1 reviews the main features of the field-driven ratchet and unveils its handicaps when dealing with bit densities and bit shifting times as compared to the current-driven case (Sec. 11.3.2). The current-driven DW shifting along a ratchet strip studied in Sec. 11.4. Full μM simulations and 1DM results are presented for perfect strips, both at zero and at finite temperature. Besides, the effect of disorder is evaluated to provide a more realistic description. Sec. 11.5 sketches how to extend the exposed ideas to implement a bi-directional device. Finally, the main conclusions are discussed in Sec. 11.6.

11.2 Geometry and Models

A ratchet FM strip with high PMA sandwiched between a HM and an Ox, as schematically depicted in Fig. 11.1, is considered. The left graph in Fig. 11.1 depicts four periods of the sawtooth profile of anisotropy ($K_u = K_u(x)$) along the longitudinal axis of the FM strip (x-axis). Within each tooth of the sawtooth the PMA constant increases linearly from K_u^- to K_u^+ over a distance d, which defines the periodicity of the sawtooth anisotropy profile along the x-axis. Each region of length d can pin one DW, which in the absence of external stimuli locates approximately at any of the points where the anisotropy energy is a minimum. The word *"approximately"* accounts for the finite width of the DW and the abrupt drop of the anisotropy from the maximum (K_u^+) to the minimum (K_u^-) for the ratchet case.

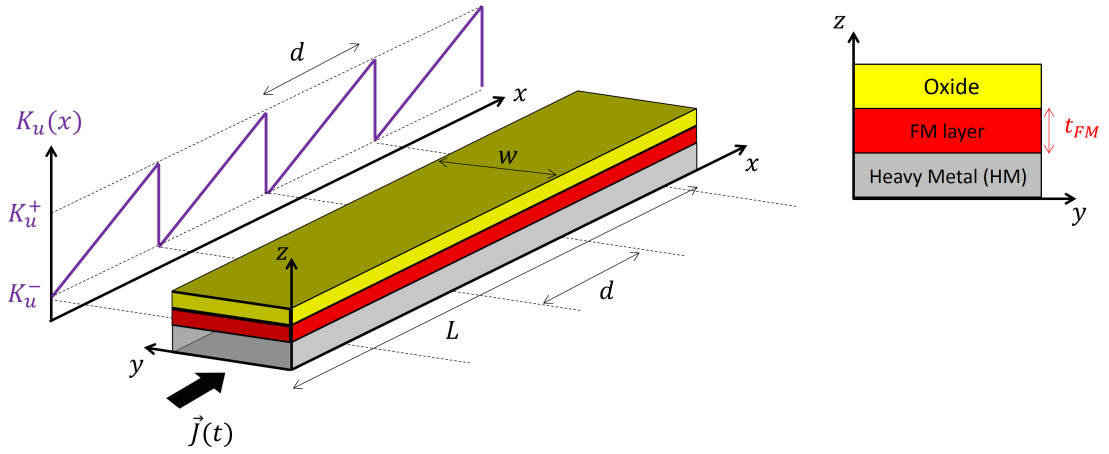

Fig. 11.1: Description of the system under study. A stack consisting of a FM strip of width w and thickness t_FM sandwiched between a HM and an Oxide is considered. The FM layer exhibits high PMA, but such an anisotropy is tailored to present a sawtooth profile along the longitudinal direction (x). This ratchet profile is defined by two extreme values K_u^+ and K_u^-, and its periodicity is given by a distance d. All minima define subsequent equilibrium positions where DWs get pinned.

11.2.1 Micromagnetic model (μM)

The temporal evolution of the normalized magnetization $\vec{m}(\vec{r},t) = \vec{M}/M_s$ is described by the Landau-Lifshitz-Gilbert (LLG) equation augmented by the spin-orbit torques [10, 12, 16, 19] (SOT) and thermal fluctuations [114]:

$$\frac{d\vec{m}}{dt} = -\gamma_0 \vec{m} \times \left(\vec{H}_{eff} + \vec{H}_{th}\right) + \alpha \vec{m} \times \frac{d\vec{m}}{dt} + \vec{\tau}_{SO} \tag{11.1}$$

where γ_0 and α are the gyromagnetic ratio and the damping parameter respectively. $\vec{H}_{eff}$ is the effective field, which includes the exchange, the perpendicular magnetic anisotropy, the magnetostatic and the Zeeman interactions, along with the DMI [41]. For the field-driven case, the applied field is pointing along the out-of-plane direction, $\vec{B}_{ext} = B_e(t)\,\vec{u}_z$, with $B_e(t) = \mu_0 H_e(t)$. $\vec{\tau}_{SO}$ represents the spin-orbit torque (SOT), which in general includes two contributions: $\vec{\tau}_{SO} = \vec{\tau}_{SL} + \vec{\tau}_{FL}$. The first one, $\vec{\tau}_{SL}$, is the Slonczewski-like (or damping-like) SOT term, which is given by $\vec{\tau}_{SL} = -\gamma_0 \vec{m} \times \vec{H}_{SL}$ where $\vec{H}_{SL} = H_{SL}^0 (\vec{\sigma} \times \vec{m})$ is the Slonczewski-like effective field [12, 14]. Here, $\vec{\sigma} = \vec{u}_z \times \vec{u}_J$ is the unit vector along the direction of the polarization of the spin current generated by the spin Hall effect (SHE) [9, 50] in the HM, which is orthogonal to both the direction of the electric current $\vec{u}_J = \vec{u}_x$ and the vector $\vec{u}_z$ standing for the normal to the HM/FM interface. $H_{SL}^0 = \frac{\hbar \theta_{SH} J_a(t)}{2\mu_0 e M_s t_{FM}}$ determines the strength of the SHE [14], where $\hbar$ is the Planck constant, $e < 0$ is the electron charge, μ_0 is the vacuum permeability, θ_{SH} is the spin Hall angle, and $J_a(t)$ is the magnitude of the current density $\vec{J}(t) = J_a(t)\,\vec{u}_x$ injected through the HM. The second contribution to the SOT ($\vec{\tau}_{FL}$) is the Field-like SOT, which is expressed as $\vec{\tau}_{FL} = -\gamma_0 \vec{m} \times \vec{H}_{FL}$ with $\vec{H}_{FL}$ being the corresponding effective field given by $\vec{H}_{FL} = H_{FL}\vec{\sigma}$. The magnitude of the Field-like SOT effective field is $H_{FL}^0 = kH_{SL}^0$, where the factor k parameterizes H_{FL}^0 in terms of the Slonczewski-like effective field H_{SL}^0. $\vec{H}_{th}$ is the thermal field included as a Gaussian-distributed random field [113, 114].

The study of the motion of a DW in such a system requires solving this equation by means of full micromagnetic simulations (μM). In order to carry out those simulations, typical material parameters of HM/FM/Ox multilayers commonly found in the literature [15, 16, 41, 72] have been considered: saturation magnetization $M_s = 1.1$MA/m, exchange constant $A_{ex} = 16$pJ/m and a Gilbert damping parameter $\alpha = 0.5$. The values $K_u^+ = 1.27\text{MJ/m}^3$, $K_u^- = 1.0\text{MJ/m}^3$ and $d = 128$nm define the anisotropy landscape. The anisotropy variation has been chosen to be compatible with the reported in recent experimental works [79]. Except otherwise indicated, a uniform DMI parameter $D = 1\text{mJ/m}^2$ has been considered [17]. This value is sufficiently high to induce the formation of homochiral Néel DWs and, therefore, to allow efficient current-driven DW movement by means of the SHE [12]. The considered spin Hall angle is $\theta_{SH} = 0.1$. The adopted magnetic parameters mimic a multilayer of Pt(3)/Co(0.6)/AlO(2) where the corresponding thicknesses between brackets are in given in nm [15, 16, 41, 72]. Although it is now well established that the main driving force on the DW in theses systems comes from the Slonczewski-like SOT term, some additional simulations were carried out considering also a finite Field-like SOT contribution, which was equal in magnitude to the Slonczewski-like SOT ($|k| = 1$). It was verified that this Field-like SOT ($|k| = 1$) does not significantly modify the results obtained in the absence of Field-Like SOT ($k = 0$), and therefore, the presented results were computed assuming $k = 0$. Indeed, the main driving force on the DW is the Slonczewski-like SOT. A FM strip with a cross section $w \times t_{FM} = 128\text{nm} \times 0.6\text{nm}$ has been analyzed. μM simulations have been performed with MuMax3 package [122] using a time 1ps. The in-plane side of the computational cells is $\Delta x = \Delta y = 1$nm. Except the contrary is said, the presented results were obtained at zero temperature. Simulations at room temperature were performed with a fixed time step $\Delta t = 0.1$ps. Several tests were performed with reduced cell sizes and time steps to assess the numerical validity of the presented results.

Part of the simulations was carried out by considering perfect samples, without imperfections nor defects. Additionally, other parts were computed under realistic conditions (see Sec. 11.4.3). In order to take into account the effects of disorder due to imperfections and defects in a realistic way, we assume that the easy axis anisotropy direction ($\vec{u}_K = \vec{u}_K(\vec{r}_G)$) is distributed among a length scale defined by a grain size [164]. The average size of the grains is 10nm. Despite the fact that the direction of the uniaxial anisotropy of each grain is mainly directed along the perpendicular direction (z-axis), a small in-plane component lower than 5% is randomly generated over the grains. The inter-grain exchange stiffness parameters was assumed to be equal to the exchange parameter A_{ex}. It was verified that a 25% reduction of the inter-grain exchange constant does not modify the presented results. Besides, a random edge roughness pattern is considered along both edges of the FM strip with a characteristic size of 4nm. Although other ways to account for imperfections could be adopted [87], we selected this one based on previous studies, which properly describe other experimental observations [163, 164].

11.2.2 One dimensional model (1DM)

The one dimensional model (1DM) assumes that the DW profile can be described by the Bloch's ansatz [124], $\theta(x,t) = 2\arctan\left[\exp\left(Q\frac{x-q(t)}{\Delta}\right)\right]$, where θ is the angle of magnetization with respect to the out-of-plane direction, z-axis, Δ is the DW width and $Q = \pm 1$ correspond to the up-down ($\uparrow\downarrow$, $Q = +1$,) and down-up ($\downarrow\uparrow$, $Q = -1$) DW configurations. The DW dynamics can be described by means of the DW position (q) along the strip axis (x-axis), and the internal DW angle (Φ), which is defined with respect to the $+x$-axis. The 1DM has been developed by several authors to account for and describe the field-driven and current-driven DW dynamics in different systems [41, 72, 145]. Here we have developed it to analyze the DW dynamics in systems depicting a modulated profile of the perpendicular magnetic anisotropy (PMA) along the strip axis, $K_u = K_u(x)$. In general, the resulting 1DM equations from Eq. (11.1) can be expressed as

$$\alpha\frac{\dot{q}}{\Delta} + Q\dot{\Phi} = -\frac{\gamma_0}{2\mu_0 M_s}\frac{\partial\sigma}{\partial q} + \gamma_0 Q H_{th} + \gamma_0 Q\frac{\pi}{2}H_{SH}\cos\Phi \tag{11.2}$$

$$Q\frac{\dot{q}}{\Delta} - \alpha\dot{\Phi} = \frac{\gamma_0}{2\mu_0 M_s}\frac{\partial\sigma}{\partial\varphi} - \gamma_0\frac{\pi}{2}H_{FL}\cos\Phi \tag{11.3}$$

where the top dot notation represents the time derivative ($\dot{q} \equiv \frac{dq}{dt}$). The term $H_{SH} \equiv H_{SL}^0 = \frac{\hbar\theta_{SH}J_a(t)}{2\mu_0 e M_s t_{FM}}$ is the Slonczewskii-like term associated to the SHE, and $H_{FL} = kH_{SL}$ is the Field-like effective field. Thermal fluctuations are accounted by the thermal term $H_{th}(t)$. σ is the total areal energy density [41] which results from the integration of the volume energy density ω over the strip axis, $\sigma = \int_{-\infty}^{\infty}\omega dx$, and it includes the same interactions as the effective field $\vec{H}_{eff}$ in Eq. (11.1): exchange, magnetostatic, DMI, PMA and interaction with an external field.

$$\begin{aligned}\sigma = \frac{2A_{ex}}{\Delta} + \Delta\mu_0 M_s^2\left(N_x\cos^2\Phi + N_y\sin^2\Phi - N_z\right) + \\ + Q\pi D\cos\Phi - 2Q\mu_0 M_s H_z q + \sigma_{PMA}\end{aligned} \tag{11.4}$$

where N_x, N_y, N_z are the magnetostatic factors, and $\sigma_{PMA} = \int_{-\infty}^{\infty}\omega_{PMA}dx$ is the areal energy density due to the PMA, with $\omega_{PMA} = K_u(x)\sin^2\theta(x)$. As here we are interested in strips with modulated PMA along their axis, $K_u = K_u(x)$, this term deserves a particular treatment. Let us initially consider a general periodic PMA profile where K_u increases linearly from K_u^- to K_u^+ over a distance d_1, and after that it decreases linearly from K_u^+ to K_u^- over a distance d_2, with $d = d_1 + d_2$ being the period of the PMA profile. This can be expressed as

$$K_u(x) = \begin{cases} K_u^- + \frac{K_u^+ - K_u^-}{d_1}\left(x - \lfloor\frac{x}{d}\rfloor d\right), & 0 \leqslant \left(x - \lfloor\frac{x}{d}\rfloor d\right) \leqslant d_1 \\ K_u^+ - \frac{K_u^+ - K_u^-}{d_2}\left(x - \lfloor\frac{x}{d}\rfloor d - d_1\right), & d_1 \leqslant \left(x - \lfloor\frac{x}{d}\rfloor d\right) \leqslant d \end{cases} \tag{11.5}$$

where $\lfloor\frac{x}{d}\rfloor$ represents the integer part of $\frac{x}{d}$. Note that here we are interested in strips where the DW width is significantly smaller than the PMA period ($\Delta \ll d$). Under this circumstance and after some algebra, the PMA areal density $\sigma_{PMA} = \int_{-\infty}^{\infty}\omega_{PMA}dx$ can be expressed as

$$\sigma_{PMA} = 2\Delta K_u^- + \\ + \left(K_u^+ - K_u^-\right) \sum_{n:-1}^{+1} \left[\frac{\Delta^2}{d_1} \log \left(\frac{\cosh \frac{d}{\Delta} a_n}{\cosh \frac{d}{\Delta} \left(a_n - \frac{d_1}{d}\right)} \right) + \frac{\Delta^2}{d_2} \log \left(\frac{\cosh \frac{d}{\Delta} a_n}{\cosh \frac{d}{\Delta} \left(a_n - \frac{d_1}{d}\right)} \right) \right] \tag{11.6}$$

where $a_n = \{\frac{q}{d}\} + n$, with the braces $\{\frac{q}{d}\}$ indicating the fractional part of $\frac{q}{d}$, and $n : -1, 0, +1$. Therefore,

$$\frac{1}{2\mu_0 M_s} \frac{\partial \sigma_{PMA}}{\partial q} \equiv H_{PMA}(q) = H_{PMA}^0 r(q) \tag{11.7}$$

where $H_{PMA}(q)$ represents the effective field due to the periodic PMA profile, with $H_{PMA}^0 = \frac{\left(K_u^+ - K_u^-\right)}{2\mu_0 M_S}$, and

$$r(q) = \sum_{n:-1}^{1} \Big[\begin{array}{l} \frac{\Delta}{d_1} \left(\tanh \frac{d}{\Delta} a_n - \tanh \frac{d}{\Delta} \left(a_n - \frac{d_1}{d}\right) \right) + \\ \frac{\Delta}{d_2} \left(\tanh \frac{d}{\Delta} \left(a_n - 1\right) - \tanh \frac{d}{\Delta} \left(a_n - \frac{d_1}{d}\right) \right) \Big] \end{array} \tag{11.8}$$

The general PMA profile $K_u = K_u(x)$ (Eq. (11.5)), and the corresponding PMA $r(q)$ function (Eq. (11.7)-(11.8)) are represented in Fig. 11.2(a) for $d_1 = 2d_2$ and $K_u^- = 1\text{MJ/m}^3$ and $K_u^+ = 1.27\text{MJ/m}^3$. This effective field $H_{PMA}(q) = H_{PMA}^0 r(q)$ drives the DW to the closest accessible energy minima in the absence of driving force: a DW located between $0 \leqslant q \leqslant d_1$ is pushed back towards $q \approx 0$ by a negative $H_{PMA}(q)$, whereas a DW between $d_1 \leqslant q \leqslant d_1 + d_2$ is forced towards $q \approx d_1 + d_2$ by a positive $H_{PMA}(q)$ (see bottom graph in Fig.11.2(a)). The magnitude of this out-of-plane PMA effective field is determined by the slope of the local PMA parameter $K_u(x) = K_u(q)$.

The ratchet case, where K_u periodically increases linearly from K_u^- to K_u^+ over a distance d (Fig. 11.2(b)), can be also obtained from Eq. (11.5) with $d = d_1$ and $d_2 = 0$. The corresponding PMA $r(q)$ function (Eq. (11.8)) is shown in the bottom graph of Fig. 11.2(b). As it can be easily understood, a DW at an intermediate location $0 \leqslant q \leqslant d$ is always forced backwards to $q \approx 0$ by the corresponding PMA effective field, $H_{PMA}(q) = H_{PMA}^0 r(q)$.

By substituting Eq. (11.4) and (11.6) in Eqs. (11.2) and (11.3) the 1DM equations can be finally expressed as:

$$\dot{q} = \frac{\gamma_0 \Delta}{1 + \alpha^2} \left[Q\Omega_A + \alpha \Omega_B \right] \tag{11.9}$$

$$\dot{\Phi} = \frac{\gamma_0}{1 + \alpha^2} \left[-\alpha \Omega_A + Q\Omega_B \right] \tag{11.10}$$

where

$$\Omega_A = Q\frac{\pi}{2} H_D \sin\Phi - \frac{H_k}{2} \sin(2\Phi) - \frac{\pi}{2} H_{FL} \cos\Phi \tag{11.11}$$

$$\Omega_B = -\frac{\pi}{2} H_{SL} \cos\Phi + QH_z + H_{th}(t) + H_{PMA}(q) \tag{11.12}$$

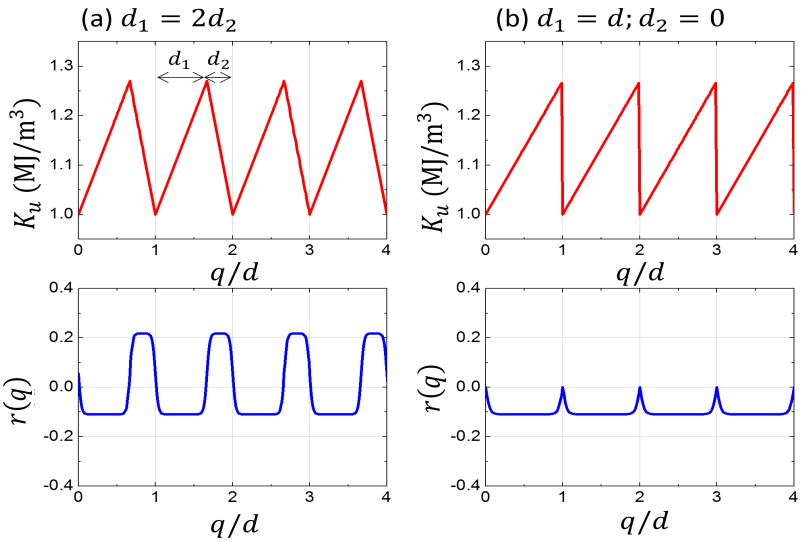

Fig. 11.2: Periodic anisotropy profile $K_u = K_u(x)$ and corresponding local pinning PMA field $r(q) \equiv H_{PMA}(q)/H^0_{PMA}$ as function of the DW position q. The period of the anisotropy profile is $d = d_1 + d_2$. (a) General case with $d_1 > d_2$. (b) Ratchet case with period $d = d_1$ and $d_2 = 0$. In both cases $K_u^- = 1\text{MJ/m}^3$ and $K_u^+ = 1.27\text{MJ/m}^3$.

$H_D = \frac{D}{\mu_0 M_s \Delta}$ is the DMI effective field [12, 14, 41], where Δ is the DW width which was assumed to be constant ($\Delta = \sqrt{\frac{A}{K_{eff}}}$ where $K_{eff} = \tilde{K}_u - \frac{1}{2}\mu_0 M_s^2$, with $\tilde{K}_u = (K_u^+ + K_u^-)/2$). $H_k = M_s(N_x - N_y) \approx M_s N_x$ is the magnetostatic shape anisotropy field, where $N_x = \frac{t_{FM}\log(2)}{\pi\Delta}$ is the magnetostatic factor [149]. Eqs. (11.9)-(11.10) are solved numerically using a Runge-Kutta scheme.

11.3 Ratchet memory: field-driven vs current-driven DW shifting.

11.3.1 Field-driven case

Before focusing our attention to the current-driven DW along a ratchet device, here we review the main features of the field-driven case, which was initially suggested by Franken et al. [80] to develop a magnetic memory device based in the unidirectional motion of trains of DWs along a ratchet strip. A periodic anisotropy sawtooth profile given by Eq. (11.6) with $d = d_1$ and $d_2 = 0$ (ratchet PMA profile) is considered to study the DW dynamics by means of μM simulations. The field-driven case requires bipolar pulses to displace trains of DWs along the same strip because up-down ($\uparrow\downarrow$) and down-up ($\downarrow\uparrow$) DWs are driven in opposite directions by the same field pulse. This fact is shown in the example depicted in Fig. 11.3(b), where three central magnetic domains ($\uparrow\downarrow\uparrow$: 101, up/down magnetized domains represent 1/0 bits respectively) are separated by down-up ($\downarrow\uparrow$) and up-down ($\uparrow\downarrow$) DWs, which are initially located at their equilibrium positions close to the minimum the sawtooth profile (K_u^-). Each domain extends over a distance equivalent to the length of two slopes of the PMA profile, the bit size being $b_s = 2d$ in this case. Note that down-up DWs are driven to the right ($x > 0$ direction) by the negative field-pulse ($B_e(t) < 0$ for $0 < t < 2$ns), whereas up-down DWs remain trapped at their initial locations. Indeed, the strength

of the applied field is not sufficiently intense to promote their movement towards the left due to the high energy barrier associated with the sawtooth anisotropy profile. A second positive field pulse ($B_e\,(t) > 0$ for 2ns $< t <$ 4ns) is needed to displace up-down DWs along the positive x-axis afterwards (see snapshots for $t \geqslant$ 2ns in Fig. 11.3(b)), whereas down-up DWs remain trapped during this second pulse. In this case, where each bit extends over a distance $b_s = 2d$, the bipolar field pulse shown in Fig. 11.3(b) drives the sequence of bits (↑↓↑: 101) a single tooth (d).

In order to illustrate the limitations of the field-driven case in terms of bit density, an analogous study to that shown in Fig. 11.3(b) is now carried out, but reducing the initial distance between the adjacent DWs to $b_s = d$. The corresponding snapshots shown in Fig. 11.3(c) indicate that down-up DWs are initially displaced towards positive x-values, whereas up-down DWs remain trapped at their initial locations for $0 < t <$ 2ns, i.e., when the out-of-plane field is negative ($B_e < 0$). Down-up and up-down DWs repel each other due to the DMI [163] and therefore, they do not annihilate. When the field switches to the positive polarity ($B_e > 0$, for $t >$ 2ns), down-up DWs move back to their initial locations whereas up-down DWs jump to the adjacent energy minima. As a result, the initially coded information is perturbed after $t =$ 2ns. Note that the right up domain has increased its length ($2d$) with respect to the initial state (d). Therefore, the proper operation of this field-driven device requires a minimum bit size equal to $2d$, where d is the period of the anisotropy profile. Moreover, a complete bit shifting requires a total time given by the duration of the bipolar field pulse. Next section demonstrates that the current-driven mechanism only requires one characteristic length d to store one bit, whereas the unidirectional bit shifting can be promoted by single unipolar current pulses.

11.3.2 Current-driven case

Let us now evaluate the current-driven DW motion in the same ratchet strip as in Fig. 11.3. A single unipolar current pulse with amplitude $J_a = 0.8\text{TA/m}^2$ and duration 2ns is applied (see Fig. 11.4(a)). An example of the current-driven mechanism is displayed in Fig. 11.4(b). As in the previous field-driven case of Fig. 11.3(b), three central domains (↑↓↑: 101) are separated by down-up (↓↑) and up-down (↑↓) DWs, which are initially at their equilibrium positions and at a distance equal to two characteristic lengths d (bite size is $b_s = 2d$). Every DW is moved in the same $x > 0$ direction when a positive $J_a > 0$ pulse is applied, and therefore a current in the opposite direction is not required. Indeed, the DWs are displaced to the subsequent equilibrium position of the anisotropy profile. Moreover, the coherent DWs displacement can be exploited to reduce the bit size to $b_s = d$, as Fig.11.4(c) shows. Contrary to the case field-driven case depicted in Fig. 11.3(c), now the coded bits (↑↓↑: 101) within the domains are preserved after the application of a single current pulse. Note also that even in the case of $b_s = 2d$ (Fig. 11.4(b)), the current-driven ratchet requires less time to promote the unidirectional bit shifting as compared to the field-driven case (Fig. 11.3(b)).

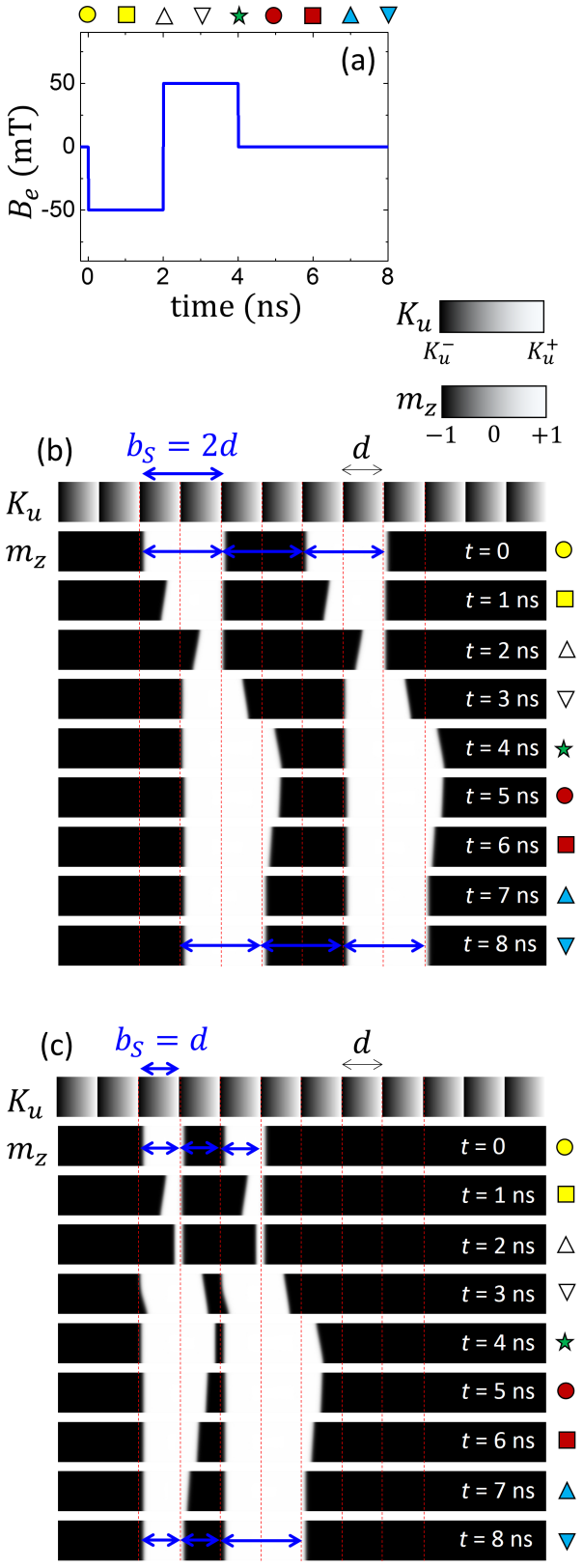

Fig. 11.3: Micromagnetic results of the field-driven DW motion along a ratchet strip. (a) shows the bipolar field pulse needed to shift the bit along the positive direction of the x-axis. The amplitude of the bipolar field pulse is $B_e = 50$mT, and it is negative during the first 2ns and positive from 2ns to 4ns. The other two panels depict transient magnetization snapshots of the bit shifting of two bits of size (b) $b_s = 2d$ and (c) $b_s = d$ with $d = 128$nm. Materials parameters are those given in Sec. 11.2. Results were obtained at zero temperature.

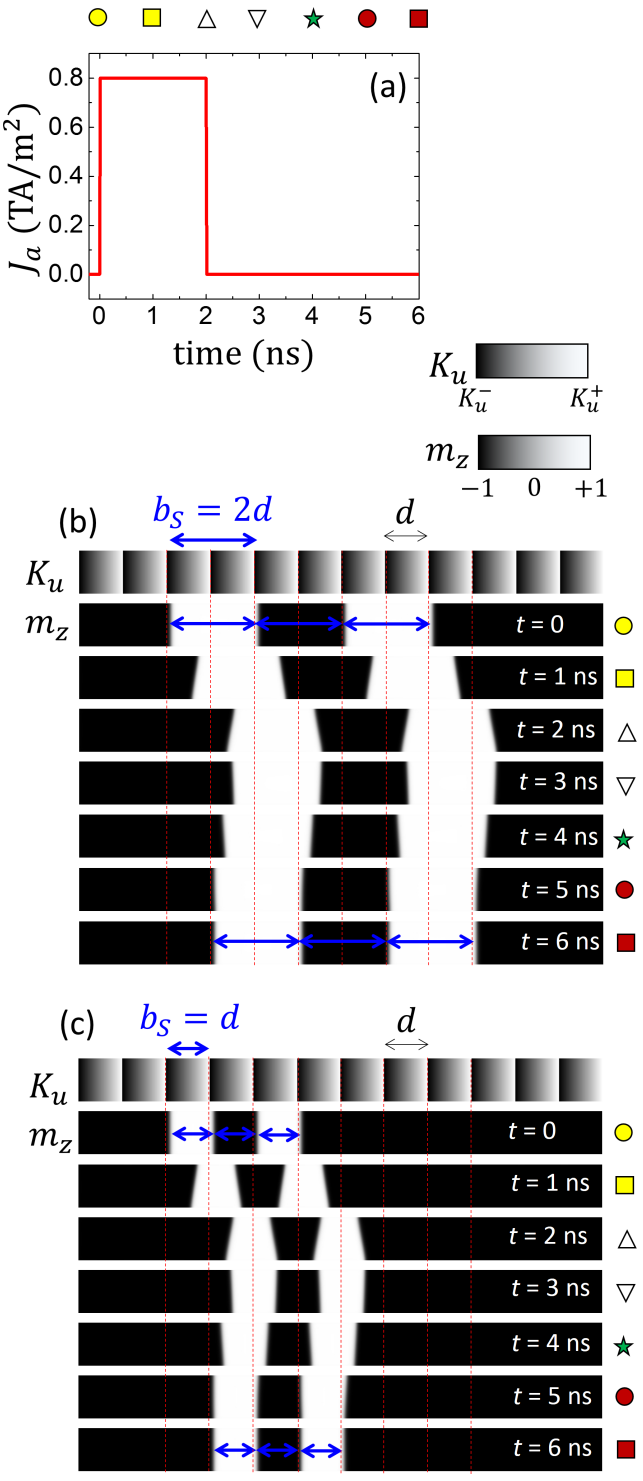

Fig. 11.4: Micromagnetic results of the current-driven DW motion along a ratchet strip. (a) shows the unipolar current pulse needed to shift the bit along the positive direction of the x-axis. The amplitude of the pulse is $J_a = 0.8\text{TA/m}^2$, and its duration is 2ns. The other two panels depict transient magnetization snapshots of the bit shifting of two bits of size (b) $b_s = 2d$ and (c) $b_s = d$ with $d = 128$nm. Materials parameters are those given in Sec. 11.2. Results were obtained at zero temperature.

11.4 Performance of current-driven DW motion along a ratchet strip

11.4.1 Micromagnetic and 1DM results. Perfect strips at zero temperature

The advantages of the current-driven mechanism over the field-driven case for a ratchet device have been highlighted in the previous section. Here we focus our attention to the analysis of the performance of these current-driven ratchet devices. The working principle of the current-driven ratchet device here proposed is described as follows. Each region of length d can pin one DW, which in the absence of external stimuli locates approximately at any of the points where the anisotropy energy is a minimum. The region size indeed defines the bit size ($b_s = d$), and bit shifting should occur after the application of current pulses $\vec{J}(t) = J_a(t)\,\vec{u}_x$, since the DWs can skip the tooth of the anisotropy profile pushed forward by the driving force associated with the current. Therefore, the proper performance of the device depends on the amplitude J_a of the injected current, its duration, which is referred to as the excitation time (t_e), and the interval between subsequent pulses, named here as the relaxing time (t_r). The ratio between the excitation time (t_e) and the total latency time ($\tau = t_e + t_r$) defines the duty cycle (t_e/τ). Different behaviors can be observed depending on these inputs J_a, t_e and t_r.

Fig. 11.5(a) presents the results obtained at zero temperature for three different current amplitudes J_a and fixed excitation and relaxation times ($t_e = t_r = 2$ns) corresponding to a 50% duty cycle. Micromagnetic results (μM) are depicted by dots and 1DM results with lines. A single DW located at the position of one of the anisotropy landscape minima is considered as the initial state, and two consecutive current pulses are applied. The temporal evolution of DW position is plotted when low (Fig. 11.5(a)), intermediate (Fig. 11.5(b)) and high (Fig. 11.5(c)) current pulses are applied. Representative micromagnetic snapshots are shown in the right panels. It can be checked that the values provided by the 1DM are in a rather good agreement with the μM results. As it has been stated, a positive current promotes DW motion from left to right. This driving force must overcome the restoring force associated with the slopes of the anisotropy profile. If the driving force overwhelms the restoring force at each point, the DW is able to skip one or several teeth of the anisotropy profile, as long as the current is on ($t < t_e$). When the current is switched off at $t = t_e$ the DW moves backwards due to the above-mentioned restoring force, going back to the local equilibrium position at an anisotropy minimum. The current is off during a relaxing time t_r which must be sufficiently long to let the DW reach such local equilibrium position. This ensures that the application of the new current pulse drives the DW in a predictable way.

Fig. 11.5(a) illustrates a frustrated jump attempt followed by a complete DW jump after the second current pulse ($J_a = 0.4\text{TA/m}^2$). Initially, the DW is driven by the current a distance shorter than d. Then, the DW does not skip the anisotropy tooth but reverses its motion due to the anisotropy profile for $t_e < t < t_e + t_r$. If the relaxation time t_r was sufficiently long, the DW would recover its starting position at equilibrium. However, the time $t_r = 2$ns is in this case rather short, and the

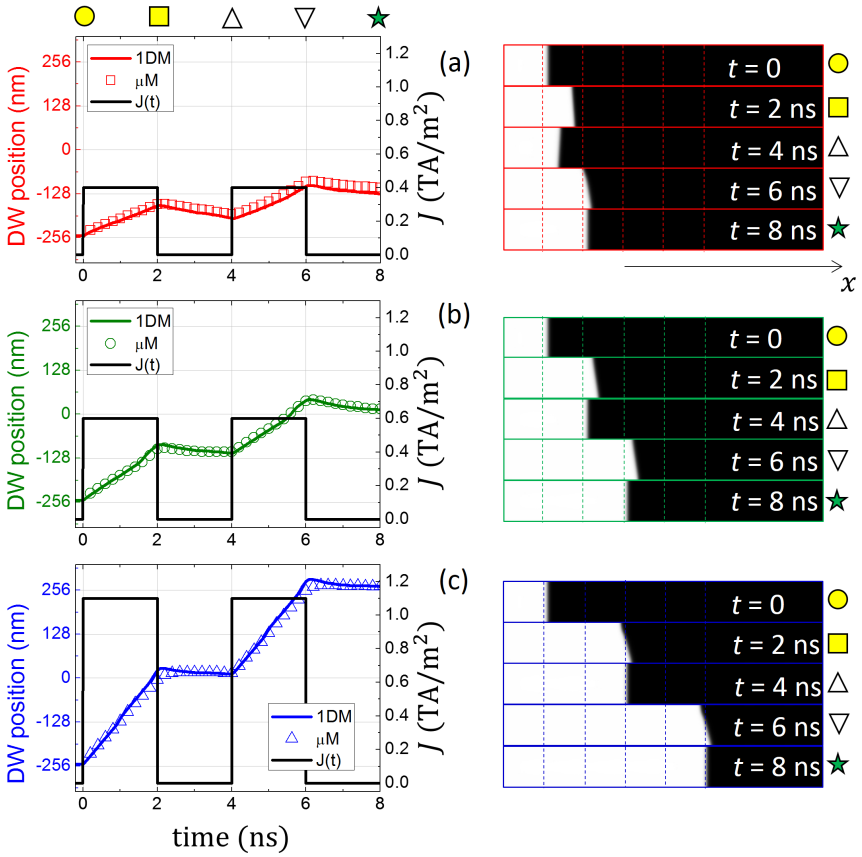

Fig. 11.5: DW position as a function of time for two successive current pulses of $t_e = 2$ns excitation time and $t_r = 2$ns relaxing time. Three different current amplitudes at zero temperature are considered: (a) $J_a = 0.4\text{TA/m}^2$, (b) $J_a = 0.6\text{TA/m}^2$, and (c) $J_a = 1.1\text{TA/m}^2$. In the left graphs, points correspond to full Micromagnetic results (μM) and lines are the results of the 1DM. Micromagnetic snapshots at the times when the current is switched on and off are shown in the right panels. Dashed lines in the snapshots indicate the peaks of the anisotropy profile.

DW acquires an intermediate position on the slope when the second current pulse is applied at $t = t_e + t_r = 4$ns. The subsequent jump is caused by the fact that the DW starts its dynamics from this non-equilibrium intermediate position after the first pulse, i.e., eventual (non predictable) bit shifting occurs during the application of the second current pulse, since DWs may skip the anisotropy tooth from such intermediate positions. This unpredictable behavior is completely undesirable for applications. Conversely, high current amplitudes can make DWs eventually advance two or more bits after every single current pulse, instead of only one. Fig. 11.5(c), which corresponds to a current pulse with $J_a = 1.1\text{TA/m}^2$, displays this behavior. The application of the first current pulse results in a double bit shift, and the second pulse also promotes a double bit shift. Finally, Fig. 11.5(b) depicts the case when the amplitude of the pulse is adequately high as to promote the DW displacement over a distance larger than d but shorter than $2d$ ($J_a = 0.6\text{TA/m}^2$). For this amplitude of the current pulse DWs do not return to the starting position after the application of each current pulse, but to the subsequent equilibrium position at a distance d provided the relaxing time is sufficiently long. This situation is achieved with a high confidence in this example, and corresponds to the desired

behavior, where a single bit is shifted only one tooth after every single current pulse. In other words, single DW jump occurs and the positions of the DWs always match an equilibrium state prior to the application of the next current pulse. As it can be checked in left graphs of Fig.11.5, the 1DM model provides us with adequate predictions of the time evolution of DWs, in agreement with full μM results.

11.4.2 Thermal effects: Joule heating and operation range

Former results were computed at zero temperature ($T = 0$). However, real devices should work at finite temperature and therefore, the effect of thermal fluctuations needs to be evaluated. Moreover, DWs are moved by an electric current and consequently, the effect of Joule heating may increase this temperature. Accordingly, thermal effects have been included in our results by means of the procedure described in Sec. 11.2, whereas the temperature increase due to the Joule heating was computed by COMSOL [169] simulations of the full HM/FM/Oxide stack (see its cross section in Fig. 11.6(a)). The thermal parameters of the different layers are given in Fig. 11.6(b), where σ is the electrical conductivity, C_p the heat capacity, k_{th} is the thermal conductivity, and ρ_m is the density. A thin silicon oxide layer (SiO) is assumed to be formed at the interface between the Si wafer and the Pt layer, which introduces an interfacial thermal resistance (R_{th}). Further details of this Joule heating evaluation are given in our previous works (see Refs. [86, 157]). The study indicates that within the range of current amplitudes considered along this work the temperature rises from room temperature ($T = 300K$) following an exponential law, with a characteristic time of a few tenths of nanoseconds. After that, when the current pulse is switched off, the temperature decreases in identical fashion. As to exemplify these statements, the temporal evolution of the temperature is shown in Fig. 11.6(c) for three current pulses with $t_e = 2$ns and different amplitudes J_a. The temporal evolution of the temperature in the FM layer obtained by COMSOL simulations can be analytically described by $T(t) = T_0 + \beta J_a^2 \left[1 - \exp\left(-t/\tau_{th}\right)\right]$ during the current pulse $0 < t < t_p$, and $T(t) = T_0 + \beta J_a^2 \exp\left(-(t - t_p)/\tau_{th}\right)$ after it ($t \geqslant t_p$), where $T_0 = 300K$, $\beta = 2.1 \times 10^{-23}\mathrm{K}/(\mathrm{A/m^2})$, and $\tau_{th} = 0.4$ns. Note that the maximum temperature reached at the end of the current pulse ($T_{max} = T(t = t_e)$) is well below the Curie temperature of conventional ferromagnetic materials. In particular, it is very well below the Curie temperature of the Co ($T_C \sim 1400K$) [92]. In Fig. 11.6(d) we plot the maximum temperature T_{max} reached at the end of the current pulse as a function of the current pulse amplitude (J_a). Although T_{max} scales with J_a^2 , the temperature remains well below the Curie threshold for the current amplitudes considered in the present study. Moreover, we have compared the DW dynamics along the ratchet device under a current pulse of $J_a = 0.65\mathrm{TA/m^2}$ and $t_e = 2$ns, assuming both a constant room temperature ($T = 300K$) and a temperature rise due to the Joule heating as described above (not shown). We checked that the dynamics is not significantly perturbed by Joule heating, and consequently, Joule heating does not constitute a drawback in the evaluated devices within the range of current amplitudes and pulse lengths considered here.

Although Joule heating seems to be negligible for the short and current pulses needed for the proper performance of these ratchet devices, thermal fluctuations can

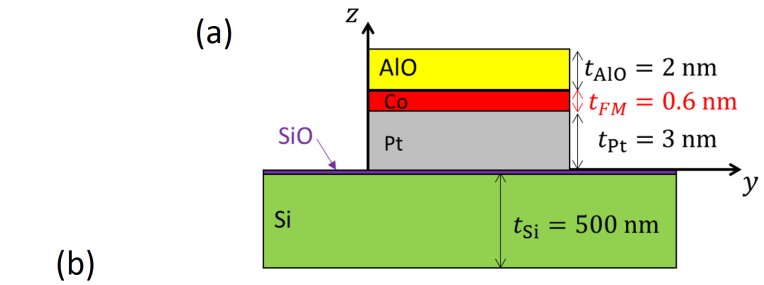

(b)

	Si	Pt	Co	AlO	SiO
σ [Ω^{-1}m^{-1}]		3.7×10^{6}	1.04×10^{6}		
C_p [J kg^{-1}K^{-1}]	700	130	417	730	
k_{th} [W K^{-1}m^{-1}]	130	71.6	100	35	
ρ_m [kg m^{-3}]	2239	21450	8900	3965	
R_{th} [K m^2 W^{-1}]					2.2×10^{-8}

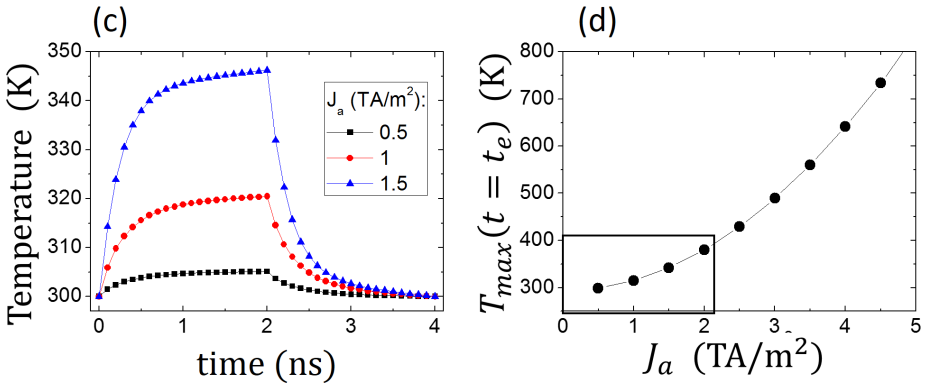

Fig. 11.6: Temperature dynamics under current pulses as computed by COMSOL simulations. (a) Cross section of the multilayer studied by COMSOL simulations for the heat transport under current pulses. (b) Thermal parameters used in the simulations. (c) Temporal evolution of the temperature for three current pulses with t_e = 2ns and different amplitudes (J_a). (d) Maximum temperature reached at the end of the current pulse ($T_{max} = T\,(t = t_e)$) as function of J_a. The box indicates the proper operation range of the considered device.

significantly reduce the reliability of the device even at fixed temperature. In order to study this reliability, the concept of proper operating range of the device can be introduced. This concept defines the range of values of the current amplitude J_a for given times t_e and t_r that promote a single DW jump after the application of one current pulse. Indeed, the wider the operating range is, the more reliable the device becomes. As an example, Fig. 11.7(a) depicts the probability of one single DW jump after the application of one current pulse, obtained from both μM simulations and the 1DM, as a function of the current amplitude J_a. Within this context, a probability of one means one single DW jump for every realization, for a total of twenty realizations at room temperature ($T = 300K$). Three different excitation times, t_e : 1ns, 1.5ns, 2ns, are considered for a 50% duty cycle ($t_e = t_r$). The curves neatly define for each excitation time a range of applied currents leading to single DW jumps, i.e., the proper operating range. Importantly, this range increases

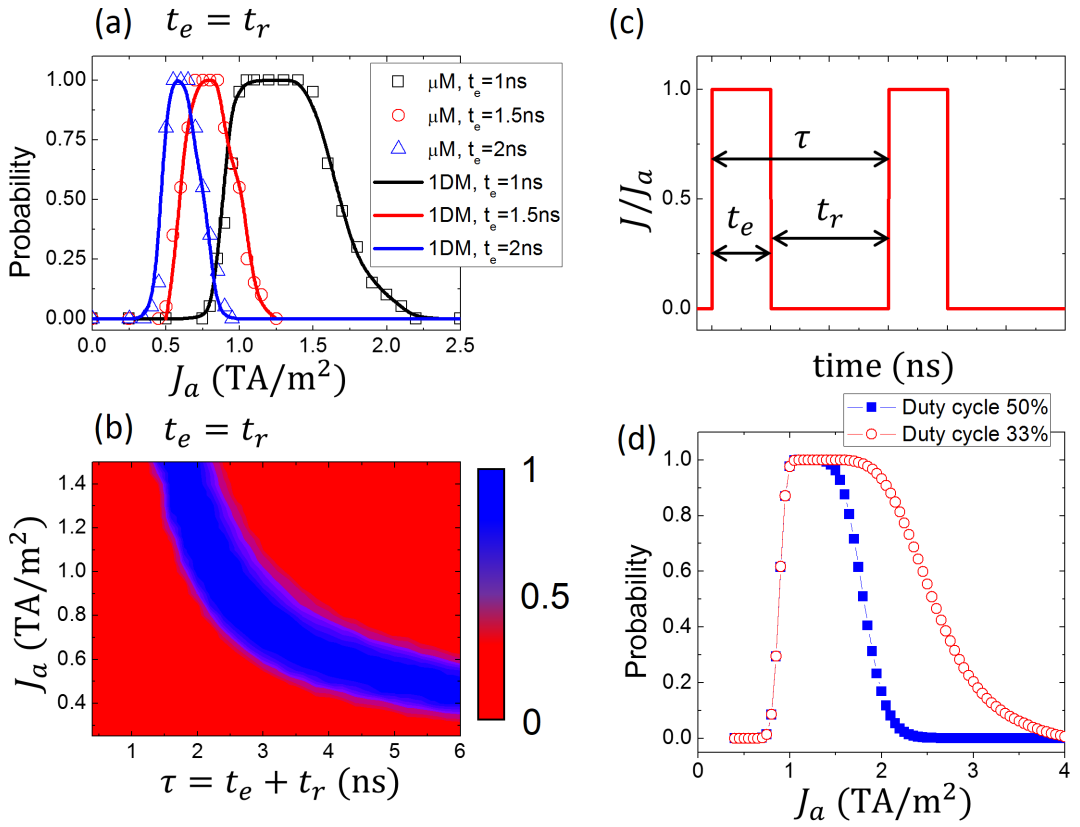

Fig. 11.7: (a) Probability of single jumps of one DW after the application of one pulse. The probability is given as a function of the current amplitude for pulses with $t_e = 1$ns, $t_e = 1.5$ns, and $t_e = 2$ns and are computed from full μM simulations (symbols) and the 1DM (lines). (b) Color map computed by using the 1DM showing the probability of single DW jumps at room temperature as a function of the current amplitude J_a and latency time $\tau = t_e + t_r$, the latter defined as the total time required to move one bit. A duty cycle of 50% is considered in both cases. (c) Applied current as a function of current amplitude J_a, pulse length t_r, and period $\tau = t_e + t_r$. (d) Probability of single jumps of one DW promoted by one current pulse with 50% and 33% duty cycles. Probabilities are calculated over 100000 jump attempts by means of the 1DM. The excitation time is $t_e = 1$ns in both cases, while the relaxing times are $t_r = 1$ns for the 50% duty cycle and $t_r = 2$ns for the 33% duty cycle.

with decreasing pulse lengths. It can be checked from the graphs in Fig. 11.7 the remarkable agreement between the results provided by full μM simulations and the 1DM even at finite temperature, in particular within the area of interest which defines the proper operating range. Actually, the use of the 1DM permits us to easily extend this study over the excitation times (t_e) along with the current amplitudes (J_a). The color map in Fig. 11.7(b) collects this study. As in previous examples, room temperature ($T = 300K$) is considered. As previously said, the proper operating range increases with decreasing excitation times. Besides, the shorter excitation times (t_e) are considered, the higher amplitudes (J_a) are required to achieve single DW jumps. The highest current amplitudes suitable for this device might be then limited by the appearance of DW tilting [19, 72] or other effects such as a non-negligible Joule heating for currents higher than 2TA/m^2. In any case, thermal fluctuations are not as intense as to endanger the performance of this device at room temperature.

With the aim of extending the operating range of this device, the following strategy can be proposed. Since the DW requires a minimal relaxing time (t_r) to reach an equilibrium position, this time can be lengthened, then reducing the duty cycle. In that way, a 50% duty cycle means that $t_e = t_r$ while a 33% duty cycle stands for $2t_e = t_r$. In order to provide a detailed statistics of the reliability of the proposed device, Fig.11.7(d) compares the probability at finite temperature ($T = 300K$) of single DW jump after one current pulse over 100000 attempts (see the previous definition of probability equal to 1) calculated by means of the 1DM. The two mentioned duty cycles, 50% and 33%, are considered with fixed excitation time $t_e = 1$ns. The results for current pulses with 50% duty cycle reveal a shorter range of currents resulting in proper working, as making the device more vulnerable to thermal fluctuations. Nevertheless, a 33% duty cycle ensures proper working for a wider range of applied currents, which increases the reliability of the device.

11.4.3 The effect of disorder

Results discussed in previous sections were evaluated assuming perfect samples, without defects nor imperfections. Here we show that current-driven DW motion along a ratchet (unidirectional) device is also reliable even under realistic conditions. The DW motion under current pulses for perfect strips (with neither edge roughness nor bulk defects) is compared with a more realistic description. Such realistic conditions were evaluated by assuming that the strip has some edge roughness and bulk defects in the form of grains (see Sec.11.2.1). In Fig. 11.8, the perfect and the realistic cases are compared under two consecutive current-pulses with $t_e = 2$ns and $t_r = 4$ns (which correspond to a duty cycle of 33%). Room temperature ($T = 300K$) and current pulse amplitudes of $J_a = 0.65\text{TA/m}^2$ were considered in both cases. Note that both thermal fluctuations and disorder make the DW profile rough as compared to the perfect case (no disorder) at zero temperature (see Fig. 11.5, for example). Anyway, the results presented in Fig. 11.8 indicate that realistic conditions (with edge roughness and bulk defects in the form of grains) do not significantly deviate from the ideal (perfect) case, and therefore, the device working principle is not compromised by realistic conditions.

11.4.4 Material parameters and variable DMI

The performance of the proposed current-driven ratchet device can be dependent in general on the material parameters. For example, studies (not shown here) on the dependence of this performance on the Gilbert damping (α: $0.1, \ldots, 0.5$) or other extreme values of the PMA constant (K_u^-, K_u^+) have also been carried out, not leading to severe qualitative modifications of this performance. Moreover, these parameters can be adequately tuned in most cases to fix the most convenient set of them for the desired characteristics. In that way, the 1DM becomes a useful tool to determine the proper parameters.

The influence of the DMI parameter deserves particular attention. In fact, a constant DMI parameter has been considered along this work. Although it has been recently demonstrated that PMA and DMI can be tuned almost independently by adjusting

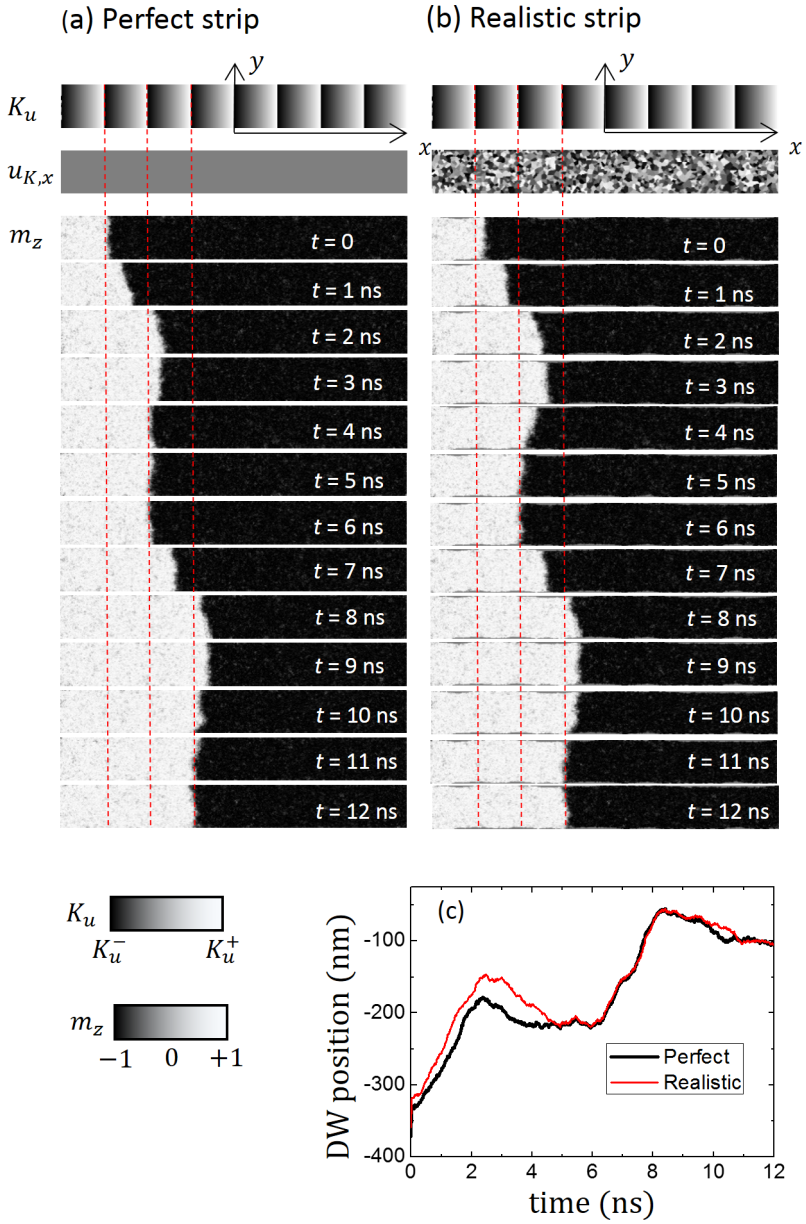

Fig. 11.8: Micromagnetic analysis of the current-driven DW motion along a ratchet strip: (a) perfect vs (b) realistic strips. μM simulations were performed with the inputs given in Sec. 11.2 and at room temperature. Here the amplitude of the current pulse is $J_a = 0.65\text{TA/m}^2$ and two consecutive current-pulses of $t_e = 2\text{ns}$ and $t_r = 4\text{ns}$ are applied. The anisotropy profile and the x-component of the uniaxial easy axis are shown on top of the snapshots. In (b), bulk grains and edge roughness are taken into account as described in Sec. 11.2.1. Snapshots from top to bottom correspond to different magnetization states at consecutive instants of time. The temporal evolution of the DW position is plot in (c).

irradiation energies and doses [48], a small variation of the DMI may be expected when tailoring the PMA by ionic irradiation. Here, a linear variation of the DMI parameter ($D(x)$), analogous to that of the PMA ($K_u(x)$), has been also considered. In this way, the DMI parameter changes linearly from $D^- = 0.8\text{mJ/m}^2$ to $D^+ = 1.0\text{mJ/m}^2$ in a periodic fashion with period $d = 128\text{nm}$. Note that within this range, the DMI parameters are still sufficiently high as to give rise to the formation of chiral Néel DWs, so that efficient current-driven DW movement by means of the SHE

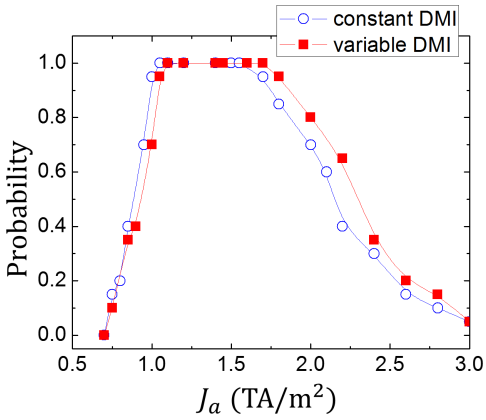

Fig. 11.9: Micromagnetically computed probability of single jumps of one DW over twenty attempts with constant DMI parameter (open symbols) and with a linear variation of the DMI parameter (filled symbols). In the first case the DMI parameter is fixed ($D = 1.0\text{mJ/m}^2$), whereas in the second one $D = D(x)$ changes linearly from $D^- = 0.8\text{mJ/m}^2$ to $D^+ = 1.0\text{mJ/m}^2$ in a periodic fashion with the same period of the PMA constant ($d = 128\text{nm}$).

is still guaranteed. μM simulations have been carried out to compare the results obtained both with constant DMI basis and with the considered linear variation of the DMI (see Sec.11.2.1 for details). 33% duty cycle current pulses are applied with an amplitude $J_a = 1.2\text{TA/m}^2$, and the probability of single DW jump after each current pulse is analyzed in both cases at finite temperature. The results are plotted in Fig. 11.9, which indicates that no drastic changes are found in the case of variable DMI with respect to the case of constant DMI, and therefore the working principle is still preserved.

11.5 Current-driven DW motion along bi-directional devices

The ratchet PMA profile (Fig. 2(b)) was designed to avoid DW backward movement in a field-driven basis. However, this results in a unidirectional motion of trains of DWs, making this device less flexible as compared to other racetracks memories devices intended for bi-directional DW motion [27, 28]. Our methods (μM and 1DM) can be straightforwardly adapted for a perpendicular profile ($K_u = K_u(x)$,) designed now to promote the bi-directional shifting of trains of DWs. This can be easily performed by considering a periodic triangular anisotropy profile, which consists on parts where $K_u(x)$ increases linearly up to K_u^+ over a distance $d_1 = d/2$, and from there, K_u decreases down to K_u^- with the same slope within an identical distance ($d_2 = d/2$). The analytical expression for this PMA profile $K_u = K_u(x)$ can be obtained from Eq. (11.5) with $d_1 = d_2 = d/2$, and it is shown in top graph of Fig. 11.10(a). The corresponding effective field due to the PMA profile ($r(q) = H_{PMA}(q)/H^0_{PMA}$) is obtained from Eq. (11.8) and it is represented in the bottom graph of Fig. 11.10(a). We have considered a single DW initially located at one of these energy minima, i.e., at a point where $K_u(q) \approx K_u^-(q(t=0) \approx -d)$, and positive current pulses are applied with fixed duration $t_e = 2\text{ns}$ and two different amplitudes: $J_a = 0.5\text{TA/m}^2$ and $J_a = 0.6\text{TA/m}^2$ (see Fig. 11.10(b)). The

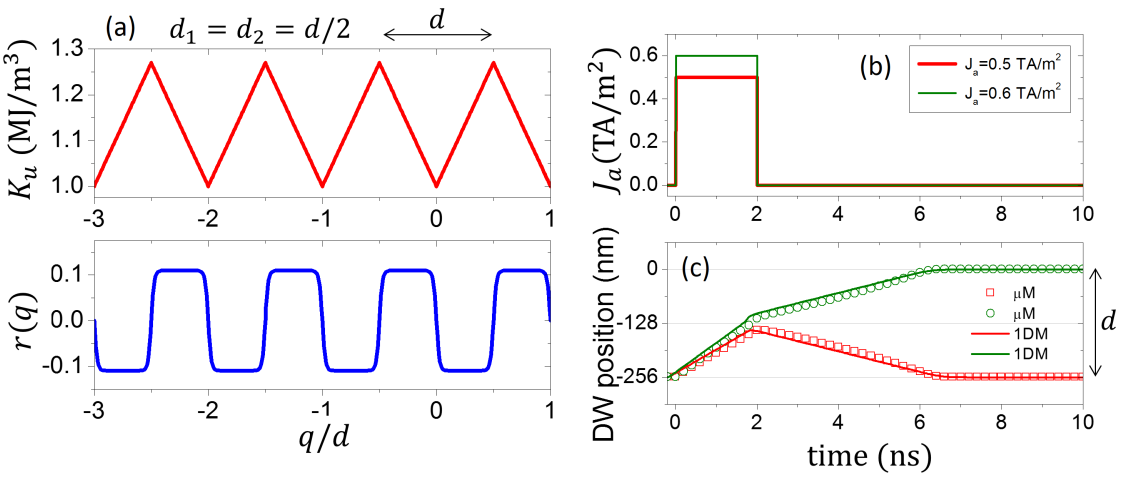

Fig. 11.10: Periodic triangular PMA profile ($K_u(x)$, Eq. (11.5)) to promote DW motion in bi-directional devices. Here $K_u^- = 1.0\text{MJ/m}^3$, $K_u^+ = 1.27\text{MJ/m}^3$, $d_1 = d_2 = d/2$, with $d = 256\text{nm}$. The bottom graph represents the corresponding $r(q) = H_{PMA}(q)/H_{PMA}^0$ along the strip axis (Eq. (11.8)). (b) Two current pulses with fixed duration $t_e = 2\text{ns}$ and two different amplitudes: $J_a = 0.5\text{TA/m}^2$ (red) and $J_a = 0.6\text{TA/m}^2$ (green). (c) Temporal evolution of the DW position initially located at under the current pulses. Open symbols correspond to μM results and solid lines were obtained by solved the 1DM Eqs. Perfect samples (without imperfections) and zero temperature conditions were assumed in both models.

temporal evolution of the DW position is depicted in Fig. 11.10(c), where open symbols corresponds to μM results and solid lines were obtained from the 1DM. For $J_a = 0.5\text{TA/m}^2$, the DW does not overcome the energy barrier at the end of the pulse, and it relaxes back to its initial location for $t > t_e = 2\text{ns}$. On the contrary, a current pulse with $J_a = 0.6\text{TA/m}^2$ is enough to overcome the energy barrier (located at $q = -d + d/2$) during the current pulse ($0 < t_e < 2\text{ns}$). Therefore, this DW relaxes to the adjacent energy minima (at $q = -d + d = 0$), where it rests for $t > 6\text{ns}$. As it is clearly seen, both μM and 1DM results are again in good quantitative agreement.

In this bi-directional device, an isolated bit of information is coded within a domain magnetized up (↑, white color in magnetic snapshots of Fig.11.11) bounded by two adjacent DWs placed at two energy minima. i.e., at points where $K_u(x) \approx K_u^-$. This domain then includes a position where a maximum of the anisotropy locates equally distant to the domain edges where down-up (↓↑) and up-down (↑↓) DWs are. The bit size is therefore $b_S = d = 2d_1$. Contrary to the unidirectional ratchet device, this PMA profile (Fig. 11.10(a)) allows the bi-directional current-driven DW motion. In order to show it, the current-driven motion of two DWs under two consecutive current pulses of opposite polarities was evaluated. Positive current pulses ($J_a > 0$) drive both down-up (↓↑) and up-down (↑↓) DWs along the positive direction ($x > 0$), whereas negative current pulses ($J_a < 0$) drive both down-up and up-down DWs along the negative direction ($x < 0$). One example of this bi-directional functionality is shown in Fig. 11.11, which was obtained by means of full μM simulations. The current amplitude is $J_a = 0.8\text{TA/m}^2$, and the pulse duration is $t_e = 2\text{ns}$. Note that such a bi-directional functionality cannot be achieved in the field-driven case, due to the simple fact that adjacent DWs move along opposite directions under a given polarity of the field. Our modeling suggests these systems as promising platforms

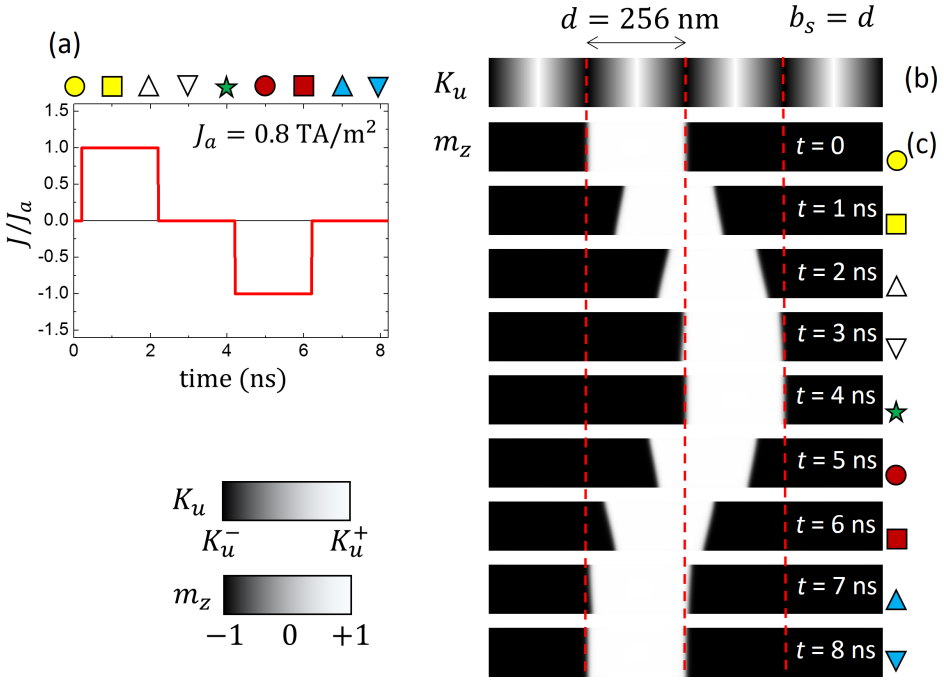

Fig. 11.11: Micromagnetic analysis of the current-driven DW motion in bi-directional devices. A perfect strip at zero temperature is considered. The perpendicular anisotropy periodically increases and decreases linearly between $K_u^- = 1.1\text{MJ/m}^3$ and $K_u^- = 1.27\text{MJ/m}^3$ within a distance $d_1 = d_2 = d/2 = 128\text{nm}$. The rest of inputs are those given in 11.2.1. The bit size, defined as the distance between two adjacent energy minima, is $b_s = d$. The anisotropy profile along the ferromagnetic strip axis is shown in (b), while the two current pulses ($J_a = 0.8\text{TA/m}^2$ and $t_e = 2\text{ns}$) injected to promote forward and backward longitudinal displacement of the two DWs are plotted in (a). Transient snapshots of consecutive magnetic states are shown in (c).

to develop DW-based devices which can be efficiently driven back and forth by short current pulses, and where the DW position can be controlled by the periodic modulation of the PMA.

11.6 Conclusions

The DW dynamics along ferromagnetic strip with periodically modulated perpendicular magnetic anisotropy has been analyzed. The work presents a theoretical study of the current-driven ratchet memory as a DW-based magnetic memory. This study has been carried out by means of full μM simulations along with the 1DM, showing that both approaches are in good agreement. The 1DM was developed for a general periodic PMA profile: a new term ($H_{PMA}(q)$) in the 1DM dynamics equations. Such a local PMA field accounts for the space dependent anisotropy profile, and forces the DW to travel the closest accessible PMA minimum in the absence of driving force. The work shows how both the bit density and shifting speed are notably enhanced if the memory device works on the current-driven basis as compared with the field-driven scheme. This enhancement roots in three main differences between the two driving forces. First of all, single pulses with a given polarity (unipolar) are required in the case of the current-driven ratchet, whereas bipolar pulses are needed in the field-driven case. Secondly, the duration of the

current pulses to achieve a single DW jump over a single anisotropy slope (tooth) is significantly shorter than the duration of the needed bipolar field pulses. Moreover, the bit size (b_s), determined by the minimum distance between two adjacent DWs, is smaller in the current-driven case than in the field driven case. Note that each bit occupies two teeth in the field-driven ratchet ($b_S = 2d$), whereas a bit only needs a single tooth in the current-driven case ($b_S = d$). Consequently, the current-driven architecture allows higher density packed information in these devices. Additionally, its performance may even be improved by a fine tuning of the pulse and relaxing times. In this way, the best results are obtained when the combined effect of the times of both the applied current pulse and the relaxing interval leads every DW from an equilibrium state to another one at the adjacent tooth of the anisotropy landscape, the former time by promoting only one single jump and the latter by allowing the DW to recover this new equilibrium position before the next pulse is applied. Finally, our study opens a new promising door to other devices with tuned anisotropy. In particular, not only ratchet-like but also current-driven bi-directional devices can be developed.

11.7 Acknowledgments

This work was supported by project WALL, FP7- PEOPLE-2013-ITN 608031 from the European Commission, projects MAT2014- 52477-C5-4-P, MAT2017-87072-C4-1-P, and MAT2017-90771-REDT) from the Spanish government, and projects SA282U14 and SA090U16 from the Junta de Castilla y Leon.

Chapter 12

Current-driven domain wall motion based memory devices: application to a ratchet ferromagnetic strip*

Ratchet memories, where perpendicular magnetocristalline anisotropy is tailored so as to precisely control the magnetic transitions, has been recently proven to be a feasible device to store and manipulate data bits. For such devices, it has been shown that the current-driven regime of domain walls can improve their performances with respect to the field-driven one. However, the relaxing time required by the traveling domain walls constitutes a certain drawback if the former regime is considered, since it results in longer device latencies. In order to speed up the bit shifting procedure, it is demonstrated here that the application of a current of inverse polarity during the DW relaxing time may reduce such latencies. The reverse current must be sufficiently high as to drive the DW to the equilibrium position faster than the anisotropy slope itself, but with an amplitude sufficiently low as to avoid DW backward shifting. Alternatively, it is possible to use such a reverse current to increase the proper range of operation for a given relaxing time, i.e., the pair of values of the current amplitude and pulse time that ensures single DW jumps for a certain latency time.

*Adapted from Luis Sánchez-Tejerina, Eduardo Martínez, Víctor Raposo, and Óscar Alejos. Current-driven domain wall motion based memory devices: Application to a ratchet ferromagnetic strip. *AIP Advances*, 8(4):047302, 2018. doi:10.1063/1.4993750.

12.1 Introduction

Multilayer strips, where high perpendicular magnetocristalline anisotropy (PMA) appears due to surface effects, have been recurrently proposed as promising data storage devices based on domain walls (DWs) motion. [27, 28, 77, 171–173] One of the essential requirements to put such devices into practice is the development of a reliable pinning system to precisely control the DWs positions. A ratchet memory device, where PMA is tailored so as to present a sawtooth profile, was proposed elsewhere [79] to achieve this goal. The field-driven regime of such a ratchet memory was studied, drawing rather interesting features. However, it has been recently shown that a current-driven regime for the DWs can be a more advantageous alternative to the field-driven one. [174]

An unavoidable requisite for such a current-driven regime is the presence in the system of spin-orbit coupling phenomena as the spin Hall effect (SHE), along with the interfacial Dzyaloshinskii-Moriya interaction (iDMI). Multilayer systems with inversion asymmetry, where a ferromagnetic layer (FM) is sandwiched between a heavy metal (HM) and an oxide (Ox) can be then proposed. [14, 19] An anisotropy profile as the one described above make this device suitable for bit storing and shifting in a denser and faster way. The application of adequately estimated current amplitudes, pulse times and duty cycles can permit the synchronous displacement of all DWs along the device. [174] In this way, every DW performs single jumps over the teeth and always recovers an equilibrium state at any of the valleys of the anisotropy landscape. The latency time of the bit shifting procedure is then given by the sum of the pulse (excitation) time, that makes the DW skip each tooth, and a relaxing time required to let the DW move backward to the closest equilibrium position, the latter time depending on the slope of the anisotropy profile. For this device, relaxing times longer than pulse times ensured the proper operation of the device after subsequent pulses.

In order to speed up the bit shifting procedure, two strategies can be proposed. Firstly, the applied current can be increased as to reduce the time needed by the DW to perform one jump. Alternatively, a reduction of the time needed by the DW to reach the equilibrium position must be achieved. The latter strategy is to be applied here by using a reverse current, i.e. a current of inverse polarity to the driving one. The work is then structured as follows. The micromagnetic analysis and the one-dimensional model (1DM) are introduced in section 12.2, while section 12.3 describes the system under study. Section 12.4 is divided up into two subsections. Section 12.4.1 deals with the variation of the single-jump probability when a reverse current J_r of different relaxing times t_r is applied. Additionally, section 12.4.2 focuses on the dependence of the proper range of operation on the reverse current, while maintaining the relaxing time constant. Finally, section 12.5 briefly presents the conclusions drawn by this study.

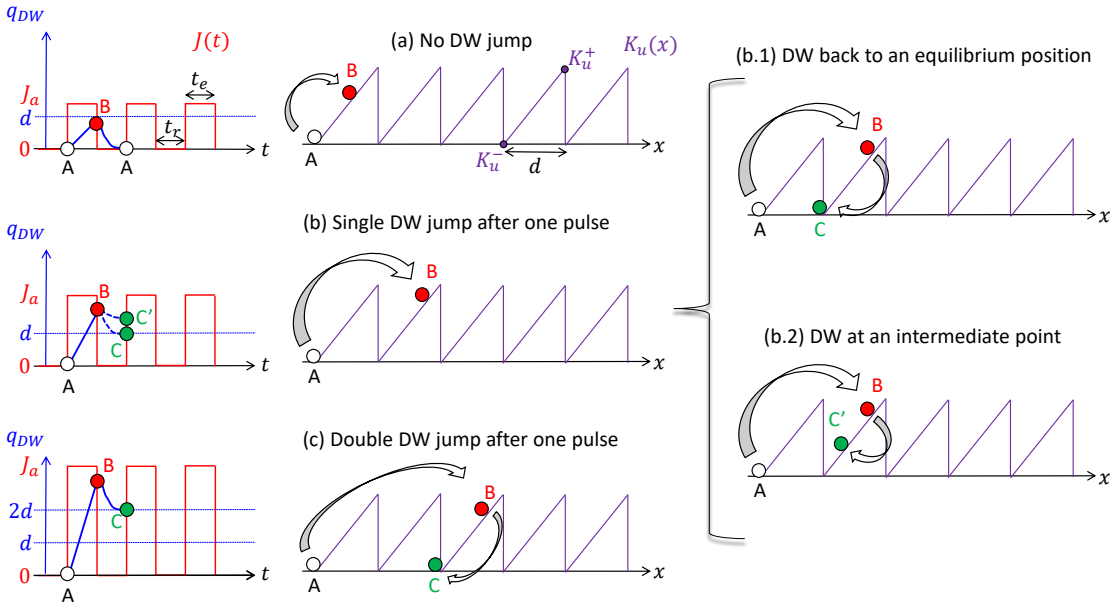

Fig. 12.1: Likely behaviors of the DW motion under the application of pulsed currents in a FM ratchet. The sawtooth anisotropy energy profile, as represented in the central column of images, is meant to drive the DW to well defined positions. The periodicity of this profile is given by a characteristic length d. (a) For low currents, the DW is not able to jump over any profile tooth, i.e., the DW maximal run distance is less than d for the excitation time t_e. (c) For high currents, multiple teeth can be overcome at once after each pulse, that is, the DW runs distances over $2d$. (b) For intermediate currents, the DW final position after the excitation and relaxing (t_r) times is located between the two subsequent teeth. However, if this final position does not match the anisotropy minimum position, as the figure (b.2) depicts, further pulses may promote multiple jumps rather than single ones. The proper performance of the device is obtained when the DW overcome one single tooth at each pulse, matching the DW final position the minimum of the anisotropy energy profile, as in (b.1).

12.2 Micromagnetic analysis and one-dimensional model

The time evolution of the normalized magnetization $\vec{m}$ is to be considered in order to predict the behavior of the system. Such a time evolution is known to be described by the Landau-Lifshitz-Gilbert (LLG) equations, augmented by the spin-orbit torques (SOT) and thermal fluctuations: [114, 117]

$$\begin{aligned}\frac{d\vec{m}}{dt} = &-\gamma_0 \vec{m} \times \left(\vec{H}_{eff} + \vec{H}_{th}\right) - \\ &-\alpha \vec{m} \times \frac{d\vec{m}}{dt} - \gamma_0 \vec{m} \times \left(\vec{m} \times \vec{H}_{SH}\right).\end{aligned} \tag{12.1}$$

where γ_0 and α are the gyromagnetic ratio and the damping parameter, and $\vec{H}_{eff}$ is the effective field, including exchange, anisotropy, and magnetostatic interactions, along with the iDMI. Finally, $\vec{H}_{SH}$ and $\vec{H}_{th}$ are, respectively, the effective field associated to the SHE and the thermal field, the former being proportional to the applied

current, [12] and the latter included as a gaussian-distributed random field. [70, 113–115, 117] The complete study of the motion of a DW in such a system requires solving this equation by means of full micromagnetic simulations (μMag). These μMag simulations have been performed with the help of the Mumax^3 package. [122]

Additionally, the one-dimensional model has also been specifically tailored to obtain a more simple approach to the DW dynamics in this system. [174] Two mutually dependent equations can be derived for such a dynamics:

$$\begin{aligned}\dot{q} = &\frac{\gamma_0\Delta}{1+\alpha^2}\left[(H_D - H_k\cos\Phi)\sin\Phi\right] + \\ &+ \frac{\gamma_0\Delta}{1+\alpha^2}\left[\alpha\left(H_{SH}\cos\Phi + H_{th} + H_r r(q)\right)\right],\end{aligned} \tag{12.2a}$$

$$\begin{aligned}\dot{\Phi} = &\frac{\gamma_0}{1+\alpha^2}\left[\alpha\left(H_k\cos\Phi - H_D\right)\sin\Phi\right] + \\ &+ \frac{\gamma_0}{1+\alpha^2}\left[H_{SH}\cos\Phi + H_{th} + H_r r(q)\right].\end{aligned} \tag{12.2b}$$

The terms H_D, H_k, stand for the iDMI and the magnetostatic interaction, respectively, and their definition can be found elsewhere.[41, 139] The other terms, H_{SH} and H_{th}, are straightforwardly derived from their counterparts in the LLG equations. Finally, the sawtooth anisotropy profile, given by a function $K_u(x)$ of the longitudinal coordinate x (see the central column of Fig. 12.1), introduces the terms $H_r = \frac{K_u^+ - K_u^-}{2\mu_0 M_s}$, and

$$\begin{aligned}r(q) = &\frac{1}{\cosh^2\left[\left(1-\{\frac{q}{d}\}\right)\frac{d}{\Delta}\right]} + \frac{1}{\cosh^2\left(\{\frac{q}{d}\}\frac{d}{\Delta}\right)} - \\ &- \frac{\frac{\Delta}{d}\sinh\left(\frac{q}{\Delta}\right)}{\cosh\left(\{\frac{q}{d}\}\frac{d}{\Delta}\right)\cosh\left[\frac{\left(1-\{\frac{q}{d}\}\right)d}{\Delta}\right]},\end{aligned} \tag{12.3}$$

where the braces stand for the fractional part function.

12.3 Description of the FM ratchet system

A FM strip with high PMA sandwiched between a HM and an oxide is considered within this work. Material parameters commonly found in the literature [41] have been used for the present study: saturation magnetization M_s of $1.1\frac{\mathrm{MA}}{\mathrm{m}}$, exchange constant A of $16\frac{\mathrm{pJ}}{\mathrm{m}}$ and a Gilbert damping parameter $\alpha = 0.5$. An interfacial DMI with a DMI parameter $D = 1\frac{\mathrm{mJ}}{\mathrm{m}^2}$ has also been considered (a brief discussion on the convenience of using a constant DMI parameter is included in our previous work[174]). This value is sufficiently high as to induce Néel DWs and, thus, to efficiently drive the DW by means of the SHE. An electric current is then applied through the HM, giving rise to a spin Hall current with a spin Hall angle of a typical value $\theta_{SH} = 0.1$. A cross section $L_y \times L_z$ of $128\mathrm{nm} \times 0.6\mathrm{nm}$ has been taken for the FM strip.

The ratchet anisotropy profile is obtained by tuning the out-of-plane anisotropy as described elsewhere.[79] Five periods of the sawtooth anisotropy profile are

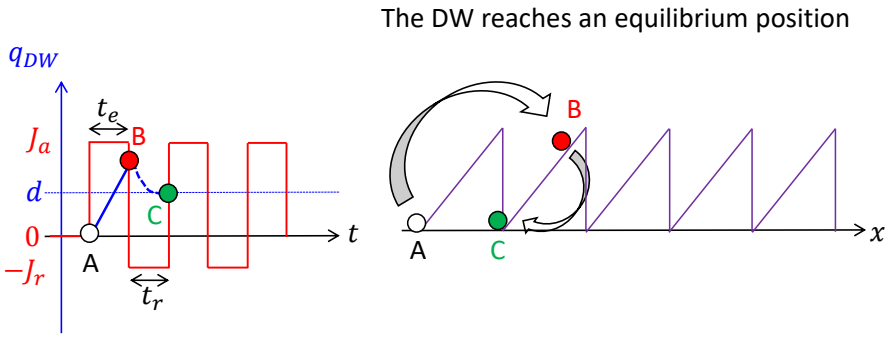

Fig. 12.2: Use of a current of inverse polarity J_r to ensure the proper operation of the ratchet system. After the application of a driving pulse current of amplitude J_a and width t_e, DWs slide backwards to an equilibrium position within the relaxing time t_r due to the combined effect of the slope of the anisotropy profile together with the reverse current J_r.

depicted in the central column of Fig. 12.1. The highest and lowest anisotropy values, $K_u^+ = 1.27\frac{\text{MJ}}{\text{m}^3}$ and $K_u^- = 1\frac{\text{MJ}}{\text{m}^3}$, respectively, are indicated. A ratchet period $d = 128$nm has been taken, as represented in the figure. Fig. 12.1 summarizes the results obtained in our previous work.[174] A sufficiently high pulsed current as to promote single DW jumps over the teeth of the sawtooth profile, but sufficiently low not to give rise to multiple DW jumps is considered in this work, i.e., the intermediate current range described in the caption of Fig. 12.1. Within this current range, the DW might not be able to reach the equilibrium position at the anisotropy energy minimum by the time the current is switch on again, as depicted in the bottom-right case of Fig. 12.1. In that case, a double jump may occur after subsequent pulses. This possibility was avoided in our previous study by prolonging the relaxing time.[174]

12.4 Results

As it has been already stated, the proper performance of the device is obtained when the DW overcome only one tooth at each current pulse, and its final position matches the equilibrium position at the energy minimum of the anisotropy profile. Such an equilibrium position must be reached in a time less than t_r after the driving pulse of amplitude J_a and width t_e is switched off. Since the DW is located at any arbitrary position between subsequent teeth by the time the driving current is switched off, the time t_r might not be sufficiently long as to let the DW slide backwards to the equilibrium position by the effect of the slope of the anisotropy profile. As an alternative, instead of switching off the driving current, a current of amplitude J_r and opposite polarity to J_a can be injected so as to drive the DW to the equilibrium state in a faster way, as Fig. 12.2 depicts. This can be of use whether a reduction of the time t_r is sought or, for a fixed t_r, the range of driving currents J_a of successful operation is to be broadened, as the following sections detail.

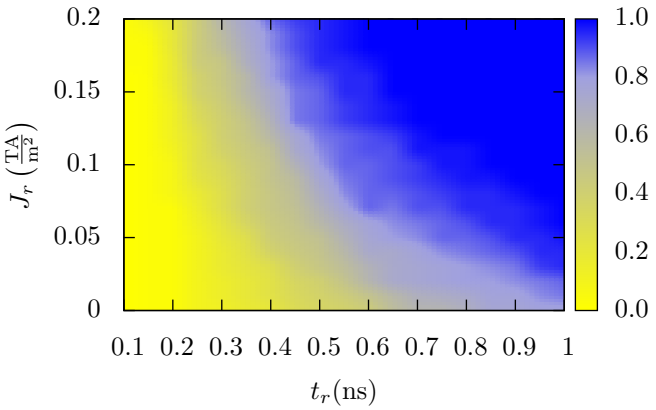

Fig. 12.3: Probability of single jumps of one DW after the application of one driving pulse of amplitude $J_a = 1.6\frac{\mathrm{TA}}{\mathrm{m}^2}$ and width $t_e = 1$ns as a function of the relaxing time t_r and reverse current J_r. The results are obtained by means of the 1DM. The probability has been statistically computed by evaluating forty different stochastic realizations for each relaxing time and current at a temperature of 300K.

12.4.1 Probability dependence on the reverse current and the relaxing time

The results that are to be presented here have been obtained by means of the tailored 1DM described in section 12.2, which has been proven to draw rather accurate results for these ratchet systems,[174] and to be rather less time consuming for the determination of the reduction of the bit shifting latencies. Along this study, a driving current $J_a = 1.6\frac{\mathrm{TA}}{\mathrm{m}^2}$ and an excitation time $t_e = 1$ns have been considered. Fig. 12.3 represents the probability of proper operation of the device, i.e, single jumps as those depicted in Fig. 12.2 as a function of the relaxing time t_r and the reverse current J_r, the values of the latter magnitude given in absolute terms. The probability has been statistically calculated after forty stochastic realizations at a temperature of 300K. It can be noticed that, in the absence of the reverse current, a rather low probability of DW single jumps is obtained, even for relaxing times t_r as long as 1ns. However, a relaxing current of $J_r = 80\frac{\mathrm{GA}}{\mathrm{m}^2}$ is sufficiently high as to drive the DW to the equilibrium position after the 1-ns long relaxing time for every realization. Additionally, it can be checked that the use of a reverse current with a modulus of 10% of the driving current J_a allows a reduction of the relaxing time to $t_r = 0.6$ns, but keeping the system within the proper operation regime. Latencies, calculated as the sum of the pulse width $t_e = 1ns$ and the relaxing time t_r, are then reduced in this case from a total time much longer than 2ns to an interval of 1.6ns.

12.4.2 Broadening of the range of operation

Alternatively to the considerations made in the previous section, a broadening of the range of operation, that is, the range of driving currents J_a leading to DW single jumps, can be achieved. This might be of particular interest in order to reduce as much as possible bit shifting error rates. Fig. 12.1 depicts the probability of proper operation of the device after the application of one current pulse 1-ns long, as a function of the current amplitude J_a for three different reverse currents J_r of values $0\frac{\mathrm{TA}}{\mathrm{m}^2}$, $0.08\frac{\mathrm{TA}}{\mathrm{m}^2}$ and $0.16\frac{\mathrm{TA}}{\mathrm{m}^2}$. Reverse currents are also applied for 1ns. Dots in

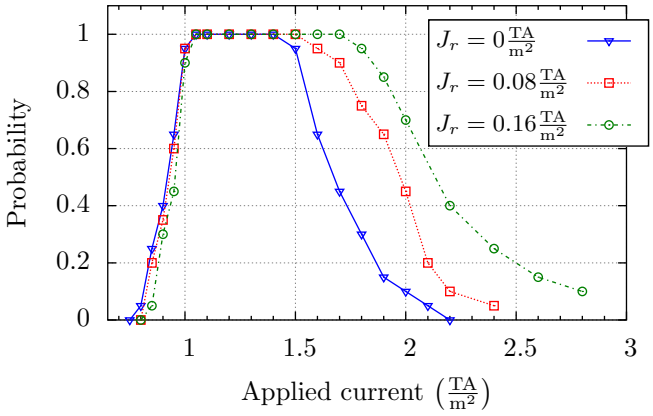

Fig. 12.4: Probability of single jumps of one DW after the application of one driving pulse of current with a width $t_e = 1$ns. A relaxing time $t_r = 1$ns is considered for three different amplitudes of the reverse current J_r. Results are computed from full μMag simulations (dots) and the 1DM (lines). The probability has been statistically obtained by evaluating twenty different realizations for each pair of driving and reverse currents, at a temperature of 300K.

these plots correspond to the results obtained by means of full μMag simulations, while lines correspond to the results obtained from the use of the 1DM. Prior to any consideration, it is timely again to insist on the rather good agreement between both the μMag and the 1DM approaches.

Under these conditions, the proper operation of the device requires the use of a driving current J_a above a certain threshold, given in this case by the value $1.1\frac{\mathrm{TA}}{\mathrm{m}^2}$. The DW run distance then exceeds the value d defining the periodicity of the anisotropy profile, almost independently of whether or not a subsequent reverse current is applied. If no reverse current is applied (red line/dots), and the driving current J_a exceeds a value of $1.4\frac{\mathrm{TA}}{\mathrm{m}^2}$, the relaxing time t_r is not sufficiently long to let the DW backward slide down to the closest equilibrium position at the anisotropy energy minima. Further increase of the driving current J_a above $2.2\frac{\mathrm{TA}}{\mathrm{m}^2}$ would give rise to DW run distances greater than $2d$. Consequently, the range of proper operation, defined as the driving currents leading to DW single jumps with a probability closest to one, is estimated to be of only $0.3\frac{\mathrm{TA}}{\mathrm{m}^2}$

However, the use of the reverse current J_r contributes to extend the range of proper operation up to $0.4\frac{\mathrm{TA}}{\mathrm{m}^2}$ for $J_r = 0.08\frac{\mathrm{TA}}{\mathrm{m}^2}$ and $0.6\frac{\mathrm{TA}}{\mathrm{m}^2}$ for $J_r = 0.16\frac{\mathrm{TA}}{\mathrm{m}^2}$. In these cases, the reverse current promotes the DW movement from the position reached over the corresponding slope of the anisotropy profile after the driving pulse current down to the anisotropy energy minimum.

As a final consideration, it must be noted that the current pulses used for this study has been taken with a negligible rise time. This might not seem sufficiently realistic. However, with the help of the described 1DM, estimations of the probability of single jumps of one DW after the application of one driving pulse can be easily calculated in a straightforward way under more practical conditions. As an example, a pulse rise time of 250ps can be defined, so that the current varies from J_a to $-J_r$ and vice versa within this interval. Each current then holds for 750ps, so that pulse and relaxing

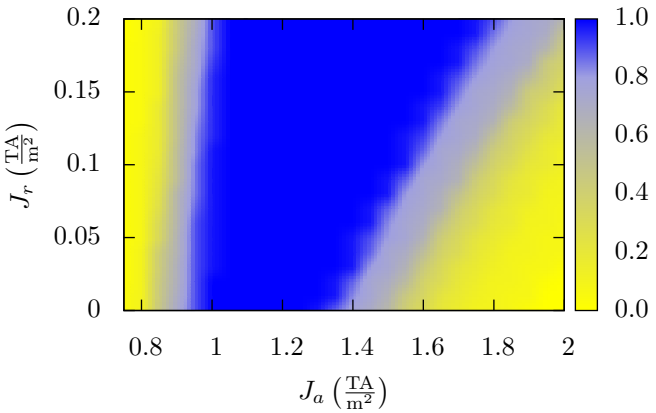

Fig. 12.5: Probability of single jumps of one DW after the application of one driving pulse. A pulse rise time of 250ps has been considered, so that the current varies either from J_a to $-J_r$ or from $-J_r$ to J_a within this interval, and then hold for 750ps, i.e., $t_e = t_r = 1$ns. The results are obtained by means of the 1DM. The probability has been statistically computed by evaluating forty different stochastic realizations for each relaxing time and current at a temperature of 300K.

times are both equal to 1ns. The dependence of the probability on the driving and reverse currents is presented as a color map in Fig. 12.5. A net, but small reduction of the proper range of operation is obtained when no reverse current is applied, if compared with the corresponding curve ($J_r = 0$) plotted in Fig. 12.1. However, this reduction is compensated as the density of the reverse current is increased, with an approximately linear increase of the range of operation.

12.5 Conclusions

The current-driven DW motion of a ratchet FM strip previously reported[174] has been considered and improved along this work. It is demonstrated that the application during the DW relaxing time of a current of inverse polarity to that applied during the DW driving procedure reduces device latencies by reducing that relaxing time. That reverse current must be sufficiently intense as to drive the DW to the equilibrium position faster than the anisotropy slope itself, but with an amplitude rather low, so that DW backward shifting is not promoted. Alternatively, it is possible to use such a reverse current to increase the proper range of operation of the device for a given relaxing time, i.e., the pair of values of the driving current amplitude and pulse time that ensures single DW jumps for a certain latency time.

12.6 Acknowledgments

This work was supported by project WALL, FP7-PEOPLE-2013-ITN 608031 from the European Commission, project MAT2014-52477-C5-4-P from the Spanish Government, and project SA090U16 from the Junta de Castilla y León.

Conclusions

This thesis deals with the domain wall motion in multilayered systems with high perpendicular magnetic anisotropy. It has been focused on the effects of the presence of strong spin-orbit coupling in the heavy metal layer which, along with the lack of inversion symmetry, allows the coherent displacement of domain walls when an electric current is applied. The last part of the thesis also includes the effect of an inhomogeneous perpendicular anisotropy landscape.

Two main tools have been used for this study. First, the performance of micromagnetic simulations allows for the numerical solution of the Landau-Lifshitz-Gilbert equation. This kind of solvers permits an accurate quantitative study of those systems, allowing us to appreciate the rich and varied complexity of them, whose macroscopic properties are the result of an intricate game of equilibria between different energetic contributions, which veil most of its details. Second, the one dimensional model allows us to simplify this complexity, clarifying the physics involved and highlighting the main features that must be taken into account in order to understand multilayered systems. In spite of the numerous approximations made to develop this model, it has been shown a rather good agreement with the predictions drawn by the micromagnetic simulations, proving the validity of the model as a tool to study those systems.

Part I presents an extended introduction to the topic itself, focusing on the aspects treated by this thesis, where a detailed explanation of the origin and meaning of the Landau-Lifshitz-Gilbert equation is given. Besides, it also gives an explanation of the used tools that should serve to understand properly the following chapters.

Part II discusses the Dzyaloshinskii domain wall dynamics in ferromagnetic strips with high perpendicular magnetic anisotropy. This study reflects the existence of degenerate ground states. It also shows the dependence of the dynamics of the system not only on the applied stimuli but also on the initial domain wall configuration. If a stationary state exists, it may be different for the different ground states. Moreover, even though when the stationary state is the same, the dynamics of the transient differs and so do final positions. In both cases, a final position dependence on the initial state appears which may be of experimental relevance. Besides, it is shown that the precessional regime of the domain wall dynamics may be promoted or avoided by the application of an electric current, even though solely an electric current never induce such a precessional regime. Summarizing, this part constitutes a step forward in the understanding of systems with moderate DMI and can clarify the nature of the precessional regime and the degeneracy of non-quiral domain walls. Further conclusions can be found in the corresponding chapters.

Part III considers the angular dependence of the current-driven domain wall motion and its consequences for the geometrically control switching. This study constitutes a first theoretical attempt to describe the noncollinear current driven domain wall dynamics. The theoretical description presented can account for the experimental behavior at high currents, even though low current density results indicate that further theoretical and experimental efforts much be done. In any case, such a description can describe the mechanism behind the geometrically control switching. The boundary conditions imposed by the DMI at the edge of the sample allow the spin current to nucleate a new domain when it is assisted by the thermal field. After that, switching is determined by the relative velocities of the two types of domain walls.

Part IV is focused on the effect of an inhomogeneous anisotropy landscape. Particularly, it is considered a ferromagnetic strip where the anisotropy has been tailored so as to present a saw-toothed profile. The domain wall motion has been studied on such a strip by means of full micromagnetic simulations and the one dimensional model, which has been updating to account for space dependent anisotropy profile. It is shown that this simplified model can properly describe the main features of the domain wall motion. Moreover, it is stated that a sawtoothed profile can constitute a feasible pinning system ensuring the proper control of domain wall positions even in a current driven basis. Besides, bit density and shifting speed are enhanced in a current driven scheme as compared to the field driven case. Additionally, current driven basis allows finer tuning of pulse length and relaxing times. This permits to apply an electric current of the opposite polarity to reduce relaxing times or to increase proper operation times. Finally, different anisotropy profiles may be proposed for which bidirectional domain wall motion is possible under a current driven basis, while it would not be possible under a field driven scheme.

These works constitute a step forward in the development of a low-consuming non-volatile magnetic memory based on domain wall motion. Moreover, they clarify some aspects of multilayered systems providing a deeper and insightful knowledge about the domain wall dynamics and the role played by the spin-orbit torques. However, this thesis must be understood in its context, where a major collective effort seeks a better understanding of nature, in general, and particularly of magnetic materials. This thesis is focused on the consequences of the presence of strong spin-orbit coupling, and a better comprehension of them has been achieved. Nevertheless, it must be pointed out that along the time this thesis has taken, the same group has also worked on other important features of multilayered systems such as the effect of disorder and temperature leading to the results in references [90] and [94] respectively. Indeed, scientific research should not be understood as an individual and isolated effort to obtained answers about a particular problem, but as a collective one where the individual works from the same or different topic support each other and mixed giving the "scientific knowledge". In that way, Newton's statement can be recalled: "If I have seen further it is by standing on ye shoulders of Giants". But those giants are not only Faraday, Maxwell, Landau or Brown but the whole scientific community working together to improve our perception of nature. Summarizing, "sure, it may give some practical results, but that's not why we do it"[†].

[†]Attribute to R. Feynman

References

[1] L. Landau and E. Lifshits. On the theory of the dispersion of magnetic permeability in ferromagnetic bodies. *Phys. Zeitsch. der Sow.*, 8:153–169, 1935.

[2] E. H. Frei, S. Shtrikman, and D. Treves. Critical size and nucleation field of ideal ferromagnetic particles. *Phys. Rev.*, 106:446–455, 1957. doi:10.1103/PhysRev.106.446.

[3] William Fuller Brown, Jr. *Micromagnetics*. John Wiley & Sons, 1963.

[4] S. S. P. Parkin, K. P. Roche, M. G. Samant, P. M. Rice, R. B. Beyers, R. E. Scheuerlein, E. J. O'Sullivan, S. L. Brown, J. Bucchigano, D. W. Abraham, M. Rooks Y. Lu, P. L. Trouilloud, R. A. Wanner, and W. J. Gallagher. Exchange-biased magnetic tunnel junctions and application to nonvolatile magnetic random access memory. *Journal of Applied Physics*, 85(8):5828, 1999. doi:10.1063/1.369932.

[5] S. Parkin, Xin Jiang, C. Kaiser, A. Panchula, K. Roche, and M. Samant. Magnetically engineered spintronic sensors and memory. *Proceedings of the IEEE*, 91(5):661–680, 2003. doi:10.1109/JPROC.2003.811807.

[6] Igor Žutić, Jaroslav Fabian, and S. Das Sarma. Spintronics: Fundamentals and applications. *Rev. Mod. Phys.*, 76:323–410, 2004. doi:10.1103/RevModPhys.76.323.

[7] Ioan Mihai Miron, Kevin Garello, Gilles Gaudin, Pierre-Jean Zermatten, Marius V. Costache, Stéphane Auffret, Sébastien Bandiera, Bernard Rodmacq, Alain Schuhl, and Pietro Gambardella. Perpendicular switching of a single ferromagnetic layer induced by in-plane current injection. *Nature*, 476:189, 2011. doi:10.1038/nature10309.

[8] Ioan Mihai Miron, Thomas Moore, Helga Szambolics, Liliana Daniela Buda-Prejbeanu, Stéphane Auffret, Bernard Rodmacq, Stefania Pizzini, Jan Vogel, Marlio Bonfim, Alain Schuhl, and Gilles Gaudin. Fast current-induced domain-wall motion controlled by the Rashba effect. *Nature Materials*, 10(6):419–423, 2011. doi:10.1038/nmat3020.

[9] Luqiao Liu, O. J. Lee, T. J. Gudmundsen, D. C. Ralph, and R. A. Buhrman. Current-induced switching of perpendicularly magnetized magnetic layers using spin torque from the spin Hall effect. *Phys. Rev. Lett.*, 109:096602, 2012. doi:10.1103/PhysRevLett.109.096602.

[10] P. P. J. Haazen, E. Mure, J. H. Franken, R. Lavrijsen, H. J. M. Swagten, and B. Koopmans. Domain wall depinning governed by the spin Hall effect. *Nature Materials*, 12:299, 2013. doi:10.1038/NMAT3553.

[11] K-S. Ryu, L. Thomas, S-H. Yang, and S. Parkin. Chiral spin torque at magnetic domain walls. *Nature Nanotechnology*, 8:527, 2013. doi:10.1038/nnano.2013.102.

[12] S. Emori, U. Bauer, S.M. Ahn, E. Martinez, and G. S. D. Beach. Current-driven dynamics of chiral ferromagnetic domain walls. *Nature Materials*, 12:611, 2013. doi:10.1038/nmat3675.

[13] Kevin Garello, Ioan Mihai Miron, Can Onur Avci, Frank Freimuth, Yuriy Mokrousov, Stefan Blügel, Stéphane Auffret, Olivier Boulle, Gilles Gaudin, and Pietro Gambardella. Symmetry and magnitude of spin–orbit torques in ferromagnetic heterostructures. *Nature Nanotechnology*, 8:587, 2013. doi:10.1038/nnano.2013.145.

[14] E. Martinez, S. Emori, and G. S. D. Beach. Current-driven domain wall motion along high perpendicular anisotropy multilayers: The role of the Rashba field, the spin Hall effect, and the Dzyaloshinskii-Moriya interaction. *Applied Physics Letters*, 103:072406, 2013. doi:10.1063/1.4818723.

[15] S. Pizzini, J. Vogel, S. Rohart, L. D. Buda-Prejbeanu, E. Jué, O. Boulle, I. M. Miron, C. K. Safeer, S. Auffret, G. Gaudin, and A. Thiaville. Chirality-induced asymmetric magnetic nucleation in Pt/Co/AlO_x ultrathin microstructures. *Phys. Rev. Lett.*, 113:047203, 2014. doi:10.1103/PhysRevLett.113.047203.

[16] O. Boulle, L. D. Buda-Prejbeanu, E. Jué, I. M. Miron, and G. Gaudin. Current induced domain wall dynamics in the presence of spin orbit torques. *Journal of Applied Physics*, 115:17D502, 2014. doi:10.1063/1.4860946.

[17] Satoru Emori, Eduardo Martinez, Kyung-Jin Lee, Hyun-Woo Lee, Uwe Bauer, Sung-Min Ahn, Parnika Agrawal, David C. Bono, and Geoffrey S. D. Beach. Spin Hall torque magnetometry of Dzyaloshinskii domain walls. *Phys. Rev. B*, 90:184427, 2014. doi:10.1103/PhysRevB.90.184427.

[18] Guoqiang Yu, Pramey Upadhyaya, Yabin Fan, Juan G. Alzate, Wanjun Jiang, Kin L. Wong, So Takei, Scott A. Bender, Li-Te Chang, Ying Jiang, Murong Lang, Jianshi Tang, Yong Wang, Yaroslav Tserkovnyak, Pedram Khalili Amiri, and Kang L. Wang. Switching of perpendicular magnetization by spin–orbit torques in the absence of external magnetic fields. *Nature Nanotechnology*, 9: 548, 2014. doi:10.1038/nnano.2014.94.

[19] E. Martinez, S. Emori, N. Perez, L. Torres, and G. S. D. Beach. Current-driven dynamics of Dzyaloshinskii domain walls in the presence of in-plane fields: Full micromagnetic and one-dimensional analysis. *Journal of Applied Physics*, 115: 213909, 2014. doi:10.1063/1.4881778.

[20] A. Hrabec, N. A. Porter, A. Wells, M. J. Benitez, G. Burnell, S. McVitie, D. McGrouther, T. A. Moore, and C. H. Marrows. Measuring and tailoring the Dzyaloshinskii-Moriya interaction in perpendicularly magnetized thin films. *Phys. Rev. B*, 90:020402, 2014. doi:10.1103/PhysRevB.90.020402.

[21] Jacob Torrejon, Junyeon Kim, Jaivardhan Sinha, Seiji Mitani, Masamitsu Hayashi, Michihiko Yamanouchi, and Hideo Ohno. Interface control of the magnetic chirality in CoFeB/MgO heterostructures with heavy-metal underlayers. *Nature Communications*, 5:4655, 2014. doi:10.1038/ncomms5655.

[22] Kevin Garello, Can Onur Avci, Ioan Mihai Miron, Manuel Baumgartner, Abhijit Ghosh, Stéphane Auffret, Olivier Boulle, Gilles Gaudin, and Pietro Gambardella. Ultrafast magnetization switching by spin-orbit torques. *Applied Physics Letters*, 105:212402, 2014. doi:10.1063/1.4902443.

[23] Eduardo Martinez, Luis Torres, Noel Perez, Maria Auxiliadora Hernandez, Victor Raposo, and Simone Moretti. Universal chiral-triggered magnetization switching in confined nanodots. *Scientific Reports*, 5:10156, 6 2015. doi:10.1038/srep10156.

[24] M. N. Baibich, J. M. Broto, A. Fert, F. Nguyen Van Dau, F. Petroff, P. Etienne, G. Creuzet, A. Friederich, and J. Chazelas. Giant magnetoresistance of (001)Fe/(001)Cr magnetic superlattices. *Phys. Rev. Lett.*, 61:2472–2475, 1988. doi:10.1103/PhysRevLett.61.2472.

[25] G. Binasch, P. Grünberg, F. Saurenbach, and W. Zinn. Enhanced magnetoresistance in layered magnetic structures with antiferromagnetic interlayer exchange. *Phys. Rev. B*, 39:4828–4830, 1989. doi:10.1103/PhysRevB.39.4828.

[26] S. S. P. Parkin, R. Bhadra, and K. P. Roche. Oscillatory magnetic exchange coupling through thin copper layers. *Phys. Rev. Lett.*, 66:2152–2155, 1991. doi:10.1103/PhysRevLett.66.2152.

[27] S. S. P. Parkin, M. Hayashi, and L. Thomas. Magnetic domain-wall racetrack memory. *Science*, 320:190, 2008. doi:10.1126/science.1145799.

[28] S. Parkin and S.H. Yang. Memory on the racetrack. *Nature Nanotechnology*, 10:195, 2015. doi:10.1038/nnano.2015.41.

[29] U. Gradmann and J. Müller. Flat ferromagnetic, epitaxial 48Ni/62Fe(111) films of few atomic layers. *Phys. Status Solidi*, 27:313, 1968.

[30] P. F. Carcia, A. D. Meinhaldt, and A. Suna. Perpendicular magnetic anisotropy in Pd/Co thin film layered structures. *Applied Physics Letters*, 47:176, 1985. doi:10.1063/1.96254.

[31] P. F. Carcia. Perpendicular magnetic anisotropy in Pd/Co and Pt/Co thin-film layered structures. *Journal of Applied Physics*, 63:5066, 1988. doi:10.1063/1.340404.

[32] F. J. A. den Broeder, D. Kuiper, A. P. van de Mosselaer, and W. Hoving. Perpendicular magnetic anisotropy of co-au multilayers induced by interface sharpening. *Phys. Rev. Lett.*, 60:2769–2772, Jun 1988. doi:10.1103/PhysRevLett.60.2769.

[33] M. Sakurai, T. Takahata, and I. Moritani. Magnetic and magneto-optical properties of co/ru multilayers. *IEEE Translation Journal on Magnetics in Japan*, 7(2):176–182, 1992. doi:10.1109/TJMJ.1992.4565351.

[34] F.J.A. den Broeder, W. Hoving, and P.J.H. Bloemen. Magnetic anisotropy of multilayers. *Journal of Magnetism and Magnetic Materials*, 93(Supplement C):562 – 570, 1991. doi:10.1016/0304-8853(91)90404-X.

[35] M. T. Johnson, P. J. H. Bloemen, F. J. A. den Broeder, and J J de Vries. Magnetic anisotropy in metallic multilayers. *Reports on Progress in Physics*, 59 (11):1409, 1996. URL http://stacks.iop.org/0034-4885/59/i=11/a=002.

[36] J. Franken. *Domain walls shift gears*. PhD thesis, Technische Universiteit Eindhoven, 2014.

[37] I. Dzyaloshinsky. A thermodynamic theory of "weak" ferromagnetism of antiferromagnetics. *J. Phys. Chem. Solids*, 4:241–255, 1958.

[38] Tôru Moriya. New mechanism of anisotropic superexchange interaction. *Phys. Rev. Lett.*, 4:228–230, 1960. doi:10.1103/PhysRevLett.4.228.

[39] Tôru Moriya. Anisotropic superexchange interaction and weak ferromagnetism. *Phys. Rev.*, 120:91–98, 1960. doi:10.1103/PhysRev.120.91.

[40] M. Bode, M. Heide, K. von Bergmann, P. Ferriani, S. Heinze, G. Bihlmayer, A. Kubetzka, O. Pietzsch, S. Blügel, and R. Wiesendanger. Chiral magnetic order at surfaces driven by inversion asymmetry. *Nature*, 447:190, 2007. doi:10.1038/nature05802.

[41] A. Thiaville, S. Rohart, É. Jué, V. Cros, and A. Fert. Dynamics of Dzyaloshinskii domain walls in ultrathin magnetic films. *Europhysics Letters*, 100(5): 57002, 2012. doi:10.1209/0295-5075/100/57002.

[42] S. Rohart and A. Thiaville. Skyrmion confinement in ultrathin film nanostructures in the presence of Dzyaloshinskii-Moriya interaction. *Phys. Rev. B*, 88: 184422, 2013. doi:10.1103/PhysRevB.88.184422.

[43] Soong-Geun Je, Duck-Ho Kim, Sang-Cheol Yoo, Byoung-Chul Min, Kyung-Jin Lee, and Sug-Bong Choe. Asymmetric magnetic domain-wall motion by the Dzyaloshinskii-Moriya interaction. *Phys. Rev. B*, 88:214401, 2013. doi:10.1103/PhysRevB.88.214401.

[44] N. Perez, L. Torres, and E. Martinez-Vecino. Micromagnetic modeling of Dzyaloshinskii-Moriya interaction in spin Hall effect switching. *IEEE Transactions on Magnetics*, 50(11):1–4, 2014. doi:10.1109/TMAG.2014.2323707.

[45] Hongxin Yang, André Thiaville, Stanislas Rohart, Albert Fert, and Mairbek Chshiev. Anatomy of Dzyaloshinskii-Moriya interaction at Co/Pt interfaces. *Phys. Rev. Lett.*, 115:267210, Dec 2015. doi:10.1103/PhysRevLett.115.267210.

[46] M. Belmeguenai, M. S. Gabor, Y. Roussigné, A. Stashkevich, S. M. Chérif, F. Zighem, and C. Tiusan. Brillouin light scattering investigation of the thickness dependence of Dzyaloshinskii-Moriya interaction in $Co_{0.5}Fe_{0.5}$ ultrathin films. *Phys. Rev. B*, 93:174407, 2016. doi:10.1103/PhysRevB.93.174407.

[47] Arseni Goussev, J. M. Robbins, Valeriy Slastikov, and Oleg A. Tretiakov. Dzyaloshinskii-Moriya domain walls in magnetic nanotubes. *Phys. Rev. B*, 93: 054418, 2016. doi:10.1103/PhysRevB.93.054418.

[48] A. L. Balk, K-W. Kim, D. T. Pierce, M. D. Stiles, J. Unguris, and S. M. Stavis. Simultaneous control of the Dzyaloshinskii-Moriya interaction and magnetic anisotropy in nanomagnetic trilayers. *Physical Review Letters*, 119:077205, 2017. doi:10.1103/PhysRevLett.119.077205.

[49] M. I. Dyakonov and V. I. Perel. Current-induced spin orientation in semiconductors. *Physics Letters*, 35A(6):459, 1971.

[50] J. E. Hirsch. Spin Hall effect. *Phys. Rev. Lett.*, 83:1834–1837, 1999. doi:10.1103/PhysRevLett.83.1834.

[51] Shufeng Zhang. Spin Hall effect in the presence of spin diffusion. *Phys. Rev. Lett.*, 85:393–396, 2000. doi:10.1103/PhysRevLett.85.393.

[52] E. Saitoh, M. Ueda, H. Miyajima, and G. Tatara. Conversion of spin current into charge current at room temperature: Inverse spin-Hall effect. *Applied Physics Letters*, 88(18):182509, 2006. doi:10.1063/1.2199473.

[53] S. O. Valenzuela and M. Tinkham. Direct electronic measurement of the spin Hall effect. *Nature*, 442:176, 2006. doi:10.1038/nature04937.

[54] T. Kimura, Y. Otani, T. Sato, S. Takahashi, and S. Maekawa. Room-temperature reversible spin Hall effect. *Phys. Rev. Lett.*, 98:156601, 2007. doi:10.1103/PhysRevLett.98.156601.

[55] S. Takahashi and S. Maekawa. Nonlocal spin Hall effect and spin–orbit interaction in nonmagnetic metals. *Journal of Magnetism and Magnetic Materials*, 310:2067–2069, 2007. doi:10.1016/j.jmmm.2006.10.1124.

[56] Yan-Ting Chen, Saburo Takahashi, Hiroyasu Nakayama, Matthias Althammer, Sebastian T B Goennenwein, Eiji Saitoh, and Gerrit E W Bauer. Theory of spin hall magnetoresistance (SMR) and related phenomena. *Journal of Physics: Condensed Matter*, 28(10):103004, 2016. doi:10.1088/0953-8984/28/10/103004.

[57] L.D. Landau and E.M. Lifshitz. *Curso de Física Teórica*, volume 3 Mecánica cuántica no relativista. Ed. Reverté, 1983.

[58] S. Mühlbauer, B. Binz, F. Jonietz, C. Pfleiderer, A. Rosch, A. Neubauer, R. Georgii, and P. Böni. Skyrmion lattice in a chiral magnet. *Science*, 323:915, 2011. doi:10.1126/science.1166767.

[59] S. X. Huang and C. L. Chien. Extended skyrmion phase in epitaxial FeGe(111) thin films. *Phys. Rev. Lett.*, 108:267201, 2012. doi:10.1103/PhysRevLett.108.267201.

[60] Giovanni Finocchio, Felix Büttner, Riccardo Tomasello, Mario Carpentieri, and Mathias Kläui. Magnetic skyrmions: from fundamental to applications. *Journal of Physics D: Applied Physics*, 49(42):423001, 2016. doi:10.1088/0022-3727/49/42/423001.

[61] H.Y. Kwon and C. Won. Effects of Dzyaloshinskii–Moriya interaction on magnetic stripe domains. *Journal of Magnetism and Magnetic Materials*, 351: 8–15, 2014. doi:10.1016/j.jmmm.2013.09.056.

[62] J.C. Slonczewski. Current-driven excitation of magnetic multilayers. *Journal of Magnetism and Magnetic Materials*, 159(1):L1 – L7, 1996. ISSN 0304-8853. doi:10.1016/0304-8853(96)00062-5.

[63] Z. Li, J. He, and S. Zhang. Effects of spin current on ferromagnets (invited). *Journal of Applied Physics*, 99(8):08Q702, 2006. doi:10.1063/1.2166590.

[64] K. Ando, S. Takahashi, K. Harii, K. Sasage, J. Ieda, S. Maekawa, and E. Saitoh. Electric manipulation of spin relaxation using the spin Hall effect. *Phys. Rev. Lett.*, 101:036601, 2008. doi:10.1103/PhysRevLett.101.036601.

[65] G. Bertotti. *Hysteresis in Magnetism. For physicists, material scientist and engineers*. Academic Press, 1998.

[66] A. P. Malozemoff and J. C. Slonczewski. *Magnetic Domain Walls in Bubble Materials*. Academic Press, 1979.

[67] E. Martínez. *Modelización de procesos dinámicos de la magnetización*. PhD thesis, Universidad de Salamanca. Facultad de Ciencias, 2005.

[68] Helmut Kronmüller. *Handbook of Magnetism and Advanced Magnetic Materials. General Micromagnetic Theory*, volume 2 Micromagnetism. John Wiley & Sons, 2007.

[69] Jacques E. Miltat and Michael J. Donahue. *Handbook of Magnetism and Advanced Magnetic Materials. Numerical Micromagnetics: Finite Difference Methods*, volume 2 Micromagnetism. John Wiley & Sons, 2007.

[70] Jr W. F. Brown. Thermal fluctuation of a single-domain particle. *Physical Review*, 130:1677, 1963. doi:10.1103/PhysRev.130.1677.

[71] N. L. Schryer and L. R. Walker. The motion of 180° domain walls in uniform dc magnetic fields. *Journal of Applied Physics*, 45(12):5406, 1974. doi:10.1063/1.1663252.

[72] O. Boulle, S. Rohart, L. D. Buda-Prejbeanu, E. Jué, I. M. Miron, S. Pizzini, J. Vogel, G. Gaudin, and A. Thiaville. Domain wall tilting in the presence of the Dzyaloshinskii-Moriya interaction in out-of-plane magnetized magnetic nanotracks. *Phys. Rev. Lett.*, 111:217203, 2013. doi:10.1103/PhysRevLett.111.217203.

[73] J. Kwon, S. Goolaup, W. L. Gan, C. H. Chang, K. Roy, and W. S. Lew. Asymmetrical domain wall propagation in bifurcated PMA wire structure due to the Dzyaloshinskii-Moriya interaction. *Applied Physics Letters*, 110(23): 232402, 2017. doi:10.1063/1.4984750.

[74] R Tomasello, V Puliafito, E Martinez, A Manchon, M Ricci, M Carpentieri, and G Finocchio. Performance of synthetic antiferromagnetic racetrack memory: domain wall versus skyrmion. *Journal of Physics D: Applied Physics*, 50(32): 325302, 2017. doi:10.1088/1361-6463/aa7a98.

[75] S. S. P. Parkin, N. More, and K. P. Roche. Oscillations in exchange coupling and magnetoresistance in metallic superlattice structures: Co/Ru, Co/Cr, and Fe/Cr. *Phys. Rev. Lett.*, 64:2304–2307, 1990. doi:10.1103/PhysRevLett.64.2304.

[76] See-Hun Yang and Stuart Parkin. Novel domain wall dynamics in synthetic antiferromagnets. *Journal of Physics: Condensed Matter*, 29(30):303001, 2017. doi:10.1088/1361-648X/aa752d.

[77] See-Hun Yang, Kwang-Su Ryu, and Stuart Parkin. Domain-wall velocities of up to $750ms^{-1}$ driven by exchange-coupling torque in synthetic antiferromagnets. *Nature Nanotechnology*, 10:221–226, 2015. doi:10.1038/nnano.2014.324.

[78] C. K. Safeer, Emilie Jué, Alexandre Lopez, Liliana Buda-Prejbeanu, Stéphane Auffret, Stefania Pizzini, Olivier Boulle, Ioan Mihai Miron, and Gilles Gaudin. Spin–orbit torque magnetization switching controlled by geometry. *Nature Nanotechnology*, 11:143, 2016. doi:10.1038/nnano.2015.252.

[79] J. H. Franken, M. Hoeijmakers, R. Lavrijsen, and H. J. M Swagten. Domain-wall pinning by local control of anisotropy in Pt/Co/Pt strips. *Journal of Physics: Condensed Matter*, 24:024216, 2012. doi:10.1088/0953-8984/24/2/024216.

[80] J. H. Franken, H. J. M. Swagten, and B. Koopmans. Shift registers based on magnetic domain wall ratchets with perpendicular anisotropy. *Nature Nanotechnology*, 7:499, 2012. doi:10.1038/nnano.2012.111.

[81] Stephen Blundell. *Magnetism in Condensed Matter*. Oxford University Press, 2001.

[82] D. A. Garanin. Fokker-planck and Landau-Lifshitz-Bloch equations for classical ferromagnets. *Phys. Rev. B*, 55:3050–3057, 1997. doi:10.1103/PhysRevB.55.3050.

[83] O. Chubykalo-Fesenko, U. Nowak, R. W. Chantrell, and D. Garanin. Dynamic approach for micromagnetics close to the curie temperature. *Phys. Rev. B*, 74: 094436, 2006. doi:10.1103/PhysRevB.74.094436.

[84] N. Kazantseva, D. Hinzke, U. Nowak, R. W. Chantrell, U. Atxitia, and O. Chubykalo-Fesenko. Towards multiscale modeling of magnetic materials: Simulations of fept. *Phys. Rev. B*, 77:184428, 2008. doi:10.1103/PhysRevB.77.184428.

[85] R. F. L. Evans, D. Hinzke, U. Atxitia, U. Nowak, R. W. Chantrell, and O. Chubykalo-Fesenko. Stochastic form of the landau-lifshitz-bloch equation. *Phys. Rev. B*, 85:014433, 2012. doi:10.1103/PhysRevB.85.014433.

[86] Simone Moretti, Victor Raposo, and Eduardo Martinez. Influence of Joule heating on current-induced domain wall depinning. *Journal of Applied Physics*, 119(21):213902, 2016. doi:10.1063/1.4953008.

[87] Simone Moretti, Victor Raposo, Eduardo Martinez, and Luis Lopez-Diaz. Domain wall motion by localized temperature gradients. *Phys. Rev. B*, 95: 064419, 2017. doi:10.1103/PhysRevB.95.064419.

[88] Gonçalo Marcos Baião de Albuquerque. *Magnetisation Precession in Confined Geometry: Physical and Numerical Aspects*. PhD thesis, Université Paris XI UFR Scientifique D'Orsay, 2002.

[89] J. Safko H. Goldstein, C. Poole. *Classical Mechanics*. Ed. Addison Wesley, 2000.

[90] Michele Voto. *Advanced modelling of domain wall dynamics for spintronic devices*. PhD thesis, Universidad de Salamanca, 2017.

[91] Neil W. Ashcroft and N. David Mermin. *Solid State Physics*. Harcourt College Publishers, 1976.

[92] Charles Kittel. *Introduction to Solid State Physics*. John Wiley & Sons, 2005.

[93] L.D. Landau and E.M. Lifshitz. *Curso de Física Teórica*, volume 8 Electrodinámica de los medios continuos. Ed. Reverté, 1981.

[94] Simone Moretti. *Micromagnetic study of magnetic domain wall motion: thermal effects and spin torques*. PhD thesis, Universidad de Salamanca, 2017.

[95] L. Berger. Exchange interaction between electric current and magnetic domain wall containing Bloch lines. *Journal of Applied Physics*, 63(5):1663–1669, 1988. doi:10.1063/1.339899.

[96] L. Berger. Motion of a magnetic domain wall traversed by fast-rising current pulses. *Journal of Applied Physics*, 71(6):2721–2726, 1992. doi:10.1063/1.351045.

[97] J.Z Sun. Current-driven magnetic switching in manganite trilayer junctions. *Journal of Magnetism and Magnetic Materials*, 202(1):157 – 162, 1999. ISSN 0304-8853. doi:10.1016/S0304-8853(99)00289-9.

[98] L. Berger. Interaction of electrons with spin waves in the bulk and in multilayers (invited). *Journal of Applied Physics*, 91(10):6795–6800, 2002. doi:10.1063/1.1446121.

[99] Gen Tatara and Hiroshi Kohno. Theory of current-driven domain wall motion: Spin transfer versus momentum transfer. *Phys. Rev. Lett.*, 92:086601, 2004. doi:10.1103/PhysRevLett.92.086601.

[100] S. Zhang and Z. Li. Roles of nonequilibrium conduction electrons on the magnetization dynamics of ferromagnets. *Phys. Rev. Lett.*, 93:127204, 2004. doi:10.1103/PhysRevLett.93.127204.

[101] A. Thiaville, Y. Nakatani, J. Miltat, and Y. Suzuki. Micromagnetic understanding of current-driven domain wall motion in patterned nanowires. *EPL (Europhysics Letters)*, 69(6):990, 2005. doi:10.1209/epl/i2004-10452-6.

[102] Gen Tatara, Hiroshi Kohno, and Junya Shibata. Microscopic approach to current-driven domain wall dynamics. *Physics Reports*, 468(6):213 – 301, 2008. doi:https://doi.org/10.1016/j.physrep.2008.07.003.

[103] O. Boulle, G. Malinowski, and M. Kläui. Current-induced domain wall motion in nanoscale ferromagnetic elements. *Materials Science and Engineering: R: Reports*, 72(9):159 – 187, 2011. doi:10.1016/j.mser.2011.04.001.

[104] J. Vandermeulen, B. Van de Wiele, A. Vansteenkiste, B. Van Waeyenberge, and L. Dupré. A collective coordinate approach to describe magnetic domain wall dynamics applied to nanowires with high perpendicular anisotropy. *Journal of Physics D: Applied Physics*, 48(3):035001, 2015. doi:10.1088/0022-3727/48/3/035001.

[105] A. V. Khvalkovskiy, V. Cros, D. Apalkov, V. Nikitin, M. Krounbi, K. A. Zvezdin, A. Anane, J. Grollier, and A. Fert. Matching domain-wall configuration and spin-orbit torques for efficient domain-wall motion. *Phys. Rev. B*, 87:020402, 2013. doi:10.1103/PhysRevB.87.020402.

[106] J. P. Tetienne, T. Hingant, L.J. Martínez, S. Rohart, A. Thiaville, L. Herrera Diez, K. Garcia, J. P. Adam, J. V. Kim, J. F. Roch, I.M. Miron, G. Gaudin, L. Vila, B. Ocker, D. Ravelosona, and V. Jacques. The nature of domain walls in ultrathin ferromagnets revealed by scanning nanomagnetometry. *Nature Communications*, 6:6:6733, 2015. doi:10.1038/ncomms7733.

[107] Han Yan, Peng-Bin He, Meng-Qiu Cai, and Zai-Dong Li. Dynamics of chiral domain wall under the spin-orbit torques in heavy metal/ferromagnet bilayers with in-plane anisotropy. *Journal of Magnetism and Magnetic Materials*, 441 (Supplement C):691 – 695, 2017. doi:10.1016/j.jmmm.2017.06.008.

[108] Yu A Bychkov and E I Rashba. Oscillatory effects and the magnetic susceptibility of carriers in inversion layers. *Journal of Physics C: Solid State Physics*, 17(33):6039, 1984. doi:10.1088/0022-3719/17/33/015.

[109] Frank Erik Meijer. *Rashba spin-orbit interaction in mesoscopic systems*. PhD thesis, Technische Universiteit Delft, 2005.

[110] A. Manchon and S. Zhang. Theory of nonequilibrium intrinsic spin torque in a single nanomagnet. *Phys. Rev. B*, 78:212405, 2008. doi:10.1103/PhysRevB.78.212405.

[111] W. Brown. Thermal fluctuation of fine ferromagnetic particles. *IEEE Transactions on Magnetics*, 15(5):1196–1208, 1979. doi:10.1109/TMAG.1979.1060329.

[112] Russell P. Cowburn. The future of universal memory. *Materials Today*, 6(7):32 – 38, 2003. ISSN 1369-7021. doi:10.1016/S1369-7021(03)00730-2.

[113] J. Luis García-Palacios and F. J. Lázaro. Langevin-dynamics study of the dynamical properties of small magnetic particles. *Physical Review B*, 58:14 937, 1998. doi:10.1103/PhysRevB.58.14937.

[114] E. Martinez, L. Lopez-Diaz, L. Torres, C. Tristan, and O. Alejos. Thermal effects in domain wall motion: Micromagnetic simulations and analytical model. *Physical Review B*, 75:174409, 2007. doi:10.1103/PhysRevB.75.174409.

[115] R. A. Duine, A. S. Núñez, and A. H. MacDonald. Thermally assisted current-driven domain-wall motion. *Physical Review Letters*, 98:056605, 2007. doi:10.1103/PhysRevLett.98.056605.

[116] J. L. Garcia-Palacios. Introduction to the theory of stochastic processes and Brownian motion problems. *eprint arXiv:cond-mat/0701242*, 2007. URL http://adsabs.harvard.edu/abs/2007cond.mat..1242G. Provided by the SAO/NASA Astrophysics Data System.

[117] Eduardo Martinez. The stochastic nature of the domain wall motion along high perpendicular anisotropy strips with surface roughness. *Journal of Physics: Condensed Matter*, 24(2):024206, 2012. doi:10.1088/0953-8984/24/2/024206.

[118] Miguel Vera Moreno, Zochil González Arenas, and Daniel G. Barci. Langevin dynamics for vector variables driven by multiplicative white noise: A functional formalism. *Phys. Rev. E*, 91:042103, 2015. doi:10.1103/PhysRevE.91.042103.

[119] Leonard Mandel and Emil Wolf. *Optical coherence and quantum optics*. Cambridge University Press, 1995.

[120] William H. Press, Saul A. Teukolsky, William T. Vetterling, and Brian P. Flannery. *Numerical Recipes in C. The Art of Scientific Computing*. Cambridge University Press, 1992.

[121] http://www.goparallel.net/index.php/en/gp software.html. http://www.goparallel.net.

[122] A. Vansteenkiste, J. Leliaert, M. Dvornik, M. Helsen, F. Garcia-Sanchez, and B. Van Waeyenberge. The design and verification of MuMax3. *AIP Advances*, 4:107133, 2014. doi:10.1063/1.4899186.

[123] J. C. Butcher. *Numerical Methods for Ordinary Differential Equations*. John Wiley & Sons, 2008.

[124] A. Thiaville, J. M. García, and J. Miltat. Domain wall dynamics in nanowires. *Journal of Magnetism and Magnetic Materials*, 242-245:1061–1063, 2002. doi:10.1016/S0304-8853(01)01353-1.

[125] Masamitsu Hayashi. *Current driven dynamics of magnetic domain walls in permalloy nanowires*. PhD thesis, Standford University, 2006.

[126] Yue Zhang, Xueying Zhang, Jingtong Hu, Jiang Nan, Zhenyi Zheng, Zhizhong Zhang, Youguang Zhang, Nicolas Vernier, Dafine Ravelosona, and Weisheng Zhao. Ring-shaped racetrack memory based on spin orbit torque driven chiral domain wall motions. *Scientific Reports*, 6:35062, 2016. doi:10.1038/srep35062.

[127] William Robert Grove. Vii. on the electro-chemical polarity of gases. *Philosophical Transactions of the Royal Society of London*, 142:87–101, 1852. doi:10.1098/rstl.1852.0008.

[128] J. Musil and J. Vlček. Magnetron sputtering of films with controlled texture and grain size. *Materials Chemistry and Physics*, 54(1):116 – 122, 1998. ISSN 0254-0584. doi:10.1016/S0254-0584(98)00020-0. Symposium H of the 4th IUMRS International Conference in Asia.

[129] P.J Kelly and R.D Arnell. Magnetron sputtering: a review of recent developments and applications. *Vacuum*, 56(3):159 – 172, 2000. ISSN 0042-207X. doi:https://doi.org/10.1016/S0042-207X(99)00189-X.

[130] G. Bräuer, B. Szyszka, M. Vergöhl, and R. Bandorf. Magnetron sputtering – milestones of 30 years. *Vacuum*, 84(12):1354 – 1359, 2010. doi:10.1016/j.vacuum.2009.12.014.

[131] M. Yuting Liu. *Electric field control of magnetic domain wall dynamics*. PhD thesis, Université Paris-Sud, 2017.

[132] E. H. Hall. On a new action of the magnet on electric currents. *American Journal of Mathematics*, 2(3):287–292, 1879. doi:10.2307/2369245.

[133] N A Sinitsyn. Semiclassical theories of the anomalous hall effect. *Journal of Physics: Condensed Matter*, 20(2):023201, 2008. doi:10.1088/0953-8984/20/02/023201.

[134] J Fassbender, D Ravelosona, and Y Samson. Tailoring magnetism by light-ion irradiation. *Journal of Physics D: Applied Physics*, 37(16):R179, 2004. doi:10.1088/0022-3727/37/16/R01.

[135] L. Herrera Diez, F. García-Sánchez, J.-P. Adam, T. Devolder, S. Eimer, M. S. El Hadri, A. Lamperti, R. Mantovan, B. Ocker, and D. Ravelosona. Controlling magnetic domain wall motion in the creep regime in he+-irradiated cofeb/mgo films with perpendicular anisotropy. *Applied Physics Letters*, 107(3):032401, 2015. doi:10.1063/1.4927204.

[136] John Kerr LL.D. Xliii. on rotation of the plane of polarization by reflection from the pole of a magnet. *The London, Edinburgh, and Dublin Philosophical Magazine and Journal of Science*, 3(19):321–343, 1877. doi:10.1080/14786447708639245.

[137] John Kerr LL.D. Xxiv. on reflection of polarized light from the equatorial surface of a magnet. *The London, Edinburgh, and Dublin Philosophical Magazine and Journal of Science*, 5(30):161–177, 1878. doi:10.1080/14786447808639407.

[138] Z. Q. Qiu and S. D. Bader. Surface magneto-optic kerr effect. *Review of Scientific Instruments*, 71(3):1243–1255, 2000. doi:10.1063/1.1150496.

[139] L. Sánchez-Tejerina, Ó. Alejos, E. Martínez, and J.M. Muñoz. Asymmetric driven dynamics of Dzyaloshinskii domain walls in ultrathin ferromagnetic strips with perpendicular magnetic anisotropy. *Journal of Magnetism and Magnetic Materials*, 409(Supplement C):155 – 162, 2016. doi:10.1016/j.jmmm.2016.02.067.

[140] D. A. Allwood, G. Xiong, C. C. Faulkner, D. Atkinson, D. Petit, and R. P. Cowburn. Magnetic domain-wall logic. *Science*, 309(5741):1688–1692, 2005. doi:10.1126/science.1108813.

[141] Ioan Mihai Miron, Gilles Gaudin, Stéphane Auffret, Bernard Rodmacq, Alain Schuhl, Stefania Pizzini, Jan Vogel, and Pietro Gambardella. Current-driven

spin torque induced by the Rashba effect in a ferromagnetic metal layer. *Nature Materials*, 9:230–234, 2010. doi:10.1038/nmat2613.

[142] Luqiao Liu, Chi-Feng Pai, Y. Li, H. W. Tseng, D. C. Ralph, and R. A. Buhrman. Spin-torque switching with the giant spin hall effect of tantalum. *Science*, 336 (6081):555–558, 2012. doi:10.1126/science.1218197.

[143] Jacob Torrejon, Felipe Garcia-Sanchez, Tomohiro Taniguchi, Jaivardhan Sinha, Seiji Mitani, Joo-Von Kim, and Masamitsu Hayashi. Current-driven asymmetric magnetization switching in perpendicularly magnetized cofeb/mgo heterostructures. *Phys. Rev. B*, 91:214434, 2015. doi:10.1103/PhysRevB.91.214434.

[144] M. Heide, G. Bihlmayer, and S. Blügel. Dzyaloshinskii-moriya interaction accounting for the orientation of magnetic domains in ultrathin films: Fe/w(110). *Phys. Rev. B*, 78:140403, 2008. doi:10.1103/PhysRevB.78.140403.

[145] Eduardo Martínez and Óscar. Alejos. Coupled dzyaloshinskii walls and their current-induced dynamics by the spin hall effect. *Journal of Applied Physics*, 116(2):023909, 2014. doi:10.1063/1.4889848.

[146] A. P. Malozemoff and J. C. Slonczewski. *Magnetic Domain Walls in Bubble Material*. Academic Press, 1979.

[147] Giancarlo Consolo, Carmela Currò, and Giovanna Valenti. Curved domain walls dynamics driven by magnetic field and electric current in hard ferromagnets. *Applied Mathematical Modelling*, 38(3):1001 – 1010, 2014. doi:https://doi.org/10.1016/j.apm.2013.07.032.

[148] Luc Thomas, Masamitsu Hayashi, Xin Jiang, Rai Moriya, Charles Rettner, and Stuart Parkin. Resonant amplification of magnetic domain-wall motion by a train of current pulses. *Science*, 315(5818):1553–1556, 2007. doi:10.1126/science.1137662.

[149] S.V. Tarasenko, A. Stankiewicz, V.V. Tarasenko, and J. Ferré. Bloch wall dynamics in ultrathin ferromagnetic films. *Journal of Magnetism and Magnetic Materials*, 189(1):19 – 24, 1998. ISSN 0304-8853. doi:10.1016/S0304-8853(98)00230-3.

[150] L Lopez-Diaz, D Aurelio, L Torres, E Martinez, M A Hernandez-Lopez, J Gomez, O Alejos, M Carpentieri, G Finocchio, and G Consolo. Micromagnetic simulations using graphics processing units. *Journal of Physics D: Applied Physics*, 45(32):323001, 2012. doi:10.1088/0022-3727/45/32/323001.

[151] L. Sánchez-Tejerina, O. Alejos, and E. Martínez. Steady-state configurations of dzyaloshinskii domain walls driven by field and current. *Journal of Magnetism and Magnetic Materials*, 423(Supplement C):405 – 410, 2017. doi:10.1016/j.jmmm.2016.09.116.

[152] Kwang-Su Ryu, See-Hun Yang 1, Luc Thomas, and Stuart S.P. Parkin. Chiral spin torque arising from proximity-induced magnetization. *Nature Communications*, 5:3910, 2014. doi:10.1038/ncomms4910.

[153] E. Martínez, O. Alejos, M. A. Hernandez, V. Raposo, L. Sanchez-Tejerina, and S. Moretti. Angular dependence of current-driven chiral walls. *Appl. Phys. Express*, 9:063008, 2016. doi:10.7567/APEX.9.063008.

[154] O. Alejos, V. Raposo, M. A. Hernandez, L. Sanchez-Tejerina, S. Moretti, and E. Martinez. Micromagnetic analysis of geometrically controlled current-driven magnetization switching. *AIP Advances*, 7(5):055909, 2017. doi:10.1063/1.4973749.

[155] Olivier Boulle, Jan Vogel, Hongxin Yang, Stefania Pizzini, Dayane de Souza Chaves, Andrea Locatelli, Tevfik Onur Menteş, Alessandro Sala, Liliana D. Buda-Prejbeanu, Olivier Klein, Mohamed Belmeguenai, Yves Roussigné, Andrey Stashkevich, Salim Mourad Chérif, Lucia Aballe, Michael Foerster, Mairbek Chshiev, Stéphane Auffret, Ioan Mihai Miron, and Gilles Gaudin. Room-temperature chiral magnetic skyrmions in ultrathin magnetic nanostructures. *Nature Nanotechnology*, 11:449, 2016. doi:10.1038/nnano.2015.315.

[156] Seonghoon Woo, Kai Litzius, Benjamin Krüger, Mi-Young Im, Lucas Caretta, Kornel Richter, Maxwell Mann, Andrea Krone, Robert M. Reeve, Markus Weigand, Parnika Agrawal, Ivan Lemesh, Mohamad-Assaad Mawass, Peter Fischer, Mathias Kläui, and Geoffrey S. D. Beach. Observation of room-temperature magnetic skyrmions and their current-driven dynamics in ultrathin metallic ferromagnets. *Nature Materials*, 15:15, 2016. doi:10.1038/nmat4593.

[157] Victor Raposo, Simone Moretti, Maria Auxiliadora Hernandez, and Eduardo Martinez. Domain wall dynamics along curved strips under current pulses: The influence of joule heating. *Applied Physics Letters*, 108(4):042405, 2016. doi:10.1063/1.4940727.

[158] Fred Lacy. Developing a theoretical relationship between electrical resistivity, temperature, and film thickness for conductors. *Nanoscale Research Letters*, 6 (1):636, 2011. doi:10.1186/1556-276X-6-636.

[159] Óscar Alejos, Eduardo Martínez, Víctor Raposo, Luis Sánchez-Tejerina, and María Auxiliadora Hernández-López. Chiral-triggered magnetization switching in patterned media. *Applied Physics Letters*, 110(7):072407, 2017. doi:10.1063/1.4976693.

[160] Luis Sánchez-Tejerina, Óscar Alejos, Víctor Raposo, and Eduardo Martínez. Current-driven domain wall motion along ferromagnetic strips with periodically-modulated perpendicular anisotropy. *Journal of Applied Physics*, 2018. doi:10.1063/1.5036601.

[161] Óscar Alejos, Víctor Raposo, Luis Sánchez-Tejerina, and Eduardo Martínez. Efficient and controlled domain wall nucleation for magnetic shift registers. *Scientific Reports*, 7:11909, 2017. doi:10.1038/s41598-017-12230-9.

[162] Óscar Alejos and Eduardo Martínez. Micromagnetic study of interaction between achiral and homochiral domain walls in ultrathin ferromagnetic strips. *Journal of Applied Physics*, 117(17):17D509, 2015. doi:10.1063/1.4914068.

[163] Rafael P. del Real, Victor Raposo, Eduardo Martinez, and Masamitsu Hayashi. Current-induced generation and synchronous motion of highly packed coupled chiral domain walls. *Nano Letters*, 17(3):1814–1818, 2017. doi:10.1021/acs.nanolett.6b05132.

[164] Jacob Torrejon, Eduardo Martinez, and Masamitsu Hayashi. Tunable inertia of chiral magnetic domain walls. *Nature Communications*, 7:13533, 2016. doi:10.1038/ncomms13533.

[165] Tomohiro Koyama, Gen Yamada, Hironobu Tanigawa, Shinya Kasai, Norikazu Ohshima, Shunsuke Fukami, Nobuyuki Ishiwata, Yoshinobu Nakatani, and Teruo Ono. Control of domain wall position by electrical current in structured co/ni wire with perpendicular magnetic anisotropy. *Applied Physics Express*, 1 (10):101303, 2008.

[166] E. Martínez, L. López-Díaz, O. Alejos, and L. Torres. Thermally activated domain wall depinning in thin strips with high perpendicular magnetocrystalline anisotropy. *Journal of Applied Physics*, 106(4):043914, 2009. doi:10.1063/1.3204496.

[167] Y. Shiota, S. Murakami, F. Bonell, T. Nozaki, T. Shinjo, and Y. Suzuki. Quantitative evaluation of voltage-induced magnetic anisotropy change by magnetoresistance measurement. *Applied Physics Express*, 4:043005, 2011. doi:10.1143/APEX.4.043005.

[168] N. Lei, T. Devolder, G. Agnus, P. Aubert, L. Daniel, J.V. Kim, W. Zhao, T. Trypiniotis, R. P. Cowburn, C. Chappert, D. Ravelosona, and P. Lecoeur. Strain-controlled magnetic domain wall propagation in hybrid piezoelectric/ferromagnetic structures. *Nature Communications*, 4:1378, 2013. doi:10.1038/ncomms2386.

[169] COMSOL Multiphysics. https://www.comsol.com/.

[170] Luis Sánchez-Tejerina, Eduardo Martínez, Víctor Raposo, and Óscar Alejos. Current-driven domain wall motion based memory devices: Application to a ratchet ferromagnetic strip. *AIP Advances*, 8(4):047302, 2018. doi:10.1063/1.4993750.

[171] Kab-Jin Kim, Jae-Chul Lee, Sang-Jun Yun, Gi-Hong Gim, Kang-Soo Lee, Sug-Bong Choe, and Kyung-Ho Shin. Electric control of multiple domain walls in pt/co/pt nanotracks with perpendicular magnetic anisotropy. *Applied Physics Express*, 3(8):083001, 2010. doi:10.1143/APEX.3.083001.

[172] A. Fert, V. Cros, and J. Sampaio. Skyrmions on the track. *Nature Nanotechnology*, 8:152–156, 2013. doi:10.1038/nnano.2013.29.

[173] J. Sampaio, V. Cros, S. Rohart, A. Thiaville, and A. Fert. Nucleation, stability and current-induced motion of isolated magnetic skyrmions in nanostructures. *Nature Nanotechnology*, 8:839–844, 2013. doi:10.1038/nnano.2013.210.

[174] Luis Sánchez-Tejerina, Óscar Alejos, Eduardo Martínez, and Víctor Raposo. Current-driven domain wall motion along ferromagnetic strips with periodically-modulated perpendicular anisotropy. 2017. URL arXiv:1705.00905.

Appendix

This appendix shows the details of the derivation of the one dimensional model. We take the LLG equation in spherical coordinates (4.4) and assumed a profile given by (4.6). It is worthy to establish some relationships. First, a new variable ζ is defined

$$\zeta = Q\frac{(x-q)\cos\chi + y\sin\chi}{\Delta} \tag{1}$$

As it can be seen, is the argument of the exponential function. It can be checked that

$$dx = \frac{Q\Delta d\zeta}{\cos\chi} \tag{2}$$

$$\Delta\zeta\tan\chi - \frac{y}{\cos\chi} = (x-q)\sin\chi - y\cos\chi \tag{3}$$

It is possible to obtain the following derivatives

$$\frac{\partial\theta}{\partial x} = -\frac{\partial\theta}{\partial q} = \frac{2Q\frac{\cos\chi}{\Delta}}{1+\exp(2\zeta)}\exp(\zeta) = Q\frac{\sin\theta}{\Delta}\cos\chi \tag{4}$$

$$\frac{\partial\theta}{\partial y} = Q\frac{\sin\theta}{\Delta}\sin\chi \tag{5}$$

$$\frac{\partial\theta}{\partial\Delta} = -Q\frac{\sin\theta}{\Delta^2}\big((x-q)\cos\chi + y\sin\chi\big) \tag{6}$$

$$\frac{\partial\theta}{\partial\chi} = Q\frac{\sin\theta}{\Delta}\left(\frac{y}{\cos\chi} - \Delta\zeta\tan\chi\right) \tag{7}$$

as well as $\frac{\partial\theta}{\partial t} = \dot{\theta}$

$$\dot{\theta} = -Q\frac{\sin\theta}{\Delta}\Bigg[\dot{q}\cos\chi \quad + ((x-q)\sin\chi - y\cos\chi)\,\dot{\chi} + \\ + ((x-q)\cos\chi + y\sin\chi)\,\frac{\dot{\Delta}}{\Delta}\Bigg] \tag{8}$$

The following integrals are known

$$\int_{-\infty}^{\infty}\frac{d\zeta}{\cosh\zeta} = \pi \tag{9}$$

$$\int_{-\infty}^{\infty} \frac{\zeta d\zeta}{\cosh \zeta} = 0 \tag{10}$$

$$\int_{a}^{b} \frac{d\zeta}{\cosh^2 \zeta} = \tanh b - \tanh a \tag{11}$$

$$\int_{a}^{b} \frac{\zeta d\zeta}{\cosh^2 \zeta} = b \tanh b - a \tanh a - \log(\cosh b) + \log(\cosh a) \tag{12}$$

$$\int_{-\infty}^{\infty} \frac{\zeta^2 d\zeta}{\cosh^2 \zeta} = \frac{\pi^2}{6} \tag{13}$$

A more detailed explanation is required for the integral of $\cos\theta$

$$\int_{-\infty}^{\infty} \cos\theta dx = \lim_{b,b' \to \infty} \int_{-b}^{q-\frac{\Delta}{2}} Q dx + \int_{q+\frac{\Delta}{2}}^{b'} -Q dx + \int_{q-\frac{\Delta}{2}}^{q+\frac{\Delta}{2}} \cos\theta dx = Q2q \tag{14}$$

where the third integral vanishes because is an odd function in a symmetric range. It must be noticed that this limit is not well defined so if b and b' are different there is a remaining contribution to the total energy. It should be checked that this integral appears due to the Zeeman energy contribution. That means that if the *mean* magnetization of the sample is not null and a magnetic field is applied, two terms will appear: a term accounting for the DW movement and an additional term. This additional term will be responsible for new domains nucleation, but it does not affect the primary DW motion. As long as we are not considering the nucleation topic, we will ignore such a term, so only the term due to the presence of the DW, $Q2q$, is considered.

In the following, the relationships given by (1)-(14) are used to derive an energy density which simplifies equations (4.4a) and (4.4b). In that way, four equations accounting for the **global** behavior of the strip and depending only on q and Φ and, if needed, on Δ and/or χ are obtained. Note the difference with the previous equation which is **local** even though only depends on θ and φ. Therefore, the assumption that properties are constant along at least one of the axis allows the simplification of the volume energy density u_V by integrating along the other axes. The result is a surface energy density σ if there are two constant axes, or a linear energy density λ if there is only one. In our case changes along y-axis may be possible so now we focus on the linear energy density λ. Nevertheless, chapters 6-12 use the surface energy density σ since it is supposed that changes along y are not significant. Then, it can be written

$$\lambda = \int_{-w/2}^{w/2} \sigma dy = \int_{-w/2}^{w/2} \int_{-\infty}^{\infty} u_V dy dx \tag{15}$$

from which it is possible to derive an expression for the variation of λ [125]

$$\delta\lambda = \int_{-w/2}^{w/2} \int_{-\infty}^{\infty} \left(\frac{\delta u_V}{\delta\theta} \delta\theta + \frac{\delta u_V}{\delta\varphi} \delta\varphi \right) dy dx \tag{16}$$

Taking into account that $\delta\theta$ can be expressed as

$$\delta\theta = \frac{\partial\theta}{\partial q}\delta q + \frac{\partial\theta}{\partial\Delta}\delta\Delta + \frac{\partial\theta}{\partial\chi}\delta\chi \tag{17}$$

$\delta\lambda$ is read

$$\delta\lambda = \int_{-w/2}^{w/2}\int_{-\infty}^{\infty}\left[\frac{\delta u}{\delta\theta}\left(\frac{\partial\theta}{\partial q}\delta q + \frac{\partial\theta}{\partial\Delta}\delta\Delta + \frac{\partial\theta}{\partial\chi}\delta\chi\right) + \frac{\delta u}{\delta\varphi}\delta\varphi\right]dydx \tag{18}$$

It may be notice that only partial with respect q, Δ and χ are considered, but no with respect its gradients ∇q, $\nabla\Delta$ and $\nabla\chi$. The reason is that we are not considering a pure bidimensional system, i.e., DW can tilt with an angle χ, but it cannot bend. This means that those gradients, and also $\nabla\varphi$, are zero [66]. Each term can be now identified with a derivative of λ with respect to each variable [125]

$$\frac{\partial\lambda}{\partial q} = \int_{-w/2}^{w/2}\int_{-\infty}^{\infty}\frac{\delta u_V}{\delta\theta}\frac{\partial\theta}{\partial q}dxdy \tag{19}$$

$$\frac{\partial\lambda}{\partial\varphi} = \int_{-w/2}^{w/2}\int_{-\infty}^{\infty}\frac{\delta u_V}{\delta\varphi}dxdy \tag{20}$$

$$\frac{\partial\lambda}{\partial\Delta} = \int_{-w/2}^{w/2}\int_{-\infty}^{\infty}\frac{\delta u_V}{\delta\theta}\frac{\partial\theta}{\partial\Delta}dxdy \tag{21}$$

$$\frac{\partial\lambda}{\partial\chi} = \int_{-w/2}^{w/2}\int_{-\infty}^{\infty}\frac{\delta u_V}{\delta\theta}\frac{\partial\theta}{\partial\chi}dxdy \tag{22}$$

Each equation must be integrated by using equations (4.4) and (1)-(14).

Partial derivative of λ with respect to q

Equation (19) is

$$\begin{aligned}\frac{\partial\lambda}{\partial q} = \frac{\mu_0 M_s}{\gamma_0}\iint\Big[&\alpha\dot{\theta} - \sin\theta\dot{\varphi} - b_j\sin\theta\left(\frac{j_x}{J}\frac{\partial\varphi}{\partial x} + \frac{j_y}{J}\frac{\partial\varphi}{\partial y}\right) + \\ &+ b_j\xi\left(\frac{j_x}{J}\frac{\partial\theta}{\partial x} + \frac{j_y}{J}\frac{\partial\theta}{\partial y}\right) + \gamma_0 H_{SH}\left(j_x\cos\varphi + j_y\sin\varphi\right) - \\ &- \gamma_0\left[\left(H_{x,th}\cos\varphi + H_{y,th}\sin\varphi\right)\cos\theta - H_{z,th}\sin\theta\right] - \\ &- \gamma_0 H_{Ra}\cos\theta\left(j_x\sin\varphi - j_y\cos\varphi\right) - \Big]Q\frac{\sin\theta}{\Delta}\cos\chi dxdy\end{aligned} \tag{23}$$

Each of the seven addends is called $I_n^{\lambda,q}$, with n an integer ranging from 1 to 7.

$$\begin{aligned}I_1^{\lambda,q} &= \alpha\iint -\left(\frac{\sin\theta}{\Delta}\right)^2\cos\chi\Big[\quad\dot{q}\cos\chi + \left((x-q)\sin\chi - y\cos\chi\right)\dot{\chi} + \\ &\qquad + \left((x-q)\cos\chi + y\sin\chi\right)\frac{\dot{\Delta}}{\Delta}\Big]dxdy = \\ &= -\alpha\frac{2\dot{q}}{\Delta}w\cos\chi\end{aligned} \tag{24}$$

Every term vanishes except the one with $\dot{q}$ because these terms are odd functions and the integration is performed in a symmetric range. The other addends are

$$I_2^{\lambda,q} = -\iint Q\frac{\sin^2\theta}{\Delta}\dot{\varphi}\cos\chi dxdy = -Q2\dot{\Phi}w \tag{25}$$

$$I_3^{\lambda,q} = -\iint b_j Q\frac{\sin^2\theta}{\Delta}\left(\frac{j_x}{J}\frac{\partial\varphi}{\partial x}+\frac{j_y}{J}\frac{\partial\varphi}{\partial y}\right)\cos\chi dxdy = 0 \tag{26}$$

$$\begin{aligned} I_4^{\lambda,q} = b_j\xi\iint\frac{\sin\theta}{\Delta}\left(\frac{j_x}{J}\frac{\sin\theta}{\Delta}\cos\chi+\frac{j_y}{J}\frac{\sin\theta}{\Delta}\sin\chi\right)\cos\chi dxdy = \\ = \frac{2b_j\xi w}{\Delta}\left(\frac{j_x}{J}\cos\chi+\frac{j_y}{J}\sin\chi\right) \end{aligned} \tag{27}$$

$$\begin{aligned} I_5^{\lambda,q} = \gamma_0 H_{SH}\iint\left(j_x\cos\varphi+j_y\sin\varphi\right)Q\frac{\sin\theta}{\Delta}\cos\chi dxdy = \\ = \gamma_0 Q\pi w H_{SH}\left(j_x\cos\Phi+j_y\sin\Phi\right) \end{aligned} \tag{28}$$

$$\begin{aligned} I_6^{\lambda,q} = -\gamma_0\iint\left[\left(H_{x,th}\cos\varphi+H_{y,th}\sin\varphi\right)\cos\theta-H_{z,th}\sin\theta\right]\sin\theta d\zeta dy = \\ = \gamma_0 Q w 2H_{z,th} \end{aligned} \tag{29}$$

$$I_7^{\lambda,q} = -\gamma_0 H_{Ra}\iint\cos\theta\left(j_x\sin\varphi-j_y\cos\varphi\right)Q\frac{\sin\theta}{\Delta}\cos\chi dxdy = 0 \tag{30}$$

where relationships (1)-(14) has been used again. Finally it can be written

$$\begin{aligned} \frac{\partial\lambda}{\partial q} = -\frac{\mu_0 M_s w}{\gamma_0}\Big[\alpha\frac{2\dot{q}}{\Delta}\cos\chi+Q2\dot{\Phi}-\frac{2b_j\xi}{\Delta}\left(\frac{j_x}{J}\cos\chi+\frac{j_y}{J}\sin\chi\right)- \\ -\gamma_0 Q2H_{z,th}-\gamma_0 Q\pi H_{SH}\left(j_x\cos\Phi+j_y\sin\Phi\right)\Big] \end{aligned} \tag{31}$$

Partial derivative of λ with respect to φ

Now, expression (20) is integrated

$$\begin{aligned} \frac{\partial\lambda}{\partial\varphi} = \frac{\mu_0 M_s}{\gamma_0}\iint\sin\theta\ \Big[&-\dot{\theta}-\alpha\sin\theta\dot{\varphi}-b_j\left(\frac{j_x}{J}\frac{\partial\theta}{\partial x}+\frac{j_y}{J}\frac{\partial\theta}{\partial y}\right)- \\ &-b_j\xi\sin\theta\left(\frac{j_x}{J}\frac{\partial\varphi}{\partial x}+\frac{j_y}{J}\frac{\partial\varphi}{\partial y}\right)+ \\ &+\gamma_0\left(-H_{x,th}\sin\varphi+H_{y,th}\cos\varphi\right)+ \\ &+\gamma_0 H_{SH}\cos\theta\left(j_x\sin\varphi-j_y\cos\varphi\right)+ \\ &+\gamma_0 H_{Ra}\left(j_x\cos\varphi+j_y\sin\varphi\right)\Big]dxdy \end{aligned} \tag{32}$$

A notation similar to the one used previously is employed, so these addends are called $I_n^{\lambda,\varphi}$.

$$I_1^{\lambda,\varphi} = \iint Q\frac{\sin^2\theta}{\Delta}\Big[\dot{q}\cos\chi + ((x-q)\sin\chi - y\cos\chi)\,\dot{\chi} + \\ + ((x-q)\cos\chi + y\sin\chi)\,\frac{\dot{\Delta}}{\Delta}\Big]dxdy = Q2\dot{q}w \tag{33}$$

$$I_2^{\lambda,\varphi} = -\alpha\iint \sin^2\theta\dot{\varphi}dxdy = -\frac{2\alpha\Delta w\dot{\Phi}}{\cos\chi} \tag{34}$$

$$I_3^{\lambda,\varphi} = -bj\iint Q\frac{\sin^2\theta}{\Delta}\left(\frac{j_x}{J}\cos\chi + \frac{j_y}{J}\sin\chi\right)dxdy = \\ = -Q2b_jw\left(\frac{j_x}{J} + \frac{j_y}{J}\tan\chi\right) \tag{35}$$

$$I_4^{\lambda,\varphi} = -b_j\xi\iint \sin\theta\left(\frac{j_x}{J}\frac{\partial\varphi}{\partial x} + \frac{j_y}{J}\frac{\partial\varphi}{\partial y}\right)dxdy = 0 \tag{36}$$

$$I_5^{\lambda,\varphi} = \gamma_0\iint \sin\theta\,(-H_{x,th}\sin\varphi + H_{y,th}\cos\varphi)\,dxdy = \\ = \gamma_0\frac{\Delta\pi w}{\cos\chi}\,(-H_{x,th}\sin\Phi + H_{y,th}\cos\Phi) \tag{37}$$

$$I_6^{\lambda,\varphi} = \gamma_0 H_{SH}\iint \sin\theta\cos\theta\,(j_x\sin\varphi - j_y\cos\varphi)\,dxdy = 0 \tag{38}$$

$$I_7^{\lambda,\varphi} = \gamma_0 H_{Ra}\iint \sin\theta\,(j_x\cos\varphi + j_y\sin\varphi)\,dxdy = \\ = \gamma_0 H_{Ra}\frac{\Delta\pi w}{\cos\chi}\,(j_x\cos\Phi + j_y\sin\Phi) \tag{39}$$

So in this case

$$\frac{\partial\lambda}{\partial\varphi} = \frac{2\mu_0 M_s w}{\gamma_0}\Big[Q\dot{q} - \frac{\alpha\Delta\dot{\Phi}}{\cos\chi} - Qb_j\left(\frac{j_x}{J} + \frac{j_y}{J}\tan\chi\right) + \\ + \gamma_0\frac{\Delta}{\cos\chi}\frac{\pi}{2}\,(-H_{x,th}\sin\Phi + H_{y,th}\cos\Phi) + \\ + \gamma_0 H_{Ra}\frac{\Delta}{\cos\chi}\frac{\pi}{2}\,(j_x\cos\Phi + j_y\sin\Phi)\Big] \tag{40}$$

Partial derivative of λ with respect to Δ

Equation (21) becomes

$$\frac{\partial\lambda}{\partial\Delta} = \frac{\mu_0 M_s}{\gamma_0}\iint\Big[\alpha\dot{\theta} - \sin\theta\dot{\varphi} - b_j\sin\theta\left(\frac{j_x}{J}\frac{\partial\varphi}{\partial x} + \frac{j_y}{J}\frac{\partial\varphi}{\partial y}\right) + b_j\xi\left(\frac{j_x}{J}\frac{\partial\theta}{\partial x} + \frac{j_y}{J}\frac{\partial\theta}{\partial y}\right) - \\ - \gamma_0\left[(H_{x,th}\cos\varphi + H_{y,th}\sin\varphi)\cos\theta - H_{z,th}\sin\theta\right] - \\ - \gamma_0 H_{Ra}\cos\theta\,(j_x\sin\varphi - j_y\cos\varphi) + \\ + \gamma_0 H_{SH}\,(j_x\cos\varphi + j_y\sin\varphi)\Big]Q\frac{\sin\theta}{\Delta}\zeta dxdy \tag{41}$$

Again, the notation is adapted to this case with $I_n^{\lambda,\Delta}$

$$\begin{aligned} I_1^{\lambda,\Delta} &= -\alpha \iint \left(\frac{\sin\theta}{\Delta}\right)^2 \Big[\dot{q}\cos\chi + ((x-q)\sin\chi - y\cos\chi)\,\dot{\chi} + \\ &\qquad + ((x-q)\cos\chi + y\sin\chi)\,\frac{\dot{\Delta}}{\Delta}\Big]\zeta dxdy = \\ &= -\alpha \iint \left(\frac{\sin\theta}{\Delta}\right)^2 \Big[\left(\Delta t\tan\chi - \frac{y}{\cos\chi}\right)\dot{\chi} + t\dot{\Delta}\Big]\zeta dxdy = \\ &= -\alpha \frac{w}{\cos\chi}\frac{\pi^2}{6}\Big(\tan\chi\dot{\chi} + \frac{\dot{\Delta}}{\Delta}\Big) \end{aligned} \tag{42}$$

$$I_2^{\lambda,\Delta} = -\iint Q\frac{\sin^2\theta}{\Delta}\dot{\varphi}\zeta dxdy = 0 \tag{43}$$

$$I_3^{\lambda,\Delta} = -b_j \iint Q\frac{\sin^2\theta}{\Delta}\left(\frac{j_x}{J}\frac{\partial\varphi}{\partial x} + \frac{j_y}{J}\frac{\partial\varphi}{\partial y}\right)\zeta dxdy = 0 \tag{44}$$

$$I_4^{\lambda,\Delta} = b_j\xi \iint \left(\frac{\sin\theta}{\Delta}\right)^2 \left(\frac{j_x}{J}\cos\chi + \frac{j_y}{J}\sin\chi\right)\zeta dxdy = 0 \tag{45}$$

$$I_5^{\lambda,\Delta} = -\gamma_0 \iint Q\big[\,(H_{x,th}\cos\varphi + H_{y,th}\sin\varphi)\cos\theta - H_{z,th}\sin\theta\big]\frac{\sin\theta}{\Delta}\zeta dxdy = 0 \tag{46}$$

$$I_6^{\lambda,\Delta} = -\gamma_0 \iint QH_{Ra}\cos\theta\,(j_x\sin\varphi - j_y\cos\varphi)\,\frac{\sin\theta}{\Delta}\zeta dxdy = 0 \tag{47}$$

$$I_7^{\lambda,\Delta} = \gamma_0 \iint QH_{SH}\,(j_x\cos\varphi + j_y\sin\varphi)\,\frac{\sin\theta}{\Delta}\zeta dxdy = 0 \tag{48}$$

So this term is expressed simply as

$$\frac{\partial\lambda}{\partial\Delta} = -\frac{\mu_0 M_s}{\gamma_0}\alpha\frac{w}{\cos\chi}\frac{\pi^2}{6}\Big(\tan\chi\dot{\chi} + \frac{\dot{\Delta}}{\Delta}\Big) \tag{49}$$

Partial derivative of λ with respect to χ

Finally equation (22) transforms as

$$\begin{aligned} \frac{\partial\lambda}{\partial\chi} = -\frac{\mu_0 M_s}{\gamma_0}\iint\Big[&\alpha\dot{\theta} - \sin\theta\dot{\varphi} - b_j\sin\theta\left(\frac{j_x}{J}\frac{\partial\varphi}{\partial x} + \frac{j_y}{J}\frac{\partial\varphi}{\partial y}\right) + b_j\xi\left(\frac{j_x}{J}\frac{\partial\theta}{\partial x} + \frac{j_y}{J}\frac{\partial\theta}{\partial y}\right) - \\ &- \gamma_0\left[(H_{x,th}\cos\varphi + H_{y,th}\sin\varphi)\cos\theta - H_{z,th}\sin\theta\right] - \\ &- \gamma_0 H_{Ra}\cos\theta\,(j_x\sin\varphi - j_y\cos\varphi) + \\ &+ \gamma_0 H_{SH}\,(j_x\cos\varphi + j_y\sin\varphi)\Big]Q\frac{\sin\theta}{\Delta}\left(\frac{y}{\cos\chi} - \Delta\zeta\tan\chi\right)dxdy \end{aligned} \tag{50}$$

Again, each addend is called $I_n^{\lambda,\chi}$

$$\begin{aligned} I_1^{\lambda,\chi} &= \alpha \iint \left(\frac{\sin\theta}{\Delta}\right)^2 \Big[\dot{q}\cos\chi + ((x-q)\sin\chi - y\cos\chi)\,\dot{\chi} + \\ &+ ((x-q)\cos\chi + y\sin\chi)\,\frac{\dot{\Delta}}{\Delta}\Big]\left(\Delta\zeta\tan\chi - \frac{y}{\cos\chi}\right)dxdy = \\ &= \alpha\left[\frac{\pi^2}{6}\frac{w\Delta}{\cos\chi}\tan^2\chi\dot{\chi} + \frac{2}{\Delta\cos^3\chi}\frac{w^3}{12}\dot{\chi} + \frac{\pi^2}{6}\frac{\tan\chi}{\cos\chi}w\dot{\Delta}\right] \end{aligned} \tag{51}$$

$$I_2^{\lambda,\chi} = \iint Q\frac{\sin^2\theta}{\Delta}\left(\Delta\zeta\tan\chi - \frac{y}{\cos\chi}\right)\dot{\varphi}dxdy = 0 \tag{52}$$

$$I_3^{\lambda,\chi} = b_j \iint Q\frac{\sin^2\theta}{\Delta}\left(\frac{j_x}{J}\frac{\partial\varphi}{\partial x} + \frac{j_y}{J}\frac{\partial\varphi}{\partial y}\right)\left(\Delta\zeta\tan\chi - \frac{y}{\cos\chi}\right)dxdy = 0 \tag{53}$$

$$\begin{aligned} I_4^{\lambda,\chi} &= b_j\xi \iint Q\frac{\sin\theta}{\Delta}\left(\frac{j_x}{J}\frac{\partial\theta}{\partial x} + \frac{j_y}{J}\frac{\partial\theta}{\partial y}\right)\left(\frac{y}{\cos\chi} - \Delta\zeta\tan\chi\right)dxdy = \\ &= b_j\xi \iint \left(\frac{\sin\theta}{\Delta}\right)^2\left(\frac{j_x}{J}\cos\chi + \frac{j_y}{J}\sin\chi\right)\left(\frac{y}{\cos\chi} - \Delta\zeta\tan\chi\right)dxdy = 0 \end{aligned} \tag{54}$$

$$\begin{aligned} I_5^{\lambda,\chi} = -\gamma_0 \iint Q\frac{\sin\theta}{\Delta}\Big[&(H_{x,th}\cos\varphi + H_{y,th}\sin\varphi)\cos\theta - \\ &- H_{z,th}\sin\theta\Big]\left(\frac{y}{\cos\chi} - \Delta\zeta\tan\chi\right)dxdy = 0 \end{aligned} \tag{55}$$

$$I_6^{\lambda,\chi} = -\gamma_0 H_{Ra} \iint Q\sin\theta\cos\theta\,(j_x\sin\varphi - j_y\cos\varphi)\left(\frac{y}{\Delta\cos\chi} - \zeta\tan\chi\right)dxdy = 0 \tag{56}$$

$$I_7^{\lambda,\chi} = \gamma_0 H_{SH} \iint (j_x\cos\varphi + j_y\sin\varphi)\,Q\frac{\sin\theta}{\Delta}\left(\frac{y}{\cos\chi} - \Delta\zeta\tan\chi\right)dxdy = 0 \tag{57}$$

so finally it is obtained

$$\frac{\partial\lambda}{\partial\chi} = -\frac{\mu_0 M_s}{\gamma_0}\alpha\left[\frac{\pi^2}{6}\frac{w\Delta}{\cos\chi}\tan^2\chi\dot{\chi} + \frac{2}{\Delta\cos^3\chi}\frac{w^3}{12}\dot{\chi} + \frac{\pi^2}{6}\frac{\tan\chi}{\cos\chi}w\dot{\Delta}\right] \tag{58}$$

Four equations relating the partial derivatives of the linear energy density and the dynamic variables have been derived. However, a useful expression of such linear energy density is still needed. Density energies given in chapter 2 are integrated in order to calculate such an expression. The additive character of the energy allows us to calculate each contribution separately and then, summing all contribution up to get the total linear energy density.

Exchange

From equation (2.35) and using (4) and (5) it can be derived

$$\begin{aligned}\lambda_{exch} &= \iint A\left[\left(\frac{\partial\theta}{\partial x}\right)^2+\sin^2\theta\left(\frac{\partial\varphi}{\partial x}\right)^2+\left(\frac{\partial\theta}{\partial y}\right)^2+\sin^2\theta\left(\frac{\partial\varphi}{\partial y}\right)^2\right]dxdy = \\ &= \iint A\left[\left(\frac{\sin\theta}{\Delta}\cos\chi\right)^2+\left(\frac{\sin\theta}{\Delta}\sin\chi\right)^2\right]dxdy = \frac{2Aw}{\Delta\cos\chi}\end{aligned} \tag{59}$$

It should be pointed out that expression $\left(\vec{\nabla}\vec{m}\right)^2 = |\left(\vec{u}_x\vec{\nabla}\right)\vec{m}|^2 + |\left(\vec{u}_y\vec{\nabla}\right)\vec{m}|^2 + |\left(\vec{u}_z\vec{\nabla}\right)\vec{m}|^2$ has been used.

Magnetic anisotropy

Taking (2.40) as the starting point, the linear magnetic anisotropy energy density in the case of a uniform and homogeneous strip is

$$\lambda_{anis} = \iint K_0 - K_1\cos^2\theta dxdy = \iint K_1\sin^2\theta dxdy = \frac{2K_1\Delta w}{\cos\chi} \tag{60}$$

Nevertheless, systems with a variable magnetic anisotropy are also considered. It is assumed that anisotropy might increase or decrease but always in a linear manner and only along the x-direction. In fact, it is assumed a periodic change of the anisotropy. So it is considered that anisotropy grows linearly from a minimum value K_u^- to a maximum value K_u^+ in a distance d_1. Then, anisotropy decreases linearly from this maximum value K_u^+ to the minimum one K_u^- in a distance d_2. It is also assumed that the minimum value K_u^- is still high enough to preserve the perpendicular anisotropy[‡]. This profile is repeated periodically. The addition of d_1 and d_2 is called $d_t = d_1 + d_2$

$$K_u = \begin{cases} K_u^- + \dfrac{K_u^+ - K_u^-}{d_1}\left(x - d_t\left(\left\lfloor\dfrac{q}{d_t}\right\rfloor - n\right)\right) \\ if\ d_t\left(\left\lfloor\dfrac{q}{d_t}\right\rfloor - n\right) < x < d_t\left(\left\lfloor\dfrac{q}{d_t}\right\rfloor - \left(n - \dfrac{d_1}{d_t}\right)\right) \\ K_u^+ - \dfrac{K_u^+ - K_u^-}{d_2}\left(x - d_t\left(\left\lfloor\dfrac{q}{d_t}\right\rfloor - \left(n - \dfrac{d_1}{d_t}\right)\right)\right) \\ if\ d_t\left(\left\lfloor\dfrac{q}{d_t}\right\rfloor - \left(n - \dfrac{d_1}{d_t}\right)\right) < x < d_t\left(\left\lfloor\dfrac{q}{d_t}\right\rfloor - (n-1)\right) \end{cases} \tag{61}$$

where $\lfloor\rfloor$ stands for the floor function. So the linear magnetic anisotropy energy density reads

$$\lambda_{anis} = \iint K\sin^2\theta dxdy = \int\left(\sum_{n=-m}^{m'} I_n + I'_n\right)dy \tag{62}$$

[‡]It should be pointed out that, from the magnetostatic point of view, this axis is the least favorable.

As long as K only change along x, it is possible to focus on this integral. Nevertheless, comments about integral along y will be made along this subsection. So I_n and I'_n are the integrals along x of the rise and fall intervals of the anisotropy function respectively. Since there are $m' + m$ of such integrals, the summation is needed, which tends to infinity for and infinite strip. In that case, this limit is well defined and addends due to slopes far from the DW vanish. It is worthy to highlight that even though q appears in (61), the anisotropy **does not** depend on the DW -or even on the existence of such a wall-. Any integer replacing the floor function leads to the same profile. However, the above expression makes the following calculations easier by choosing a proper coordinate origin, depending on the DW position.

First, I_n is considered, accounting for the linear anisotropy rising

$$\begin{aligned} I_n &= \int_{d_t\left(\left\lfloor \frac{q}{d_t}\right\rfloor - \left(n-\frac{d_1}{d_t}\right)\right)}^{d_t\left(\left\lfloor \frac{q}{d_t}\right\rfloor - n\right)} K_u^- + \frac{K_u^+ - K_u^-}{d_1}\left(x - d_t\left(\left\lfloor \frac{q}{d_t}\right\rfloor - n\right)\right)\sin^2\theta dx = \\ &= \int_{\zeta_{min}}^{\zeta_{max}} K_u^- + \frac{K_u^+ - K_u^-}{d_1}\left(\frac{Q\Delta\zeta + y\sin\chi}{\cos\chi} + d_t\left(\left\{\frac{q}{d_t}\right\} + n\right)\right)\sin^2\theta\frac{Q\Delta}{\cos\chi}d\zeta \end{aligned} \tag{63}$$

with

$$\begin{aligned} \zeta_{max} &= \frac{Q}{\Delta}\left[d_t\left(-\left\{\frac{q}{d_t}\right\} - \left(n - \frac{d_1}{d_t}\right)\right)\cos\chi - y\sin\chi\right] \\ \zeta_{min} &= \frac{Q}{\Delta}\left[d_t\left(-\left\{\frac{q}{d_t}\right\} - n\right)\cos\chi - y\sin\chi\right] \end{aligned}$$

where x has been replaced by t, and the fact that $\frac{q}{d_t} - \left\lfloor \frac{q}{d_t}\right\rfloor = \left\{\frac{q}{d_t}\right\}$ is used, being $\{\}$ the fractional part function. I_n is computed term by term

$$I_n^1 = \int_{\zeta_{min}}^{\zeta_{max}} K_u^- \sin^2\theta\frac{Q\Delta}{\cos\chi}d\zeta =$$

$$\begin{aligned} &= \frac{\Delta K_u^-}{\cos\chi}\left[\tanh\left[\frac{d_t}{\Delta}\left(-\left\{\frac{q}{d_t}\right\} - \left(n - \frac{d_1}{d_t}\right)\right)\cos\chi - \frac{y}{\Delta}\sin\chi\right] - \right. \\ &\left. - \tanh\left[\frac{d_t}{\Delta}\left(-\left\{\frac{q}{d_t}\right\} - n\right)\cos\chi - \frac{y}{\Delta}\sin\chi\right]\right] \end{aligned} \tag{64}$$

$$I_n^2 = \int_{\zeta_{min}}^{\zeta_{max}} \frac{K_u^+ - K_u^-}{d_1} d_t\left(\left\{\frac{q}{d_t}\right\} + n\right)\sin^2\theta\frac{Q\Delta}{\cos\chi}d\zeta =$$

$$\begin{aligned} &= \frac{K_u^+ - K_u^-}{d_1}\frac{d_t\Delta}{\cos\chi}\left(\left\{\frac{q}{d_t}\right\} + n\right)\left[\tanh\left[\frac{d_t}{\Delta}\left(\left\{\frac{q}{d_t}\right\} + n\right)\cos\chi + \frac{y}{\Delta}\sin\chi\right] - \right. \\ &\left. - \tanh\left[\frac{d_t}{\Delta}\left(\left\{\frac{q}{d_t}\right\} + \left(n - \frac{d_1}{d_t}\right)\right)\cos\chi + \frac{y}{\Delta}\sin\chi\right]\right] \end{aligned} \tag{65}$$

$$I_n^3 = \int_{\zeta_{min}}^{\zeta_{max}} \frac{K_u^+ - K_u^-}{d_1} \frac{Q\Delta\zeta + y\sin\chi}{\cos\chi} \sin^2\theta \frac{Q\Delta}{\cos\chi} d\zeta =$$
$$= \frac{K_u^+ - K_u^-}{d_1} \left(\frac{\Delta}{\cos\chi}\right)^2 \left[\zeta_{max}\tanh\zeta_{max} - \zeta_{min}\tanh\zeta_{min} + \right. \tag{66}$$
$$\left. + \log\left(\frac{\cosh\zeta_{min}}{\cosh\zeta_{max}}\right)\right]$$

where the term with y of I_n^3 has been discarded because it vanishes when integration along y is made. In the case of the fall of the anisotropy, a similar expression can be cast

$$I'_n = \int_{d_t\left(\left\lfloor\frac{q}{d_t}\right\rfloor - \left(n-\frac{d_1}{d_t}\right)\right)}^{d_t\left(\left\lfloor\frac{q}{d_t}\right\rfloor - (n-1)\right)} K_u^+ - \frac{K_u^+ - K_u^-}{d_2}\left(x - d_t\left(\left\lfloor\frac{q}{d_t}\right\rfloor - \left(n - \frac{d_1}{d_t}\right)\right)\right)\sin^2\theta dx =$$
$$= \int_{\zeta'_{min}}^{\zeta'_{max}} K_u^+ - \frac{K_u^+ - K_u^-}{d_2}\left(\frac{Q\Delta t + y\sin\chi}{\cos\chi} + d_t\left(\left\{\frac{q}{d_t}\right\} + n - \frac{d_1}{d_t}\right)\right)\sin^2\theta\frac{Q\Delta}{\cos\chi}d\zeta \tag{67}$$

with

$$\zeta'_{max} = \frac{Q}{\Delta}\left[d_t\left(-\left\{\frac{q}{d_t}\right\} - (n-1)\right)\cos\chi - y\sin\chi\right]$$
$$\zeta'_{min} = \frac{Q}{\Delta}\left[d_t\left(-\left\{\frac{q}{d_t}\right\} - \left(n - \frac{d_1}{d_t}\right)\right)\cos\chi - y\sin\chi\right]$$

So in this case

$$I'^1_n = \int_{\zeta'_{min}}^{\zeta'_{max}} K_u^+ \sin^2\theta\frac{Q\Delta}{\cos\chi}d\zeta =$$
$$= \frac{\Delta K_u^+}{\cos\chi}\left[\tanh\left[\frac{d_t}{\Delta}\left(-\left\{\frac{q}{d_t}\right\} - (n-1)\right)\cos\chi - \frac{y}{\Delta}\sin\chi\right] - \right. \tag{68}$$
$$\left. - \tanh\left[\frac{d_t}{\Delta}\left(-\left\{\frac{q}{d_t}\right\} - \left(n - \frac{d_1}{d_t}\right)\right)\cos\chi - \frac{y}{\Delta}\sin\chi\right]\right]$$
$$I'^2_n = \int_{\zeta'_{min}}^{\zeta'_{max}} -\frac{K_u^+ - K_u^-}{d_2} d_t\left(\left\{\frac{q}{d_t}\right\} + n - \frac{d_1}{d_t}\right)\sin^2\theta\frac{Q\Delta}{\cos\chi}d\zeta =$$
$$= \frac{K_u^+ - K_u^-}{d_2}\frac{d_t\Delta}{\cos\chi}\left(\left\{\frac{q}{d_t}\right\} + n - \frac{d_1}{d_t}\right)\left[\tanh\left[\frac{d_t}{\Delta}\left(\left\{\frac{q}{d_t}\right\} + (n-1)\right)\cos\chi + \frac{y}{\Delta}\sin\chi\right] - \right.$$
$$\left. - \tanh\left[\frac{d_t}{\Delta}\left(\left\{\frac{q}{d_t}\right\} + \left(n - \frac{d_1}{d_t}\right)\right)\cos\chi + \frac{y}{\Delta}\sin\chi\right]\right] \tag{69}$$

$$I_n'^3 = \int_{\zeta'_{min}}^{\zeta'_{max}} -\frac{K_u^+ - K_u^-}{d_2}\left(\frac{Q\Delta t + y\sin\chi}{\cos\chi}\right)\sin^2\theta\frac{Q\Delta}{\cos\chi}d\zeta = \\ = -\frac{K_u^+ - K_u^-}{d_2}\left(\frac{\Delta}{\cos\chi}\right)^2\left[\zeta'_{max}\tanh\zeta'_{max} - \zeta'_{min}\tanh\zeta'_{min} + \right. \\ \left. + \log\left(\frac{\cosh\zeta'_{min}}{\cosh\zeta'_{max}}\right)\right] \tag{70}$$

At this point it can be assumed that DW width is much smaller than the anisotropy period d_t. This means that I_n^1 and $I_n'^1$ vanish for $n > 1$ and $n < -1$. Then it can be written

$$\sum_{-m}^{m'} I_n^1 = \frac{\Delta K_u^-}{\cos\chi}\left[1 - \sum_{-1}^{1}\tanh\left[\frac{d_t}{\Delta}\left(\left\{\frac{q}{d_t}\right\} + \left(n - \frac{d_1}{d_t}\right)\right)\cos\chi + \frac{y}{\Delta}\sin\chi\right] + \right. \\ \left. + \sum_{-1}^{0}\tanh\left[\frac{d_t}{\Delta}\left(\left\{\frac{q}{d_t}\right\} + n\right)\cos\chi + \frac{y}{\Delta}\sin\chi\right]\right] \tag{71}$$

$$\sum_{-m}^{m'} I_n'^1 = \frac{\Delta K_u^+}{\cos\chi}\left[1 + \sum_{-1}^{1}\tanh\left[\frac{d_t}{\Delta}\left(\left\{\frac{q}{d_t}\right\} + \left(n - \frac{d_1}{d_t}\right)\right)\cos\chi + \frac{y}{\Delta}\sin\chi\right] - \right. \\ \left. - \sum_{-1}^{0}\tanh\left[\frac{d_t}{\Delta}\left(\left\{\frac{q}{d_t}\right\} + n\right)\cos\chi + \frac{y}{\Delta}\sin\chi\right]\right] \tag{72}$$

Summing up both contributions one gets

$$A = \sum_{-m}^{m'} I_n^1 + I_n'^1 = \frac{\Delta}{\cos\chi}\left(K_u^+ + K_u^-\right) + \\ + \frac{\Delta}{\cos\chi}\left(K_u^+ - K_u^-\right)\left[-\sum_{-1}^{0}\tanh\left[\frac{d_t}{\Delta}\left(\left\{\frac{q}{d_t}\right\} + n\right)\cos\chi + \frac{y}{\Delta}\sin\chi\right] + \right. \\ \left. + \sum_{-1}^{1}\tanh\left[\frac{d_t}{\Delta}\left(\left\{\frac{q}{d_t}\right\} + \left(n - \frac{d_1}{d_t}\right)\right)\cos\chi + \frac{y}{\Delta}\sin\chi\right]\right] \tag{73}$$

Again I_n^2 and $I_n'^2$ vanish for $n > 1$ and $n < -1$. It can be defined $a_n = \left\{\frac{q}{d_t}\right\} + n$ so in this case

$$\sum_{-m}^{m'} I_n^2 = \frac{K_u^+ - K_u^-}{d_1}\frac{d_t\Delta}{\cos\chi}\left[\sum_{-1}^{1} a_n\left[\tanh\left(\frac{d_t}{\Delta}a_n\cos\chi + \frac{y}{\Delta}\sin\chi\right) - \right.\right. \\ \left.\left. - \tanh\left(\frac{d_t}{\Delta}\left(a_n - \frac{d_1}{d_t}\right)\cos\chi + \frac{y}{\Delta}\sin\chi\right)\right]\right] \tag{74}$$

$$\sum_{-m}^{m'} I_n'^2 = \frac{K_u^+ - K_u^-}{d_2}\frac{d_t\Delta}{\cos\chi}\left[\sum_{-1}^{1}\left(a_n - \frac{d_1}{d_t}\right)\left[\tanh\left(\frac{d_t}{\Delta}\left(a_n - 1\right)\cos\chi + \frac{y}{\Delta}\sin\chi\right) - \right.\right. \\ \left.\left. - \tanh\left(\frac{d_t}{\Delta}\left(a_n - \frac{d_1}{d_t}\right)\cos\chi + \frac{y}{\Delta}\sin\chi\right)\right]\right] \tag{75}$$

and its addition is

$$B = \sum_{-m}^{m'} I_n^2 + I_n'^2 = \left(K_u^+ - K_u^-\right) \frac{d_t \Delta}{\cos\chi} \sum_{-1}^{1} \left[\frac{a_n}{d_1} \tanh\left(\frac{d_t}{\Delta} a_n \cos\chi + \frac{y}{\Delta} \sin\chi \right) + \right.$$
$$+ \frac{1}{d_2} \left(a_n - \frac{d_1}{d_t} \right) \tanh\left(\frac{d_t}{\Delta} \left(a_n - 1 \right) \cos\chi + \frac{y}{\Delta} \sin\chi \right) -$$
$$\left. - \left(a_n \left(\frac{1}{d_1} + \frac{1}{d_2} \right) - \frac{d_1}{d_2 d_t} \right) \tanh\left(\frac{d_t}{\Delta} \left(a_n - \frac{d_1}{d_t} \right) \cos\chi + \frac{y}{\Delta} \sin\chi \right) \right] \tag{76}$$

It is convenient to work on tanh addends and log addends separately when taking into account I_n^3 and $I_n'^3$. In the case of tanh terms it can be written

$$c_n = \left(K_u^+ - K_u^-\right) \frac{Q\Delta}{\cos\chi} \left[\frac{d_t}{d_1} \Big[a_n \tanh\zeta_{min} - \left(a_n - \frac{d_1}{d_t} \right) \tanh\zeta_{max} \Big] + \right.$$
$$\left. + \frac{d_t}{d_2} \Big[\left(a_n - 1 \right) \tanh\zeta'_{max} - \left(a_n - \frac{d_1}{d_t} \right) \tanh\zeta'_{min} \Big] \right] \tag{77}$$

where terms with y has been discarded as they vanish when making the integral along y. It can be checked that for $n > 1$ and $n < -1$ the integral vanishes again. Then, taking into account that $\zeta_{max} = \zeta'_{min}$ it is possible to write the addition

$$C = -\left(K_u^+ - K_u^-\right) \frac{d_t \Delta}{\cos\chi} \sum_{-1}^{1} \left[\frac{a_n}{d_1} \tanh\left[\left(\frac{d_t}{\Delta} a_n \cos\chi + \frac{y}{\Delta} \sin\chi \right) \right] - \right.$$
$$- \left(\frac{1}{d_1} + \frac{1}{d_2} \right) \left(a_n - \frac{d_1}{d_t} \right) \tanh\left[\left(\frac{d_t}{\Delta} \left(a_n - \frac{d_1}{d_t} \right) \cos\chi + \frac{y}{\Delta} \sin\chi \right) \right] +$$
$$\left. + \frac{1}{d_2} \left(a_n - 1 \right) \tanh\left[\left(\frac{d_t}{\Delta} \left(a_n - 1 \right) \cos\chi + \frac{y}{\Delta} \sin\chi \right) \right] \right] \tag{78}$$

It can be checked that the addition of B (76) and C (78) cancels out most of their addends

$$B + C = \left(K_u^+ - K_u^-\right) \frac{d_t \Delta}{\cos\chi} \sum_{-1}^{1} \left[\frac{1}{d_2} \left(1 - \frac{d_1}{d_t} \right) \tanh\left[\left(\frac{d_t}{\Delta} \left(a_n - 1 \right) \cos\chi + \frac{y}{\Delta} \sin\chi \right) \right] + \right.$$
$$\left. + \left(\frac{d_1}{d_2 d_t} - \frac{d_t}{d_1 d_2} \frac{d_1}{d_t} \right) \tanh\left[\left(\frac{d_t}{\Delta} \left(a_n - \frac{d_1}{d_t} \right) \cos\chi + \frac{y}{\Delta} \sin\chi \right) \right] \right] =$$
$$= \left(K_u^+ - K_u^-\right) \frac{\Delta}{\cos\chi} \sum_{-1}^{1} \left[\tanh\left[\left(\frac{d_t}{\Delta} \left(a_n - 1 \right) \cos\chi + \frac{y}{\Delta} \sin\chi \right) \right] - \right.$$
$$\left. - \tanh\left[\left(\frac{d_t}{\Delta} \left(a_n - \frac{d_1}{d_t} \right) \cos\chi + \frac{y}{\Delta} \sin\chi \right) \right] \right] \tag{79}$$

and finally summing A (73) up it is obtained

$$A + B + C = \frac{2\Delta}{\cos\chi} K_u^- \tag{80}$$

where the assumption that $\Delta << d_t$ has been used. Finally, the log terms from I_n^3 and $I_n'^3$ must be considered. It can be checked that for $|n| > 1$

$$\frac{\Delta}{d_1}\log\left(\frac{\cosh\zeta_{min}}{\cosh\zeta_{max}}\right) \approx \frac{n}{|n|} \qquad \frac{\Delta}{d_2}\log\left(\frac{\cosh\zeta'_{max}}{\cosh\zeta'_{min}}\right) \approx -\frac{n}{|n|}$$

So the addition of log terms is

$$\begin{aligned} C' &= \frac{(K_u^+ - K_u^-)\,\Delta}{\cos^2\chi}\sum_{-m}^{m'}\frac{\Delta}{d_1}\log\left(\frac{\cosh\zeta_{min}}{\cosh\zeta_{max}}\right) + \frac{\Delta}{d_2}\log\left(\frac{\cosh\zeta'_{max}}{\cosh\zeta'_{min}}\right) = \\ &= \frac{(K_u^+ - K_u^-)\,\Delta}{\cos^2\chi}\Big[\,(m'-2) - (m-2) - (m'-2) + (m-2)\,\Big] + \\ &+ \frac{(K_u^+ - K_u^-)}{\cos^2\chi}\sum_{-1}^{1}\left[\frac{\Delta^2}{d_1}\log\left(\frac{\cosh\left(\frac{d_t}{\Delta}a_n\right)}{\cosh\left(\frac{d_t}{\Delta}\left(a_n - \frac{d_1}{d_t}\right)\right)}\right) + \frac{\Delta^2}{d_2}\log\left(\frac{\cosh\left(\frac{d_t}{\Delta}\left(a_n-1\right)\right)}{\cosh\left(\frac{d_t}{\Delta}\left(a_n - \frac{d_1}{d_t}\right)\right)}\right)\right] \end{aligned} \tag{81}$$

Taking into account both, (80) and (81), the final expression for the linear magnetic anisotropy energy density can be written as

$$\begin{aligned} \lambda_{anis} = \frac{w\Delta}{\cos\chi}\Bigg[2K_u^- + \frac{(K_u^+ - K_u^-)}{\cos\chi}\sum_{-1}^{1}\frac{\Delta}{d_1}\log\left(\frac{\cosh\left(\frac{d_t}{\Delta}a_n\right)}{\cosh\left(\frac{d_t}{\Delta}\left(a_n - \frac{d_1}{d_t}\right)\right)}\right) + \\ + \frac{\Delta}{d_2}\log\left(\frac{\cosh\left(\frac{d_t}{\Delta}\left(a_n-1\right)\right)}{\cosh\left(\frac{d_t}{\Delta}\left(a_n - \frac{d_1}{d_t}\right)\right)}\right)\Bigg] \end{aligned} \tag{82}$$

Expression (82) is still valid even though $\Delta << d_t$ is not true if just the summation is extended to take into account more slopes. In order to derive the expression used in chapters 11 and 12 it must be noticed that the limit when $d_2 \to 0$ is

$$\lim_{d_2\to 0}\frac{1}{d_2}\log\frac{\cosh\frac{d_t a_n}{\Delta}}{\cosh\frac{d_t\left(a_n - \frac{d_1}{d_t}\right)}{\Delta}} = \frac{1}{\Delta}\tanh\left(\frac{d_1}{\Delta}\left(1 - a_n\right)\right)$$

Magnetostatic terms

From equation (2.44) it is possible to derive the term accounting for the applied field

$$\begin{aligned} \lambda_{ext} &= -\mu_0\iint M_s\left(H_x\sin\theta\cos\varphi + H_y\sin\theta\sin\varphi + H_z\cos\theta\right)dxdy = \\ &= -\mu_0 M_s\frac{\Delta w}{\cos\chi}\left(\pi H_x\cos\Phi + \pi H_y\sin\Phi + 2QH_z q\frac{\cos\chi}{\Delta}\right) \end{aligned} \tag{83}$$

The accountant for the demagnetizing energy requires computing an expression for the demagnetizing field, $\vec{H}_{dmg} = -\mathcal{N}\vec{M}$. There always exists a proper coordinate system for which the demagnetizing tensor $\mathcal{N}$ is diagonal, so the demagnetizing field depends only on the diagonal components, N_x, N_y and N_z. Usually, this system coincides with that defined in figure 4.1. However, when $\chi \neq 0$, both systems differ by this angle χ as it is represented in figure 6. This means that expression (2.49) depends on ω rather than φ.

$$\begin{aligned} u_{dmg} &= \frac{1}{2}\mu_0 M_s^2 \left(N_x m_x^2 + N_y m_y^2 + N_z m_z^2\right) = \\ &= \frac{1}{2}\mu_0 M_s^2 \left[\sin^2\theta \left(N_x \cos^2(\varphi - \chi) + N_y \sin^2(\varphi - \chi) - N_z\right) + N_z\right] \end{aligned} \tag{84}$$

It is possible to drop off the constant since it does not affect the behavior of the system. The linear demagnetizing energy density reads

$$\begin{aligned} \lambda_{dmg} &= \frac{1}{2}\mu_0 M_s^2 \iint \sin^2\theta \left(N_x \cos^2(\varphi - \chi) + N_y \sin^2(\varphi - \chi) - N_z\right) dxdy = \\ &= \frac{\Delta \mu_0 M_s^2 w}{\cos\chi} \left(N_x \cos^2(\Phi - \chi) + N_y \sin^2(\Phi - \chi) - N_z\right) \end{aligned} \tag{85}$$

Dzyaloshinskii-Moriya interaction

Finally, the term accounting for the DMI can be obtained from (2.51) taking into account that in our case $\vec{u}_n = \vec{u}_z$

$$\begin{aligned} u_{DMI} &= D\left[(\vec{m}\vec{u}_n)\,\vec{\nabla}\vec{m} - \vec{m}\vec{\nabla}\,(\vec{m}\vec{u}_z)\right] = \\ &= D\left[m_z\frac{\partial m_x}{\partial x} - m_x\frac{\partial m_z}{\partial x} + m_z\frac{\partial m_y}{\partial y} - m_y\frac{\partial m_z}{\partial y}\right] \end{aligned} \tag{86}$$

This equation can be worked out so finally it can be expressed as

$$\begin{aligned} u_{DMI} &= D\left[\cos\theta\left(\cos\theta\cos\varphi\frac{\partial\theta}{\partial x} - \sin\theta\sin\varphi\frac{\partial\varphi}{\partial x}\right) + \sin\theta\cos\varphi\sin\theta\frac{\partial\theta}{\partial x} + \right. \\ &\left. + \cos\theta\left(\cos\theta\sin\varphi\frac{\partial\theta}{\partial y} + \sin\theta\cos\varphi\frac{\partial\varphi}{\partial y}\right) + \sin^2\theta\sin\varphi\frac{\partial\theta}{\partial y}\right] = \\ &= D\left[\cos\varphi\frac{\partial\theta}{\partial x} + \sin\varphi\frac{\partial\theta}{\partial y} - \sin\theta\cos\theta\sin\varphi\frac{\partial\varphi}{\partial x} + \sin\theta\cos\theta\cos\varphi\frac{\partial\varphi}{\partial y}\right] \end{aligned} \tag{87}$$

Recalling that φ is constant along the whole strip the expression for the linear DMI energy density can be written as

$$\begin{aligned} \lambda_{DMI} &= D\iint\left[\cos\varphi\frac{\partial\theta}{\partial x} + \sin\varphi\frac{\partial\theta}{\partial y}\right]dxdy = \\ &= D\iint\left[\cos\varphi Q\frac{\sin\theta}{\Delta}\cos\chi + \sin\varphi Q\frac{\sin\theta}{\Delta}\sin\chi\right]dxdy = \\ &= \frac{Q\pi D w}{\cos\chi}\left(\cos\Phi\cos\chi + \sin\Phi\sin\chi\right) = \frac{Q\pi D w}{\cos\chi}\cos(\Phi - \chi) \end{aligned} \tag{88}$$

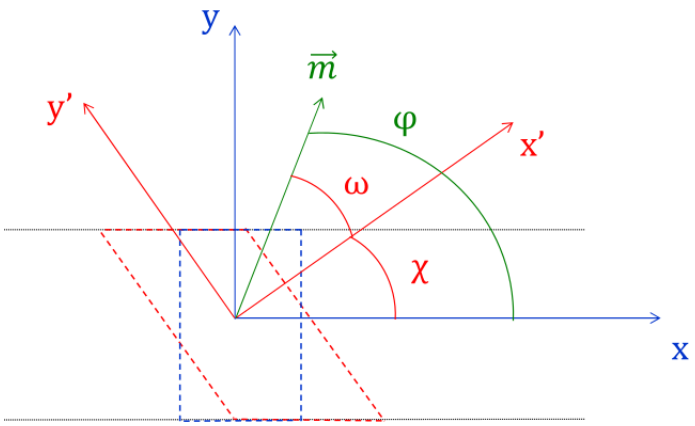

Fig. 6: DW tilting angle and relationship between tilting angle χ, DW orientation Φ and ω. Since demagnetizing tensor is diagonal for the primed system, is ω the angle to be used for the demagnetizing energy.

Final expressions and comments

Adding all contributions up leads to an expression for the linear energy density

$$\begin{aligned}\lambda = \frac{w}{\cos\chi}\Bigg[&\frac{2A}{\Delta} - \mu_0 M_s \Delta\left(\pi H_x \cos\Phi + \pi H_y \sin\Phi + 2QH_z q\frac{\cos\chi}{\Delta}\right) + \\ &+ \Delta\mu_0 M_s^2\left(N_x\cos^2(\Phi-\chi) + N_y\sin^2(\Phi-\chi) - N_z\right) + \\ &+ Q\pi D\cos(\Phi-\chi) + 2\Delta K_u^- + \frac{\left(K_u^+ - K_u^-\right)\Delta^2}{\cos\chi}S(q,\Delta)\Bigg]\end{aligned} \tag{89}$$

where S is

$$S(q,\Delta) = \sum_{-1}^{1}\frac{1}{d_1}\log\left(\frac{\cosh\left(\frac{d_t}{\Delta}a_n\right)}{\cosh\left(\frac{d_t}{\Delta}\left(a_n - \frac{d_1}{d_t}\right)\right)}\right) + \frac{1}{d_2}\log\left(\frac{\cosh\left(\frac{d_t}{\Delta}\left(a_n-1\right)\right)}{\cosh\left(\frac{d_t}{\Delta}\left(a_n - \frac{d_1}{d_t}\right)\right)}\right)$$

Taking into account (89), (19), (20), (21) and (22) it is possible to derive four equations describing the system dynamics

$$\begin{aligned}\frac{\partial\lambda}{\partial q} = &-\mu_0 w M_s 2QH_z + \frac{\left(K_u^+ - K_u^-\right)w}{\cos^2\chi}\sum_{-1}^{1}\frac{\Delta}{d_1}\left(\tanh\frac{d_t}{\Delta}a_n - \tanh\frac{d_t}{\Delta}\left(a_n - \frac{d_1}{d_t}\right)\right) + \\ &\frac{\Delta}{d_2}\left(\tanh\frac{d_t}{\Delta}\left(a_n-1\right) - \tanh\frac{d_t}{\Delta}\left(a_n - \frac{d_1}{d_t}\right)\right) = \\ = -\frac{\mu_0 M_s w}{\gamma_0}\Big[&\alpha\frac{2\dot{q}}{\Delta}\cos\chi + Q2\dot{\Phi} - \frac{2b_j\xi}{\Delta}\left(\frac{j_x}{J}\cos\chi + \frac{j_y}{J}\sin\chi\right) - \\ &-\gamma_0 Q2H_{z,th} - \gamma_0 Q\pi H_{SH}\left(j_x\cos\Phi + j_y\sin\Phi\right)\Big]\end{aligned} \tag{90}$$

$$\begin{aligned}\frac{\partial\lambda}{\partial\varphi} &= \frac{w}{\cos\chi}\Big(\mu_0 M_s\Delta\left(\pi H_x\sin\Phi-\pi H_y\cos\Phi\right)-Q\pi D\sin\left(\Phi-\chi\right)+\\ &+\Delta\mu_0 M_s^2\sin 2\left(\Phi-\chi\right)\left(N_y-N_x\right)\Big)=\\ &=\frac{2\mu_0 M_s w}{\gamma_0}\Big[Q\dot{q}-\frac{\alpha\Delta\dot{\Phi}}{\cos\chi}-Qb_j\left(\frac{j_x}{J}+\frac{j_y}{J}\tan\chi\right)+\\ &+\gamma_0\frac{\Delta}{\cos\chi}\frac{\pi}{2}\left(-H_{x,th}\sin\Phi+H_{y,th}\cos\Phi\right)+\\ &+\gamma_0 H_{Ra}\frac{\Delta}{\cos\chi}\frac{\pi}{2}\left(j_x\cos\Phi+j_y\sin\Phi\right)\Big]\end{aligned} \tag{91}$$

$$\begin{aligned}\frac{\partial\lambda}{\partial\Delta} &= \frac{w}{\cos\chi}\Big(\frac{-2A}{\Delta^2}-\mu_0 M_s\left(\pi H_x\cos\Phi+\pi H_y\sin\Phi\right)+\\ &+\mu_0 M_s^2\left(N_x\cos^2\left(\Phi-\chi\right)+N_y\sin^2\left(\Phi-\chi\right)-N_z\right)\Big)+\\ &+\frac{2wK_u^-}{\cos\chi}+\frac{2\Delta w}{\cos\chi}\frac{\left(K_u^+-K_u^-\right)}{\cos\chi}S\left(q,\Delta\right)-\\ &-\frac{d_t w}{d_1}\frac{\left(K_u^+-K_u^-\right)}{\cos^2\chi}\sum_{-1}^{1}\left(\tanh\frac{d_t}{\Delta}a_n-\tanh\frac{d_t}{\Delta}\left(a_n-\frac{d_1}{d_t}\right)\right)-\\ &-\frac{d_t w}{d_2}\frac{\left(K_u^+-K_u^-\right)}{\cos^2\chi}\left(\tanh\frac{d_t}{\Delta}\left(a_n-1\right)-\tanh\frac{d_t}{\Delta}\left(a_n-\frac{d_1}{d_t}\right)\right)=\\ &=-\frac{\mu_0 M_s}{\gamma_0}\alpha\frac{w}{\cos\chi}\frac{\pi^2}{6}\Big(\tan\chi\dot{\chi}+\frac{\dot{\Delta}}{\Delta}\Big)\end{aligned} \tag{92}$$

$$\begin{aligned}\frac{\partial\lambda}{\partial\chi} &= \lambda\tan\chi+\frac{w}{\cos\chi}\left[2Q\mu_0 M_s H_z q\sin\chi+Q\pi D\sin\left(\Phi-\chi\right)\right]-\\ &-\frac{w}{\cos\chi}\Delta\mu_0 M_s^2\frac{\sin 2\left(\Phi-\chi\right)}{2}\left(N_y-N_x\right)+\\ &+\frac{\left(K_u^+-K_u^-\right)w\Delta^2}{\cos^2\chi}\tan\chi S\left(q,\Delta\right)=\\ &=-\frac{\mu_0 M_s}{\gamma_0}\alpha\left[\frac{\pi^2}{6}\frac{w\Delta}{\cos\chi}\tan^2\chi\dot{\chi}+\frac{2}{\Delta\cos^3\chi}\frac{w^3}{12}\dot{\chi}+\frac{\pi^2}{6}\frac{\tan\chi}{\cos\chi}w\dot{\Delta}\right]\end{aligned} \tag{93}$$

These expressions can be simplified by defining some additional parameters

$$H_D=-\frac{\pi D}{2\mu_0 M_s\Delta}\qquad H_k=M_s\left(N_x-N_y\right)$$

$$H_r=\frac{\left(K_u^+-K_u^-\right)}{2\mu_0 M_s}\qquad H_{exch}=\frac{A}{\mu_0 M_s\Delta^2}$$

$$\begin{aligned}r\left(q,\Delta\right)=\sum_{-1}^{1}\frac{\Delta}{d_1}&\left(\tanh\frac{d_t}{\Delta}a_n-\tanh\frac{d_t}{\Delta}\left(a_n-\frac{d_1}{d_t}\right)\right)+\\ &+\frac{\Delta}{d_2}\left(\tanh\frac{d_t}{\Delta}\left(a_n-1\right)-\tanh\frac{d_t}{\Delta}\left(a_n-\frac{d_1}{d_t}\right)\right)\end{aligned}$$

The above expressions become now

$$\begin{aligned}\alpha\frac{\dot{q}}{\Delta}\cos\chi + Q\dot{\Phi} = \gamma_0\Big[&QH_z + \frac{b_j\xi}{\gamma_0\Delta}\left(\frac{j_x}{J}\cos\chi + \frac{j_y}{J}\sin\chi\right) + QH_{z,th} + \\ &+ Q\frac{\pi}{2}H_{SH}\left(j_x\cos\Phi + j_y\sin\Phi\right) - \frac{H_r}{\cos^2\chi}r\left(q,\Delta\right)\Big]\end{aligned} \tag{94}$$

$$\begin{aligned}Q\frac{\dot{q}}{\Delta}\cos\chi - \alpha\dot{\Phi} = \gamma_0\Big[&\left(\frac{\pi}{2}H_x\sin\Phi - \frac{\pi}{2}H_y\cos\Phi\right) + QH_D\sin\left(\Phi-\chi\right) - \\ &- H_k\frac{\sin 2\left(\Phi-\chi\right)}{2} + Q\frac{b_j}{\gamma_0\Delta}\cos\chi\left(\frac{j_x}{J} + \frac{j_y}{J}\tan\chi\right) + \\ &+ \frac{\pi}{2}\left(H_{x,th}\sin\Phi - H_{y,th}\cos\Phi\right) - H_{Ra}\frac{\pi}{2}\left(j_x\cos\Phi + j_y\sin\Phi\right)\Big]\end{aligned} \tag{95}$$

$$\begin{aligned}\tan\chi\dot{\chi} + \frac{\dot{\Delta}}{\Delta} = \frac{12\gamma_0}{\pi^2\alpha}\Bigg[&H_{exch} + \left(\frac{\pi}{2}H_x\cos\Phi + \frac{\pi}{2}H_y\sin\Phi\right) - \\ &- \frac{M_s}{2}\left(N_x\cos^2\left(\Phi-\chi\right) + N_y\sin^2\left(\Phi-\chi\right) - N_z\right) - \\ &- \frac{K_u^-}{\mu_0 M_s} - \frac{2\Delta}{\cos\chi}H_r S\left(q,\Delta\right) + \frac{d_t}{\Delta\cos\chi}H_r r\left(q,\Delta\right)\Bigg]\end{aligned} \tag{96}$$

$$\begin{aligned}\tan\chi\left(\tan\chi\dot{\chi} + \frac{\dot{\Delta}}{\Delta}\right) + \frac{w^2\dot{\chi}}{\Delta^2\pi^2\cos^2\chi} = \frac{12\gamma_0}{\pi^2\alpha}\Bigg[&\Bigg[\frac{\pi}{2}H_x\cos\Phi + \frac{\pi}{2}H_y\sin\Phi - \\ &- H_{exch} - \frac{K_u^-}{\mu_0 M_s} + QH_D\cos\omega - \\ &- \frac{M_s}{2}\left(N_x\cos^2\omega + N_y\sin^2\omega - Nz\right)\Bigg]\tan\chi + \\ &+ \left(QH_D - \frac{H_k}{2}\cos\omega\right)\sin\omega\Bigg]\end{aligned} \tag{97}$$

The equation describing the time derivative of the DW position q is calculated multiplying (94) by $Q\alpha$ and adding (95)

$$\begin{aligned}\dot{q} = Q\frac{v_0}{\cos\chi}\Big[&\alpha\left(H_z + H_{z,th} - \frac{QH_r}{\cos^2\chi}r\left(q,\Delta\right)\right) + \\ &+ \frac{\pi}{2}\left(j_x\cos\Phi + j_y\sin\Phi\right)\left(\alpha H_{SH} - H_{Ra}\right) + \\ &+ \frac{\pi}{2}\left(H_x + H_{x,th}\right)\sin\Phi - \frac{\pi}{2}\left(H_y + H_{y,th}\right)\cos\Phi + \\ &+ \left(QH_D - H_k\cos\left(\Phi-\chi\right)\right)\sin\left(\Phi-\chi\right) + \\ &+ Q\frac{b_j}{\gamma_0\Delta}\left(\frac{j_x}{J}\cos\chi + \frac{j_y}{J}\sin\chi\right)\left(1+\alpha\xi\right)\Big]\end{aligned} \tag{98}$$

where $v_0 = \dfrac{\Delta\gamma_0}{1+\alpha^2}$. In the same way, the time derivative of Φ is derived multiplying (95) by $-Q\alpha$ and adding (94)

$$\begin{aligned}\dot{\Phi} = \frac{v_0}{\Delta}\Big[& H_z + H_{z,th} + Q\frac{b_j}{\gamma_0\Delta}\left(\frac{j_x}{J}\cos\chi + \frac{j_y}{J}\sin\chi\right)(\xi-\alpha) + \\ & + \frac{\pi}{2}\left(j_x\cos\Phi + j_y\sin\Phi\right)\left(H_{SH} + \alpha H_{Ra}\right) - \frac{QH_r}{\cos^2\chi}r\left(q,\Delta\right) - \\ & - \alpha\frac{\pi}{2}\left(H_x + H_{x,th}\right)\sin\Phi + \alpha\frac{\pi}{2}\left(H_y + H_{y,th}\right)\cos\Phi + \\ & + \alpha\left(H_k\cos\left(\Phi-\chi\right) - QH_D\right)\sin\left(\Phi-\chi\right)\Big]\end{aligned} \tag{99}$$

The time derivative of χ can be computed in a similar way multiplying (96) by $-\tan\chi$ and summing it to (97)

$$\begin{aligned}\dot{\chi} = \frac{12\gamma_0}{\alpha}\left(\frac{\Delta}{w}\right)^2\Bigg[& QH_D\sin\Phi\cos\chi - H_{exch}\sin 2\chi - \\ & - \frac{d_t}{\Delta}H_r r\left(q,\Delta\right)\sin\chi - H_k\frac{\sin 2\left(\Phi-\chi\right)}{4}\cos^2\chi\Bigg]\end{aligned} \tag{100}$$

Now it is possible to find the time derivative of Δ from (96) taking into account (100)

$$\begin{aligned}\frac{\dot{\Delta}}{\Delta} = \frac{12\gamma_0}{\pi^2\alpha}\Bigg[& H_{exch}\left(1 + 2\left(\frac{\pi\Delta}{w}\right)^2\sin^2\chi\right) + \frac{\pi}{2}\left(H_x\cos\Phi + H_y\sin\Phi\right) - \\ & - \frac{M_s}{2}\left(N_x\cos^2\left(\Phi-\chi\right) + N_y\sin^2\left(\Phi-\chi\right) - N_z\right) - \frac{K_u^-}{\mu_0 M_s} - \\ & - \frac{2\Delta}{\cos\chi}H_r S\left(q,\Delta\right) + \frac{d_t}{\Delta\cos\chi}H_r r\left(q,\Delta\right)\left(1 + \left(\frac{\pi\Delta}{w}\right)^2\sin^2\chi\right) - \\ & - \left(\frac{\pi\Delta}{w}\right)^2\left(QH_D - \frac{H_k}{2}\sin\left(\Phi-\chi\right)\cos\chi\right)\sin\Phi\sin\chi\Bigg]\end{aligned} \tag{101}$$

Equations (98), (99), (100) and (101) describe in a simplified manner the dynamic behaviour of the sample.

Acronyms

1DM	One dimensional model
AC	Alternating current
AHE	Anomalous Hall effect
BC	Boundary condition
BDW	Bloch wall
DC	Direct current
DW	Domain wall
DDW	Dzyaloshinskii domain wall
FFT	Fast Fourier Transform
FM	Ferromagnetic
GMR	Giant magnetoresistance
GPU	Graphics processor unit
HM	Heavy metal
iDMI	Interfacial Dzyaloshinskii-Moriya interaction
IEC	Interlayer exchange coupling
LLB	Landau-Lifshitz-Bloch
LLG	Landau-Lifshitz-Gilbert
MOKE	Magneto-optical Kerr effect
MRAM	Magnetic ramdon access memory
ODE	Ordinary diferential equation
PMA	Perpendicular magnetic anisotropy
NDW	Néel wall
RF	Radio frequency
RKKY	Ruderman-Kittel-Kasuya-Yosida
SHE	Spin Hall effect
SOC	Spin-orbit coupling
SOT	Spin-orbit torque
STT	Spin transfer torque
μMag	Micromagnetic

List of Symbols

A	Exchange constant
D	Dzyaloshinkii-Moriya parameter
$\vec{H}_{eff}$	Effective field
$\vec{H}_{th}$	Thermal field
$\hbar$	Reduced Planck's constant
K_u	Uniaxial anisotropy constant
L	Lagrangian
l_V	Lagrangian volume density
M_s	Saturation magnetization
$\vec{m}$	Normalized magnetization
N_i	Demagnetizing factors
q	Domain wall position
u_S	Potential energy surface density
u_V	Potential energy volume density
α	Gilbert damping parameter
γ	Gyromagnetic ratio
Δ	Domain wall width
θ	Polar angle
θ_{SH}	Spin Hall angle
λ	Linear energy density
μ	Magnetic dipole
μ	Vacuum permeability
σ	Surface energy density
τ	Torque
φ	Azimuthal angle
Φ	Domain wall in-plane angle
χ	Tilting angle

$$H_D = -\frac{\pi D}{2\mu_0 M_s \Delta}$$

$$H_k = M_s \left(N_x - N_y\right)$$

$$H_{SH} = \frac{\hbar \theta_{SH}}{2et\mu_0 M_s}$$

List of Figures

List of Tables

List of Publications

1. L. Sánchez-Tejerina, Ó. Alejos, E. Martínez, and J.M. Muñoz. Asymmetric driven dynamics of Dzyaloshinskii domain walls in ultrathin ferromagnetic strips with perpendicular magnetic anisotropy. *J. Magn. Magn. Mater.*, 409(Supplement C):155 – 162, 2016. doi:10.1016/j.jmmm.2016.02.067

2. L. Sánchez-Tejerina, O. Alejos, and E. Martínez. Steady-state configurations of dzyaloshinskii domain walls driven by field and current. *J. Magn. Magn. Mater.*, 423(Supplement C):405 – 410, 2017. doi:10.1016/j.jmmm.2016.09.116

3. E. Martínez, O. Alejos, M. A. Hernandez, V. Raposo, L. Sanchez-Tejerina, and S. Moretti. Angular dependence of current-driven chiral walls. *Appl. Phys. Express*, 9:063008, 2016. doi:10.7567/APEX.9.063008

4. O. Alejos, V. Raposo, M. A. Hernandez, L. Sanchez-Tejerina, S. Moretti, and E. Martinez. Micromagnetic analysis of geometrically controlled current-driven magnetization switching. *AIP Adv.*, 7(5):055909, 2017. doi:10.1063/1.4973749

5. O. Alejos, E. Martínez, V. Raposo, L. Sánchez-Tejerina, and M. A. Hernández-López. Chiral-triggered magnetization switching in patterned media. *Appl. Phys. Lett.*, 110(7):072407, 2017. doi:10.1063/1.4976693

6. O. Alejos, V. Raposo, L. Sánchez-Tejerina, and E. Martínez. Efficient and controlled domain wall nucleation for magnetic shift registers. *Sci. Rep.*, 7:11909, 2017. doi:10.1038/s41598-017-12230-9

7. L. Sánchez-Tejerina, E. Martínez, V. Raposo, and O. Alejos. Current-driven domain wall motion based memory devices: Application to a ratchet ferromagnetic strip. *AIP Adv.*, 8(4):047302, 2018. doi:10.1063/1.4993750

8. O. Alejos, V. Raposo, L. Sanchez-Tejerina, R. Tomasello, G. Finocchio, and E. Martinez. Current-driven domain wall dynamics in ferromagnetic layers synthetically exchange-coupled by a spacer: A micromagnetic study. *Journal of Applied Physics*, 123(1):013901, 2018. doi:10.1063/1.5009739

9. Luis Sánchez-Tejerina, Óscar Alejos, Víctor Raposo, and Eduardo Martínez. Current-driven domain wall motion along ferromagnetic strips with periodically-modulated perpendicular anisotropy. *Journal of Applied Physics*, 2018. doi:10.1063/1.5036601